Rialtas na hÉireann
Government of Ireland

Geological Survey
Suirbhéireacht Gheolaíochta
Ireland | Éireann

Variability in the Tellus Waterford Test-line FEM Data

Geological Survey Ireland Report 2022

Geological Survey Ireland is a division of the Department of the Environment, Climate and Communications

Document Information

Project title: Variability in the Tellus Waterford Test-line FEM Data Date 17/11/2022		
Prepared By	**Date**	**Comment**
M. R. Muller	17/11/2022	

Reviewed By	**Date**	**Comment**
M. Ture	23/06/2022	Review of V1.0 draft
J. Hodgson	24/06/2022	Review of V1.0 draft

Approved By	**Date**	**Comment**
J. Hodgson	06/12/2022	

Version History

Ver. No.	**Ver. Date**	**Comment**	**Revised By**
1.0	22/06/2022	First draft	M. R. Muller
2.1	17/11/2022	Response to V1.0 review and completion of report	M. R. Muller
2.2	06/12/2022	Minor edits, Final version	J. A. Hodgson
2.3	09/12/2022	Disclaimer	J. A. Hodgson
2.4	22/12/2022	Maths symbology conversion errors	M. R. Muller

The Tellus Project

Tellus is a national programme to gather geochemical and geophysical data across the island of Ireland. The survey examines the chemical and physical properties of our soils, rocks and waters to inform the management of Ireland's environment and natural resources. The project is managed by Geological Survey, Ireland (GSI) and is funded by the Department of Environment, Climate and Communications (DECC).

For more information on the Tellus Project please visit www.tellus.ie

Disclaimer

Copyright

Citation

Muller, M. R. (2022) Variability in the Tellus Waterford Test-line FEM Data.
Geological Survey Ireland report.

Table of Contents

1 Introduction

Multiple repeat flights, flown at different times along test-lines in Waterford (Figures 1.1 to 1.4), provide opportunity to assess the variability and repeatability of Tellus airborne frequency-domain electromagnetic (FEM) data. As part of the Tellus airborne geophysics programme, repeat flights are flown along test-lines at the start and end of each survey period or survey block. Test-lines in Bundoran, Co. Donegal were used during the period 2011 to 2019, while the northern half of the country was surveyed. As Tellus survey operations moved into the southern half of the country, the Bundoran test-line was replaced by the Waterford test-line (located near the coastal town of Bunmahon) in 2019. The work of this report focusses only on the Waterford test-line data. Analysis of the Bundoran test-line data remains work for the future.

FEM data have been acquired along the Waterford test-line on five different occasions since 2019: 22 April 2019, 13 September 2019, 11 October 2020, 16 July 2021 and 22 September 2021. Three parallel lines are flown (Lines L1, L2 and L3, Figure 1.1), 100 m apart, on headings of 165° and 345° E of N (the standard Tellus traverse-line directions). The western and eastern lines (L1 and L3) are coincident with traverse lines flown within the Waterford data acquisition block and are flown with a nominal flight clearance of 60 m only in both heading directions.

The central Waterford test-line (L2) is flown with clearances of 60 m, 90 m, 120 m and 150 m in both heading directions. The 60 m clearance passes are repeated in both heading directions, providing four 60 m clearance passes on each occasion the test-line is flown. A total of 20 repeat passes, at 60 m clearance, along L2 are therefore provided by the five test-line sorties flown to date (Table 1.1).

The line name nomenclature in Table 1.1 follows the format LHHHDAV.YY, where: L = line number, 1, 2 or 3 (from west to east); H = nominal flight-height in metres ('060' in the case of the lines assessed in this report); D = flight direction, either 0 (for northbound, on heading 345° E of N) or 1 (for southbound, on heading 165° E of N); A = attempt number, starts at 1, increments for each new test flight; V = version number, starts at 0, increments for each pass within a test flight; and Y = year of flights. In order to distinguish between the two test-flight sorties flown in 2021, A = 1 for the earlier sortie in July and A = 2 for the later sortie in September. In short, flight-lines with the last three digits (before .YY) equal to or greater than 100 were flown on a heading of 165° E of N, while those with the last three digits less than 100 were flown on 345° E of N.

Table 1.1: Summary of repeat flights flown on central Waterford test-line L2 with 60 m nominal clearance above ground level. Line length and number of data points correspond with the line extents inside the onshore polygon of Figures 1.1 and 1.2. Note that the July series of flights flown in 2021 is referred to as the '2021.1' series, while the September series of 2021 is referred to as the '2021.2' series.

Series Name	Date	Line Number	Heading Direction (° E of N)	Average Clearance (m)	Number of Data Points	Line Length (m)
2018	22/04/2019	L2060010.18	345	65.7	666	4412
		L2060011.18	345	65.5	694	4413
		L2060110.18	165	61.2	830	4416
		L2060111.18	165	63.2	806	4413
2019	13/09/2019	L2060000.19	345	66.4	744	4415
		L2060001.19	345	71.5	733	4419
		L2060100.19	165	62.5	778	4416
		L2060101.19	165	64.1	768	4414
2020	11/10/2020	L2060010.20	345	63.0	680	4415
		L2060011.20	345	66.0	683	4412
		L2060110.20	165	62.2	722	4416
		L2060111.20	165	63.1	723	4415
2021.1	16/07/2021	L2060010.21	345	63.6	737	4419
		L2060011.21	345	64.8	734	4411
		L2060110.21	165	63.1	707	4412
		L2060111.21	165	64.0	732	4414
2021.2	22/09/2021	L2060020.21	345	67.1	706	4415
		L2060021.21	345	67.6	697	4412
		L2060120.21	165	62.8	682	4412
		L2060121.21	165	64.4	704	4414

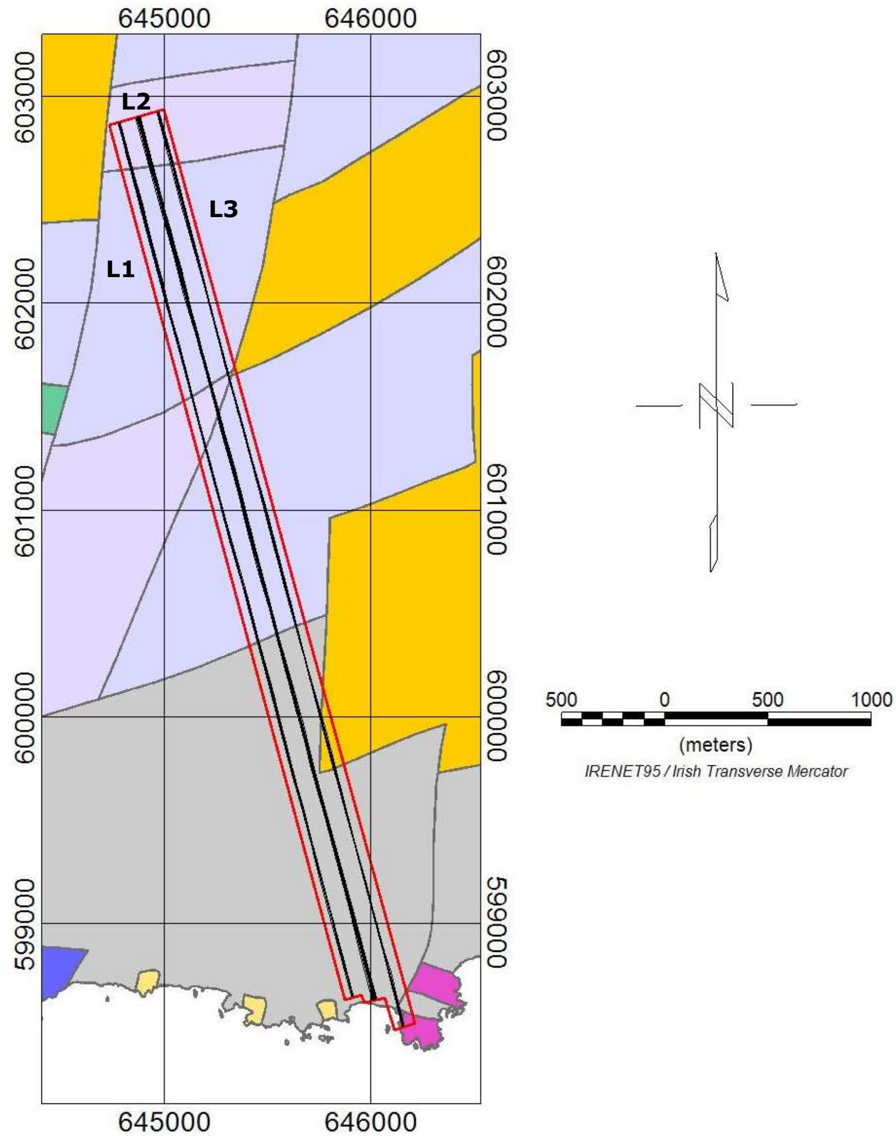

Figure 1.1: Location of Waterford test-lines (L1, L2 and L3) (black lines) overlaid on GSI 1:100K bedrock geology map. Extent of test-lines shown is limited to the onshore polygon shown (red polygon).

The mapped bedrock geology beneath the test-line (Figure 1.1) comprises Ordovician rocks of the Dunbrattin and Campile Formations, which respectively, are located beneath the southern 1,800 m of the line and the northern 2,600 m of the line. The Dunbrattin Formation consists of laminated shales and siltstones, while the Campile Formation comprises rhyolitic volcanics, grey and brown slates, grey, green and black shales and minor tuffs. A series of cross-cutting faults are present, with bedrock mostly dipping to the north. The area has been actively mined in the past for copper and is part of the

UNESCO Copper Coast Geopark. Overlying Quaternary sediments mostly consist of till derived from acidic volcanics (Figure 1.2) and are of variable thickness across the area. Thin slithers of alluvium are mapped in the area along river channels.

The test-line was chosen in an area with as little cultural (man-made or anthropogenic) noise as possible. The flight lines included an off-shore segment (not illustrated in the maps of Figures 1.1 to 1.4), while the land-side of the lines avoided overflying any residential properties, the latter partly to minimise cultural noise interference and partly to avoid nuisance to the landowners in the area. A series of small minor roads and low-voltage powerlines, and one high-voltage powerline, cross the test-line at various locations (Figures 1.3 and 1.4).

The analysis presented here is restricted to the on-shore portions of the twenty 60 m-clearance repeat lines on L2. Given that the EM imaging footprint is larger than the maximum 17.3 m swath-width of the 20 repeat lines and larger than the ~6 m sample interval along the flight-lines (see Sections 2.4 and 3.3), the geological signal recorded on each repeat line is expected, at least for each annual sortie of four repeat flights, to be very similar and show little variation from flight-to-flight. Temporal year-to-year or seasonal variability in the shallow (overburden) geology, and its resistivity structure, along the test-line may be significant, leading to variable FEM responses when comparing the data from each of the five annual sorties with each other. Groundwater in the vicinity of the test-line is likely to be characterised by high hydraulic gradients, due to the elevation of the terrain above sea-level (~38 – 82 m along the line) and the proximity to the coastline. A high hydraulic gradient provides potential for groundwater saturation levels – in the overburden, in the transition zone (the weathered layer above bedrock) and in the bedrock below the transition zone – to change quite rapidly with time and to be seasonally variable, giving rise to temporally variable resistivity structure and EM responses. The analysis that follows therefore considers both the 'intra-series' data variability (the variability between each of the four flights flown during the same sortie) and the 'inter-year' variability (the variability between each of the five repeat series, including the variability between all twenty repeat flights).

Analysis of the 60 m clearance repeat flights on Waterford test-lines L1 and L3, and of the 90 m, 120 m and 150 m clearance repeat flights on line L2, and assessment of the effect of increasing flight clearance on the FEM data, remains work for the future.

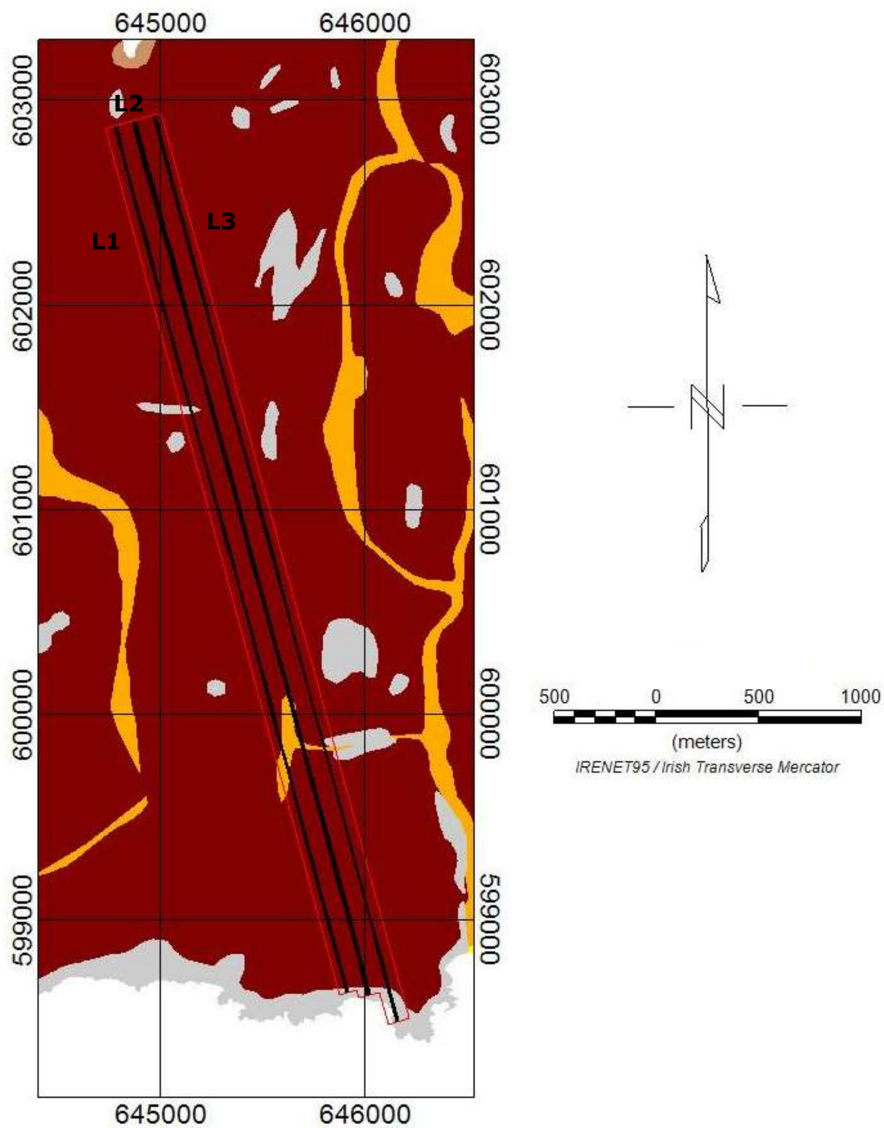

Figure 1.2: Location of Waterford test-lines (L1, L2 and L3) (black lines) overlaid on GSI 1:100K Quaternary geology map. Extent of test-lines shown is limited to the onshore polygon shown (red polygon).

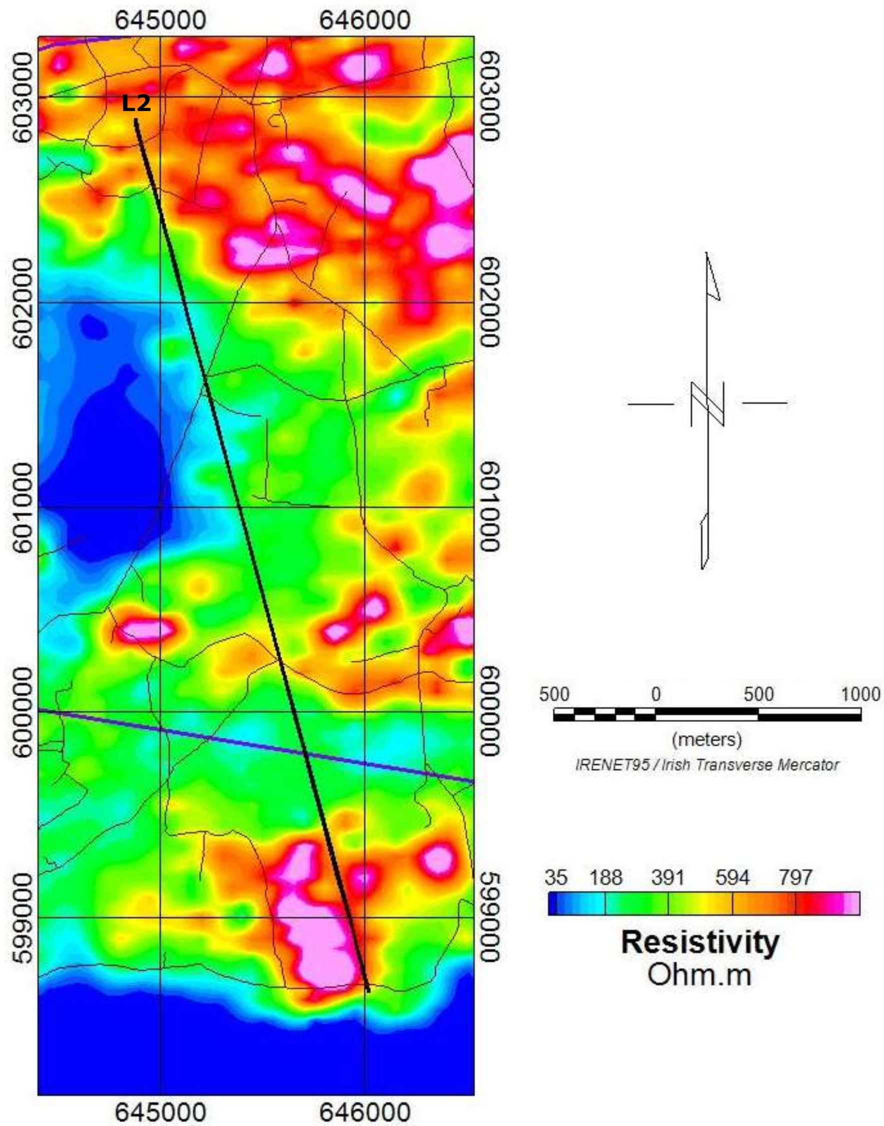

Figure 1.3: Location of Waterford test-line L2 (black line) overlaid on 12 kHz resistivity model grid from the Waterford Block survey (gridded resistivity data are from SGL delivery DLV2088, 'ExtendedRes12_Grid' data channel). Extent of test-line shown is limited to onshore portion. ESB high-voltage powerlines (purple lines) and road network (brown lines) also shown.

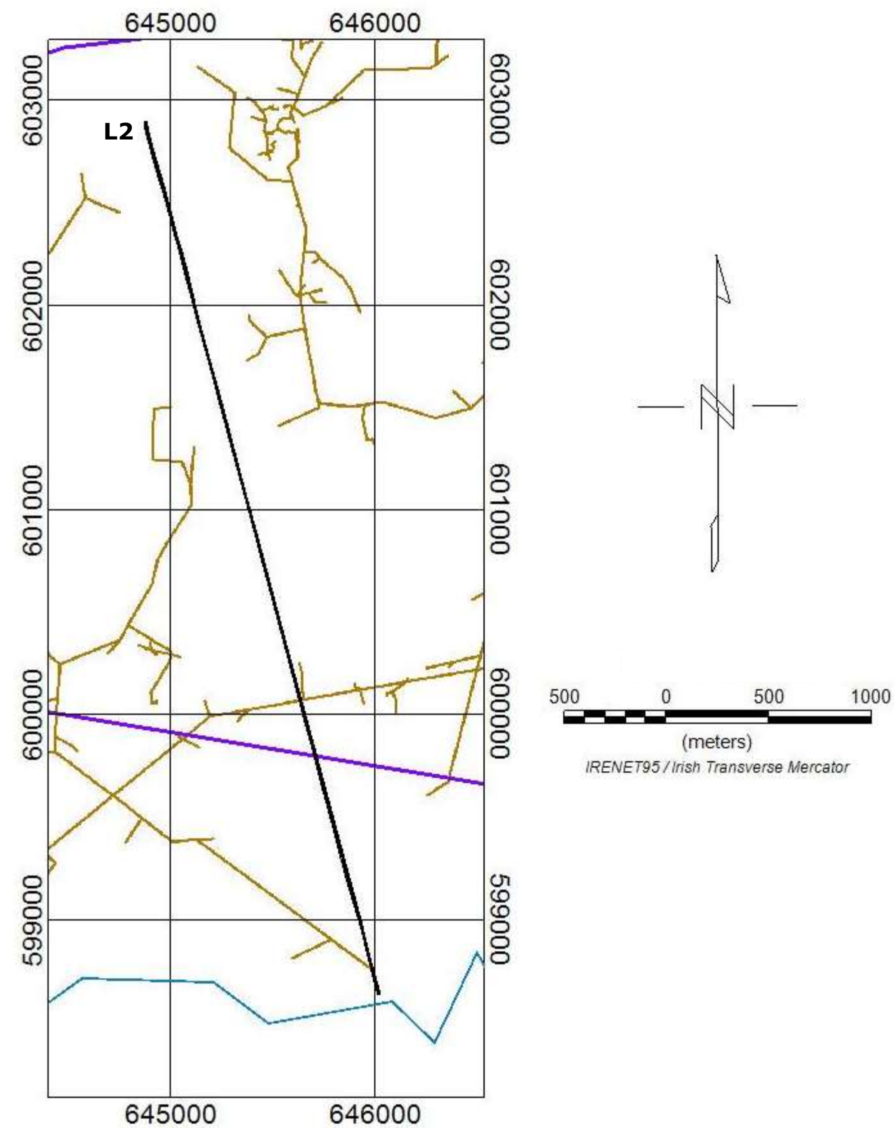

Figure 1.4: Location of Waterford test-line L2 (black line) overlaid on ESB low-voltage powerline network (brown lines). Extent of test-line shown is limited to onshore portion. ESB high-voltage powerlines (purple lines) and coarse Irish coastline (blue line) also shown.

Section 2 of the report discusses the strategy adopted for assessing the data variability (including the interpolation method and statistical parameters used), considers the lateral scale of the FEM footprint using estimates published in literature and examines the wavelength-scale of features recorded in the FEM responses along the test-line. The FEM data variability assessment that follows consists of four components of work:

i. <u>Flight-to-flight variability of the eight recorded EM responses (P09lev, P3lev, P12lev, P25lev, Q09lev, Q3lev, Q12lev and Q25lev)</u> **<u>(Section 3)</u>**. The metric used to assess the variability of the EM responses is the standard deviation of the mean (of the twenty repeat flights and of the four repeat flights of each series). Variability in flight clearance, speed, heading, power-line monitor, temperature, topography, perpendicular distance from the 'average' line and full 'swath-width' along the repeat lines is assessed to identify parameters that might correlate with and account for any variability observed in the EM responses.

ii. Application of Principal Component Analysis filters to the FEM response data **(Section 4)** to assess whether the filter application results in a reduction in the variability of the EM responses, potentially providing insights into the nature of the EM data signals – both geological and cultural 'noise' signals – that might account for the observed EM response variability.

iii. Flight-to-flight variability in resistivity models derived independently for each FEM frequency **(Section 5)**. Two resistivity datasets are evaluated: firstly, Sander Geophysics Limited's (SGL's) 'Extended Resistivity' models, and secondly, resistivity models generated using Geosoft's HEM inversion software. Potential variability in the FEM responses due to variability in flight-clearance is subdued or removed in the resistivity models.

iv. Computation of 1-D EM resistivity inversion models **(Section 6)**, using the *aempy* code, for all 20 repeat flights, to assess the extent to which variability in the FEM responses results in variability in the output EM resistivity models. Potential variability in the EM responses due to variability in flight-clearance is effectively removed through the EM inversion process (as clearance is an input parameter accounted for in the EM inversion models). 1-D inversion models derived both from the original FEM response data and from 'Npca1' filtered FEM responses are examined in the work. As discussed in Sections 4 and 6, the 'Npca1' filter retains only the most significant Principal Component of the data in the reconstructed (filtered) FEM responses.

2 Methodology

2.1 Strategy

The analysis presented here considers the data variability along the onshore portions of the twenty 60 m-clearance repeat flights on the central test-line, L2. Data recorded on the L2 repeat flights are deleted outside an 'onshore' polygon (Figure 1.1) in which the northern and southern ends are oriented perpendicular to the flight-line direction (see detail of the southern end of the polygon in Figure 2.1).

EM measurements along the twenty repeat flight-lines are not recorded at identical locations as, firstly, the flights themselves are not exactly coincident (Figure 2.1) and secondly, the spatial sample interval along the lines is variable around a mean of approximately 6 m, depending on the instantaneous flight speed at any location along the line. The maximum swath-width (the distance between the western and eastern most flight-lines, perpendicular to the flight-line direction) for all twenty flights at any location along the test-line is 17.3 m, with a mean swath-width of 11.4 m and standard deviation of 2.9 m. The maximum swath-width for any series of four flights is 14.3 m, for the 2021.2 series. The mean sample interval for all twenty lines is 6.09 m, with a standard deviation of 0.38 m. 99.7% (±3 standard deviations) of the sample intervals lie in the range 5.0 – 7.2 m.

If averages and standard deviations of the FEM responses and resistivity models along the test-line are to be computed, a strategy is needed to interpolate and resample the data on each repeat flight to a common reference. The approach adopted here is to use flight-line distance as the common reference.

Flight-line distance is the cumulative distance to each data point along the flight-line, starting from the first data point on the line, which here is the first data point inside the onshore polygon on the southern end of each profile. A correction distance, D, parallel to the flight-line direction (Figure 2.1), is added to the flight-line distance to reference it to the 'zero reference line' (being the southern end of the onshore polygon, oriented perpendicular to flight-line direction). The maximum D value applied to the twenty lines is 5.96 m (i.e., less than one sample interval). The (zero-referenced) flight-line distance channel, and all other data channels (e.g., EM response channels, altitude channel, etc.)

are then interpolated at 1 m intervals along the line using a ‘one-way’ spline (see Interpolation section below).

Interpolated data channels may then be averaged (and standard deviations computed) across all twenty flights (or selected subsets of the twenty flights). The process effectively amounts to an averaging of the data from the different flights in a direction perpendicular to the flight-line direction.

An alternative interpolation approach might have consisted of, for example, interpolating the data channels to a regular sampling of the ITM_Y coordinate data, in which case the data from the different flights would be average in an east-west direction.

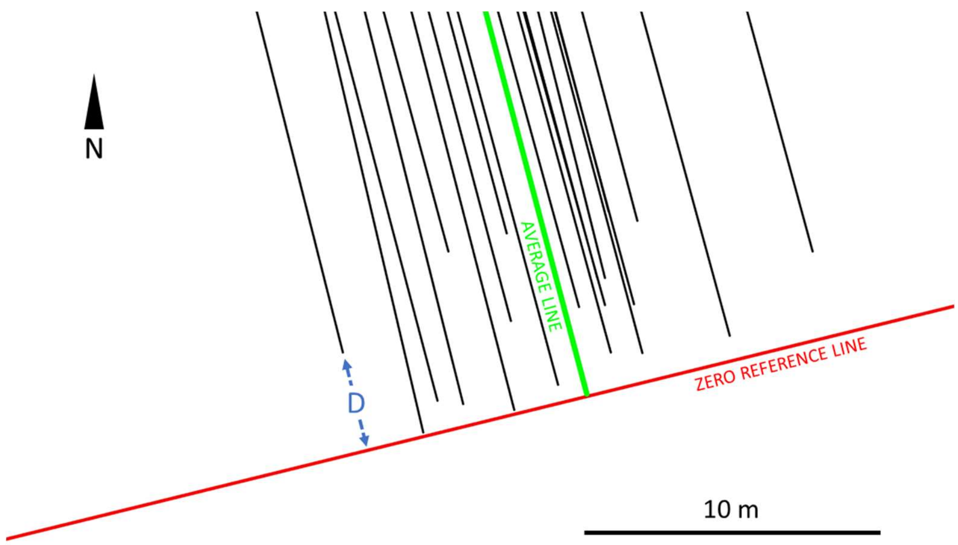

Figure 2.1: Detail map of southern ends of twenty repeat flights flown at 60 m clearance on test-line L2 (thin black lines). D is the flight-line parallel distance from the first data location on each line to the zero-reference line. Distance along each flight-line is defined relative to the zero line. The ‘average line’ (green) is defined by the average ITM_X and average ITM_Y coordinates at any distance along the lines (average of the twenty lines).

Ideally, it would be preferable to average FEM response and resistivity-model data from the different repeat flights in a direction parallel to the geological strike direction. Considering the regional geological strike direction apparent in the bedrock geological map (Figure 1.1) and the 12 kHz resistivity map (Figure 1.2), averaging in a direction perpendicular to the flight-line direction (as done in this work) appears broadly more appropriate than averaging, for example, in an E-W direction. However, local geological strike direction and its variability along the test-line is unknown. If the wavelengths of the

FEM and resistivity responses along the flight-lines are large with respect to the approximately 15 m swath-width of the test-lines (the lateral distance over which the repeat data are averaged), then the data projection and averaging direction chosen will not affect significantly the computed data averages and standard deviations – as examined and discussed further below ('Data Wavelengths and Geological Strike-angle', Section 2.3). Data averaging in a direction perpendicular to the flight-line direction is also better suited to the shape of the EM footprint associated with the vertical co-planar loop configuration of the SGL EM system, which is elongated in a direction perpendicular to the flight-line direction – as discussed further below (Section 2.4, 'EM Footprint').

2.2 Interpolation

All data channels recorded on the twenty repeat flights were interpolated and resampled at a constant 1 m distance interval along the flight lines. A very tightly constrained 'one-way' spline function was used – a constrained version of the Bessel spline (SRS1 Software, 2015) – producing no overshoots and oscillations with respect to the original data.

Interpolation was performed in Excel using the free add-in software 'SRS1 Cubic Spline for Excel' (Version 2.5.1.0) (SRS1 Software, 2015). The SRS1 software offers four different interpolation spline functions, which are, in order of increasing constraint (i.e., fewer overshoots and oscillations): cubic, Bessel, one-way and linear. Performance and behaviour of the four splines was tested on a small portion of data on line L2060000.19, as illustrated in Figure 2.2. A range of interpolation intervals, from 1 m to 6 m was also investigated (Figure 2.3).

While all four splines share the characteristic that the interpolated curves must pass through all the original data points, the less constrained interpolators (Bessel and cubic) have a tendency to introduce oscillations (peaks or troughs) not present in the original data (Figure 2.2). An increase in the amplitude of peaks and troughs relative to the original data is undesirable and the Bessel and cubic interpolators are therefore not favoured. The one-way and linear interpolators produce almost identical curves, the former being somewhat smoother, and both accurately reproduce the recorded data without unconstrained oscillations. The one-way interpolation has been used for this work.

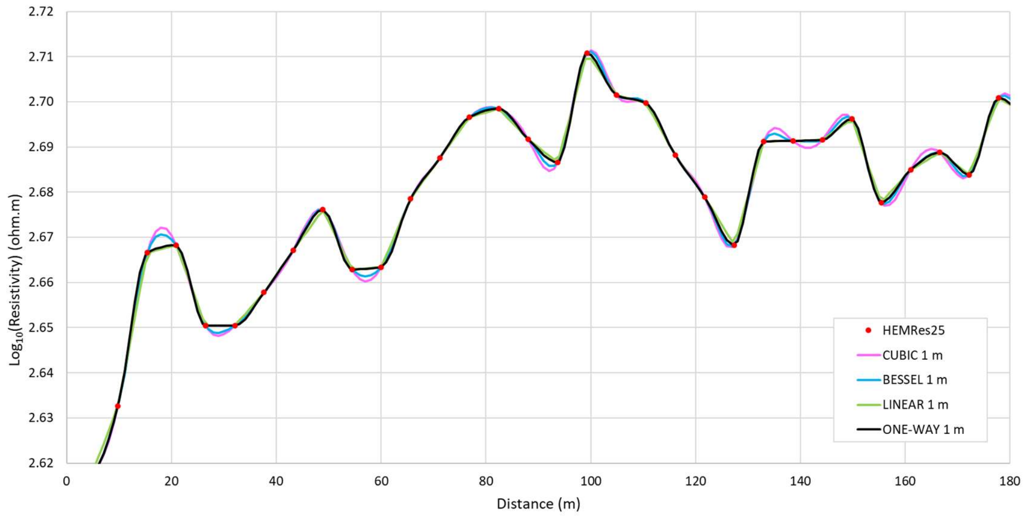

Figure 2.2: Test of four interpolation splines (SRS1 Software, 2015) with a 1 m sample interval over a 180 m section of Line 2060000.19: cubic (magenta), Bessel (blue), linear (green) and one-way (black). Original data (red points) are Geosoft HEM resistivity models at 25 kHz. All splines are required to pass through the original data points (which visibly they do). The cubic and Bessel splines, however, have a tendency to overshoot and undershoot local maxima and minima in the original ~6 m sampled data.

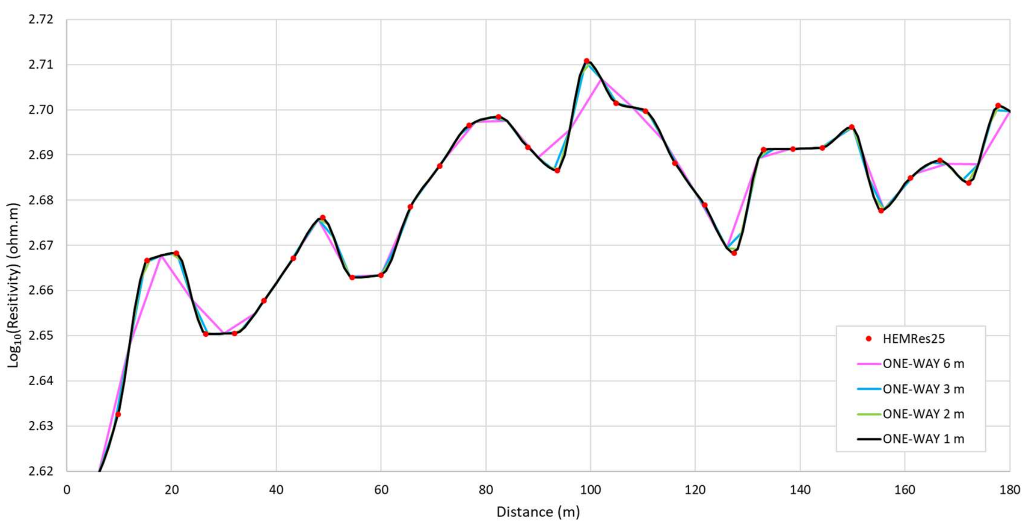

Figure 2.3: Test of four interpolation sample intervals over a 180 m section of Line 2060000.19: 6 m (magenta), 3 m (blue), 2 m (green) and 1 m (black), using a 'one-way' interpolation spline. Original data (red points) are Geosoft HEM resistivity models at 25 kHz. Note that the although the 6 m-interval spline has a sample interval very close to the original data sample interval, its sample locations are not the same as the sample locations of the original data, and has the effect of changing the wavelength content of the original data. A sample interval of a maximum of 3 m (original sample interval divided by two, Nyquist theory) is required to retain the wavelength content of the original data.

2.3 Data Wavelengths and Geological Strike-angle

The inline distance, A, over which data from the twenty repeat flights will be averaged for any geological strike direction, θ (with respect to the flight-line perpendicular direction), for a flight-line swath-width, W, (Figure 2.4) is given by:

$$A = W.\tan\theta \qquad (1)$$

The distance A represents the inline offset, or shift, of an EM anomaly recorded on the western- and eastern-most repeat flight lines for a given strike-angle (of the geological feature giving rise to the EM anomaly). Dependence of the inline offset distance on the strike-angle is illustrated in Figure 2.5 for a swath-width of 15 m. A rapid exponential increase in inline offset is apparent above a strike-angle of around 70°.

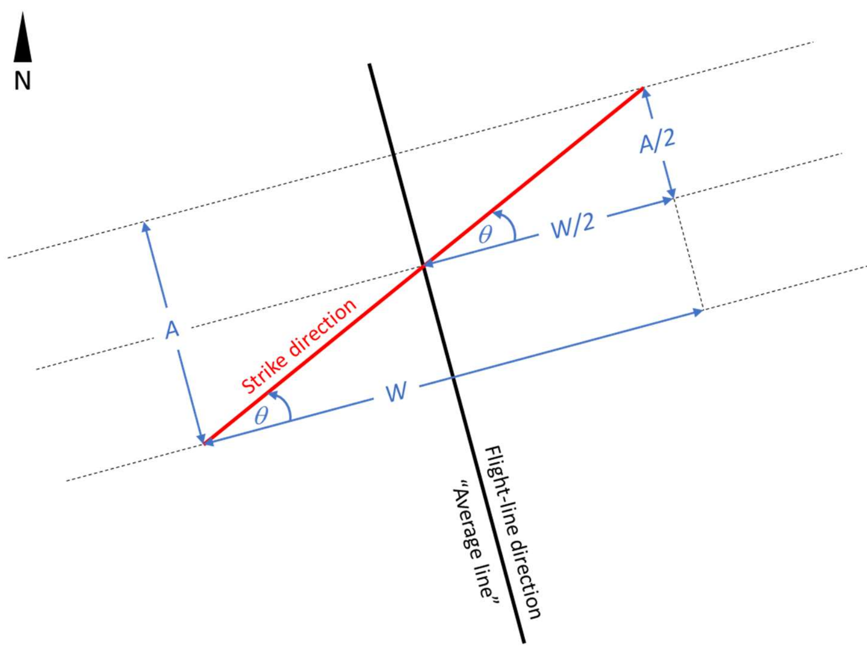

Figure 2.4: Schematic diagram illustrating the inline distance, A, over which data will be averaged for a given geological strike direction, θ, and flight-line full swath-width, W. Swath-width is the distance from the western-most to eastern-most repeat flight lines, measured perpendicular to the flight-line direction.

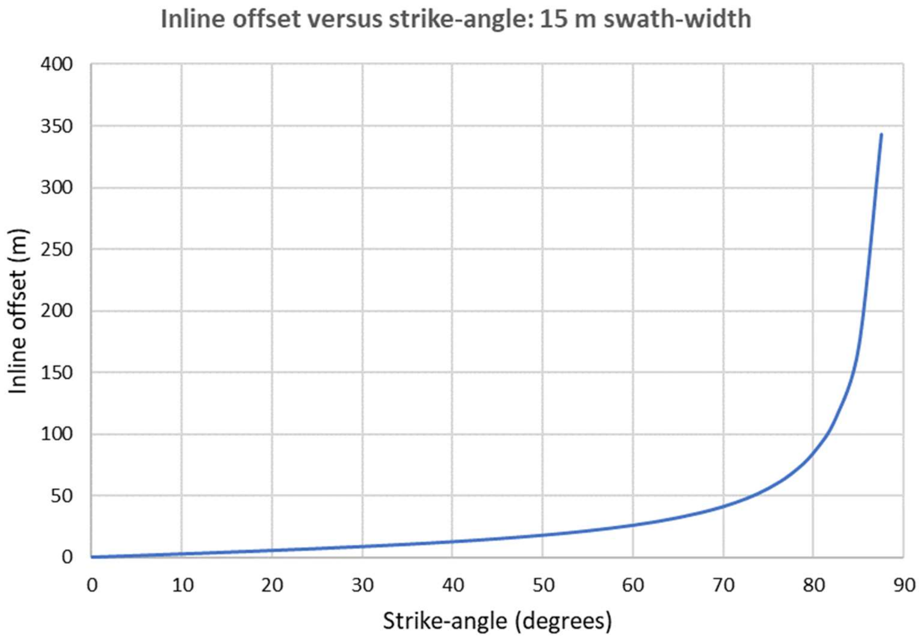

Figure 2.5: Schematic diagram illustrating the inline distance (offset), A, over which data will be averaged for a given geological strike direction, θ, and for flight-line swath-width W = 15 m. Swath-width is the distance from the western-most to eastern-most repeat flight lines, measured perpendicular to the flight-line direction. Strike-angle is defined with respect to the direction perpendicular to the flight-line direction (Figure 2.4).

Whether an inline offset will have a significant impact on the averaging of data across the twenty repeat flights (and on the data variability defined by the standard deviation) depends on the wavelengths, λ, of the anomalies being averaged. A criterion based on an allowable 'fractional-wavelength' inline shift is helpful. Figure 2.6 illustrates schematically that an inline shift of greater than about $\lambda/8$ would significantly degrade both the data average and the standard deviation as a measure of data variability. A stronger criterion, such as $\lambda/16$, may be more appropriate.

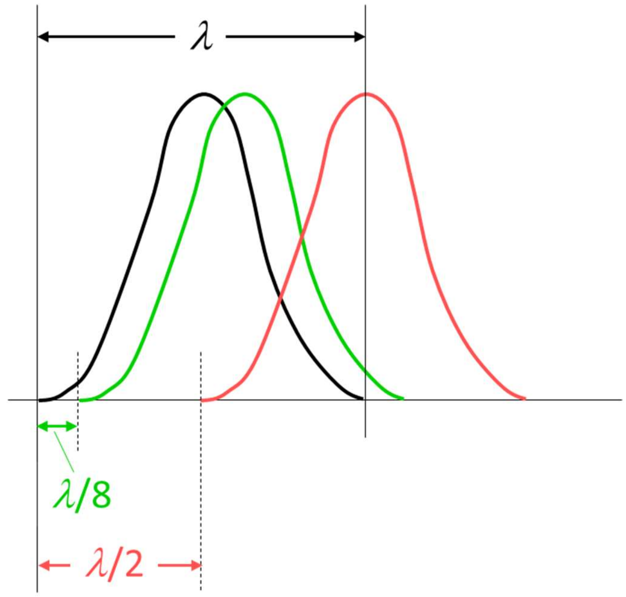

Figure 2.6: Schematic diagram illustrating the inline shift of an anomaly of wavelength λ (black line) by a distance of λ/8 (green anomaly) and λ/2 (red anomaly).

If *A* is replaced with $\lambda/8$ (or $\lambda/16$) in Equation 1 and rearranged for λ, then the resulting graph of wavelength, λ, versus strike-angle (Figure 2.7) defines the minimum wavelength for which the data average may be reliably computed for any strike-angle, depending on the inline shift criterion chosen (i.e., $\lambda/8$ or $\lambda/16$). All 'acceptable' wavelengths lie in the area above the graph curves. For example, for the $\lambda/16$ criterion and a strike-angle of 40°, data wavelengths greater than 200 m would return reliable averages, while wavelengths less than 200 m might be expected to result in averages and standard deviations that are not representative of the true variability in the data.

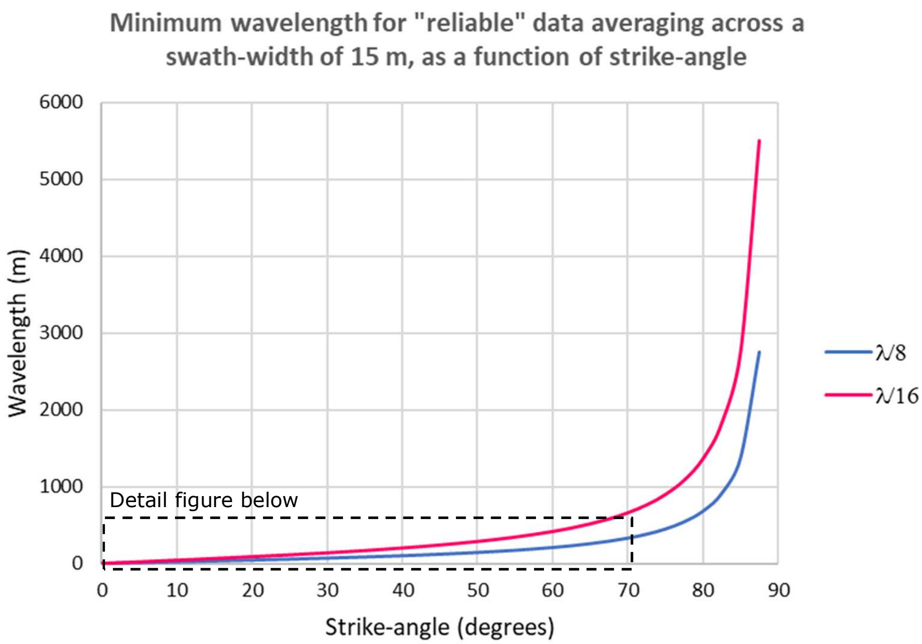

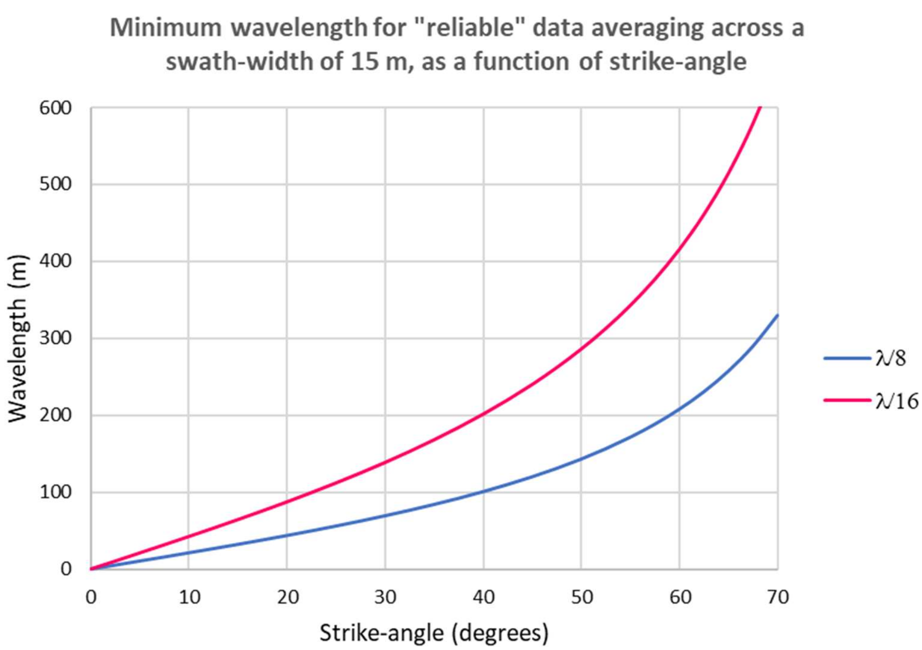

Figure 2.7: Graph of wavelength versus geological strike-angle – defining the minimum wavelength for which the data average may be reliably computed for any strike-angle, depending on the inline-shift criterion chosen. Results are computed and shown for a 15 m full swath-width. Two criteria are illustrated: $\lambda/8$ (blue line) and $\lambda/16$ (red). All acceptable wavelengths lie in the area above the graph lines. Dashed box in the upper figure illustrates the portion of the graph shown in detail in the lower figure. Strike-angle is defined with respect to the direction perpendicular to the flight-line direction.

The wavelength content of the FEM data at four frequencies has been examined using 1-D FFT (Fast Fourier Transform) spectral analysis of the in-phase and quadrature data profiles along the repeat lines. The 6 m data sample interval and 4,400 m line length provide data wavelengths that lie in the range 12 m (sample interval times two) and 2,200 m (line length divided by two). Results of the analysis are presented in Figures 2.8 to 2.11, using the example of the 25 and 0.9 kHz in-phase data on line L2060110.18, which are representative of the characteristics observed of all eight data components on all repeat flight lines.

The power spectra of both the 25 and 0.9 kHz in-phase data (Figures 2.8 and 2.9 respectively) indicate an absence of signal, above background noise level, at wavelengths less than about 30 m (i.e., the spectrum is flat between wavelengths of 12 – 30 m). Applying a low-pass filter to the data, with a 100 m cut-off wavelength, indicates that wavelengths less than 100 m do not contribute significantly to the observed data profiles – there is little difference between the input and filtered data profiles in Figures 2.8 and 2.9 (lower panels).

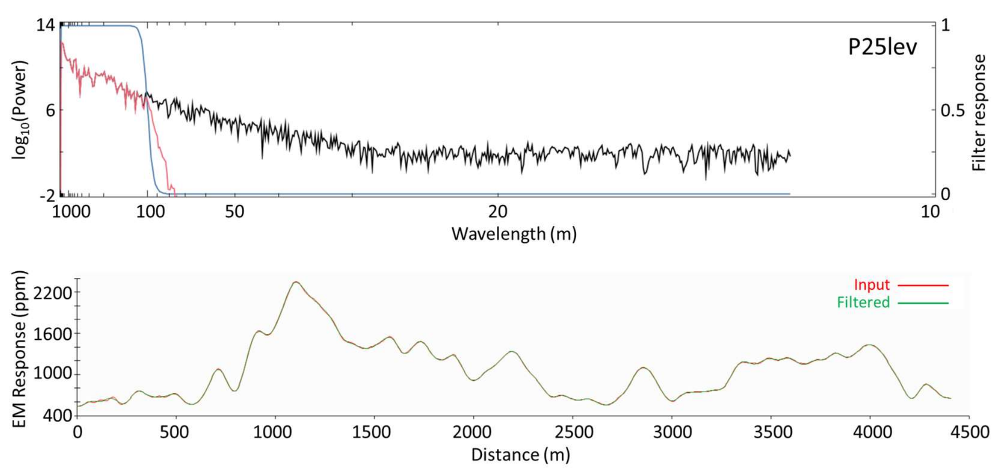

Figure 2.8: (Top) Wavelength power spectrum (black line) of in-phase 25 kHz data (P25lev channel) for line L2060110.18, shown against log_{10}(Power) axis on left-hand side of graph. Wavelength scale on horizontal axis is in m units. Wavelength spectrum after application of Butterworth low-pass filter (100 m cut-off wavelength, filter degree = 32) shown (red line). Filter response (blue line) shown against axis on right-hand side of graph. (Bottom) Comparison between unfiltered (input) data profile (red line) and low-pass filtered data profile (green line).

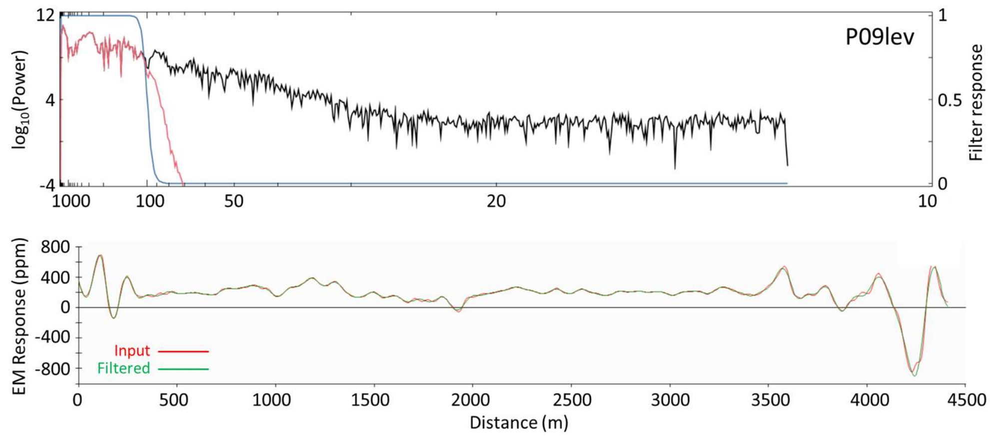

Figure 2.9: (Top) Wavelength power spectrum (black line) of in-phase 0.9 kHz data (P09lev channel) for line L2060110.18, shown against $\log_{10}$(Power) axis on left-hand side of graph. Wavelength scale on horizontal axis is in m units. Wavelength spectrum after application of Butterworth low-pass filter (100 m cut-off wavelength, filter degree = 32) shown (red line). Filter response (blue line) shown against axis on right-hand side of graph. (Bottom) Comparison between unfiltered (input) data profile (red line) and low-pass filtered data profile (green line).

Comparing the effects of low-pass filters with cut-off wavelengths of 100, 150 and 200 m (Figures 2.10 and 2.11) confirms that there is little loss of data content along the profile in rejecting wavelengths less than 100 m. While there is moderate loss of data content arising from rejecting wavelengths less than 150 m, rejecting wavelengths less than 200 m results in a clear degradation in the detail of the profile data.

In the absence of significant signal wavelengths less than 100 m, the graph of Figure 2.7 (λ/16 criterion, lower panel) suggests that reliable averaging of data (and computation of standard deviation statistics) across a 15 m swath-width of the repeat test flights will be maintained for all geological strike-angles up to around 22° (with respect to the perpendicular to the flight-line direction). Allowing for a minimal contribution of wavelengths less than 150 m to the recorded data, reliable data averages might be maintained up to geological strike-angles of around 32°.

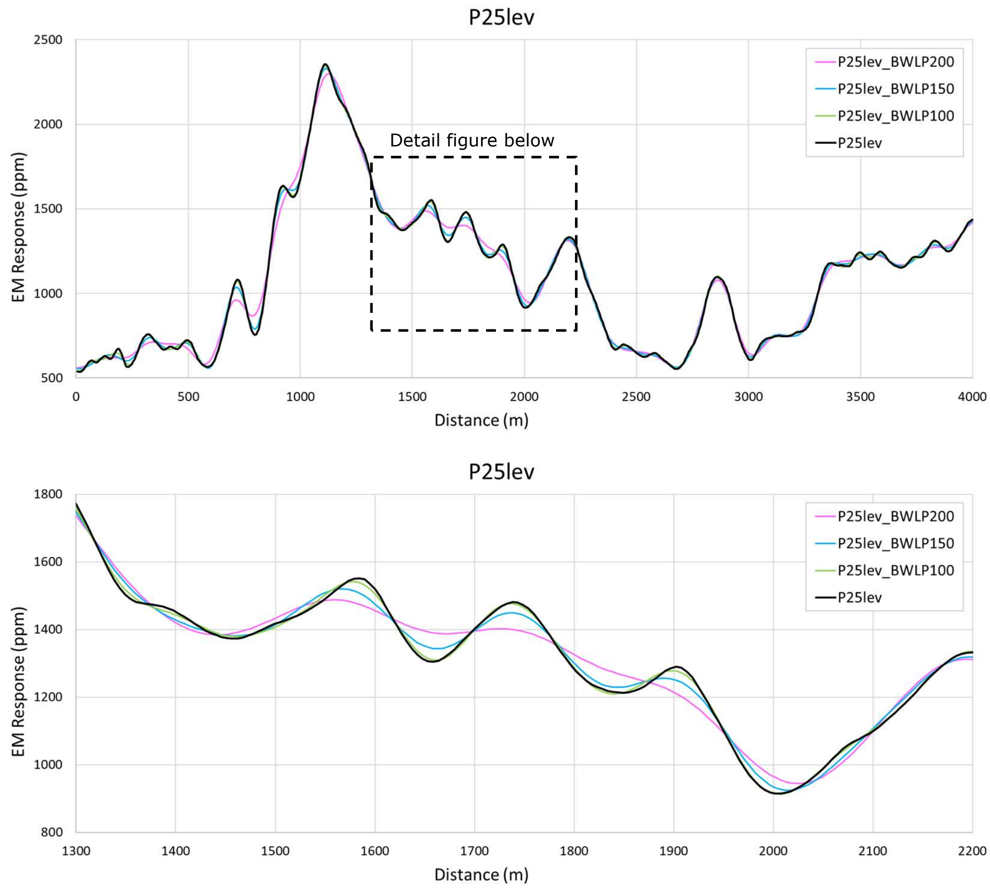

Figure 2.10: In-phase 25 kHz data profile (P25lev channel) along line L2060110.18 (black line) compared with data profiles after application of Butterworth low-pass filter (filter degree = 8) with cut-off wavelengths of 100 m (green line), 150 m (blue) and 200 m (pink). Dashed box in the upper figure illustrates the portion of the graph shown in detail in the lower figure.

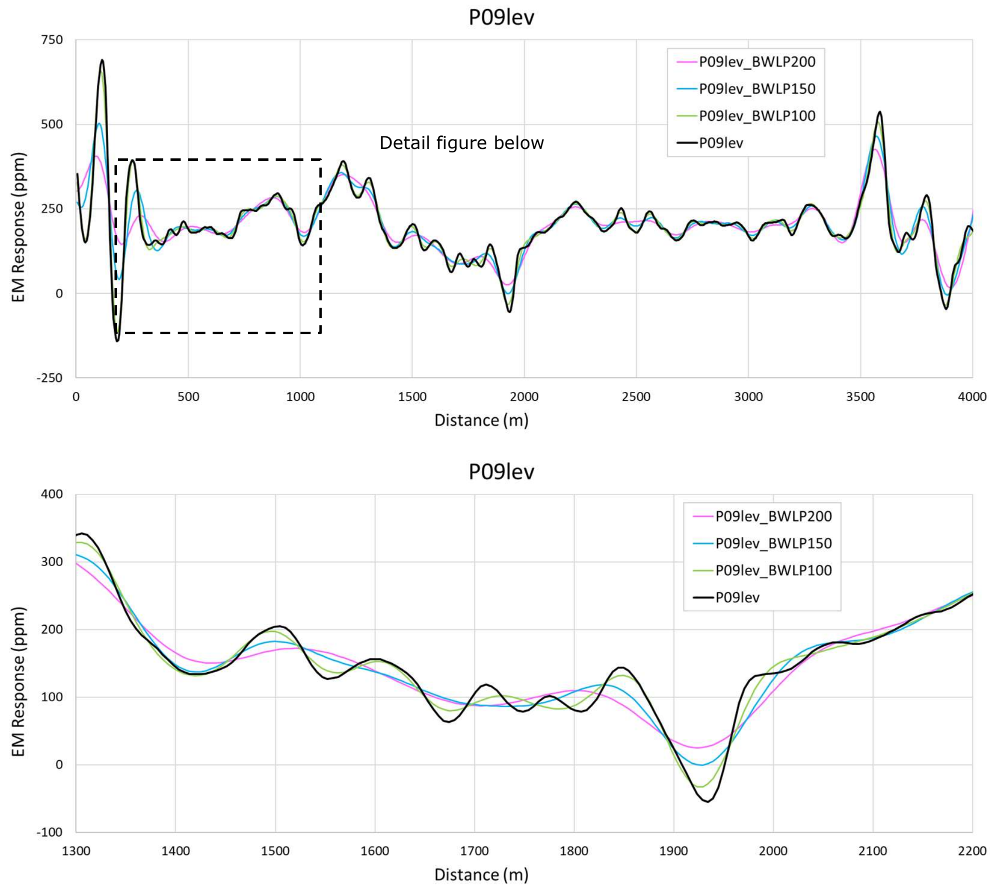

Figure 2.11: In-phase 0.9 kHz data profile (P09lev channel) along line L2060110.18 (black line) compared with data profiles after application of Butterworth low-pass filter (filter degree = 8) with cut-off wavelengths of 100 m (green line), 150 m (blue) and 200 m (pink). Dashed box in the upper figure illustrates the portion of the graph shown in detail in the lower figure.

As local geological strike direction and strike variation along the test-line is largely unknown, the point of the analysis above is to illustrate the potential for 2-D geological structure and strike variation along the line to distort estimates of data variability based on the computation of averages and standard deviations across the 15 m swath-width of the twenty repeat flights, depending on the wavelengths present in the data.

2.4 EM Footprint

The airborne EM footprint may be described generally as the lateral scale – both an 'at-surface' area and a subsurface volume – that influences the EM measurements (e.g., Beamish, 2003). An examination particularly of the size of the at-surface EM footprint, with respect to the ~15 m swath-width of the repeat flights, is helpful in assessing whether significantly different FEM responses might be recorded on each repeat line, in the case that subsurface geological variability is present at a scale smaller than the 15 m swath-width. If the size of the EM footprint is large with respect to the swath-width, regardless of the scale of lateral geological variability, then very similar FEM responses should be expected on all repeat flights.

Different scale metrics have been used to define the size of the EM footprint. Liu and Becker (1990) and Kovacs et al. (1995) define the footprint as the length of the side of a square surface, centred directly below the transmitter coil, that contains the induced currents that account for 90% of the observed secondary magnetic field. Similarly, Yin et al. (2014) define the footprint as the subsurface volume in which the induced current contributes 90% to the total secondary magnetic field at the EM receiver (and from which the surface extents of the footprint can be measured). Beamish (2003) defines a transmitter footprint in terms of the electromagnetic 'skin-distance', which is the distance, both laterally and with depth, at which the amplitude of the induced electric field decays to 1/e (~37%) of the maximum value (using a definition analogous to that for the conventional plane-wave 'skin-depth'). As the Beamish (2003) footprint incorporates a volume accounting for only ~63% of the electric-field induced by the transmitter, it is smaller in dimension than the footprints of Liu and Becker (1990), Kovacs et al. (1995) and Yin et al. (2014), which incorporate a volume accounting for 90% of the secondary magnetic field at the receiver (Yin et al., 2014).

The four studies referred to above consider footprint dimensions for both horizontal and vertical transmitter-receiver loop configurations (as illustrated in Figure 2.12), for a range of different flight heights, system frequencies and ground resistivities. The SGL/Tellus system consists of vertical coplanar transmitter and receiver loops (VCP configuration), with the loop magnetic dipoles aligned horizontally (HMD configuration) in the direction of the flight-lines. Table 2.1 provides a summary of illustrative EM footprint dimensions at-surface taken from these studies, for vertical loop (HMD) configurations only and, where possible, for equivalent system frequency and ground resistivity parameters. Figures 2.13 and 2.14, taken from the work of Beamish (2003) and Yin et al. (2014), illustrate the shapes of the at-surface and volumetric EM footprints, respectively, for vertical loop configurations.

None of the studies reflected in Table 2.1 considers the specific loop configuration of the SGL EM system that acquired the data analysed in this report – a vertical co-planar, horizontal magnetic dipole loop configuration (HMD-VCP configuration, Figure 2.12). Liu and Becker (1990), Kovacs et al. (1995) and Yin et al. (2014) all consider a vertical co-axial (HMD-VCA) configuration, with a 6.5 m transmitter-receiver loop separation in the case of the former two references, and an 8 m separation for the latter. Beamish (2003) considers only the general case of a horizontal magnetic dipole (HMD) transmitter loop. However, the location and geometry of the EM footprint defined in the work of Yin et al. (2014) illustrates that the effect of introducing the receiver loop into the system is largely to translate the transmitter footprint towards the receiver, and to place the locus of maximum contribution to the recorded secondary magnetic field midway between the transmitter and receiver. The footprint dimensions defined for an HMD-VCA loop configuration and for a generalised HMD transmitter loop, and presented in Table 2.1, are therefore considered applicable to the case of an HMD-VCP loop configuration.

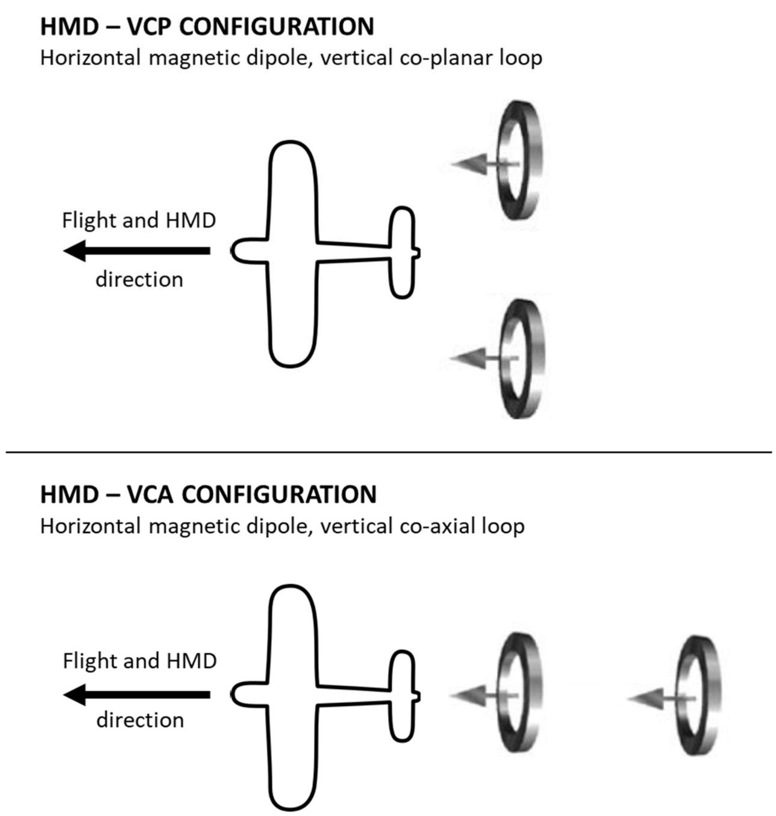

Figure 2.12: Schematic illustration of vertical transmitter-receiver loop configurations (horizontal magnetic dipole, HMD, configurations) (modified after Beamish, 2003). In the configurations shown, the HMDs (grey arrows) are all aligned (polarised) in the direction of the flight-line. The upper figure, VCP (vertical co-planar) configuration, illustrates the SGL Tellus airborne EM system.

Table 2.1: Summary of 'at-surface' EM footprint dimensions from a number of studies for vertical co-axial (VCA), horizontal magnetic dipole (HMD) loop configurations, 60 m flight-height (i.e., loop location/s above ground level) (except for entry 7, where flight height is 30 m), 10 kHz transmitter frequency and different ground resistivities. Empirical equations describing footprint dimensions as a function of flight-height, where used, are shown in right-hand column. Long axes (LSD and Y in empirical equations) and short axis (SSD in equations) are defined and shown in Figure 2.13. Note that footprint dimensions recorded in the table are 'full-widths' (and not the 'half-width' extending from footprint centre to edge). Orientation of long axis of footprint is perpendicular to the polarisation (alignment) direction of the HMD, which for the SGL/Tellus system is perpendicular to the flight-line direction.

	Study reference	Loop config.	Transmitter frequency (kHz)	Half-space resistivity (ohm.m)	Frequency/ resistivity ratio	Flight height (H) (m)	Footprint (full-width)		Footprint criterion	Empirical equation for footprint dimensions / Comments
							Long axis (m)	Short axis (m)		
1.	Liu and Becker (1990)	VCA - HMD 6.5 m coil separation	Frequency indep.	Infinitely conductive thin sheet	N/A	60	81	*(i)*	Square surface (side = F) that contains the induced currents that account for 90% of the observed secondary magnetic field	F = 1.35*H Frequency-independent due to infinite conductivity
2.	Kovacs et al. (1995)	VCA - HMD 6.5 m coil separation	Frequency indep.	Infinitely conductive thin sheet	N/A	60	78	*(i)*	Square surface (side = F) that contains the induced currents that account for 90% of the observed secondary magnetic field	F = 1.3*H Frequency-independent due to infinite conductivity
3.	Yin et al. (2014)	VCA - HMD 8 m coil separation	10	10	1000	60	159	*(ii)*	Subsurface volume in which the induced current contributes 90% to the total secondary magnetic field at the EM receiver	Y = 32.76 + 2.11*H Amplitude footprint (modulus of IP and Q responses)

4.	Beamish (2003)	HMD Tx only	10	10	1000	60	134	63	‘Skin-distance' at surface, being the distance at which the amplitude of the induced electric field decays to 1/e (~37%) of the maximum value	LSD = 7.694 + 0.987*H SSD = 3.414 + 0.466*H
5.	Yin et al. (2014)	VCA - HMD 8 m coil separation	10	1000	10	60	337	*(ii)*	Subsurface volume in which the induced current contributes 90% to the total secondary magnetic field at the EM receiver	Y = 147.14 + 3.17*H Amplitude footprint (modulus of IP and Q responses)
6.	Beamish (2003)	HMD Tx only	10	1000	10	60	181	80	‘Skin-distance' at surface, being the distance at which the amplitude of the induced electric field decays to 1/e (~37%) of the maximum value	LSD = 5.000 + 1.425*H SSD = 1.561 + 0.642*H
7.	Yin et al. (2014)	VCA - HMD 8 m coil separation	10	100	100	30	148	140	Subsurface volume in which the induced current contributes 90% to the total secondary magnetic field at the EM receiver	From Table 1 in reference. Amplitude footprint (modulus of IP and Q responses)
(i) No separate long and short axes are defined in these two studies – only a single value defining the side of a square footprint. (ii) No empirical equation defined in this study for the short axis.										

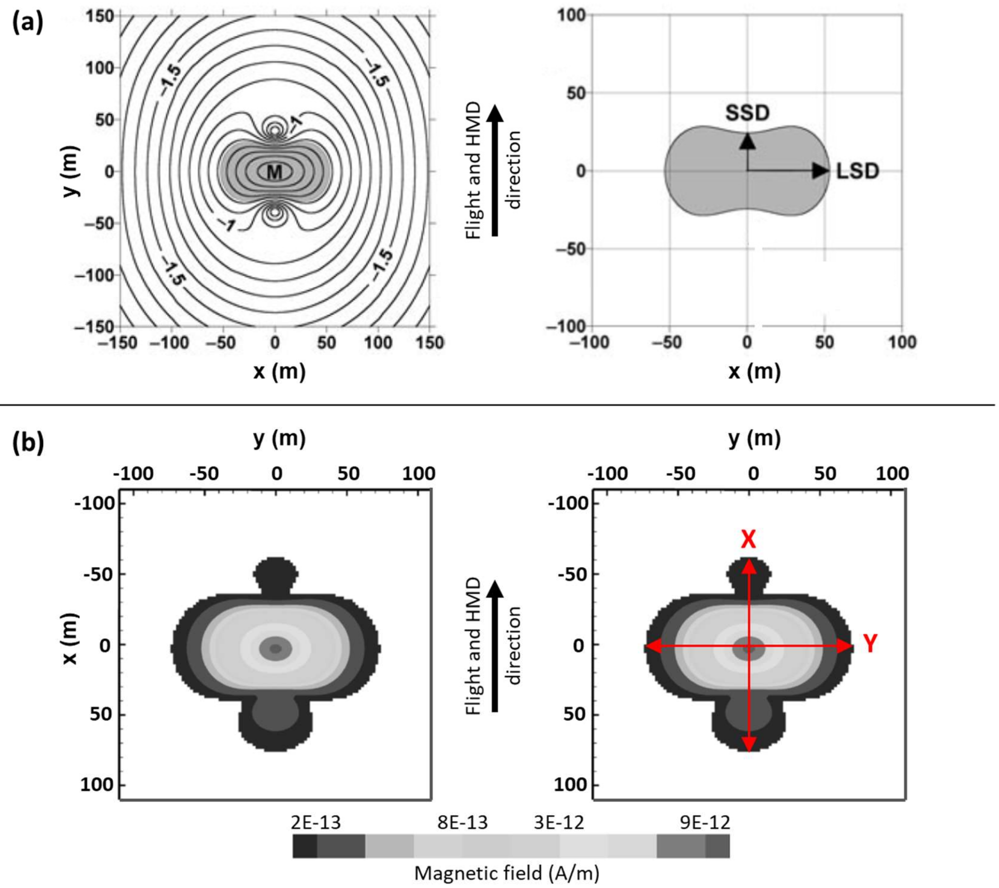

Figure 2.13: Plan views of EM footprints at surface. <u>(a.) From Beamish (2003)</u>. (Left) Modulus of the induced horizontal electric-field (in μV/m) contoured in the x-y (horizontal) plane for a horizontal magnetic dipole (HMD) polarised (aligned) in the y-direction. Source has dipole moment of 1 A/m and frequency of 3 kHz. Ground model consists of 10 Ω.m half-space. Coil height above surface is 40 m. Electric-field contoured in logarithmic intervals. Grey infill (the EM footprint) denotes area where the electric-field is greater than 1/e (~37%) of the maximum field. Letter M denotes location of maximum electric-field. HMD (transmitter loop) is located at (x, y) = (0, 0). (Right) EM footprint dimensions defined in Beamish (2003) (and referred to in Table 2.1), SSD = short skin-distance, LSD = long skin-distance. <u>(b.) From Yin et al. (2014)</u>. (Left) Amplitude of magnetic-field (in A/m) contoured in the x-y plane for a VCA coil configuration with transmitter-receiver separation of 8 m and HMDs polarised in the x-direction. Source has frequency of 10 kHz. Ground model consists of 100 Ω.m half-space. Height of coils above surface is 30 m. The transmitter and receiver loops are located at (x, y) locations (0, 0) and (8, 0) respectively. (Right) EM footprint dimensions defined in Yin et al. (2014) (and referred to in Table 1.2), X = dimension in HMD and flight-line direction, Y = dimension perpendicular to HMD and flight-line direction. The area contoured in plan-view (the EM footprint) is the upper surface of the underground volume within which the induced current contributes 90% to the total secondary magnetic field at the receiver. Note in the two sets of figures that the coordinate axis systems used in the two studies (a.) and (b.) are rotated by 90° with respect to each other.

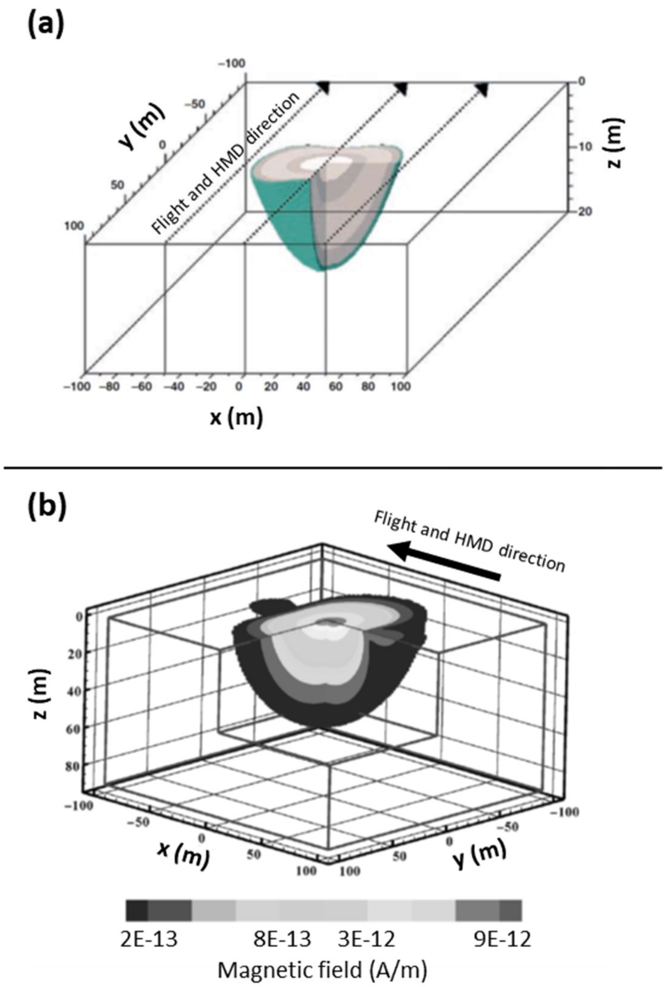

Figure 2.14: Three-dimensional perspective views of volumetric EM footprints. <u>(a.) From Beamish (2003)</u>. Volume shown is the skin-distance volume, the volume within which the electric-field is greater than 1/e (~37%) of the maximum field, for a horizontal magnetic dipole (HMD) polarised (aligned) in the y-direction. Source has dipole moment of 1 A/m and frequency of 10 kHz. Ground model consists of 100 Ω.m half-space. Coil height above surface is 30 m. HMD (transmitter loop) is located at (x, y) = (0, 0). Vertical exaggeration = 4. The SE quadrant of the volume has been cut for illustrative purposes. Dotted lines illustrate hypothetical flight-lines separated by 50 m. <u>(b.) From Yin et al. (2014)</u>. Contoured amplitude of magnetic-field (in A/m) for a VCA coil configuration with transmitter-receiver separation of 8 m and HMDs polarised in the x-direction. Source has frequency of 10 kHz. Ground model consists of 100 Ω.m half-space. Height of coils above surface is 30 m. The transmitter and receiver loops are located at (x, y) locations (0, 0) and (8, 0) respectively. The outer contour surface defines the volume within which the induced current contributes 90% to the total secondary magnetic field at the receiver. The near quadrant of the volume has been cut for illustrative purposes. Note in the two sets of figures that the coordinate axis systems used in the two studies (a.) and (b.) are rotated by 90° with respect to each other.

In plan-view, the at-surface EM footprint (Figure 2.13) for HMD and HMD-VCA loop configurations (Beamish, 2003 and Yin et al., 2014 respectively), is oval in shape, with its long axis oriented perpendicular to the polarisation (alignment) direction of the HMD (and perpendicular to the flight-line direction where the HMD is oriented parallel to the flight-lines, as is the case for the SGL/Tellus EM system). The primary control on the size of the footprint is the flight-height (Beamish, 2003 and Yin et al., 2014). Secondary controls are the transmitter frequency and the ground resistivity – the footprint is larger for lower frequencies and for higher resistivities. Beamish (2003) and Yin et al. (2014), in computing EM footprint dimensions for a range of different flight-heights (for specific transmitter frequencies and ground resistivities), are able to define, through linear regression, empirical relationships (equations) between flight-height and footprint dimension. A number of these empirical linear equations are considered and defined in Table 2.1.

The discussion that follows refers to footprint dimensions that are 'full-width' (c.f., Table 2.1) and not 'half-width' dimensions, the later extending from the footprint centre to footprint edge. Considering initially the studies defining the footprint size based on the area/volume contributing 90% of the secondary magnetic signal at the receiver, the studies of Liu and Becker (1990) and Kovacs et al. (1995) (entries 1 and 2, Table 2.1), in assuming an infinitely conductive thin sheet model (corresponding with zero depth-of-penetration below surface), provide a measurement of the *minimum* size of the footprint, around 80 m for a 60 m flight-height. The infinite conductivity model, furthermore, leads, to effective frequency independence in the solution, i.e., the footprint dimension is the same for all transmitter frequencies.

For a 10 kHz transmitter frequency, 60 m flight-height and model resistivities of 10 Ω.m and 1000 Ω.m, the footprint sizes (long-axis, perpendicular to the HMD alignment and flight-line direction) are 159 m and 337 m respectively (Yin et al., 2014, Table 2.1., entries 3 and 5). The 10 Ω.m and 1000 Ω.m model resistivities used here are broadly representative of the actual ground resistivities modelled along the Waterford test-line, which lie in the range 85 Ω.m to 3,700 Ω.m (Table 2.2, for the 'average' models at each frequency). A ground resistivity of 85 Ω.m would lead to a footprint size larger than 159 m, while a resistivity of 3,700 Ω.m, would lead to a footprint size larger than 337 m. The lower SGL/Tellus transmitter frequencies of 912 Hz and 3,005 Hz would lead to larger footprint dimensions than reported for 10 kHz in Table 2.1, while the higher SGL/Tellus frequencies of 11,962 Hz and 24,510 Hz would lead to smaller footprint dimensions (but not smaller than the ~80 m minimum of Liu and Becker (1990) and Kovacs et al. (1995)).

Note that the much wider range of Waterford test-line model resistivities indicated in the statistics of all the *individual* flight lines, 0.1 Ω.m to 43,100 Ω.m (Table 2.2), is likely the result of high cultural noise levels in particularly the 912 and 3,005 Hz data (as discussed subsequently in the report), which give rise to exceptionally low and high EM response amplitudes and therefore exceptionally high and low modelled resistivity values. The statistics of the 'average' models in Table 2.2 are felt to provide a more stable and reasonable indication of subsurface resistivities along the profile.

Table 2.2: Minimum and maximum resistivities for 'Extended Resistivity' (SGL) and Geosoft HEM models for each EM frequency. The minimum and maximum resistivity values reported in the table are (i) for the average models at each frequency (i.e., the averages of the twenty repeat flights, with data resampled at 1 m intervals along the lines, see Section 5) and (ii) for all individual models on the twenty repeat lines at each frequency (using original ~6 m sample interval data).

Models	Frequency (Hz)	AVERAGE MODELS AT EACH FREQUENCY		ALL INDIVIDUAL MODELS AT EACH FREQUENCY	
		Resistivity (ohm.m)		Resistivity (ohm.m)	
		Minimum	Maximum	Minimum	Maximum
EXTENDED RESISTIVITY	912	85	438	0.10	912
	3,005	121	935	0.13	3,005
	11,962	162	836	91	1,212
	24,510	149	1,460	76	2,522
HEM	912	101	2,316	6	30,410
	3,005	122	3,705	12	43,112
	11,962	112	772	73	1,360
	24,510	111	962	67	1,720

More conservative (smaller) estimates of the at-surface footprint dimensions arise from the Beamish (2003) criterion that incorporates a volume accounting for only ~63% of the electric-field induced by the transmitter. For a 10 kHz transmitter frequency, 60 m flight-height and model resistivities of 10 Ω.m and 1000 Ω.m, the footprint sizes (long-axis, perpendicular to the HMD alignment and flight-line direction) are 134 m and 181 m respectively (Beamish, 2003, Table 2.1., entries 4 and 6).

The primary conclusion from the results presented above is that, for a 60 m flight-height, for all frequencies transmitted and all ground resistivities encountered, the size of the EM footprint perpendicular to the flight-line direction is large with respect to the ~17 m maximum swath-width of the twenty repeat flights. Very similar EM responses (of geological origin) should, therefore, be expected on all the repeat flights within each annual series of four repeat flights.

The small contribution of wavelengths less than 100 m to the recorded EM responses (Section 2.3) is consistent with the short-axis (in-line) dimensions of the EM footprints indicated in Table 2.1. While the work of Yin et al. (2014) provides no empirical equation for the short-axis dimension of the footprint as a function of flight-height (and therefore no means of calculating the in-line footprint specifically for a 60 m flight-height), the short-axis dimension is shown to be less than 10% smaller than the long-axis dimension for a flight-height of 30 m (Table 2.1, entry 7). The Yin et al. (2014) definition (90% of the total secondary magnetic field at the EM receiver) therefore suggests an in-line dimension of around 150 m for a 10 kHz signal and 10 Ω.m ground resistivity (c.f., Table 2.1, entry 3). The Beamish (2003) definition (decay of the induced electric field to 37% of the maximum) predicts smaller in-line footprint dimensions of 63 m and 80 m, for a 10 kHz signal and ground resistivities of 10 Ω.m and 1000 Ω.m, respectively (entries 4 and 6 respectively, Table 2.1).

3 Variability in FEM Responses and Other Measured Parameters

3.1 First-order Assessment

The Waterford test-line dataset that forms the basis of the variability assessment presented here is the SGL delivery **DLV2402** of 12th October 2021. DLV2402 contains test-line data acquired immediately after the completion of the A8 survey block in September 2021, as well as data for all prior flights on the test-line since 2019. Some minor levelling changes were applied by SGL to the EM responses of earlier flights contained in DLV2402, and DLV2402 therefore *replaces* the data of all earlier deliveries (DLV2379 of 13 August 2021, DLV2307 of 10 November 2020 and DLV2170 of 1 October 2019).

The variability analysis is restricted to the onshore portions of the twenty repeat flights flown at a nominal clearance of 60 m along the central Waterford test-line (line L2, Figures 1.1 to 1.4). As discussed in Section 2.1, the statistical measure used to define the variability of the data recorded on the repeat flights is the standard deviation of the mean. The term 'variability' is used throughout the report and its use should be taken explicitly to mean the standard deviation of the mean. To assess spatial differences in variability along the flight-lines, data are interpolated to constant 1 m distance intervals along the flight lines prior to averaging and computation of the standard deviation (see Section 2.2).

In addition to assessing the variability in the eight recorded EM responses (in-phase and quadrature components for the four frequencies), variability in a range of additional measured and derived parameters, associated with the flights and flight path, is also assessed, as summarised in Table 3.1. The objective in determining the variability of the additional parameters is to examine whether any flight parameters might correlate with, and potentially account for, variability observed in the EM responses.

Table 3.1. Summary of EM response and flight parameters assessed for variability. Several of the parameters are recorded directly during flight, while others are derived (calculated) from various recorded parameters, as indicated.

	Parameter	Data channels used	Section number	Figure numbers
1.	Eight EM responses: 2 components at each frequency	P09lev, P3lev, P12lev, P25lev, Q09lev, Q3lev, Q12lev, Q25lev	3.2	3.8 – 3.15
2.	Clearance	RADAR	3.3	3.16
3.	Speed	Derived from: ITM_X, ITM_Y, TIME	3.3	3.17
4.	Heading	Derived from: ITM_X, ITM_Y, TIME	3.3	3.18
5.	Temperature	TEMP	3.3	3.19
6.	Digital elevation model	Derived from: MSLHGT, RADAR	3.3	3.20
7.	Power-line monitor	PLM_nT	3.3	3.21
8.	Flight-line perpendicular distance from average line	Derived from: ITM_X, ITM_Y	3.3	3.22
9.	Flight-line full swath-width	Derived from: ITM_X, ITM_Y	3.3	3.23
10.	Eight EM responses: 2 components at each frequency - PCA filtered, order = 1 (Npca1 filter)	Derived from: P09lev, P3lev, P12lev, P25lev, Q09lev, Q3lev, Q12lev, Q25lev	4.2	4.3 – 4.10
11.	Four half-space resistivity models: at each frequency - SGL extended resistivity models	ExtendedRes09, ExtendedRes3, ExtendedRes12, ExtendedRes25	5.2	5.1 – 5.4
12.	Four half-space resistivity models: at each frequency - Geosoft HEM resistivity models	Derived from: P09lev and Q09lev, P3lev and Q3lev, P12lev and Q12lev, P25lev and Q25lev, with RADAR	5.3	5.5 – 5.8

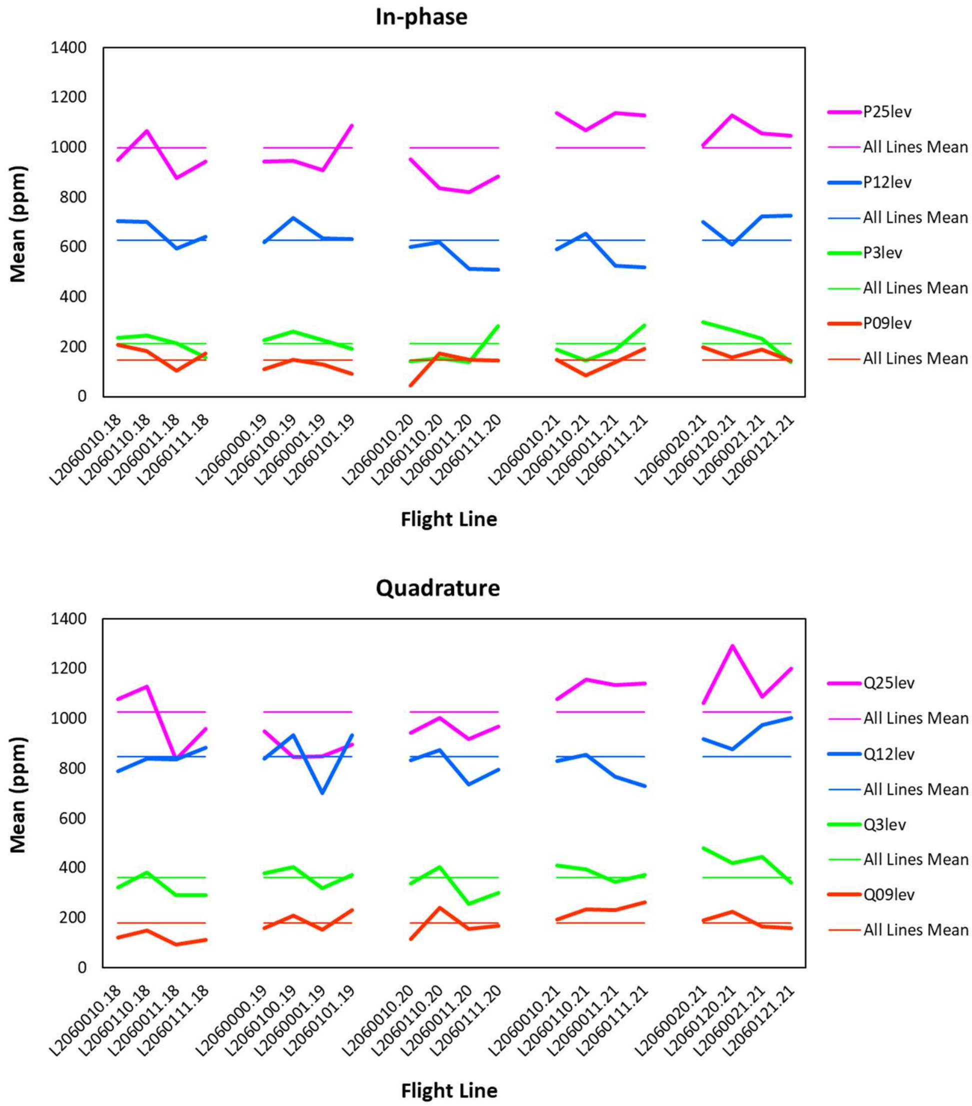

Figure 3.1: Mean EM response amplitude for each flight for in-phase components (upper figure) and quadrature components (lower figure), plotted against the average for all twenty repeat flights. Data used and plotted are the original ~6 m sampled data. Source data given in Tables 3.2 and 3.3.

A broad, or first-order, assessment of the variability in the recorded EM responses is provided by an examination of the line averages of each FEM component for each of the twenty repeat flights – as illustrated in Figure 3.1 for both the in-phase and quadrature data components. For visual comparison, the average EM response amplitudes for each line and each component in Figure 3.1 are plotted against the average for all twenty lines. The line-mean data plotted in Figure 3.1 are tabulated in Tables 3.2 and 3.3, together with standard deviations for each four-line series and for all twenty lines together. In figure 3.1, within each group of four flights ordered along the horizontal axis and flown on the same day, the first two flights were flown in quick succession, the first on a heading of 345° E of N (away from the coastline) and the second on 165° E of N (towards the coastline). The third and fourth flights of each group were again flown in quick succession, about one hour after the first two flights (see Figure 3.2), on headings of 345° E of N and 165° E of N respectively.

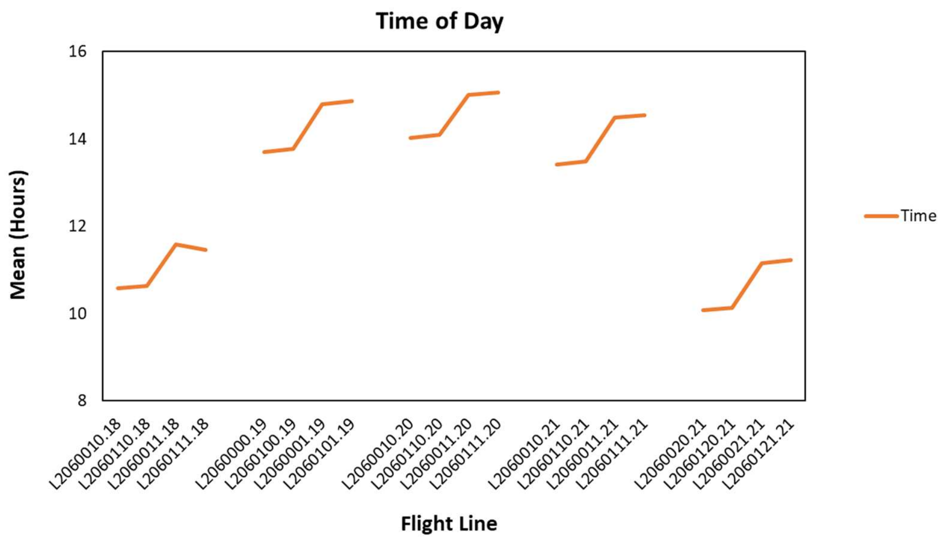

Figure 3.2: Mean time of day for each flight. Data used and plotted are the original ~6 m sampled data. The month of the year for each flight-series is illustrated in Figure 5.15.

Differences in the mean amplitudes of the FEM components on each repeat flight-line may be the result of (i) differences in flight altitude (with higher altitudes resulting in lower FEM response amplitudes), (ii) differences (potentially inaccuracies) in the zero levels defined for each of the components for each flight-line (dependent on calibration and drift corrections applied), (iii) variable levels of cultural noise recorded on each flight line (higher noise levels potentially resulting in a higher mean amplitude for the line), and (iv) real differences in the subsurface resistivity structure at the time of the flights (likely relevant only in considering differences between the five series of flights).

Two first-order features apparent in the line mean-amplitudes of Figure 3.1 are considered in the sections that follow: (i) variation in the mean amplitudes within each series of 4 repeat lines (intra-series variability) and (ii) variation in the mean amplitudes when comparing each series of repeat flight-lines with each other (inter-series/inter-year variability).

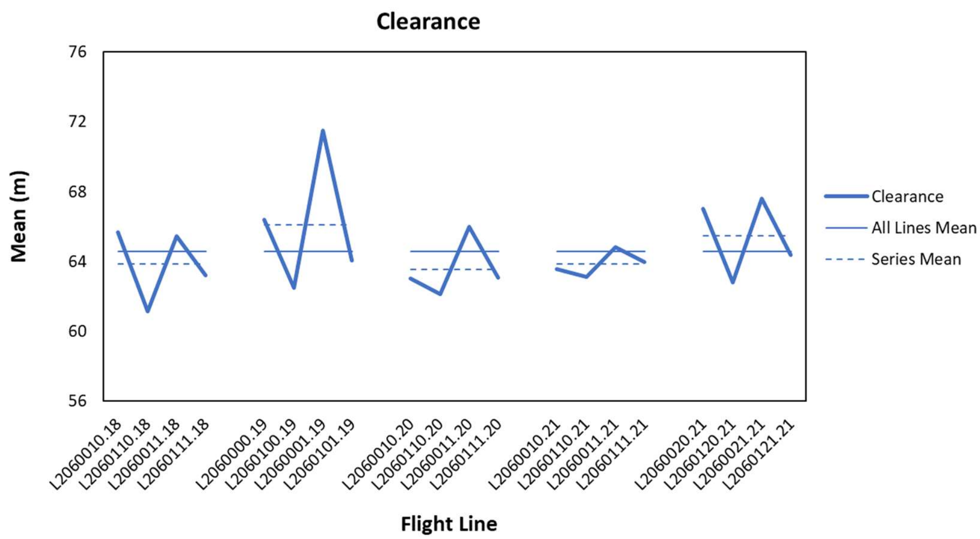

Figure 3.3: Mean flight clearance for each flight, plotted against the average for all twenty repeat flights (thin blue line) and the four-line average for each flight-series (thin dashed line). Data used and plotted are the original ~6 m sampled data.

3.1.1 Intra-series variability

The amount of intra-series variation in the line-mean EM response amplitudes is visually similar for all components and frequencies, with the exceptions of Q25lev–2018 series, Q25lev–2021.2 and Q12lev–2019, where significantly greater intra-series variation is observed. The larger visual variation for these three particular components–series is confirmed in Table 3.3, where the standard deviations of the four mean values are greater than 100 ppm. The standard deviations of all other components–series lie in the range 25 – 80 ppm. It is often, but not always, the case that sympathetic changes in line-mean amplitudes are observed within each series from frequency to frequency, as exemplified by the quadrature components for the 2020 series, where line-mean amplitudes are lower for all quadrature frequencies for lines L2060010.20 and L2060011.20 and higher for lines L2060110.20 and L2060111.20. The same sympathetic changes in the quadrature components of the 2020 series are not repeated in the in-phase components. The extent of sympathetic change in the line-mean amplitudes is variable across all the eight in-phase and quadrature components, the four frequencies and the five series.

It is also often, but not always, the case that changes in the line-mean EM response amplitudes are antithetic (inverse) to changes in line-mean flight clearances (Figure 3.3), with lower mean response amplitudes corresponding with higher mean clearances. The relationship between mean EM response amplitude and mean flight clearance for each flight-line is examined in the cross-plots of Figure 3.4. The linear trendlines added to the cross-plots for each flight-series are intended to illustrate the general trend present in the data, rather than to model the amplitude-clearance relationship explicitly. A negative gradient in the trendlines is expected where mean clearance has an influence on the mean amplitude variation. Consistently negative trendlines and greater sensitivity to mean flight clearance is apparent in all quadrature components, as well as the in-phase 25 kHz (P25 lev) and 12 kHz (P12lev) components. Scatter around the trendlines, as well as zero to positive gradients in the in-phase 3 kHz (P3lev) and 0.9 kHz (P09lev) components, suggests additional control, other than flight clearance, on the observed variation in the mean amplitudes. The 2021.2 flight-series (green data points, Figure 3.4) is noticeably anomalous in the number of data components characterised by positive gradient trends in the cross-plots, and therefore showing little sensitivity to flight-clearance on the recorded EM data amplitudes: P25lev, P12lev, P09lev, Q12lev and Q3lev. The potential origin and nature of the additional (stronger) control on mean EM response amplitudes is examined in subsequent sections of the report.

An analogous analysis to the above, examining the variation in line-mean resistivities (derived from both SGL 'Extended Resistivity' and Geosoft HEM single-frequency resistivity models), is presented in Section 5. The examination of line-to-line variation in mean resistivity provides opportunity to examine data variation in the absence of flight-clearance variation, which is accounted for in the computation of the resistivity models.

Table 3.2. Summary of the mean amplitudes ('Line Mean') of the FEM responses for each repeat flight, for all in-phase data components. Also shown are the means and standard deviations (SD) of the four 'Line Mean' values for each series of flights, as well the mean and standard deviation of the twenty 'Line Mean' values for all flights. Data used are the original ~6 m sampled data.

Series (Year)	Line Number	P25lev					P12lev				
		Line Mean (ppm)	Series Mean (ppm)	Series SD (ppm)	All Lines Mean (ppm)	All Lines SD (ppm)	Line Mean (ppm)	Series Mean (ppm)	Series SD (ppm)	All Lines Mean (ppm)	All Lines SD (ppm)
2018	L2060010.18	948.5	958.3	78.4	995.8	105.6	702.9	658.9	52.7	626.1	71.3
	L2060110.18	1065.8					699.9				
	L2060011.18	877.8					592.7				
	L2060111.18	941.2					640.4				
2019	L2060000.19	943.7	971.2	78.9			619.6	651.1	44.5		
	L2060100.19	945.2					717.0				
	L2060001.19	908.9					634.6				
	L2060101.19	1086.8					633.1				
2020	L2060010.20	952.4	872.3	59.7			598.7	560.1	57.8		
	L2060110.20	836.5					620.4				
	L2060011.20	818.5					511.1				
	L2060111.20	881.9					510.2				
2021.1	L2060010.21	1137.2	1118.0	32.6			591.0	571.2	63.8		
	L2060110.21	1069.4					652.7				
	L2060011.21	1136.9					523.3				
	L2060111.21	1128.4					517.7				
2021.2	L2060020.21	1009.4	1059.3	48.9			699.9	689.5	54.6		
	L2060120.21	1126.2					609.4				
	L2060021.21	1056.1					723.4				
	L2060121.21	1045.6					725.1				

Series (Year)	Line Number	P3lev					P09lev				
		Line Mean (ppm)	Series Mean (ppm)	Series SD (ppm)	All Lines Mean (ppm)	All Lines SD (ppm)	Line Mean (ppm)	Series Mean (ppm)	Series SD (ppm)	All Lines Mean (ppm)	All Lines SD (ppm)
018	L2060010.18	236.8	213.6	38.7	211.0	54.4	208.1	166.9	43.6	145.5	40.2
	L2060110.18	244.3					181.5				
	L2060011.18	214.6					105.6				
	L2060111.18	158.7					172.3				
2019	L2060000.19	227.1	226.5	28.0			109.4	119.2	23.4		
	L2060100.19	260.8					146.9				
	L2060001.19	225.7					128.0				
	L2060101.19	192.3					92.7				
2020	L2060010.20	140.7	179.1	70.2			45.6	128.7	56.7		
	L2060110.20	152.9					173.7				
	L2060011.20	138.7					149.4				
	L2060111.20	284.0					146.0				
2021.1	L2060010.21	190.1	202.1	60.0			146.8	141.0	43.6		
	L2060110.21	143.9					85.7				
	L2060011.21	188.1					139.4				
	L2060111.21	286.2					192.2				
2021.2	L2060020.21	297.4	233.9	68.6			197.8	171.8	25.5		
	L2060120.21	265.9					157.2				
	L2060021.21	233.7					188.4				
	L2060121.21	138.6					143.9				

Table 3.3. Summary of the mean amplitudes ('Line Mean') of the FEM responses for each repeat flight, for all quadrature data components. Also shown are the means and standard deviations (SD) of the four 'Line Mean' values for each series of flights, as well the mean and standard deviation of the twenty 'Line Mean' values for all flights. Data used are the original ~6 m sampled data.

Series (Year)	Line Number	Q25lev					Q12lev				
		Line Mean (ppm)	Series Mean (ppm)	Series SD (ppm)	All Lines Mean (ppm)	All Lines SD (ppm)	Line Mean (ppm)	Series Mean (ppm)	Series SD (ppm)	All Lines Mean (ppm)	All Lines SD (ppm)
2018	L2060010.18	1076.7	999.8	130.5	1026.0	131.7	788.3	836.7	39.1	847.3	81.9
	L2060110.18	1127.9					838.1				
	L2060011.18	835.1					836.6				
	L2060111.18	959.5					884.0				
2019	L2060000.19	950.6	885.1	49.2			839.5	851.8	109.7		
	L2060100.19	845.7					933.4				
	L2060001.19	848.8					701.1				
	L2060101.19	895.2					933.1				
2020	L2060010.20	941.9	957.3	37.2			833.3	809.6	58.8		
	L2060110.20	1003.6					873.8				
	L2060011.20	916.5					735.4				
	L2060111.20	967.2					795.9				
2021.1	L2060010.21	1077.7	1127.5	34.4			828.6	795.5	57.8		
	L2060110.21	1156.2					856.4				
	L2060011.21	1133.7					768.3				
	L2060111.21	1142.4					728.7				
2021.2	L2060020.21	1061.0	1160.3	107.1			917.7	943.1	56.6		
	L2060120.21	1293.1					877.3				
	L2060021.21	1087.2					973.3				
	L2060121.21	1200.0					1004.1				

Series (Year)	Line Number	Q3lev					Q09lev				
		Line Mean (ppm)	Series Mean (ppm)	Series SD (ppm)	All Lines Mean (ppm)	All Lines SD (ppm)	Line Mean (ppm)	Series Mean (ppm)	Series SD (ppm)	All Lines Mean (ppm)	All Lines SD (ppm)
2018	L2060010.18	321.0	320.3	43.2	362.2	57.3	119.4	116.9	23.6	177.4	48.2
	L2060110.18	381.1					147.6				
	L2060011.18	288.6					91.0				
	L2060111.18	290.5					109.7				
2019	L2060000.19	378.5	367.7	35.9			159.3	186.7	37.4		
	L2060100.19	403.7					207.3				
	L2060001.19	318.2					151.5				
	L2060101.19	370.5					228.9				
2020	L2060010.20	337.7	323.7	61.8			115.2	169.7	52.4		
	L2060110.20	402.1					240.9				
	L2060011.20	256.8					156.4				
	L2060111.20	298.5					166.4				
2021.1	L2060010.21	408.0	379.9	27.9			192.2	228.9	28.7		
	L2060110.21	394.8					232.2				
	L2060011.21	344.3					229.1				
	L2060111.21	372.6					262.2				
2021.2	L2060020.21	477.0	419.3	58.4			190.2	184.5	30.2		
	L2060120.21	418.1					225.0				
	L2060021.21	442.5					163.9				
	L2060121.21	339.5					159.1				

3.1.2 Inter-series (inter-year) variability

Inter-series variation is markedly higher for the 25 kHz and 12 kHz EM responses, for both in-phase and quadrature components, than for the 3 kHz and 0.9 kHz responses (Figure 3.1). Greater series-to-series variation in the two higher frequencies is reflected in the larger standard deviations of the line-means across all twenty flight-lines (Tables 3.2 and 3.3): greater than 100 ppm for both 25 kHz components and greater than 70 ppm for the 12 kHz components, in comparison with less than 60 ppm for the 3 kHz components and less than 50 ppm for the 0.9 kHz components.

Inter-series variation in mean flight-clearance (Figure 3.3) appears unlikely to account for the inter-series variation in mean EM response amplitudes at 25 and 12 kHz. Higher or lower mean clearances for different series (in Figure 3.3) do not translate consistently into lower and higher amplitude EM responses respectively. Nor does inter-series variation in mean flight-clearance account for instances where the average separation in amplitude between the 25 kHz and 12 kHz components decreases or increases (e.g., the 2021.1 series for both in-phase and quadrature (increased separation) and the 2019 series for quadrature (decreased separation)). The broad clusters defined by all twenty data points together in the mean EM amplitude versus mean clearance cross-plots of Figure 3.4 do not define any recognisable trends suggesting any systematic relationship between the average flight clearance and average EM amplitudes from series-to-series.

While temporal variations in cultural noise levels and in the definition of the zero-levels of the data components cannot be ruled out in accounting for the observed inter-series variation in mean EM response amplitudes, particularly at 25 and 12 kHz, such variation may be accounted for by real temporal variation in the shallow hydrogeological (and resistivity) subsurface structure.

It may be worthwhile ascertaining from SGL, whether significant repairs or modifications to the EM instrumentation took place between any of the five test-line series, and whether there is potential for the baselines (zero levels) of any of the data components to have been changed in the process.

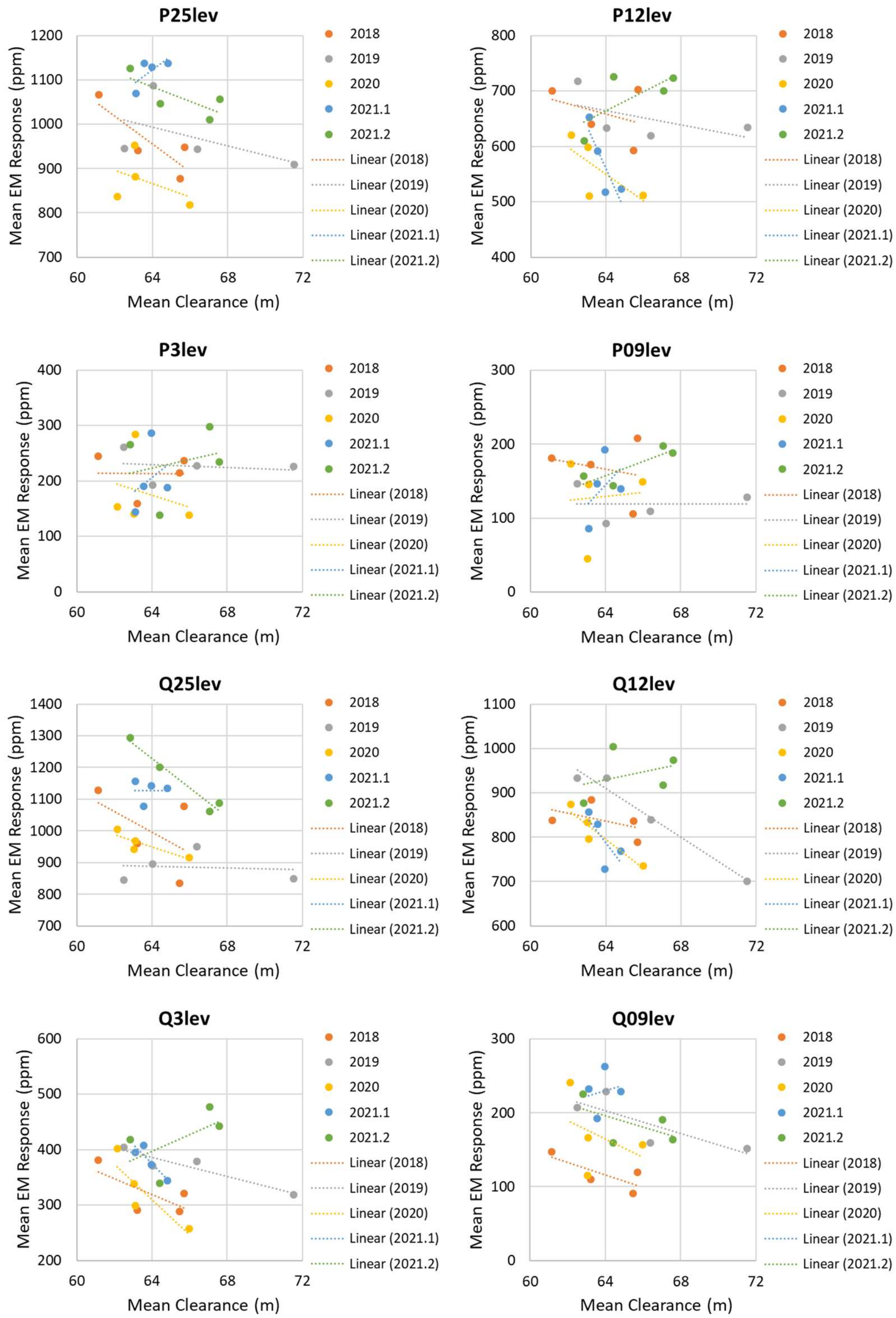

Figure 3.4: Cross-plots of mean EM response amplitude versus mean flight clearance for each repeat flight, colour coded by flight-series (year). Upper four panels show in-phase responses at each frequency, lower four panels show quadrature responses. A linear trendline is shown in the cross-plots for each flight-series (consisting of four repeat flights).

3.1.3 First-order temperature variability

Drift in the baselines (zero-levels) of the eight EM data components arises primarily due to temperature changes during flight. External air temperature is measured and recorded during flight. The relationship between external air temperature, EM system temperature and instrument drift is complex and not well understood (pers. comm., Luc Lafrenière, SGL, 10 June 2022). Drift corrections, applied during data processing to each of the eight EM components independently, aim to practically correct for zero-level drift of the EM system without using the recorded temperature data explicitly. Where sufficient constraints on drift exist, drift corrections should remove any potential temperature effects on the EM data. First-order characteristics of temperature changes during the test flights are examined to assess whether any temperature effects might correlate with the inter-series (inter-year) mean amplitude variations of the EM responses, particularly with respect to the 12 and 25 kHz responses.

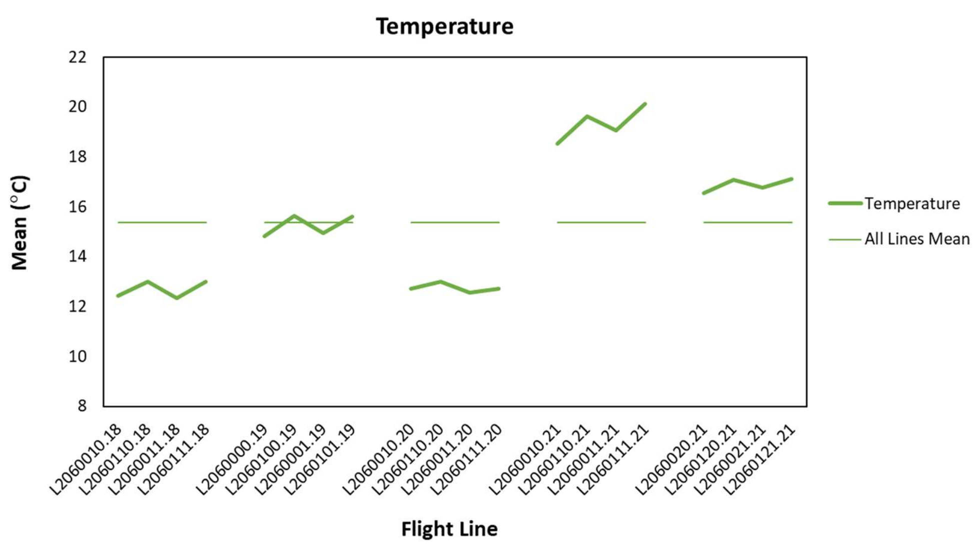

Figure 3.5: Mean temperature for each flight. Data used and plotted are the original ~6 m sampled data.

The mean temperature recorded during flight for each of the four flights within a test-line series (Figure 3.5) is characterised by a distinctive zig-zag pattern in which the average temperature is lower (by about 0.3°C – 1.1°C) during the northward, in-land directed flights (345° heading) compared with the southward directed flights (165° heading). The association of mean temperature with heading direction appears to be coincidental, as there is also a strong sympathetic relationship with mean flight clearance (Figure 3.3) which is characterised by a similar zig-zag pattern, with higher mean clearances associated with northward (345°) directed flights. A cross-plot of mean clearance versus mean temperature (Figure 3.6) illustrates strong linear trends, with negative gradients, for each of the individual series, where higher mean temperatures are associated with lower mean clearances.

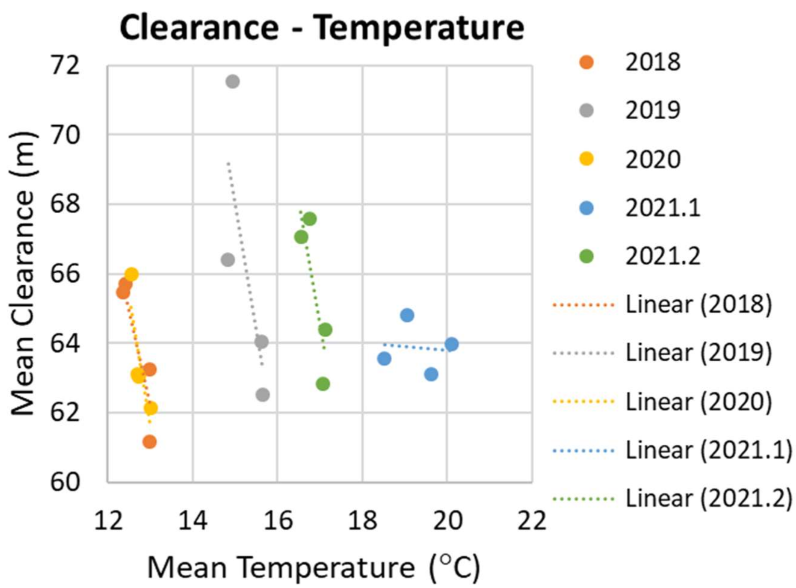

Figure 3.6: Cross-plot of mean clearance versus mean temperature for each repeat flight, colour coded by flight-series (year).

Cross-plots of mean EM response amplitude versus mean temperature for all eight data components are shown in Figure 3.7, with linear trendlines added for illustrative purposes. The association between mean temperature and mean clearance is seen to persist in Figure 3.7 when examining the data for each individual series. With some exceptions, generally series with negative gradient trendlines in the graphs of mean EM response amplitude versus clearance (Figure 3.4) correspond with positive gradient trendlines in the graphs of mean EM response amplitude versus temperature (Figure 3.7). It is difficult, therefore, to separate out in the data the effects of temperature and clearance on the mean EM responses.

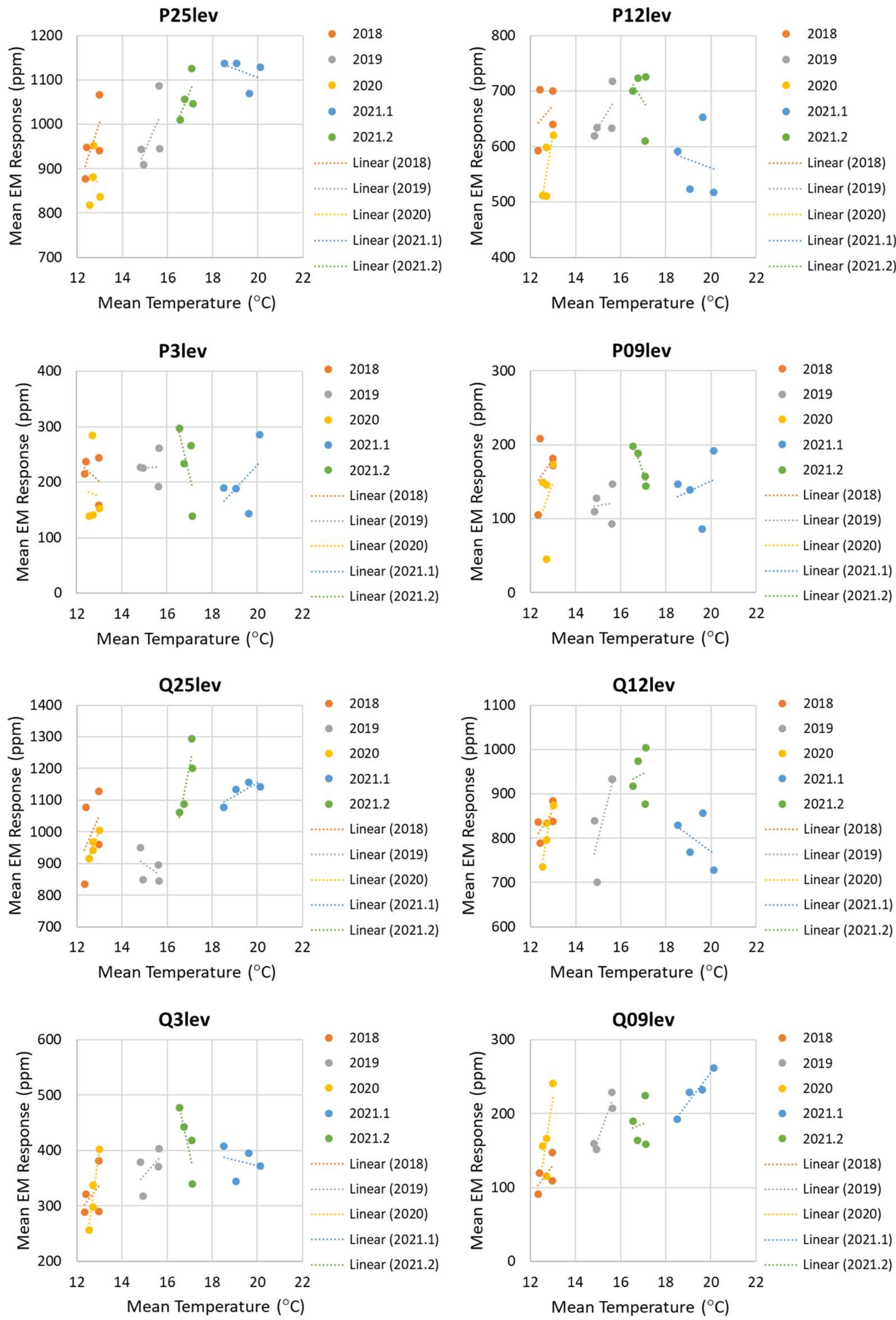

Figure 3.7: Cross-plots of mean EM response amplitude versus mean temperature for each repeat flight, colour coded by flight-series (year). Upper four panels show in-phase responses at each frequency, lower four panels show quadrature responses. A linear trendline is shown in the cross-plots for each flight-series (consisting of four repeat flights).

The clusters of data defined by all twenty data points together in the mean EM response amplitude versus temperature cross-plots (Figure 3.7) generally do not define any recognisable trends to suggest any systematic relationship between the average flight temperature and average EM amplitudes from series-to-series. The one exception is the 25 kHz in-phase (P25lev) data, where there does appear to be a trend of increasing EM response amplitudes with increasing temperature from series-to-series.

3.2 Variability in FEM Responses

While the previous section (Section 3.1) assessed first-order variability in the EM responses, by examining the variation in line-mean EM amplitudes, the section here assesses variability in the EM responses and changes in variability with distance along the flight-lines. The variability is assessed by calculating means and standard deviations of the mean along the test-line for each series of four flights and for all twenty flights together. The EM responses are interpolated at a 1 m distance interval along each flight line before averaging, as discussed in greater detail in Section 2.2.

Figures 3.8 – 3.15 that follow provide a catalogue of the EM response variability along the test-line for each of the eight data components. In each figure, the top panel plots individually the EM responses for all twenty flight-lines, together with the twenty-line mean response. The middle panel plots the four-line mean responses for each data series (year), together with the twenty-line mean response. The bottom panel plots the four-line standard deviation of the mean for each data series (year), together with the twenty-line standard deviation.

Two points are worth keeping in mind when viewing the catalogue: (i) the EM responses retain sensitivity to flight-clearance and its variability along the test-line – the effect of which is considered further in Sections 3.3 and 3.4, and (ii) the twenty-line mean responses and standard deviations may be impacted on by real shallow, hydrogeological (and hence resistivity) variation with time across all five data series. Annotated on each standard deviation plot, for reference, are the locations of nine standard deviation anomalies (N1 – N9) observed in the 3 and 0.9 kHz EM responses. Also plotted for reference are two significant radar (clearance) standard deviation anomalies (R1 and R2) (see Figure 3.16). Both sets of anomaly locations are considered further in Section 3.4.

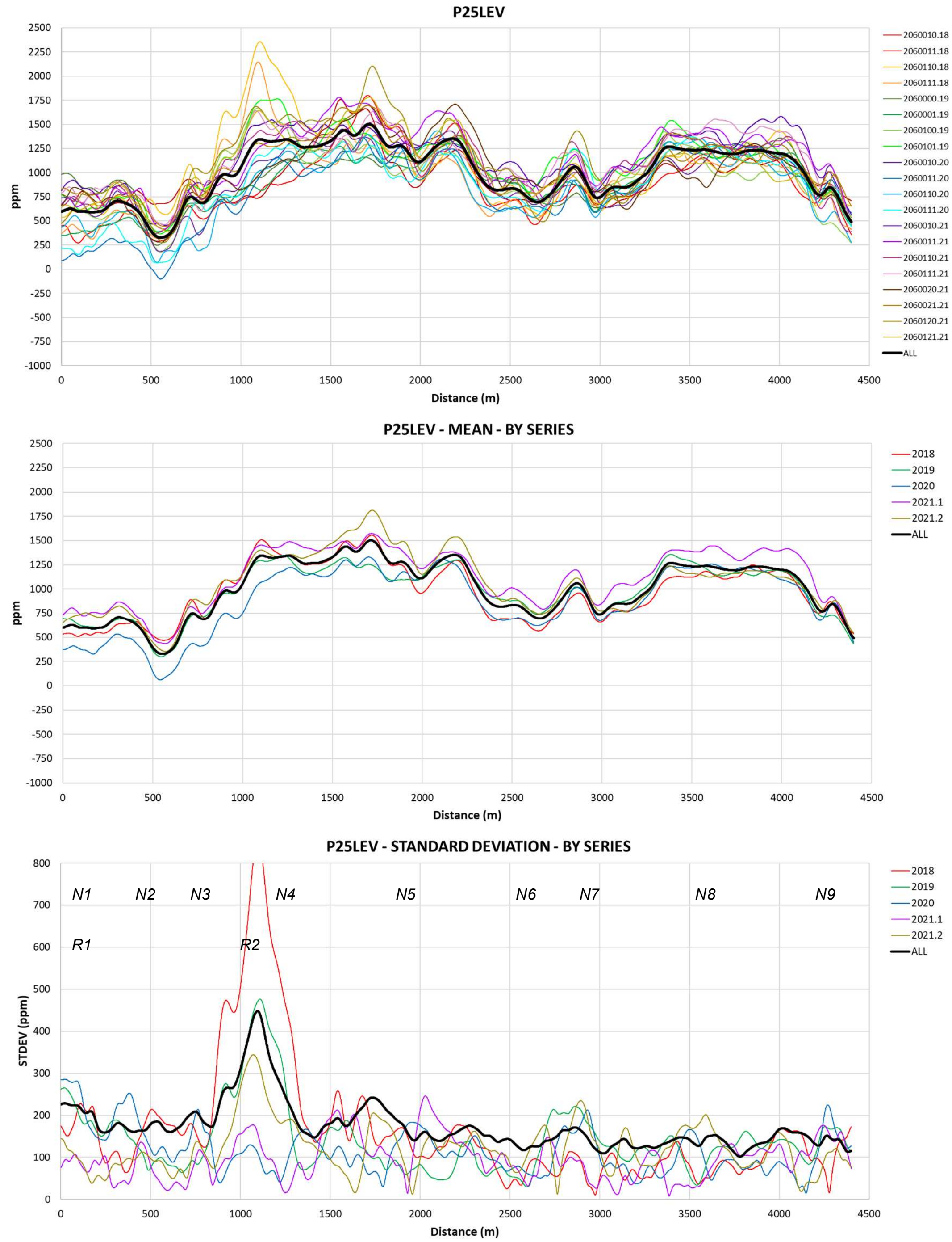

Figure 3.8: 25 kHz in-phase responses (P25lev data channel), plotted against flight-distance, interpolated at 1 m intervals. Southern end of line (coast-line) located at 0 m distance. (Upper panel) P25lev responses, coloured coded by flight, together with the twenty-flight mean (black line). (Middle panel) Mean P25lev responses by series, colour-coded, and shown together with the twenty-flight mean (black line). (Lower panel) P25lev standard deviation of the mean (STDEV) by series, colour-coded, and shown together with STDEV for all twenty lines. Location of STDEV peaks in 3 and 0.9 kHz EM data (N1 to N9) annotated, as well as STDEV peaks in clearance data (R1 and R2).

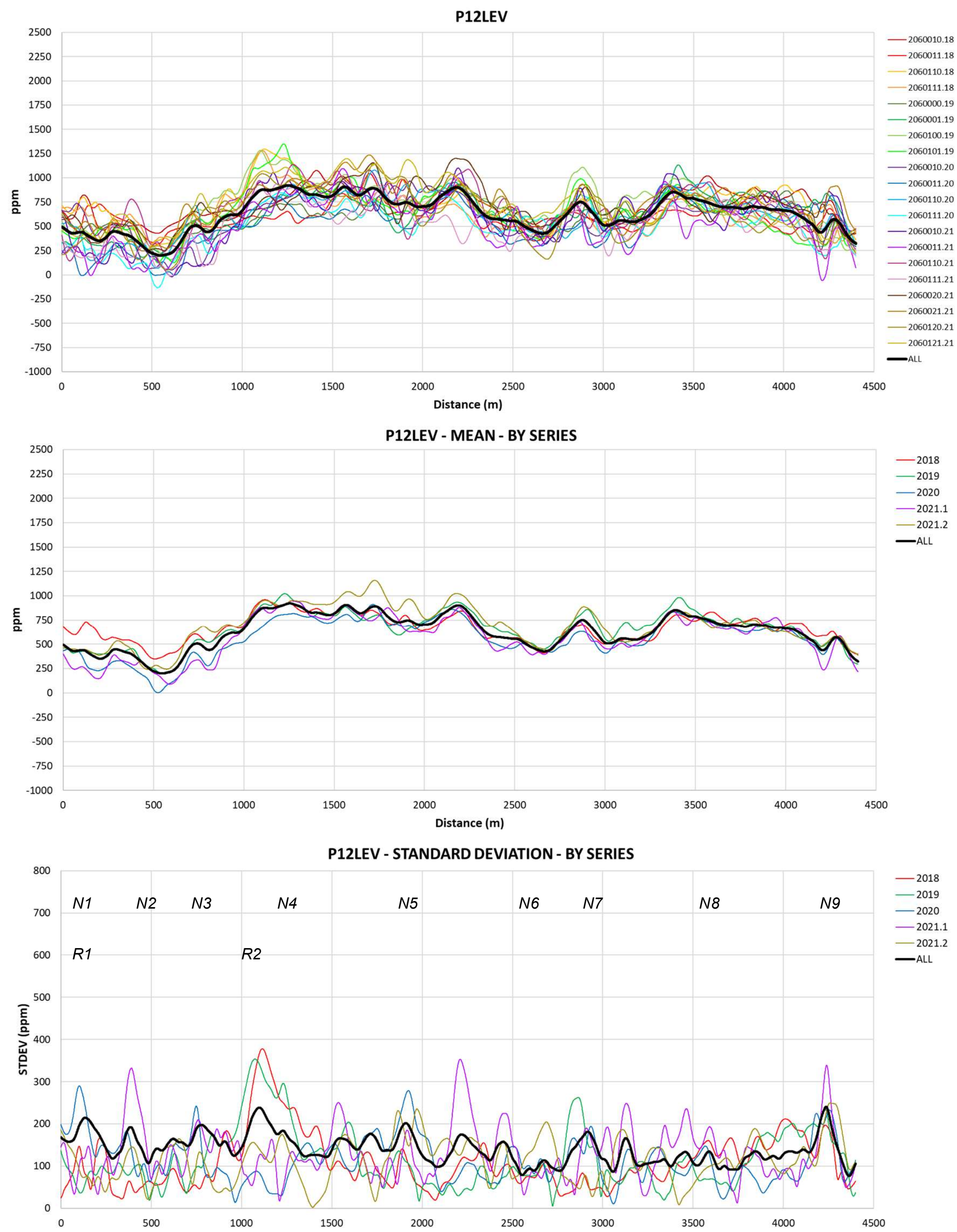

***Figure 3.9:** 12 kHz in-phase responses (P12lev data channel), plotted against flight-distance, interpolated at 1 m intervals. Southern end of line (coast-line) located at 0 m distance. (Upper panel) P12lev responses, coloured coded by flight, together with the twenty-flight mean (black line). (Middle panel) Mean P12lev responses by series, colour-coded, and shown together with the twenty-flight mean (black line). (Lower panel) P12lev standard deviation of the mean (STDEV) by series, colour-coded, and shown together with STDEV for all twenty lines. Location of STDEV peaks in 3 and 0.9 kHz EM data (N1 to N9) annotated, as well as STDEV peaks in clearance data (R1 and R2).*

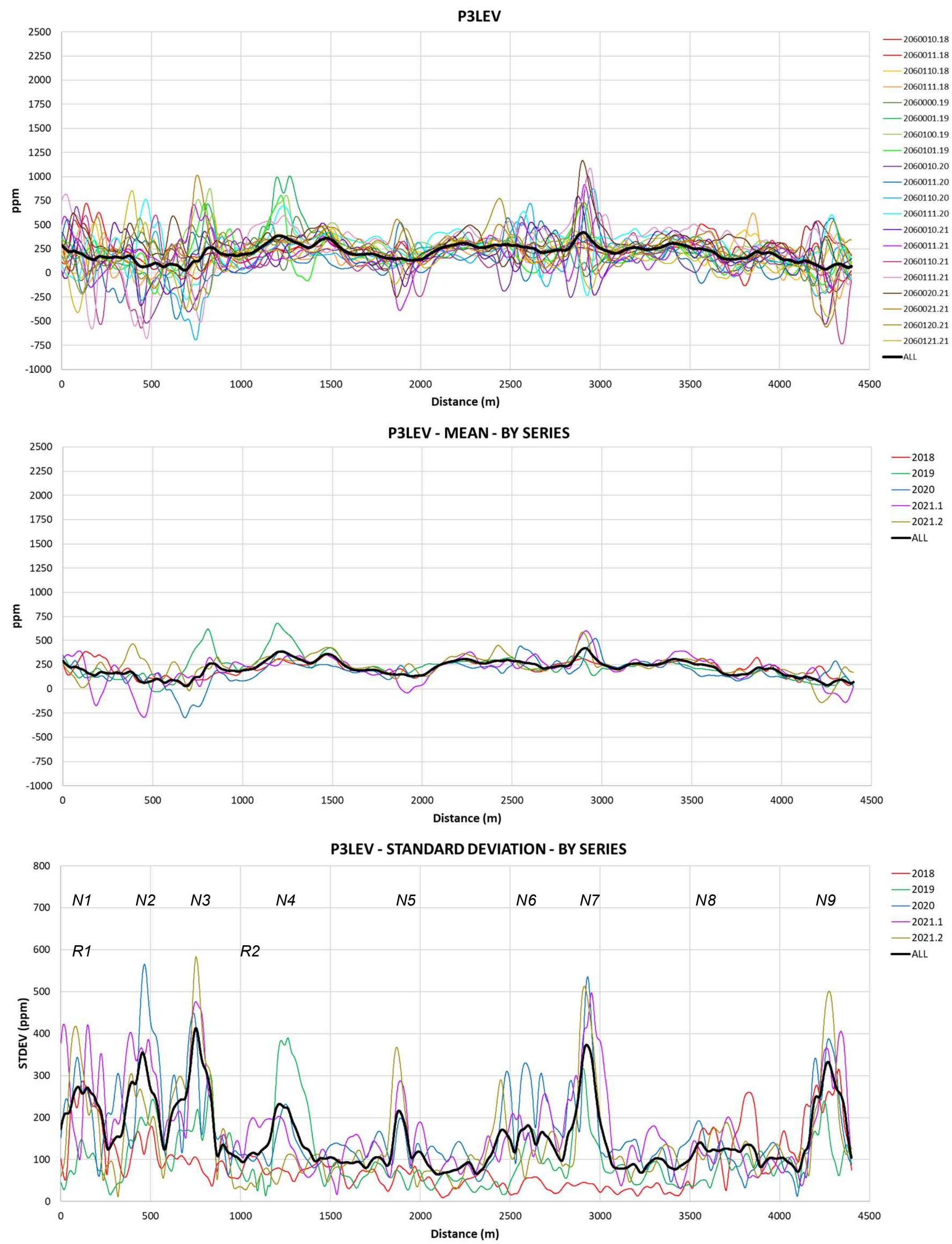

Figure 3.10: 3 kHz in-phase responses (P3lev data channel), plotted against flight-distance, interpolated at 1 m intervals. Southern end of line (coast-line) located at 0 m distance. (Upper panel) P3lev responses, coloured coded by flight, together with the twenty-flight mean (black line). (Middle panel) Mean P3lev responses by series, colour-coded, and shown together with the twenty-flight mean (black line). (Lower panel) P3lev standard deviation of the mean (STDEV) by series, colour-coded, and shown together with STDEV for all twenty lines. Location of STDEV peaks in 3 and 0.9 kHz EM data (N1 to N9) annotated, as well as STDEV peaks in clearance data (R1 and R2).

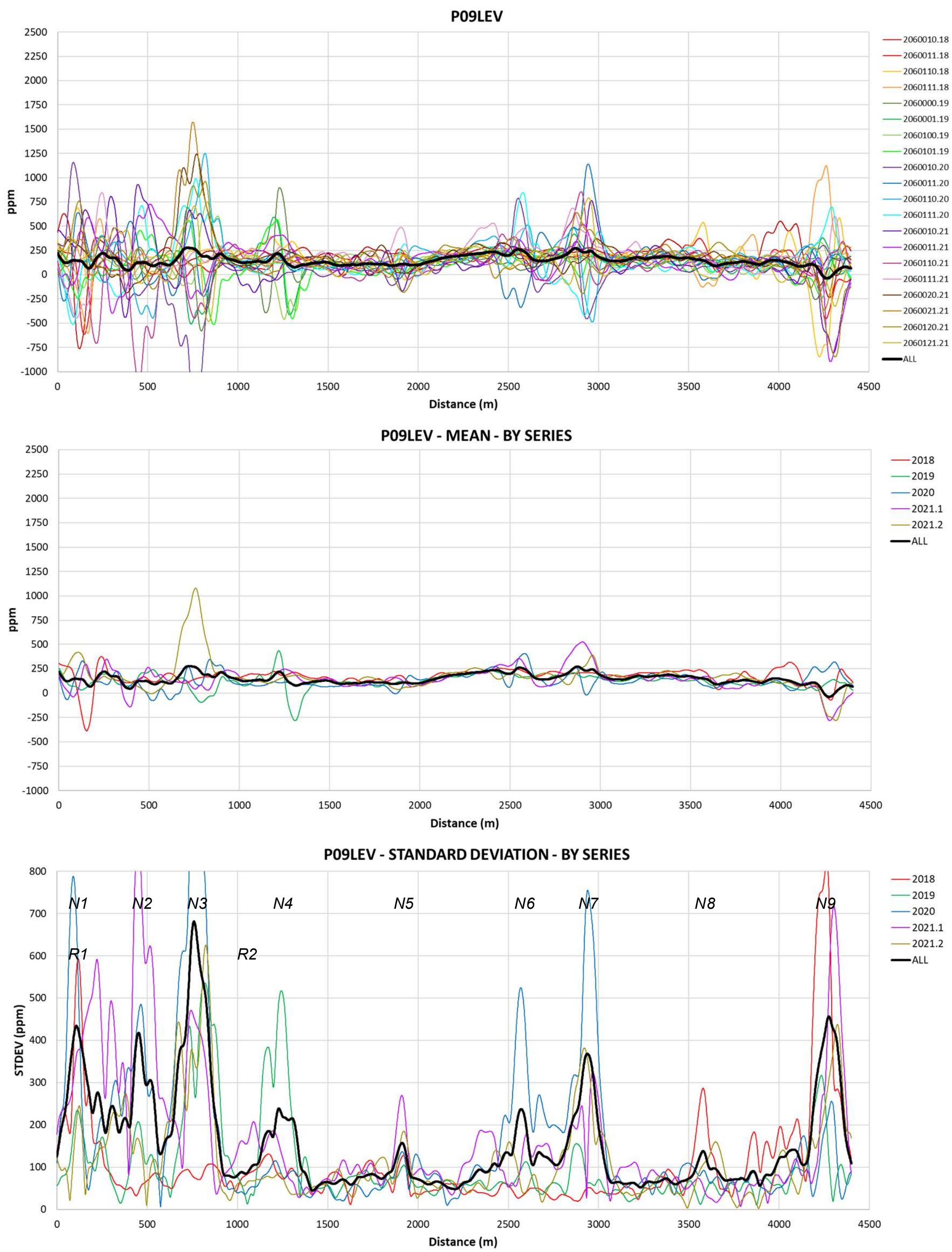

Figure 3.11: 0.9 kHz in-phase responses (P09lev data channel), plotted against flight-distance, interpolated at 1 m intervals. Southern end of line (coast-line) located at 0 m distance. (Upper panel) P09lev responses, coloured coded by flight, together with the twenty-flight mean (black line). (Middle panel) Mean P09lev responses by series, colour-coded, and shown together with the twenty-flight mean (black line). (Lower panel) P09lev standard deviation of the mean (STDEV) by series, colour-coded, and shown together with STDEV for all twenty lines. Location of STDEV peaks in 3 and 0.9 kHz EM data (N1 to N9) annotated, as well as STDEV peaks in clearance data (R1 and R2).

Figure 3.12: 25 kHz quadrature responses (Q25lev data channel), plotted against flight-distance, interpolated at 1 m intervals. Southern end of line (coast-line) located at 0 m distance. (Upper panel) Q25lev responses, coloured coded by flight, together with the twenty-flight mean (black line). (Middle panel) Mean Q25lev responses by series, colour-coded, and shown together with the twenty-flight mean (black line). (Lower panel) Q25lev standard deviation of the mean (STDEV) by series, colour-coded, and shown together with STDEV for all twenty lines. Location of STDEV peaks in 3 and 0.9 kHz EM data (N1 to N9) annotated, as well as STDEV peaks in clearance data (R1 and R2).

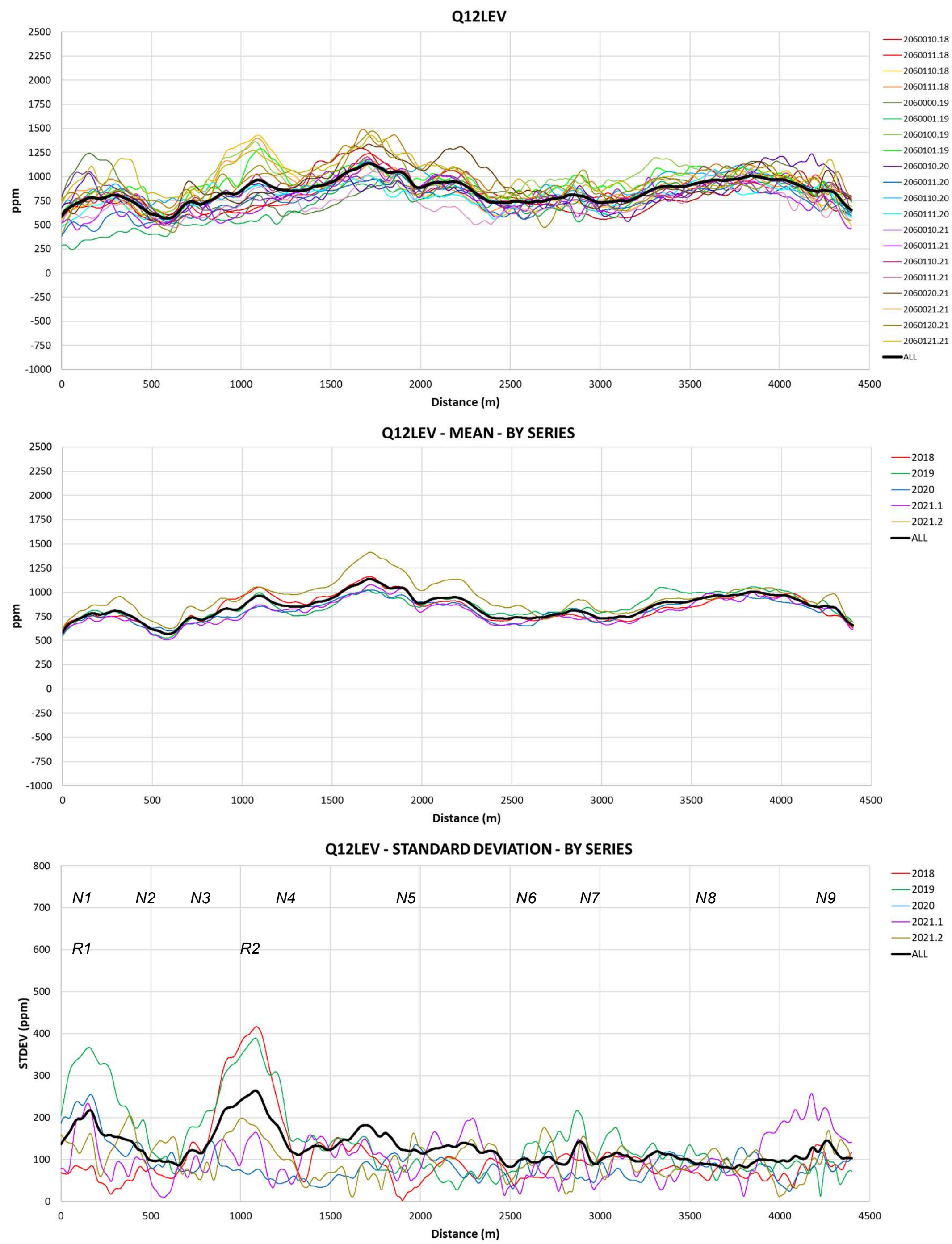

Figure 3.13: 12 kHz quadrature responses (Q12lev data channel), plotted against flight-distance, interpolated at 1 m intervals. Southern end of line (coast-line) located at 0 m distance. (Upper panel) Q12lev responses, coloured coded by flight, together with the twenty-flight mean (black line). (Middle panel) Mean Q25lev responses by series, colour-coded, and shown together with the twenty-flight mean (black line). (Lower panel) Q12lev standard deviation of the mean (STDEV) by series, colour-coded, and shown together with STDEV for all twenty lines. Location of STDEV peaks in 3 and 0.9 kHz EM data (N1 to N9) annotated, as well as STDEV peaks in clearance data (R1 and R2).

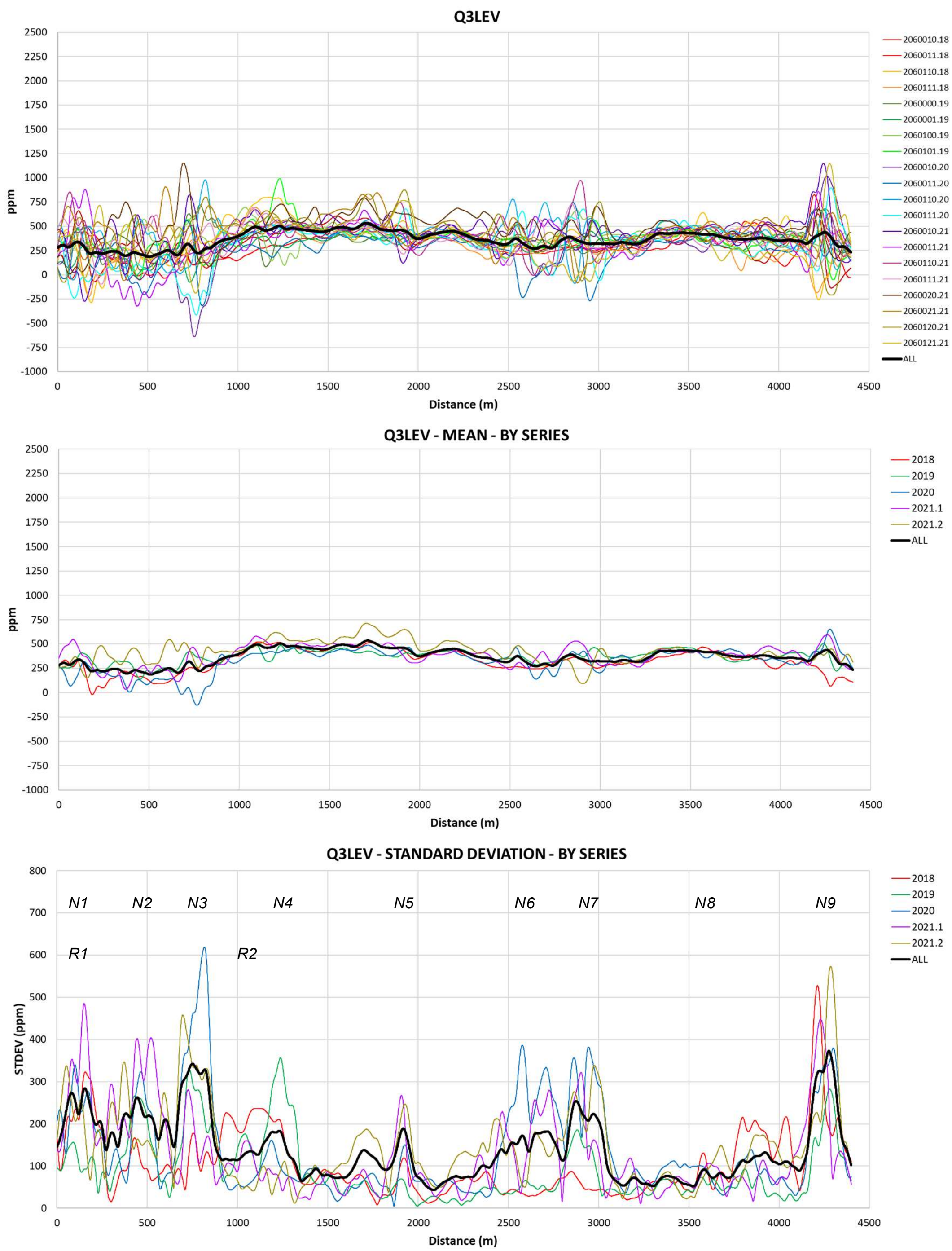

Figure 3.14: 3 kHz quadrature responses (Q3lev data channel), plotted against flight-distance, interpolated at 1 m intervals. Southern end of line (coast-line) located at 0 m distance. (Upper panel) Q3lev responses, coloured coded by flight, together with the twenty-flight mean (black line). (Middle panel) Mean Q3lev responses by series, colour-coded, and shown together with the twenty-flight mean (black line). (Lower panel) Q3lev standard deviation of the mean (STDEV) by series, colour-coded, and shown together with STDEV for all twenty lines. Location of STDEV peaks in 3 and 0.9 kHz EM data (N1 to N9) annotated, as well as STDEV peaks in clearance data (R1 and R2).

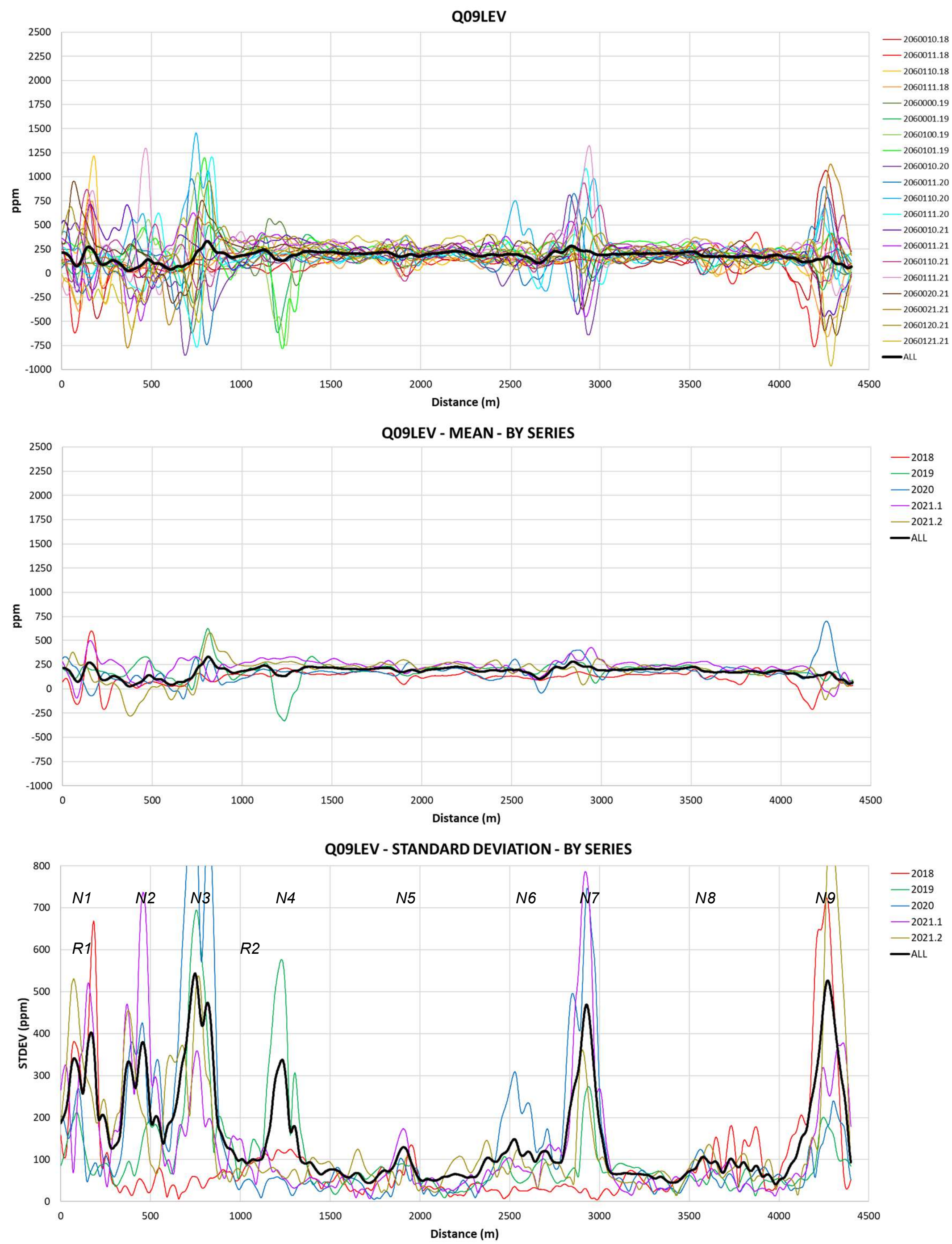

Figure 3.15: 0.9 kHz quadrature responses (Q09lev data channel), plotted against flight-distance, interpolated at 1 m intervals. Southern end of line (coast-line) located at 0 m distance. (Upper panel) Q09lev responses, coloured coded by flight, together with the twenty-flight mean (black line). (Middle panel) Mean Q09lev responses by series, colour-coded, and shown together with the twenty-flight mean (black line). (Lower panel) Q09lev standard deviation of the mean (STDEV) by series, colour-coded, and shown together with STDEV for all twenty lines. Location of STDEV peaks in 3 and 0.9 kHz EM data (N1 to N9) annotated, as well as STDEV peaks in clearance data (R1 and R2).

3.3 Variability in Other Measured Parameters

The variability in a range of different parameters that are directly measured and recorded during flight, or which can be calculated from recorded parameters, is assessed to identify parameters that might correlate with and account for the variability observed in the EM responses of Figures 3.8 – 3.15 in Section 3.2. Variability in the following parameters is assessed: flight clearance, flight speed, flight heading, power-line monitor, temperature, topography, perpendicular distance from the 'average' line and the full swath-width (being the distance from the western-most to eastern most flight-line, at any location along the line, measured perpendicular to the flight direction). Not all the parameters are necessarily anticipated to correlate with EM response variability, but the full suite is nevertheless presented and assessed for completeness.

i. Flight clearance is measured directly by the aircraft's radar altimeter (RADAR data channel).

ii. Flight speed is calculated from the aircraft's coordinate (location) information (ITM_X and ITM_Y channels) and the time channel (reflecting the 10 Hz sample interval). Aircraft speed defines the spatial sample interval along the flight-lines.

iii. Flight heading is the instantaneous flight direction between two adjacent sample locations defined by their ITM_X and ITM_Y coordinates, and nominally is close to either 165° or 345° E of N. The approach adopted here has been to add 180° to all headings around 165°, to bring all the data into the northward heading quadrant. Implicit in bringing all data into the northward heading quadrant is the assumption that the location of the transmitter coils, whether on the western or eastern side of the aircraft/flight-line, has no effect on the recorded EM responses and that the only parameter of interest is, effectively, the direction of the line between the transmitter and the receiver coils (being perpendicular to the instantaneous heading direction). Aircraft yaw will also affect the angle of the line between the transmitter and receiver coils with respect to the heading direction. However, as aircraft yaw data are not provided as part of the test-line dataset, the effects of yaw cannot be assessed in this work.

iv. Powerline monitor data (PLM_nT channel) are recorded by the aircraft's magnetometer and provide a measurement of the strength of the magnetic field generated by powerlines traversed by the aircraft.

v. Temperature data (TEMP channel) record the external air temperature during flight (see also Section 3.1.3).

vi. Topography (or Digital Elevation Model, DEM) beneath the flight-line is calculated as the difference between the aircraft's vertical location (Z coordinate) with respect to sea level (MSLHGT channel) and the flight clearance above ground surface (RADAR channel).

vii. Perpendicular distance from the 'average' line. The 'average' line is the mean line of the twenty repeat flights. It is defined by the mean ITM_X and ITM_Y coordinates at every (interpolated) 1 m distance location along the test-line. The distance between any location (distance) on any of the twenty test-lines and the average line can then be calculated (using the ITM_X and ITM_Y coordinates) to provide the perpendicular distance from the 'average' line at that location. The convention adopted is that distances are negative for lines west of the average line and positive for distances east of the average line.

viii. Full swath-width is the distance from western-most to eastern-most flight line at any location along the line, in a direction perpendicular to flight-line direction. It is calculated at any location along the line as the sum of the largest positive perpendicular distance and the absolute value of the largest negative perpendicular distance (perpendicular distance being defined above).

Figures 3.16 – 3.23 that follow provide a catalogue of the variability of the measured/calculated parameters listed above. In each figure, the top panel plots individually the parameter for all twenty flight-lines, together with the parameter twenty-line mean. The middle panel plots the four-line (series) means of the parameter, together with the twenty-line mean. The bottom panel plots the four-line standard deviation of the mean for each data series, together with the twenty-line standard deviation. Annotated on each standard deviation plot, for reference, are the locations of nine standard deviation anomalies (N1 – N9) observed in the 3 and 0.9 kHz EM responses and considered further in Section 3.4.

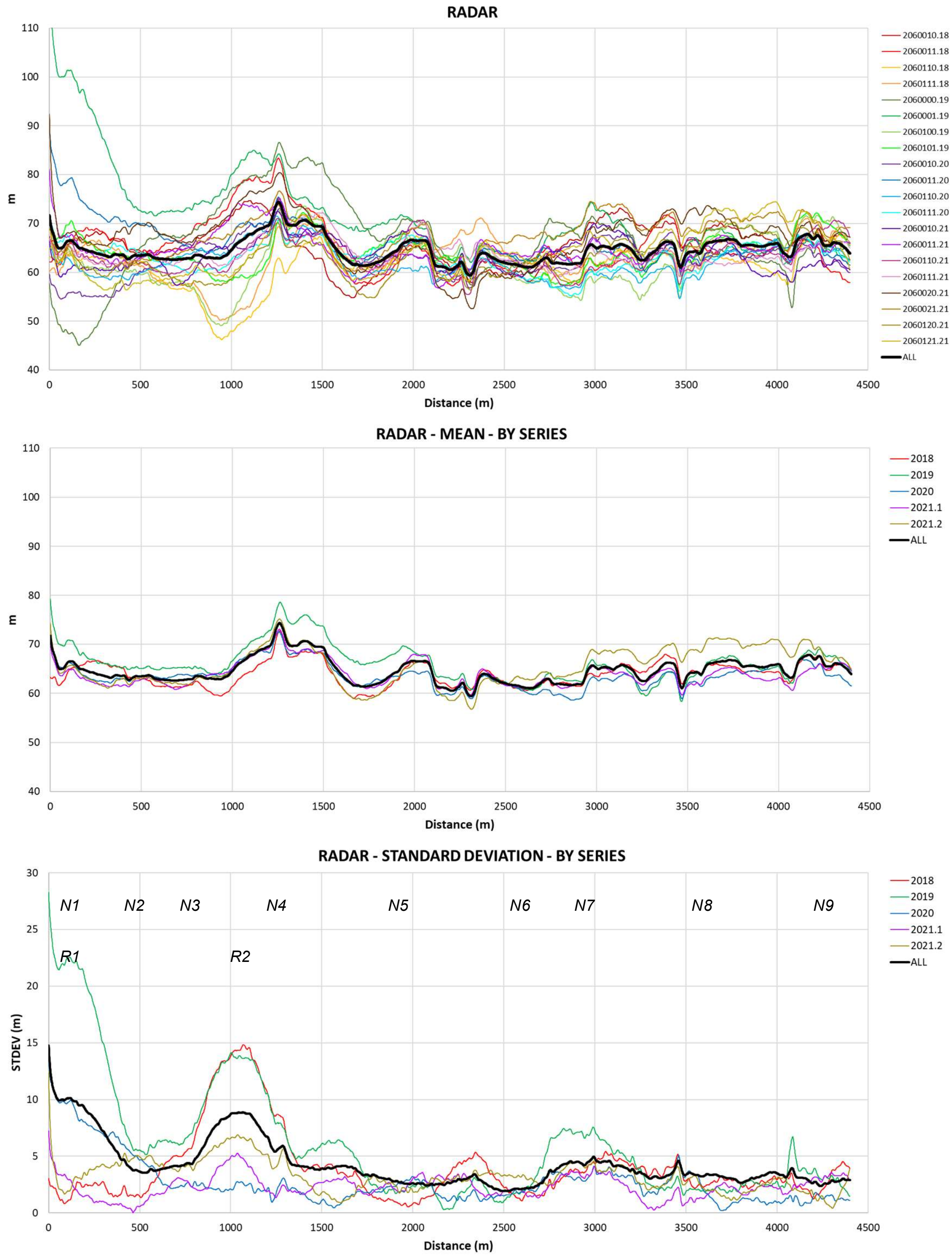

Figure 3.16: Flight clearance (RADAR data channel), plotted against flight-distance, interpolated at 1 m intervals. Southern end of line (coast-line) located at 0 m distance. (Upper panel) RADAR data, coloured coded by flight, together with the twenty-flight mean (black line). (Middle panel) Mean RADAR data by series, colour-coded, and shown together with the twenty-flight mean (black line). (Lower panel) RADAR standard deviation of the mean (STDEV) by series, colour-coded, and shown together with STDEV for all twenty lines. Location of STDEV peaks in 3 and 0.9 kHz EM data (N1 to N9) annotated, as well as STDEV peaks in clearance data (R1 and R2).

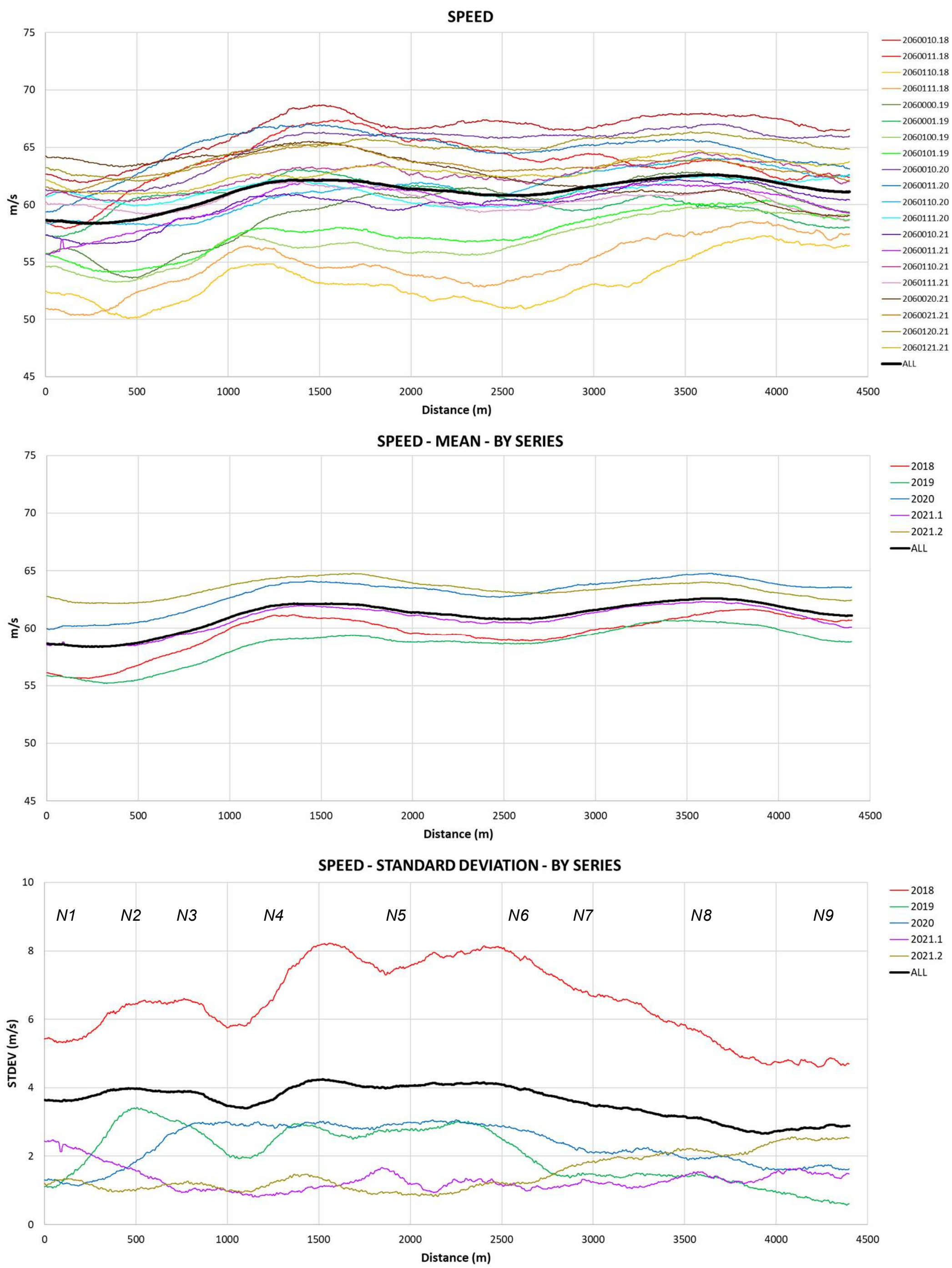

Figure 3.17: Flight speed (calculated from ITM_X, ITM_Y and TIME data channels), plotted against flight-distance, interpolated at 1 m intervals. Southern end of line (coast-line) located at 0 m distance. (Upper panel) Speed data, coloured coded by flight, together with the twenty-flight mean (black line). (Middle panel) Mean speed data by series, colour-coded, and shown together with the twenty-flight mean (black line). (Lower panel) speed standard deviation of the mean (STDEV) by series, colour-coded, and shown together with STDEV for all twenty lines. Location of STDEV peaks in 3 and 0.9 kHz EM data (N1 to N10) annotated.

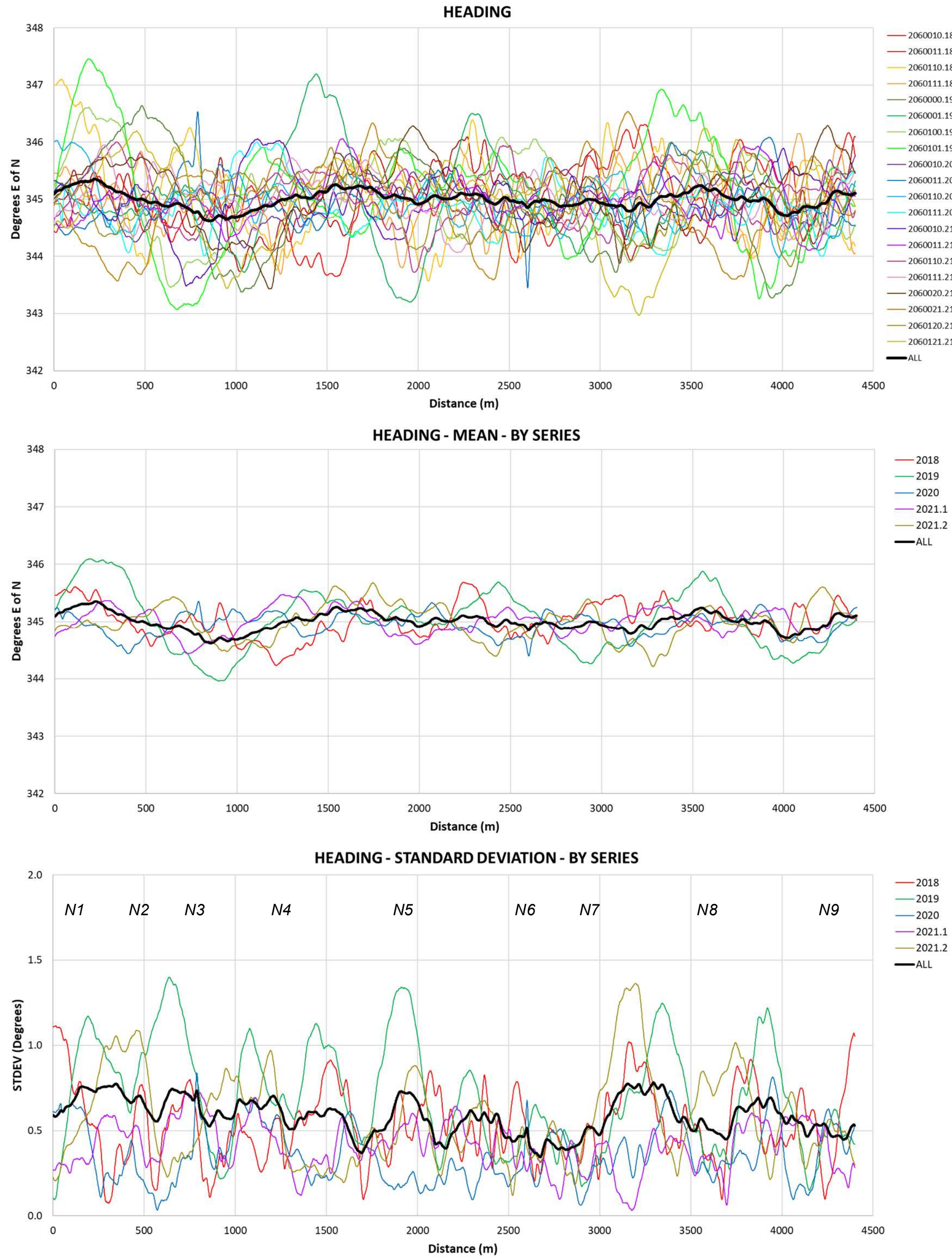

Figure 3.18: Flight heading (calculated from ITM_X, ITM_Y and TIME data channels), plotted against flight-distance, interpolated at 1 m intervals. 180° added to heading where original heading is ~165° E of N. Southern end of line (coast-line) located at 0 m distance. (Upper panel) Heading data, coloured coded by flight, together with the twenty-flight mean (black line). (Middle panel) Mean heading data by series, colour-coded, and shown together with the twenty-flight mean (black line). (Lower panel) heading standard deviation of the mean (STDEV) by series, colour-coded, and shown together with STDEV for all twenty lines. Location of STDEV peaks in 3 and 0.9 kHz EM data (N1 to N9) annotated.

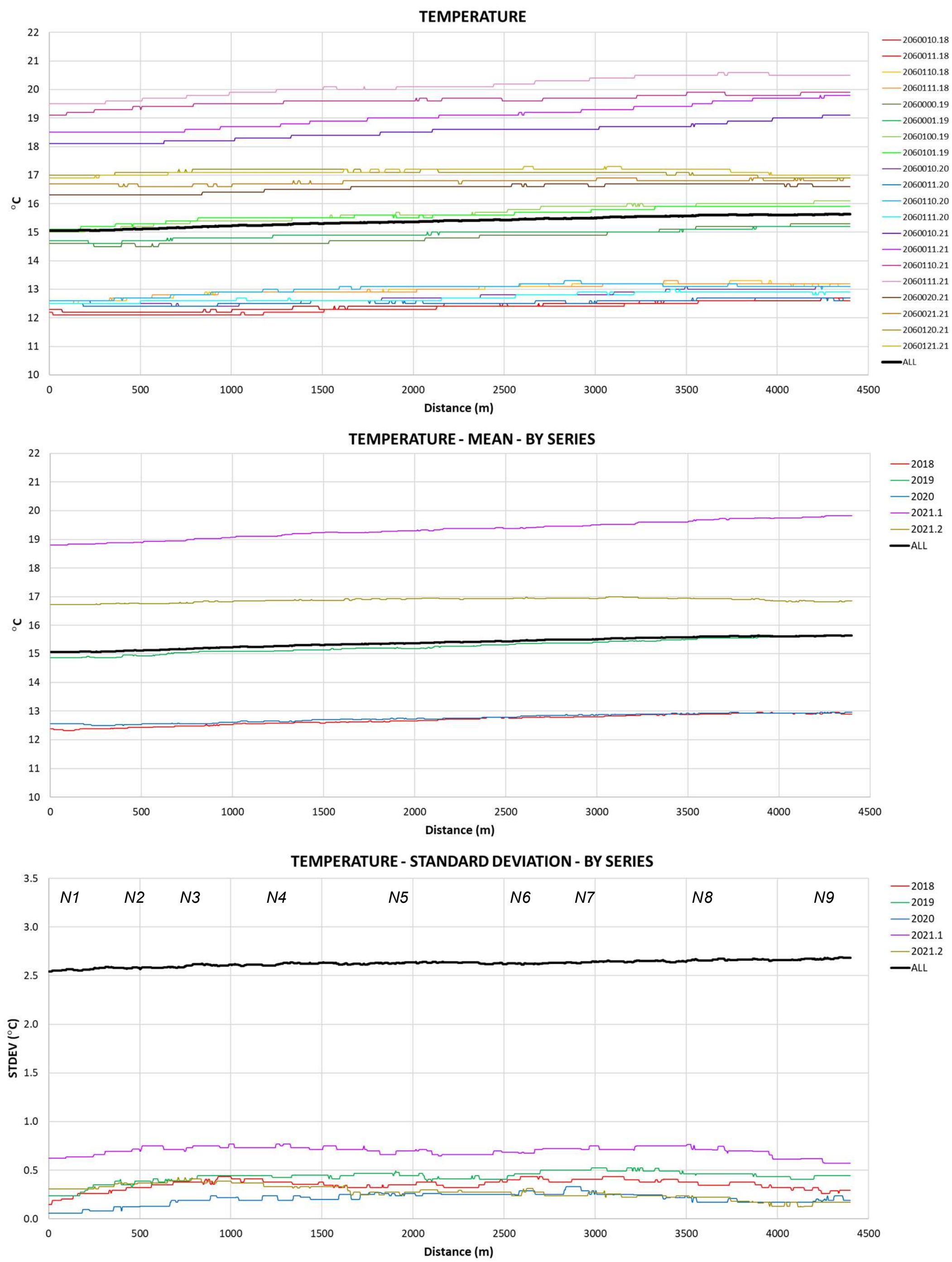

Figure 3.19: Flight temperature (TEMP data channel), plotted against flight-distance, interpolated at 1 m intervals. Southern end of line (coast-line) located at 0 m distance. (Upper panel) Temperature data, coloured coded by flight, together with the twenty-flight mean (black line). (Middle panel) Mean temperature data by series, colour-coded, and shown together with the twenty-flight mean (black line). (Lower panel) Temperature standard deviation of the mean (STDEV) by series, colour-coded, and shown together with STDEV for all twenty lines. Location of STDEV peaks in 3 and 0.9 kHz EM data (N1 to N9) annotated.

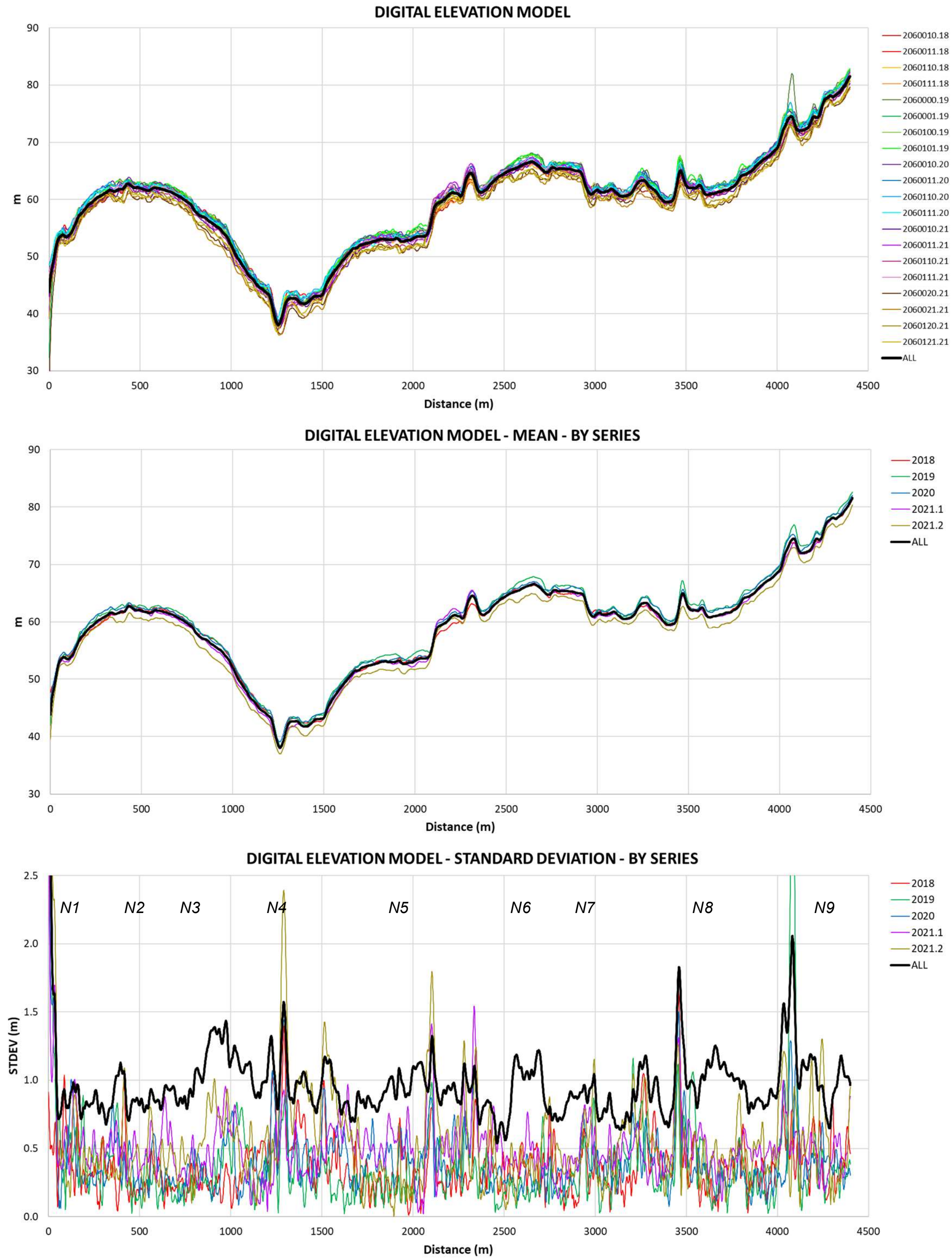

Figure 3.20: Flight digital elevation model (DEM) (calculated from RADAR and MSLHGT data channels), plotted against flight-distance, interpolated at 1 m intervals. Southern end of line (coast-line) located at 0 m distance. (Upper panel) DEM data, coloured coded by flight, together with the twenty-flight mean (black line). (Middle panel) Mean DEM data by series, colour-coded, and shown together with the twenty-flight mean (black line). (Lower panel) DEM standard deviation of the mean (STDEV) by series, colour-coded, and shown together with STDEV for all twenty lines. Location of STDEV peaks in 3 and 0.9 kHz EM data (N1 to N9) annotated.

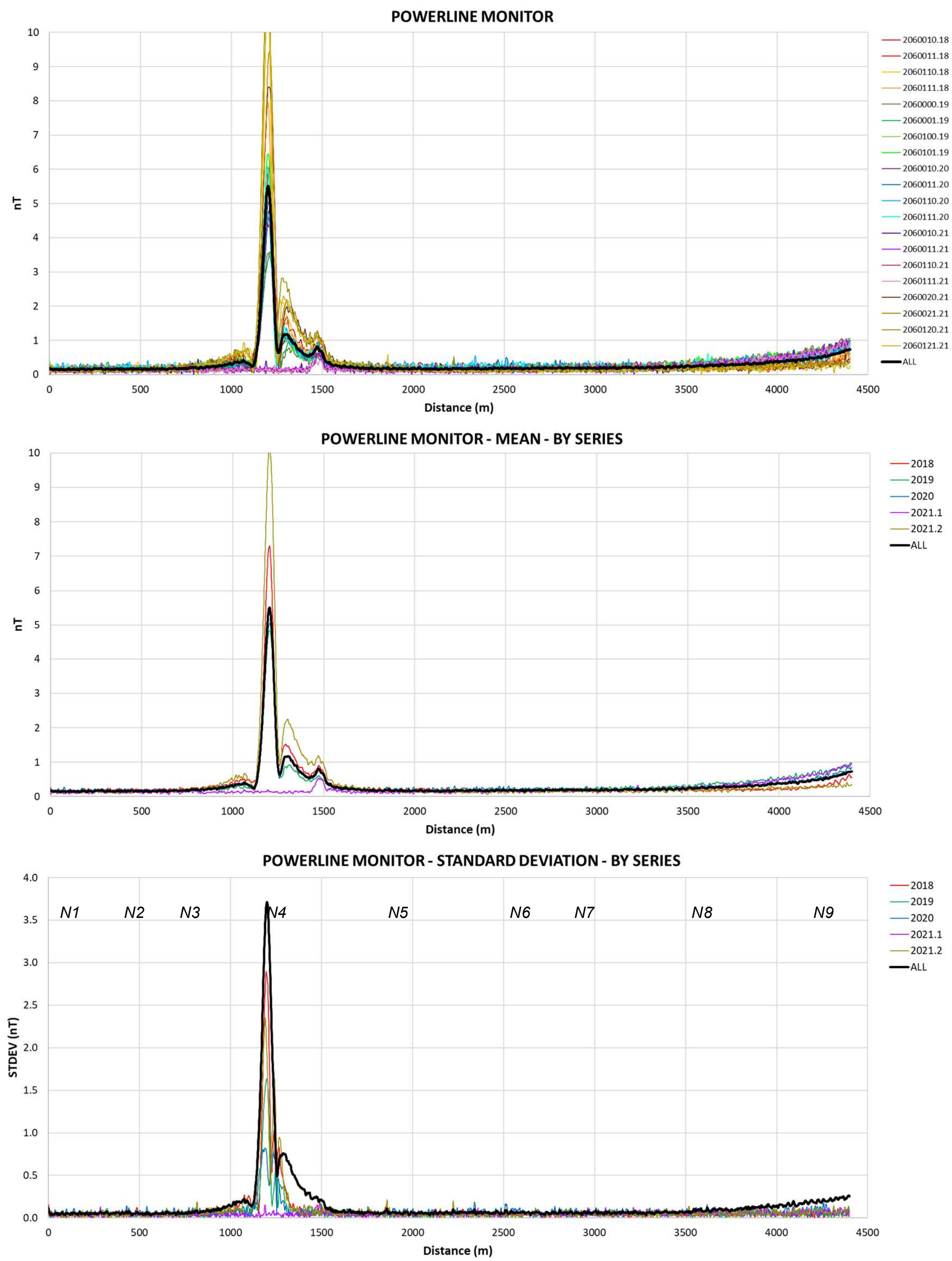

Figure 3.21: Flight powerline monitor (PLM) (PLM_nT data channel), plotted against flight-distance, interpolated at 1 m intervals. Southern end of line (coast-line) located at 0 m distance. (Upper panel) PLM data, coloured coded by flight, together with the twenty-flight mean (black line). (Middle panel) Mean PLM data by series, colour-coded, and shown together with the twenty-flight mean (black line). (Lower panel) PLM standard deviation of the mean (STDEV) by series, colour-coded, and shown together with STDEV for all twenty lines. Location of STDEV peaks in 3 and 0.9 kHz EM data (N1 to N9) annotated.

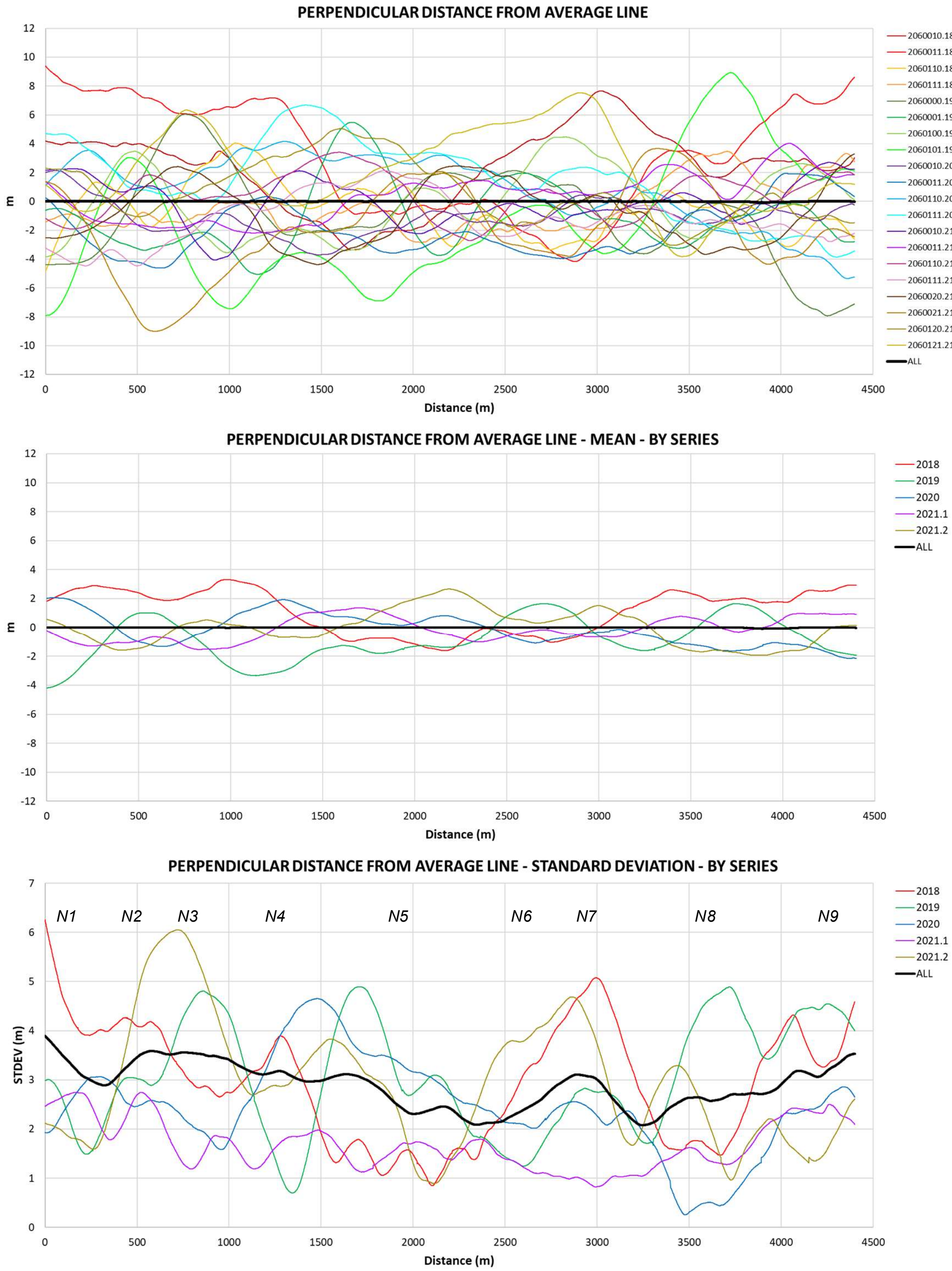

Figure 3.22: Flight path perpendicular distance from average line, plotted against flight-distance, interpolated at 1 m intervals. Average line defined by mean ITM_X and mean ITM_Y coordinates for all twenty lines at each distance interval along line. Negative perpendicular distance = west of average line, positive distance = east of average line. Southern end of line (coast-line) located at 0 m distance. (Upper panel) perpendicular distance, coloured coded by flight, together with the twenty-line mean (black line). (Middle panel) Mean perpendicular distance by series, colour-coded, and shown together with the twenty-line mean (black line). (Lower panel) Perpendicular distance standard deviation of the mean (STDEV) by series, colour-coded, and shown together with STDEV for all twenty lines. Location of STDEV peaks in 3 and 0.9 kHz EM data (N1 to N9) annotated.

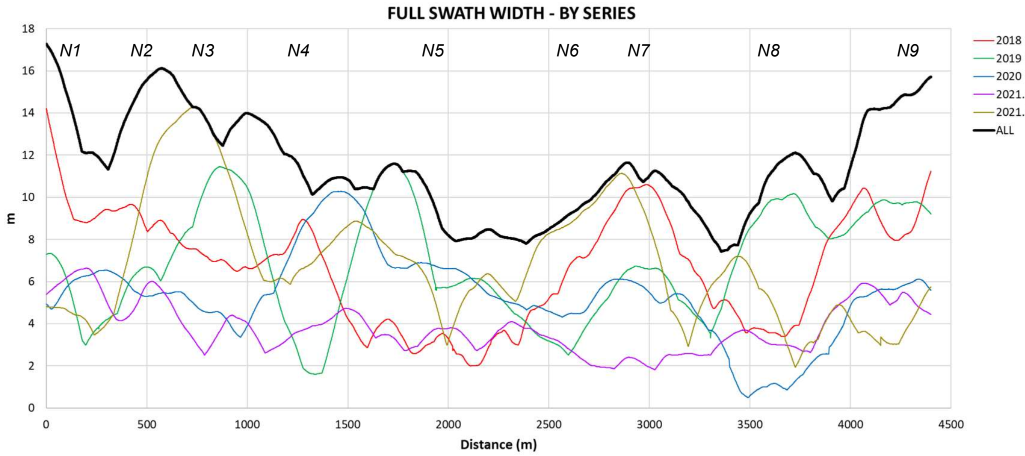

Figure 3.23: Full swath-width (distance from western-most to eastern-most flight line in direction perpendicular to flight-line direction), colour-coded by series and for all twenty lines together (black line). Location of STDEV peaks in 3 and 0.9 kHz EM data (N1 to N9) annotated. The maximum swath-width for each of the 2018, 2019, 2020, 2021.1 and 2021.2 series is 14.2 m, 11.6 m, 10.3 m, 6.6 m and 14.3 m respectively. The maximum swath-width for all twenty repeat flights is 17.3 m.

<u>Note on the standard deviation statistics for 'perpendicular distance from average line'</u>.

In terms of the data presented above for the 'perpendicular distance from average line' parameter (Figure 3.22), it is noted that the standard deviation statistics for each four-line series will be the same whether the reference line is taken as (i) the twenty-line average line (as done here) or (ii) the four-line average line. The standard deviation is the same regardless of which reference is used. However, while the averages of the four-line perpendicular distances from the four-line average line would be zero, they are non-zero with respect to the twenty-line average line, as is seen in Figure 3.22 (middle panel). The important point regarding the statistics of Figure 3.22 is that they are statistics based on the *differences* from a reference, and not on *'actual'* (or non-referenced) values – the standard deviations of the *differences* are not dependent on the reference used.

3.4 Summary of Data Variability

Figures 3.24 – 3.29 provide a catalogue of summary plots, for all twenty lines and for each series separately, illustrating the variability (standard deviations) of the EM responses in comparison with the variability in the additional recorded or calculated parameters described above.

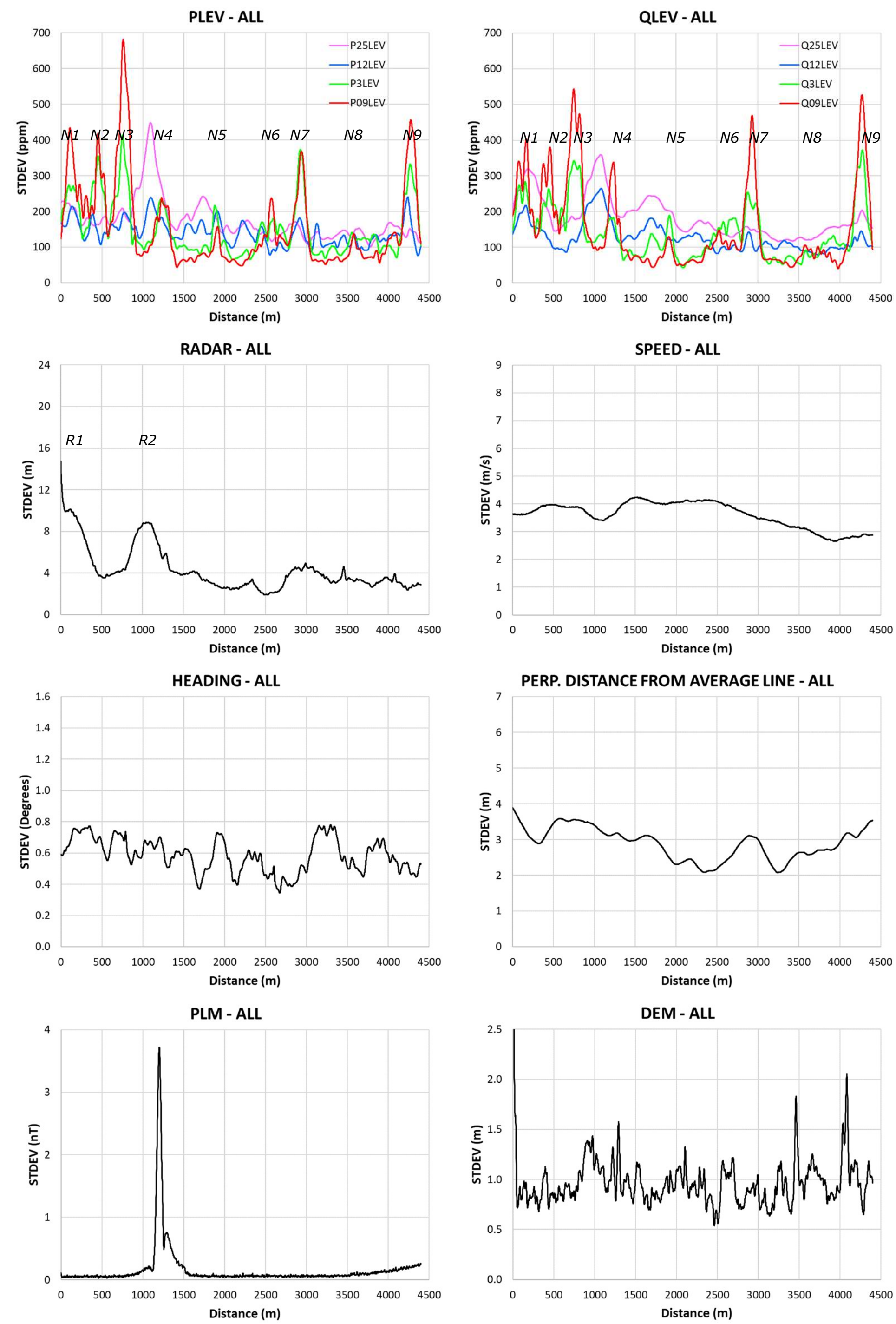

Figure 3.24: Summary of data variability (standard deviations) for the eight EM responses and additional recorded or calculated parameters – <u>for all twenty repeat lines together</u>. Location of standard deviation (STDEV) peaks in 3 and 0.9 kHz EM data (N1 to N9) annotated in in-phase (PLEV) and quadrature (QLEV) panel, as well as STDEV peaks in the clearance data (R1 and R2).

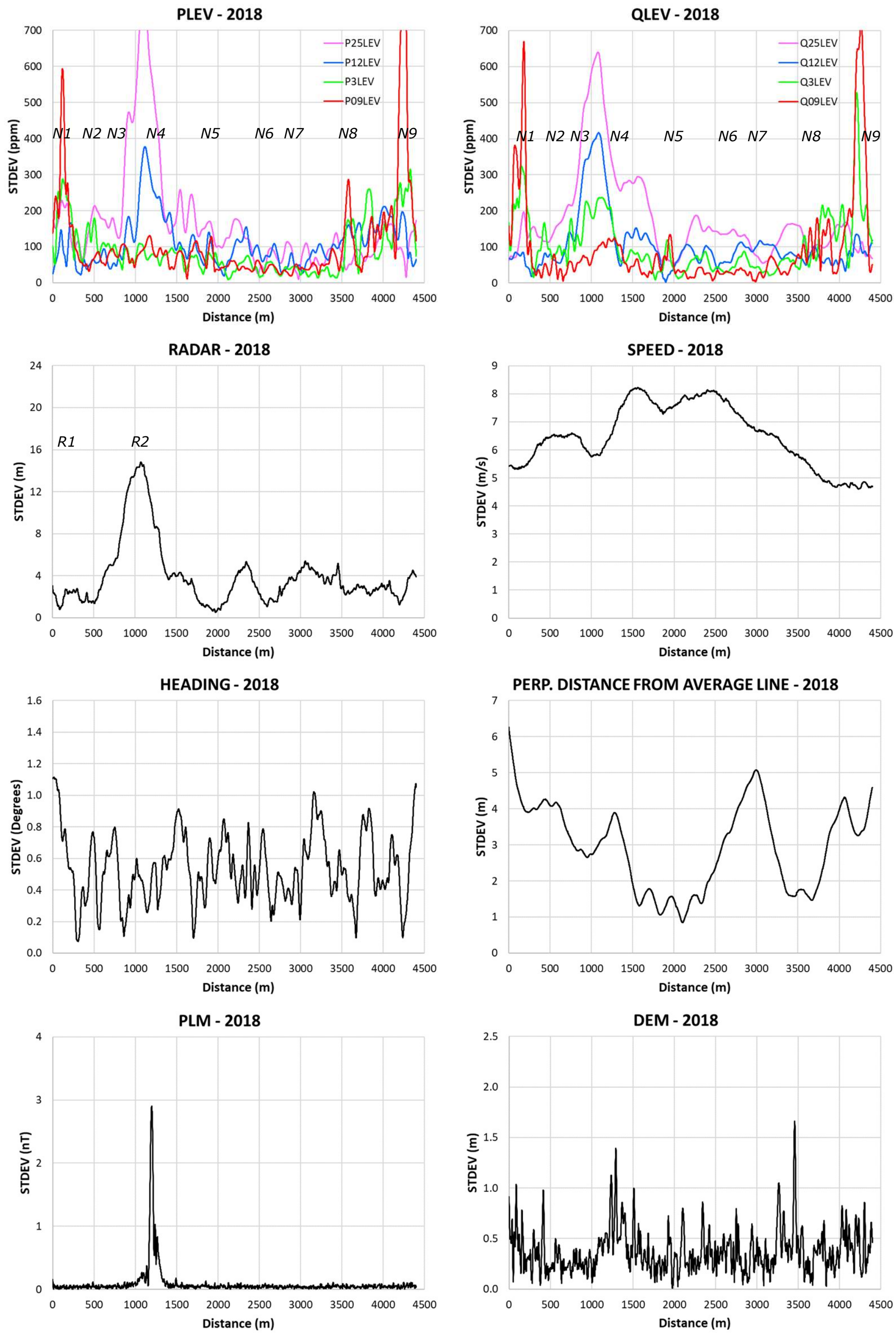

Figure 3.25: Summary of data variability (standard deviations) for the eight EM responses and additional recorded or calculated parameters – <u>for the 2018 series of four repeat lines only</u>. Location of standard deviation (STDEV) peaks in 3 and 0.9 kHz EM data (N1 to N9) annotated in in-phase (PLEV) and quadrature (QLEV) panels, as well as STDEV peaks in the clearance data (R1 and R2).

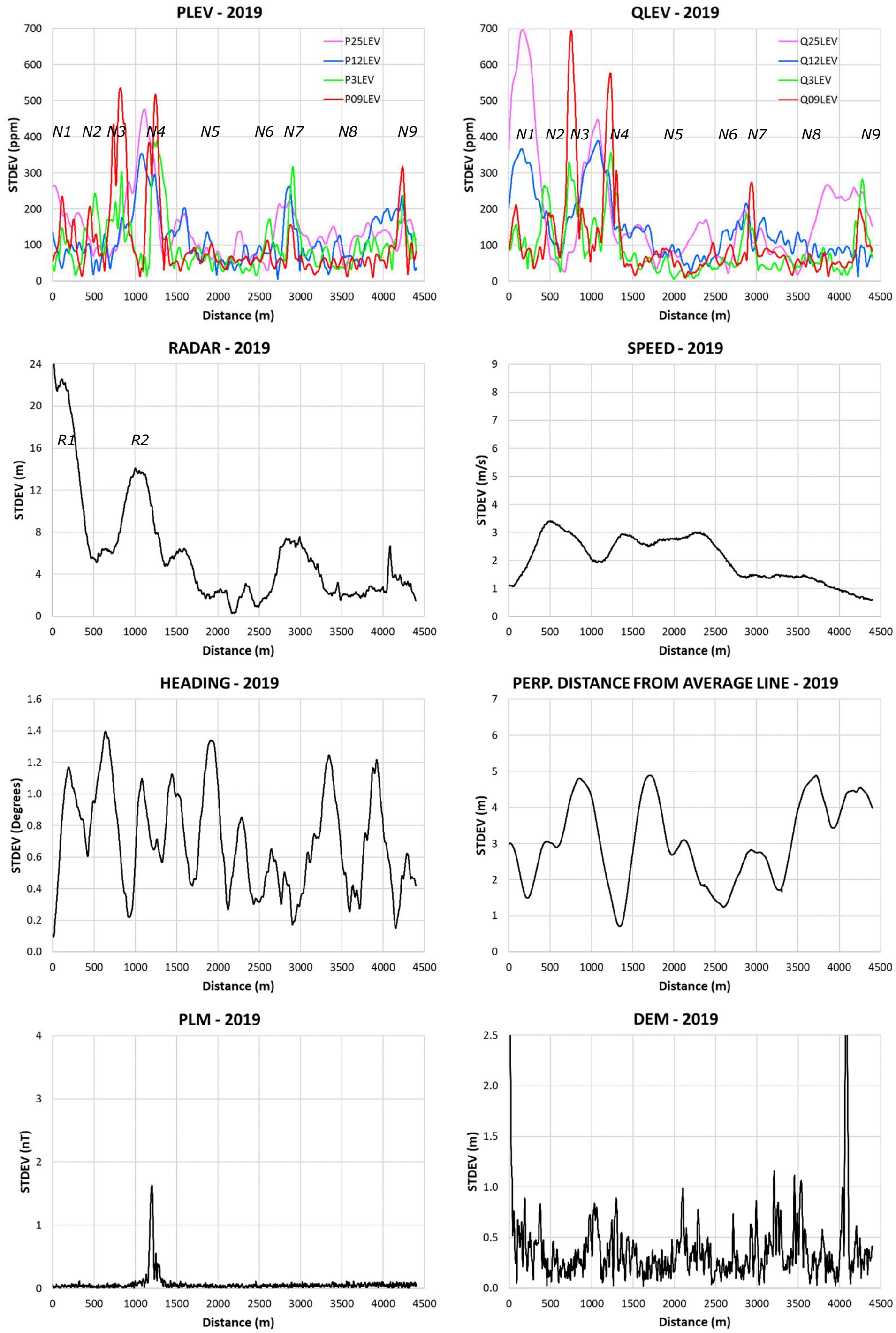

Figure 3.26: Summary of data variability (standard deviations) for the eight EM responses and additional recorded or calculated parameters – <u>for the 2019 series of four repeat lines only</u>. Location of standard deviation (STDEV) peaks in 3 and 0.9 kHz EM data (N1 to N9) annotated in in-phase (PLEV) and quadrature (QLEV) panels, as well as STDEV peaks in the clearance data (R1 and R2).

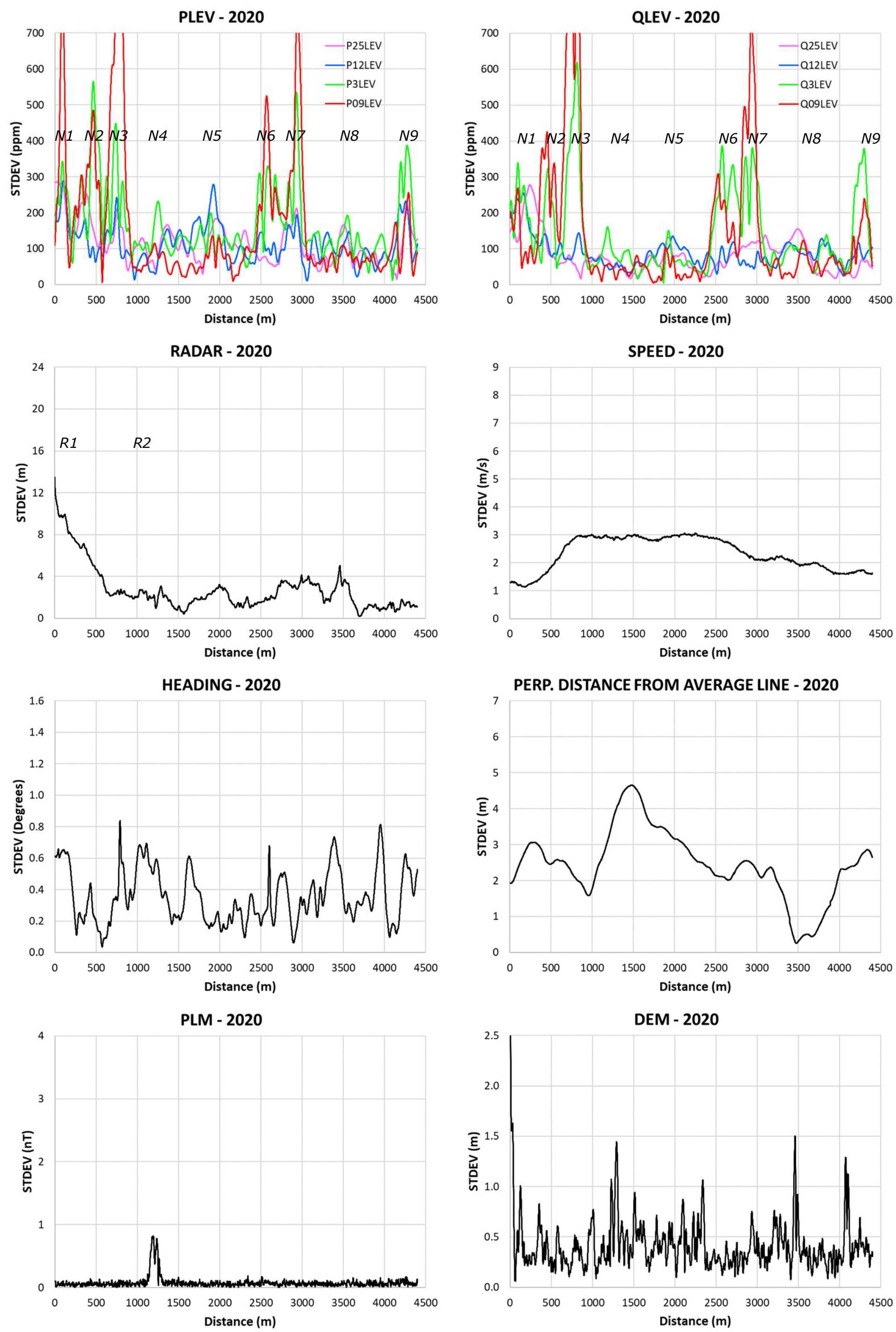

Figure 3.27: Summary of data variability (standard deviations) for the eight EM responses and additional recorded or calculated parameters – <u>for the 2020 series of four repeat lines only</u>. Location of standard deviation (STDEV) peaks in 3 and 0.9 kHz EM data (N1 to N9) annotated in in-phase (PLEV) and quadrature (QLEV) panels, as well as STDEV peaks in the clearance data (R1 and R2).

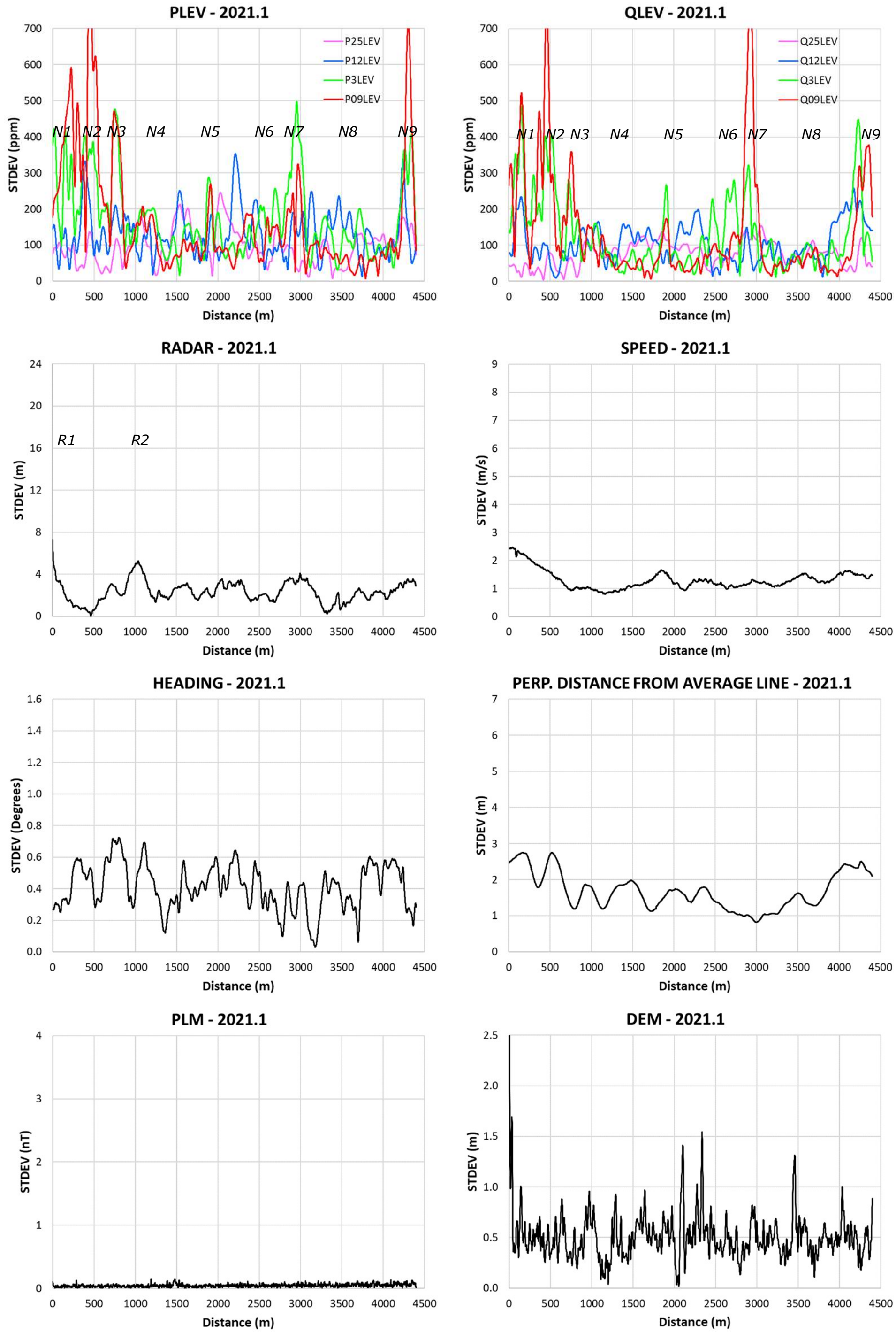

Figure 3.28: Summary of data variability (standard deviations) for the eight EM responses and additional recorded or calculated parameters – <u>for the 2021.1 series of four repeat lines only</u>. Location of standard deviation (STDEV) peaks in 3 and 0.9 kHz EM data (N1 to N9) annotated in in-phase (PLEV) and quadrature (QLEV) panels, as well as STDEV peaks in the clearance data (R1 and R2).

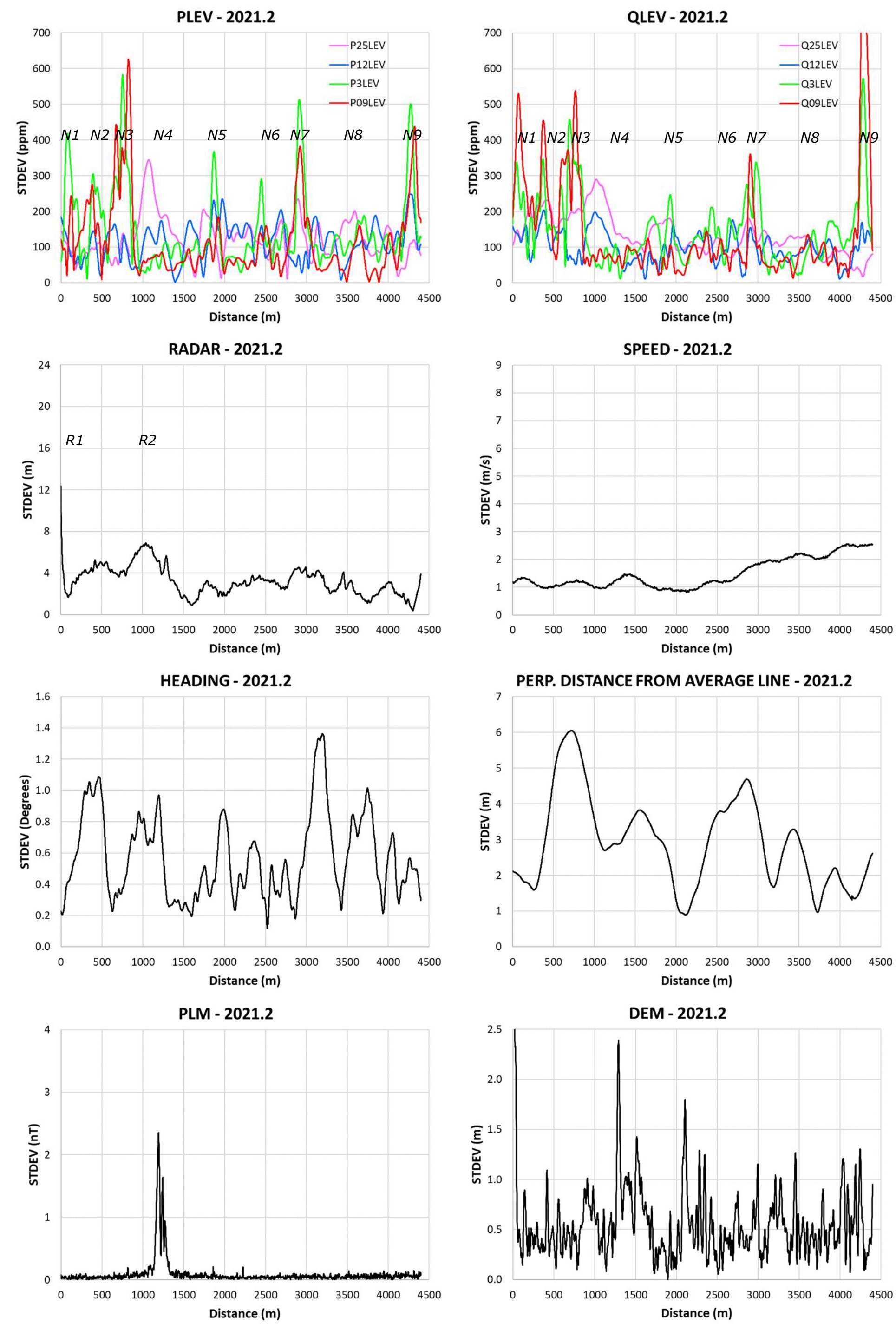

Figure 3.29: Summary of data variability (standard deviations) for the eight EM responses and additional recorded or calculated parameters – <u>for the 2021.2 series of four repeat lines only</u>. Location of standard deviation (STDEV) peaks in 3 and 0.9 kHz EM data (N1 to N9) annotated in in-phase (PLEV) and quadrature (QLEV) panels, as well as STDEV peaks in the clearance data (R1 and R2).

Plots of the temperature data variability (Figure 3.19) are not included in the summary figures above as the very long wavelength standard deviation trends in evidence appear unable to account for the shorter wavelength variations in standard deviation along the flight-line that are apparent in the EM responses.

Several observations emerge from visual examination of the summary catalogue of Figures 3.24 – 3.29, supported by the 'full' catalogue of Figures 3.16 – 3.23:

i. There is a distinct difference in the character of the variability in the two higher frequency EM responses when compared with the two lower frequencies. Variability in the 0.9 and 3 kHz EM responses is dominated by high amplitude spikes at various locations along the test-line (labelled N1 to N9). These distinct spikes are largely absent in the 12 and 25 kHz responses, although in a few instances, a coincident spike is observed in the 3 kHz responses (e.g., at location N9). The strongest visible control on variability in the 12 and 25 kHz responses is flight clearance. High EM response variability at 12 and 25 kHz corresponds particularly with two locations of high flight-clearance variability (labelled R1 and R2). Variability in the 0.9 and 3 kHz EM responses shows generally very little sensitivity to flight-clearance variability.

ii. Flight-clearance variability at location R1 during the 2019 and 2020 series of flights is very likely associated with the steep topography present on the coastline and the aircraft's (pilot's) management of the ascent/descent from/to the offshore portion of the line. Flight-clearance variability is observed at location R2 during the 2018, 2019, 2021.1 and 2021.2 series of flights. The reason for the clearance variability at location R2 is unknown but may relate to the presence of the high-voltage powerline located at ~1,205 m distance on the test-line. Flight-clearance variability is reflected in co-located variability in the 12 and 25 kHz EM responses in each of the affected flight-series and in the twenty-line ('ALL') variability. The variability at both locations R1 and R2 is more pronounced in the (12 and 25 kHz) quadrature responses than in the in-phase responses. There is some (lower) sensitivity to flight-clearance variability in evidence in the 3 kHz quadrature responses in places (e.g., at location R2 in the 2018 series, Figure 3.25).

iii. The 0.9 and 3 kHz EM responses appear to be subject to what is interpreted as 'sporadic' noise at several specific locations along the test-line (locations N1 – N9).

‘Sporadic’ is used in the sense of the interpreted noise having a variable signature on each flight-line within a series, accounting for high variability peaks (standard deviations) within each series and/or a variable signature from series-to-series, accounting for high variability observed in the twenty-line standard deviations. Table 3.4 indicates which of the noise locations appear ‘active’ during each of the test-flight series (i.e., whether a standard deviation peak is visible in each series at each of the locations N1 – N9). Only N1 and N9 appear to have been active during all five flight-series. Location N4 appears to be coincident with the location of the high-voltage powerline and is only reflected in the variability profiles for all twenty lines (‘ALL’) and for the 2019 series. The powerline does not appear to have been operational (carrying current) during the 2021.1 series (Figures 3.21 and 3.28). Except for 2019, it is inferred that the powerline signal in the EM responses is consistent on all four flights within each series, accounting for low or no variability for the series at the location of the powerline. However, the powerline signal in the EM responses is inferred to vary from series-to-series, accounting for the standard deviation peak observed for all twenty lines.

iv. The inference that the noise in the 0.9 and 3 kHz data has a sporadic (i.e., different) signature on each flight-line within a series of four lines – giving rise to the variability (standard deviation) peaks in the 0.9 and 3 kHz EM responses for each of the four-line series – suggests that either (i) the noise signal is temporally variable over the time period between each of the four flights, or (ii) the noise signal recorded depends strongly on the distance between the aircraft and the noise source, which is different on each of the four lines of the series.

v. There is spatial correlation between a number of the low-frequency noise locations and mapped ground infrastructure (Figure 3.30): N1 with the low-voltage powerline network, N4 with the high-voltage network, and N7 and N9 with the road network. It would be useful to further examine circumstances on the ground at each of the nine locations, to see if a potential source of noise can be identified, possibly in discussion with local farmers.

vi. It is difficult to track visually all possible correlations between the EM response variability and the variability in the measured/calculated parameters. The possibility of applying multivariate statistical approaches to draw out correlations between the standard deviation profiles of all the measured parameters might be usefully considered.

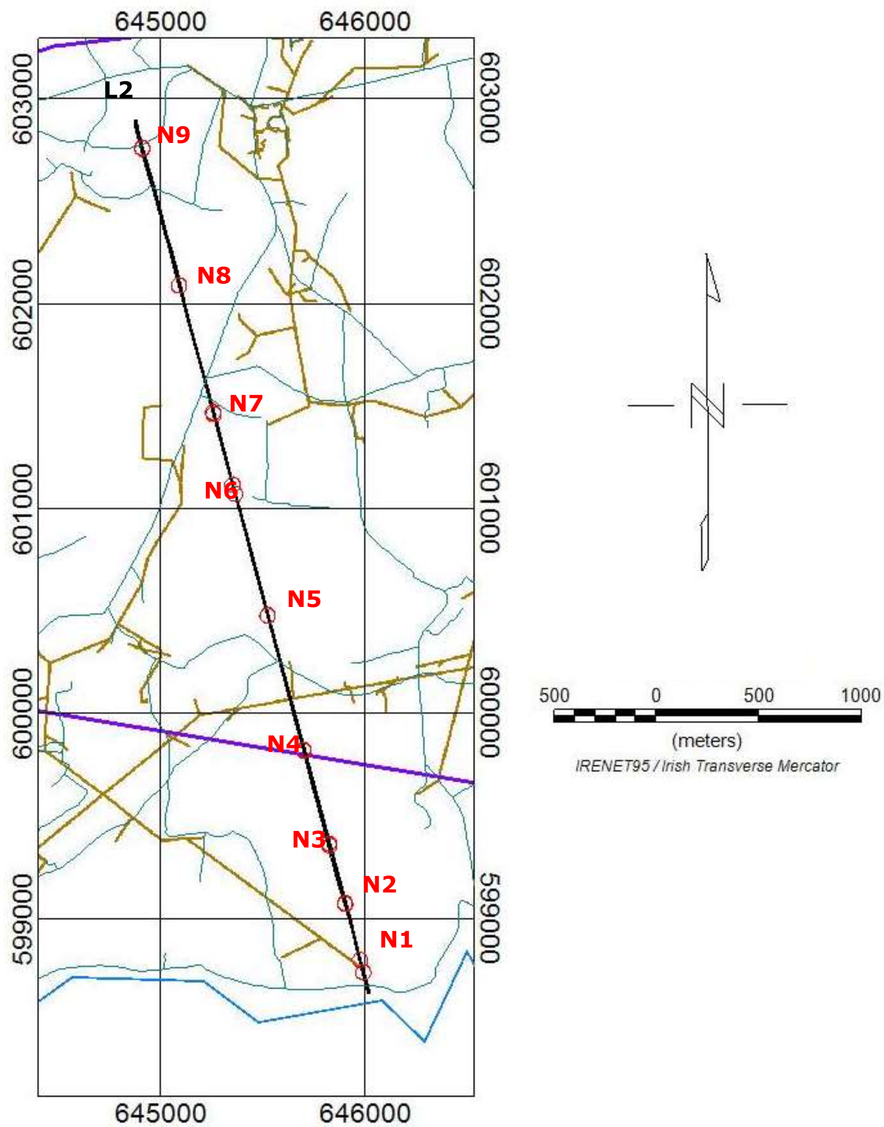

Figure 3.30: Locations of high variability in 0.9 kHz EM in-phase and quadrature responses (locations N1 to N9, red circles, Table 3.4) on Waterford test-line L2 (black line), overlaid on ESB low-voltage powerline network (brown lines), ESB high-voltage powerlines (purple lines) and road network (teal lines). Extent of test-line shown is limited to onshore portion. Coarse Irish coastline (blue line) also shown. Where two circles are visible at a single location, there is some separation between the locations of the in-phase and quadrature variability (standard deviation) peaks.

Table 3.4: Locations of standard deviation peaks N1 to N9 in 0.9 kHz in-phase and quadrature responses, identified in the twenty-line ('ALL') standard deviation profiles (Figures 3.11, 3.15 and 3.24). ITM_X and ITM_Y coordinates are taken from the twenty-line average line. Presence of peaks N1 to N9 in the twenty-line and four-line series standard deviation profiles are subjectively scored where 2 = distinct, high-amplitude peak and 1 = present, moderate to low amplitude peak. No score indicates peak is not in evidence in the series.

SD Peak	Compo-nent	Distance (m)	ITM_X	ITM_Y	ALL	2018	2019	2020	2021.1	2021.2
N1	P09	108	645990	598738	2	2	2	2	2	1
	Q09	170	645974	598798						
N2	P09	453	645902	599072	2		2	2	2	1
	Q09	457	645901	599076						
N3	P09	759	645822	599367	2		2	2	2	2
	Q09	748	645825	599357						
N4	P09	1,229	645699	599821	2		2			
	Q09	1,234	645697	599826						
N5	P09	1,912	645523	600481	1	1		1	1	1
	Q09	1,909	645524	600478						
N6	P09	2,572	645353	601118	1			2	1	1
	Q09	2,525	645365	601073						
N7	P09	2,938	645257	601472	2		1	2	2	2
	Q09	2,928	645260	601462						
N8	P09	3,579	645091	602091	1	2		1		1
	Q09	3,578	645092	602090						
N9	P09	4,275	644911	602763	2	2	2	2	2	2
	Q09	4,271	644912	602759						

The variability in the eight EM data components is further summarised by calculating the mean standard deviation for each four-line series and for all twenty lines together (Table 3.5 and Figure 3. 31). Mean standard deviation in flight-clearance is illustrated for each four-line series and all twenty lines in Figure 3.32. Several observations emerge from these summary data, several reinforcing the data variability characteristics discussed above:

i. The 25 kHz in-phase and quadrature responses (P25lev and Q25lev) are most sensitive to flight clearance variability: those series with the largest mean EM response variabilities (2018, 2019 and 2021.2) correspond with the largest flight clearance variabilities. Qualitatively, all series with mean clearance standard deviations greater than 3 m correspond with mean P25lev and Q25lev standard deviations of greater than 120 ppm (Figure 3.31).

ii. The correlation between mean flight clearance and mean EM response variability is weaker in the 12 kHz in-phase and quadrature data (P12lev and Q12lev), although the 2019 series with the highest clearance variability does correspond with the highest EM response variability in quadrature. There is also no consistent correlation between the mean series variability in the 25 kHz and 12 kHz responses: series with low mean variabilities at 25 kHz do not always correlate with low mean variabilities at 12 kHz, and similarly for high mean variabilities.

iii. There is little correlation between mean flight clearance variability and mean EM response variability in the 0.9 and 3 kHz data: the two series with the highest clearance variability, 2018 and 2019, are characterised by the lowest mean EM response variability in all components (P3lev, Q3lev, P09lev and Q09 lev). The characteristics of the variability in the 0.9 kHz and 3 kHz EM responses differs from that of the two higher frequencies within each series: the 2020, 2021.1 and 2021.2 series are characterised by high mean variabilities in the 0.9 and 3 kHz EM responses and low mean variabilities in the 12 and 25 kHz responses. As illustrated and discussed further in sections that follow below, it is inferred that high and variable cultural noise levels are the primary contributor to the variability observed in the 0.9 and 3 kHz data, and that the impact of the same cultural noise is much more subdued in the 12 and 25 kHz data.

Table 3.5: Mean EM response variability (mean standard deviation, SD) for eight data components, by series and for all twenty lines.

Series (Year)	Line Number	P25lev		P12lev		P3lev		P09lev	
		Mean SD All (ppm)	Mean SD Series (ppm)	Mean SD All (ppm)	Mean SD Series (ppm)	Mean SD All (ppm)	Mean SD Series (ppm)	Mean SD All (ppm)	Mean SD Series (ppm)
2018	L2060010.18	173.6	166.1	141.4	111.1	153.9	90.8	158.8	105.6
	L2060110.18								
	L2060011.18								
	L2060111.18								
2019	L2060000.19		141.2		116.3		103.5		104.8
	L2060100.19								
	L2060001.19								
	L2060101.19								
2020	L2060010.20		116.7		114.9		170.4		172.0
	L2060110.20								
	L2060011.20								
	L2060111.20								
2021.1	L2060010.21		96.7		132.3		175.9		168.7
	L2060110.21								
	L2060011.21								
	L2060111.21								
2021.2	L2060020.21		122.2		113.9		149.5		117.4
	L2060120.21								
	L2060021.21								
	L2060121.21								

Series (Year)	Line Number	Q25lev		Q12lev		Q3lev		Q09lev	
		Mean SD All (ppm)	Mean SD Series (ppm)	Mean SD All (ppm)	Mean SD Series (ppm)	Mean SD All (ppm)	Mean SD Series (ppm)	Mean SD All (ppm)	Mean SD Series (ppm)
2018	L2060010.18	185.0	176.8	128.6	104.9	142.1	105.8	154.8	91.9
	L2060110.18								
	L2060011.18								
	L2060111.18								
2019	L2060000.19		183.2		145.2		90.6		109.0
	L2060100.19								
	L2060001.19								
	L2060101.19								
2020	L2060010.20		81.6		89.4		142.7		144.6
	L2060110.20								
	L2060011.20								
	L2060111.20								
2021.1	L2060010.21		75.1		104.5		129.9		132.9
	L2060110.21								
	L2060011.21								
	L2060111.21								
2021.2	L2060020.21		135.4		100.8		147.8		140.2
	L2060120.21								
	L2060021.21								
	L2060121.21								

Figure 3.31: Bar plots of mean variability (standard deviation) for eight FEM responses, by series and for all twenty lines. Standard deviation level of 120 ppm highlighted by blue lines.

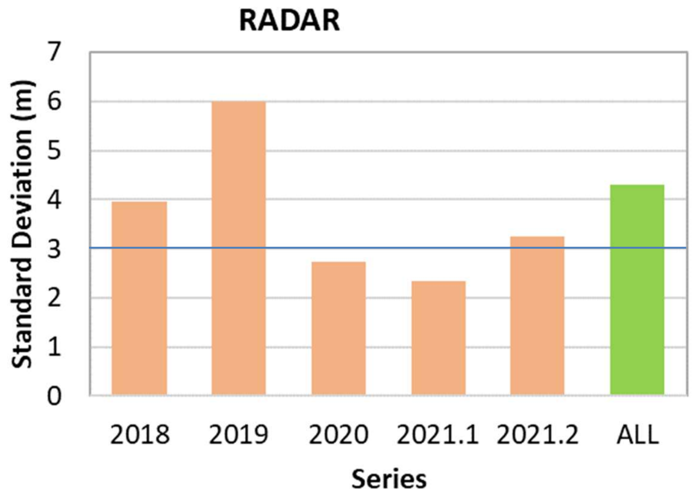

Figure 3.32: Bar plots of mean clearance (RADAR) variability (standard deviation), by series and for all twenty lines. Standard deviation level of 3 m highlighted by blue line.

4 Variability in FEM Responses After PCA Filter Application

4.1 PCA Filter Method

Electromagnetic noise levels are observed to be high across many parts of Ireland, originating from multiple cultural noise sources such as power-lines, gas pipelines, towns, industrial centres, farms and dwellings, and have a detrimental effect on the EM response data, particularly at the low 0.9 and 3 kHz transmission frequencies. The distinct series of high standard deviation (high data variability) peaks observed in the 0.9 and 3 kHz Waterford test-line data are interpreted (in Section 3.4 above) to be the result of cultural noise sources located at various locations along the line. The interpretation that these high-variability peaks are the result of cultural noise signals is further scrutinised here, using the capacity provided by Principal Component Analysis (PCA) and filtering to isolate, and potentially identify, different signal components in the EM responses.

The *aempy* software toolbox (Kiyan et al., 2022), developed by Duygu Kiyan and Volker Rath at Dublin Institute for Advanced Studies under GSI *Short-Call* project funding, is currently used by GSI to compute 1-D smooth, layered resistivity models from the recorded Tellus FEM responses using a Tikhonov-type inversion approach. To date, GSI has completed and published 1-D inversion models for the Tellus A5, A6 and Waterford survey blocks.

One useful utility within the *aempy* toolbox is a noise rejection filter based on Principal Component Analysis (PCA) and decomposition of the EM response data. In application of the PCA filter, the EM dataset is reconstructed using the strongest and most coherent principal components only, with the weaker principal components (inferred to be noise) rejected. Previous applications of the PCA approach to airborne EM data (Reninger et al., 2011; Minsley et al., 2012) have illustrated reasonable success in reducing noise contamination and in imposing regularity (consistency) on the data. The results presented below provide further evidence of the efficacy of PCA filtering in isolating and removing noise signals from the recorded EM responses.

4.1.1 Theory

In *aempy*, the PCA is based on the singular value decomposition (SVD) (Lanczos, 1961; Golub and van Loan, 1996) of the data observation matrix, D, which has n_{data} rows and n_{site} columns. After removing the average of the rows, matrix D can be decomposed into an orthonormal set of basic functions using the SVD:

$$D = USV^T \qquad (2)$$

where U and V are unitary matrices, and S is diagonal and contains the singular values in decreasing sequence. By choosing the k largest values in S and truncating the matrices correspondingly, an approximate matrix D' is obtained, which contains only the coherent components of D. Matrix D' is thus an output filtered (de-noised) version of the input data of matrix D.

In the context of Tellus data, the number of data rows in matrix D is equal to eight (in-phase and quadrature components for 4 frequencies) and as the filter is applied on a line-by-line basis in *aempy*, the number of site columns in matrix D is equal to the number of sites (measurement locations) on the flight line.

4.1.2 Application of PCA filters to test-line EM responses

The Principal Component Analysis filter is applied to the EM response data with the objective of reducing noise and imposing regularity and consistency on the data. Consistency in the data refers to (desired) consistency between all eight of the EM data components. The 'strength' of the filter is controlled by the choice of how many of the amplitude-ordered singular values (principal components) are retained in the reconstruction of the data (i.e., filter strength is controlled by the choice of the value for k referred to above in Section 4.1.1). A choice of $k = 1$ (referred to in this work as an Npca1 filter) retains only the first and most significant principal component in the data. $k = 1$ is the 'strongest' filter possible. Similarly, $k = 3$ retains the first three most significant components (Npca3 filter). Choosing $k = 8$ (Npca8 filter) retains all eight principal components and reconstructs the input data exactly (i.e., $k = 8$ has no filtering effect at all). The assumption, in choosing k, is that all principal components up to and including k contain significant, coherent EM signal, while all components greater than k contain incoherent signal (i.e., noise). It is reiterated that PCA filters are applied, in *aempy*, on a line-by-line basis, i.e., each line is processed and filtered entirely independently of all other lines. (The user has control on the length of line to be processed and filtered, as needed and as appropriate).

In the work presented and analysed here, PCA filters of order k = 1 to k = 7 have been applied to all twenty repeat flights. Similar to the treatment of the original EM response data, data averages and standard deviations were then computed for each filter order, across all twenty lines and across each of the four-line series. The analysis of these results aims to assess how the variability in the data is changed through application of PCA filters of decreasing order (or increasing 'strength') and further to identify the nature or character of each of the principal components – whether, for example, a particular component comprises coherent, geological signal or noise – and how the signal in each of the principal components is reflected in each of the four EM frequencies.

Figures 4.1 and 4.2 provide examples, on two lines of the impact of PCA filters of decreasing order, from k = 3 to k = 1, on the EM response data. Orders higher than k = 3, although computed, are not illustrated here as the changes in the output data are visually very small.

Examining the EM responses in Figures 4.1 and 4.2, it is apparent that there is little change in the four data components at the two highest frequencies, i.e., 25 kHz in-phase (IP) and quadrature (Q) and 12 kHz IP and Q, as filter strength increases from order k = 3 (Npca3) to order k = 1 (Npca1). The first principal component therefore contains the bulk of the (coherent) signal in these four data channels, and little signal is added by the introduction of the second and subsequently third principal components (Npca2- and Npca3-filtered outputs respectively). The 3 kHz and 0.9 kHz IP and Q data channels are also characterised by signal in the first principal component that is visibly coherent with the higher frequency data channels, although the signal amplitude in the 0.9 and 3 kHz IP data channels in the L2060011.18 example (Figure 4.1) is very low.

Considering the 0.9 and 3 kHz data on line L2060011.18 (Figure 4.1), it is apparent that the introduction of the second principal component (in the Npca2-filtered responses), in comparison with the Npca1 data, adds significant high-amplitude signal to the 0.9 kHz IP and Q data channels only. The introduction of the third principal component in the Npca3

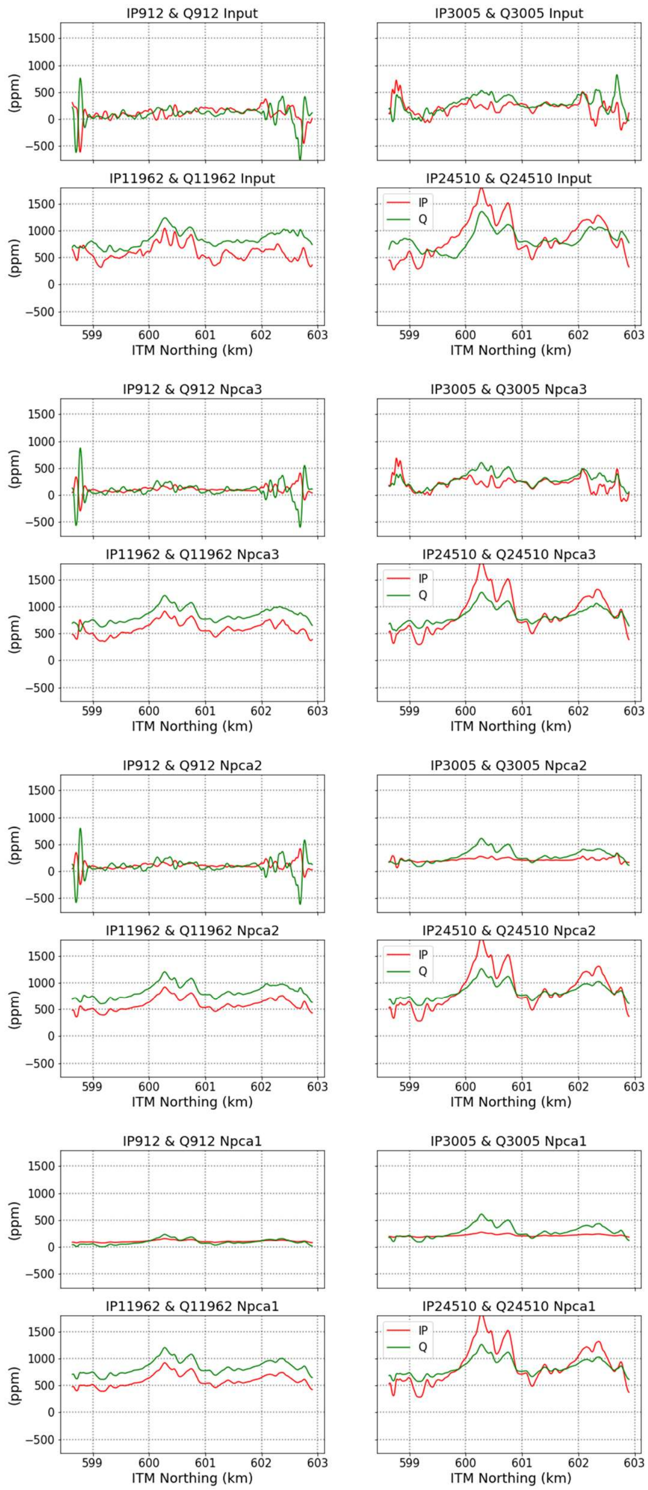

Figure 4.1. L2060011.18: example of PCA filtered EM responses. (Top panel) Original data at four frequencies (in-phase, IP, in red, quadrature, Q, in green). (Second panel) Npca3 filtered (k = 3) EM responses. (Third panel) Npca2 filtered EM responses. (Bottom panel) Npca1 filtered EM responses.

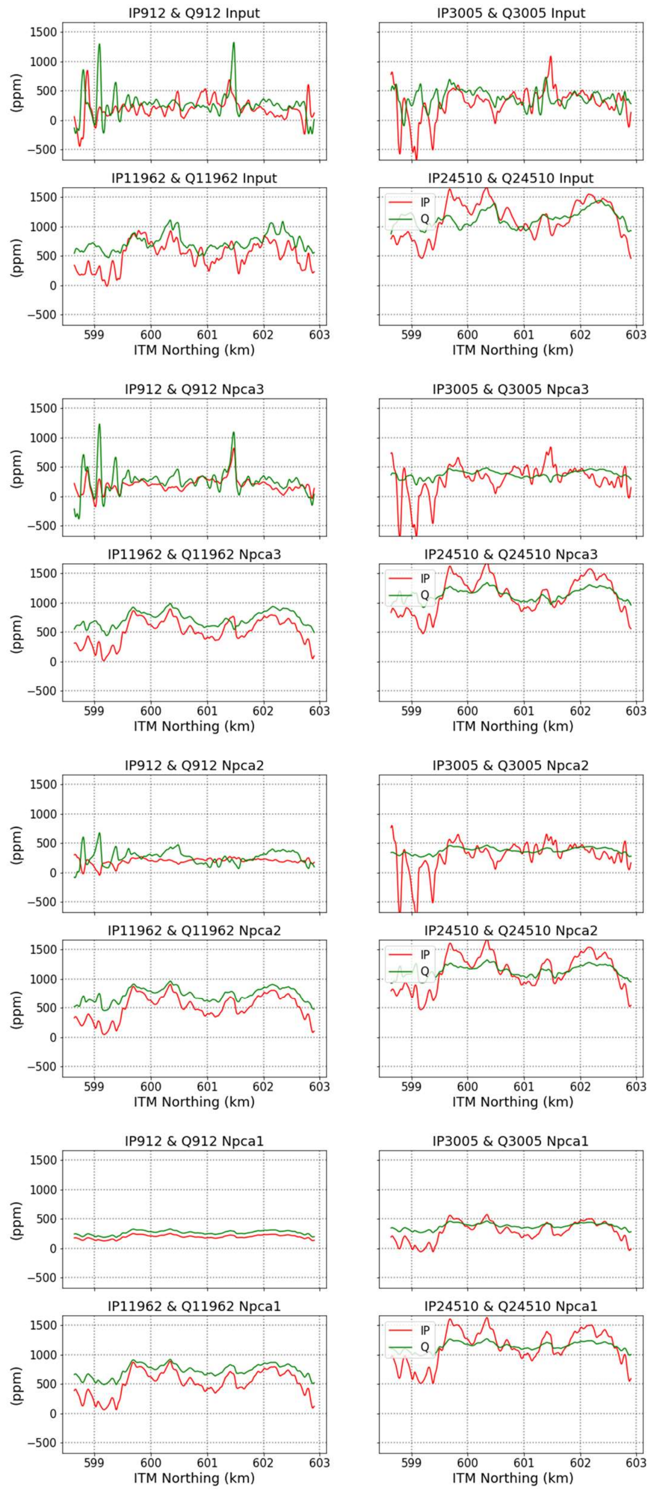

Figure 4.2. L2060111.21: example of PCA filtered EM responses. (Top panel) Original data at four frequencies (in-phase, IP, in red, quadrature, Q, in green). (Second panel) Npca3 filtered (k = 3) EM responses. (Third panel) Npca2 filtered EM responses. (Bottom panel) Npca1 filtered EM responses.

data adds signal to 3 kHz IP and Q responses. Note again that little signal is added to the 12 and 25 kHz data components by the introduction of the second and third principal components. As the signal that is added to 0.9 and 3 kHz data by the second and third principal components is visibly not coherent with the responses in the 12 and 25 kHz data, the additional signal introduced by principal components two and three is interpreted as noise. The behaviour of the EM data on line L2060111.21 (Figure 4.2), in response to the addition of principal components two and three, is similar to line L2060011.18. Principal Components two and three add, in comparison with the Npca1-filtered responses, significant signal (inferred noise) to the 0.9 kHz IP and Q and 3 kHz IP responses. The substantial difference between the 3 kHz Q responses in the Npca3-filtered and original data (on line L2060111.21), suggests that a significant component of additional signal (again inferred noise) still resides in principal components four and higher.

4.2 FEM Responses After Application of Npca1 Filter

Visible inspection of the EM responses after application of principal component filters, in Section 4.1.2 above, suggests that the bulk of the coherent geological signal recorded on the test-lines is contained in the first principal component. The second and third principal components add signal, primarily to the 0.9 and 3 kHz responses, which is not coherent with the signal in principal component 1 and which is inferred to be noise.

Figures 4.3 – 4.10 that follow, provide a catalogue of the EM response variability, after application of an Npca1 filter, along the test-line for each of the eight data components. These figures may be directly compared with the original EM response data and variability in Figures 3.8 – 3.15. In each figure of the catalogue, the top panel plots individually the EM responses for all twenty flight-lines (after Npca1 filter), together with the twenty-line mean response. The middle panel plots the four-line mean responses for each data series (year), together with the twenty-line mean response. The bottom panel plots the four-line standard deviation of the mean for each data series (year), together with the twenty-line standard deviation.

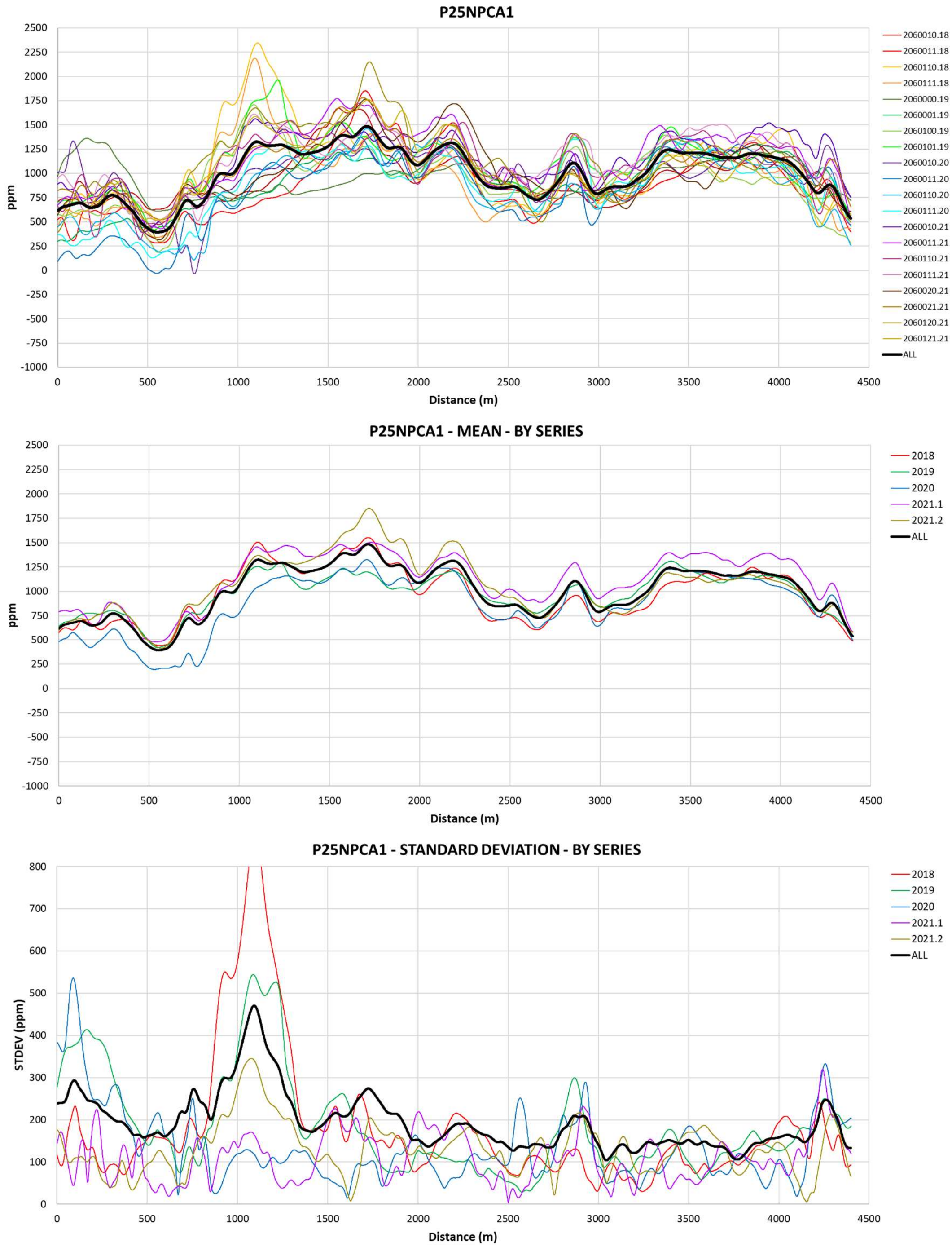

Figure 4.3: 25 kHz in-phase responses after application of Npca1 filter (P25NPCA1 data), plotted against flight-distance, interpolated at 1 m intervals. Southern end of line (coast-line) located at 0 m distance. (Upper panel) P25NPCA1 responses, coloured coded by flight, together with the twenty-flight mean (black line). (Middle panel) Mean P25NPCA1 responses by series, colour-coded, and shown together with the twenty-flight mean (black line). (Lower panel) P25NPCA1 standard deviation of the mean (STDEV) by series, colour-coded, and shown together with STDEV for all twenty lines.

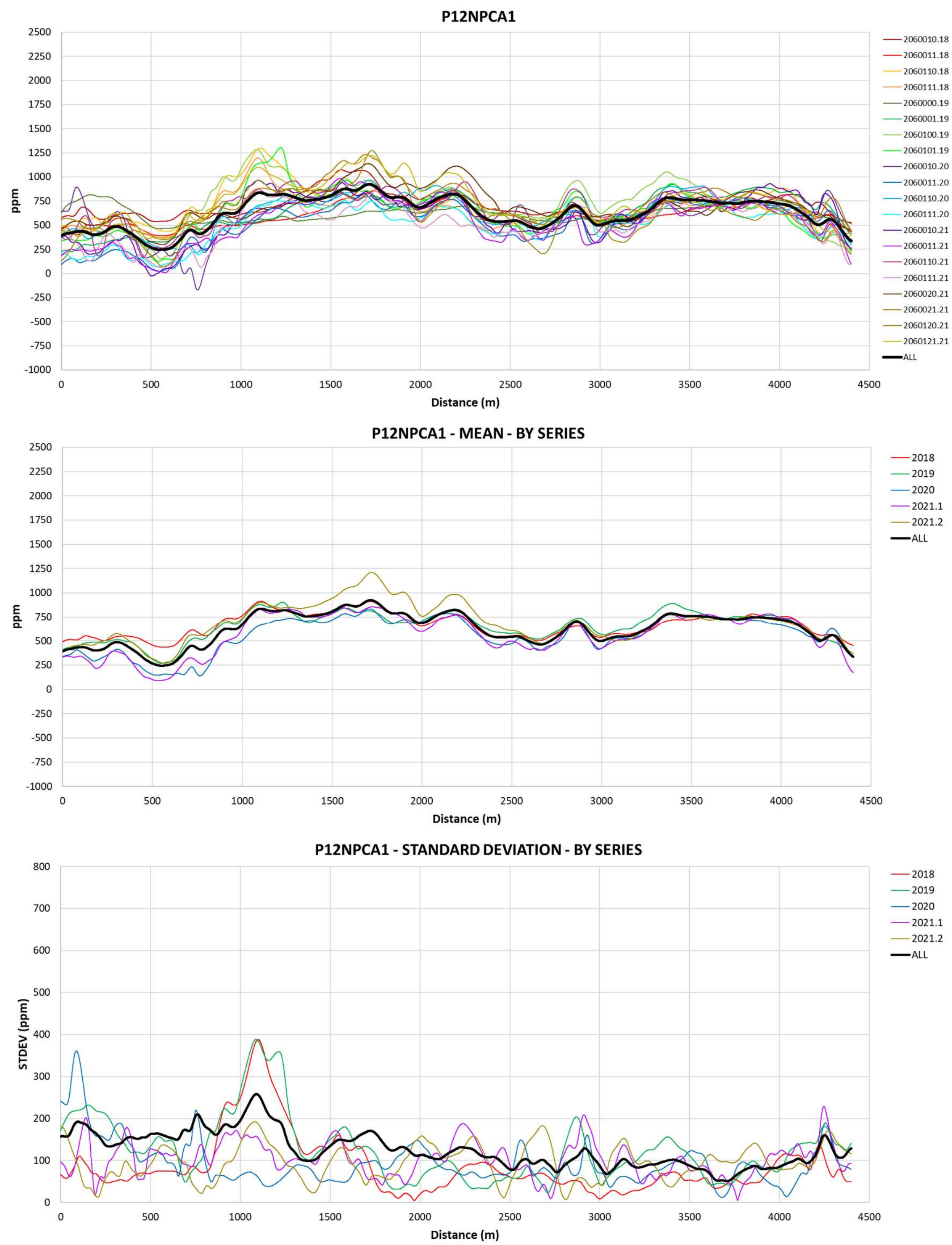

Figure 4.4: 12 kHz in-phase responses after application of Npca1 filter (P12NPCA1 data), plotted against flight-distance, interpolated at 1 m intervals. Southern end of line (coast-line) located at 0 m distance. (Upper panel) P12NPCA1 responses, coloured coded by flight, together with the twenty-flight mean (black line). (Middle panel) Mean P12NPCA1 responses by series, colour-coded, and shown together with the twenty-flight mean (black line). (Lower panel) P12NPCA1 standard deviation of the mean (STDEV) by series, colour-coded, and shown together with STDEV for all twenty lines.

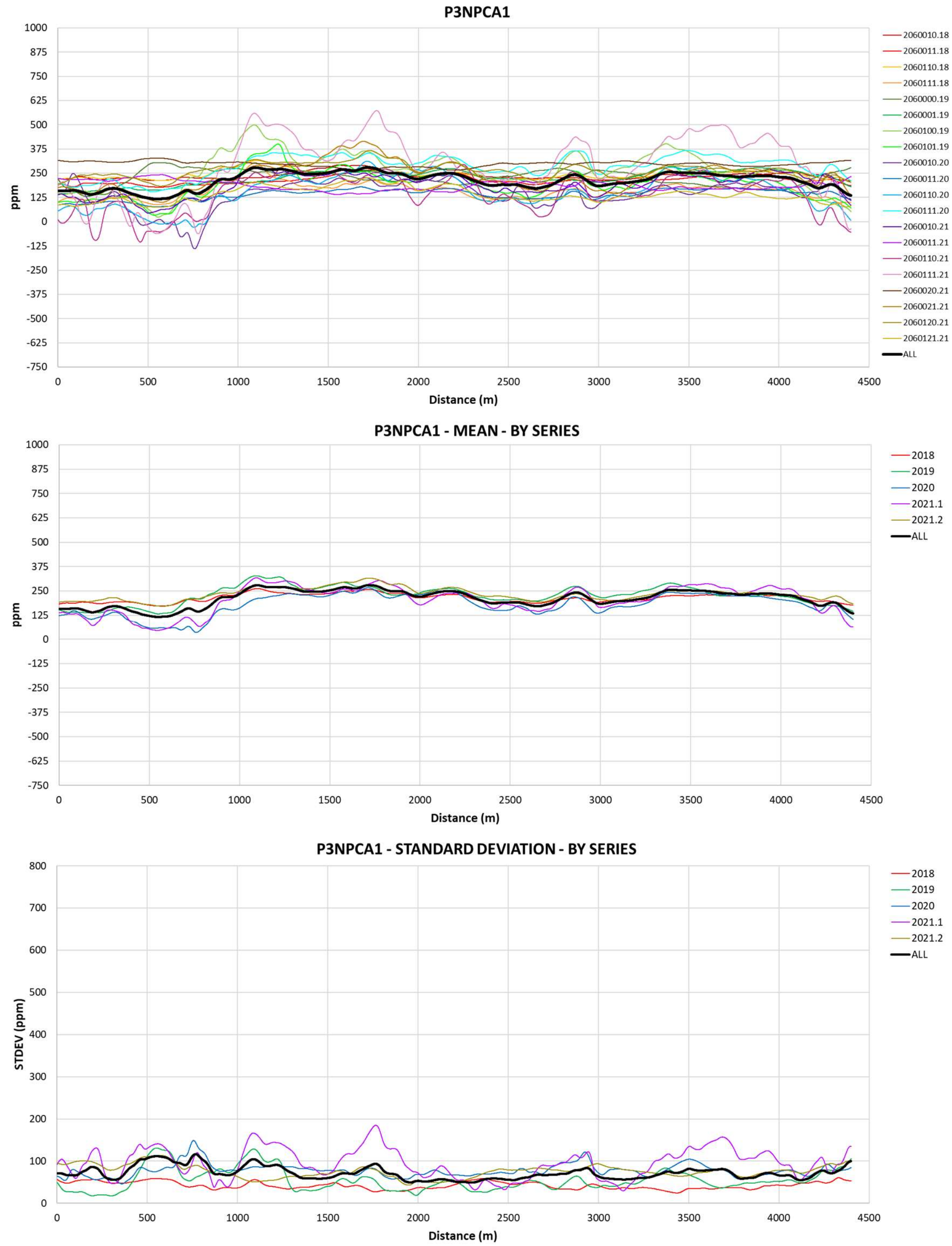

Figure 4.5: 3 kHz in-phase responses after application of Npca1 filter (P3NPCA1 data), plotted against flight-distance, interpolated at 1 m intervals. Southern end of line (coast-line) located at 0 m distance. (Upper panel) P3NPCA1 responses, coloured coded by flight, together with the twenty-flight mean (black line). (Middle panel) Mean P3NPCA1 responses by series, colour-coded, and shown together with the twenty-flight mean (black line). (Lower panel) P3NPCA1 standard deviation of the mean (STDEV) by series, colour-coded, and shown together with STDEV for all twenty lines.

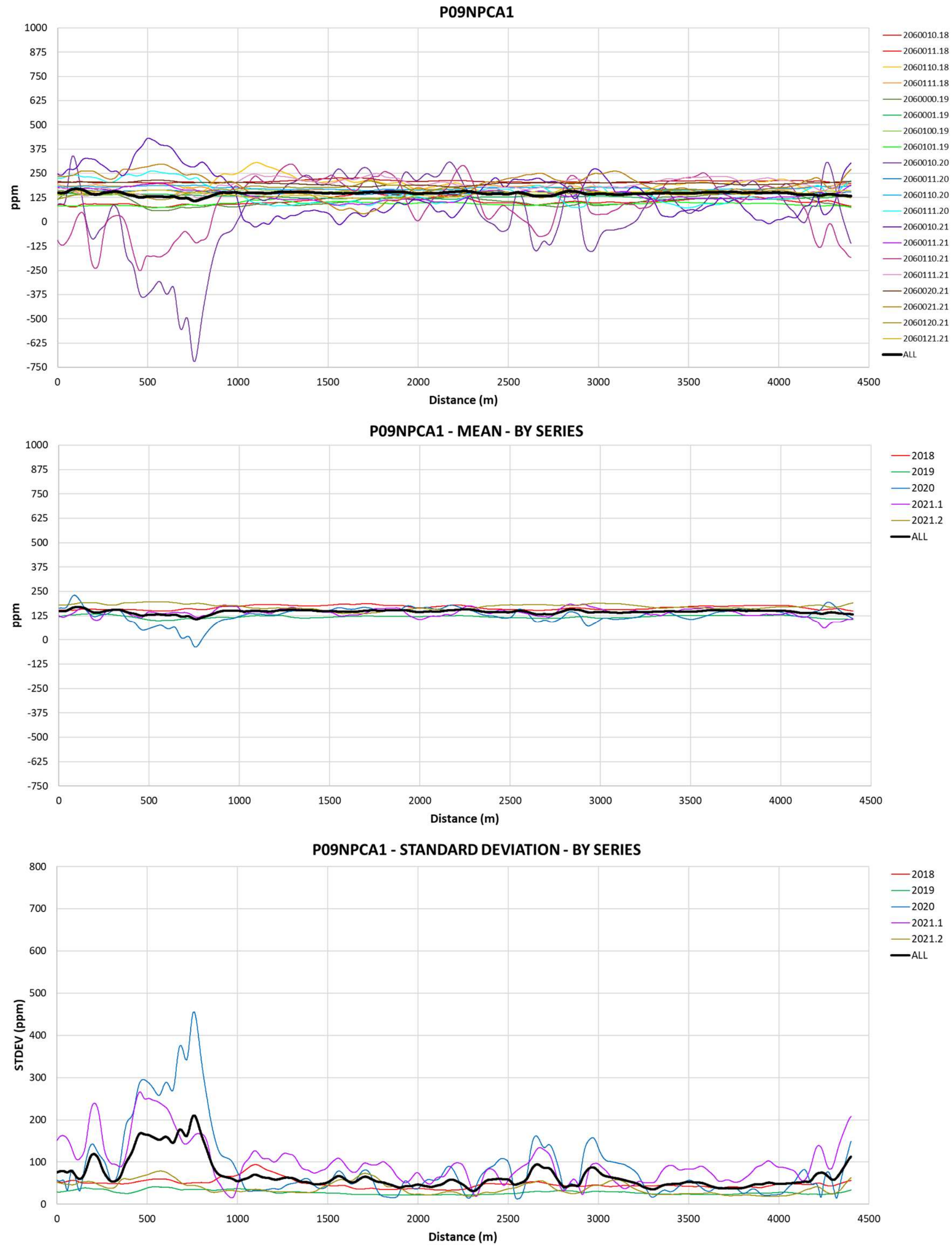

Figure 4.6: 0.9 kHz in-phase responses after application of Npca1 filter (P09NPCA1 data), plotted against flight-distance, interpolated at 1 m intervals. Southern end of line (coast-line) located at 0 m distance. (Upper panel) P3NPCA1 responses, coloured coded by flight, together with the twenty-flight mean (black line). (Middle panel) Mean P09NPCA1 responses by series, colour-coded, and shown together with the twenty-flight mean (black line). (Lower panel) P09NPCA1 standard deviation of the mean (STDEV) by series, colour-coded, and shown together with STDEV for all twenty lines.

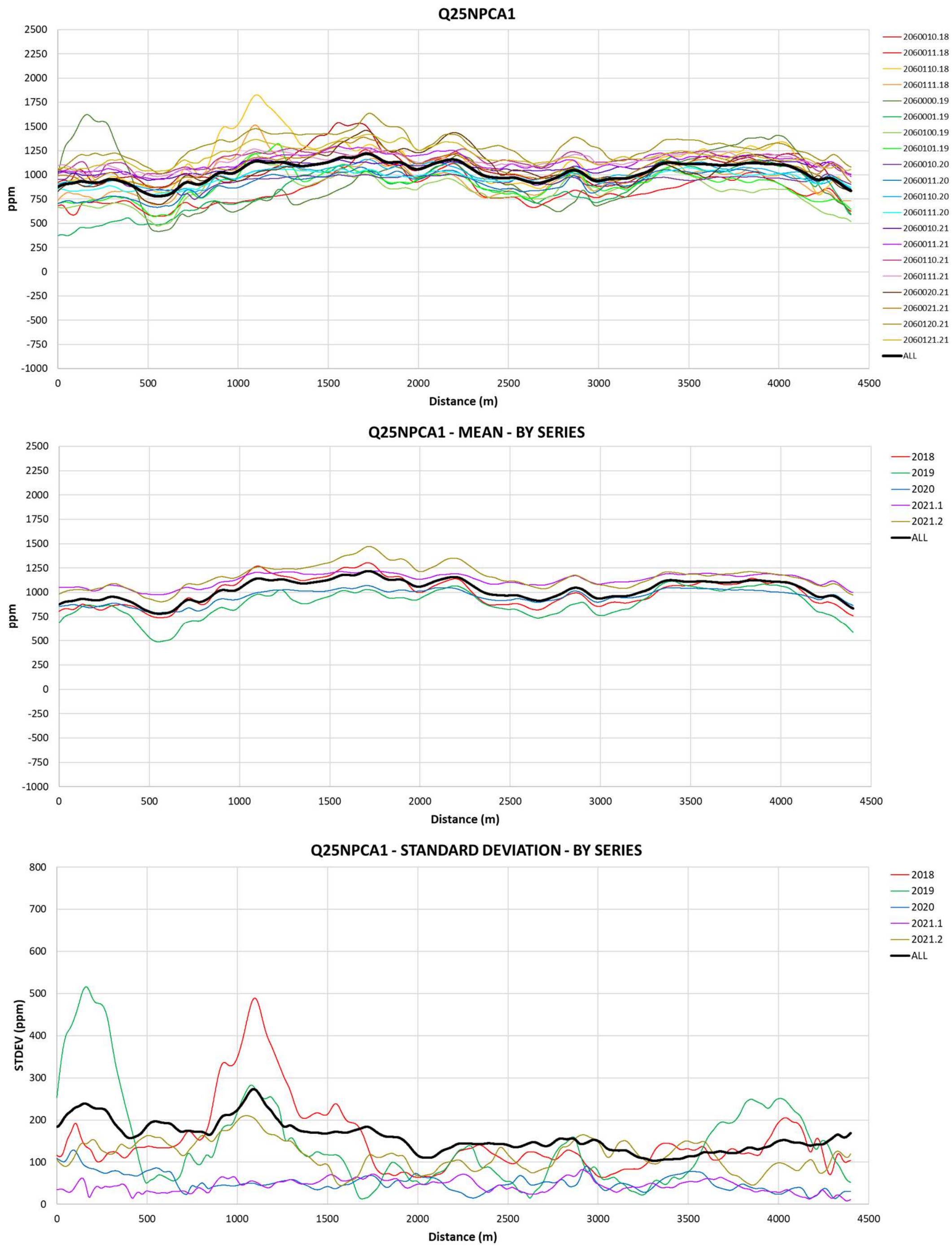

Figure 4.7: 25 kHz quadrature responses after application of Npca1 filter (Q25NPCA1 data), plotted against flight-distance, interpolated at 1 m intervals. Southern end of line (coast-line) located at 0 m distance. (Upper panel) Q25NPCA1 responses, coloured coded by flight, together with the twenty-flight mean (black line). (Middle panel) Mean Q25NPCA1 responses by series, colour-coded, and shown together with the twenty-flight mean (black line). (Lower panel) Q25NPCA1 standard deviation of the mean (STDEV) by series, colour-coded, and shown together with STDEV for all twenty lines.

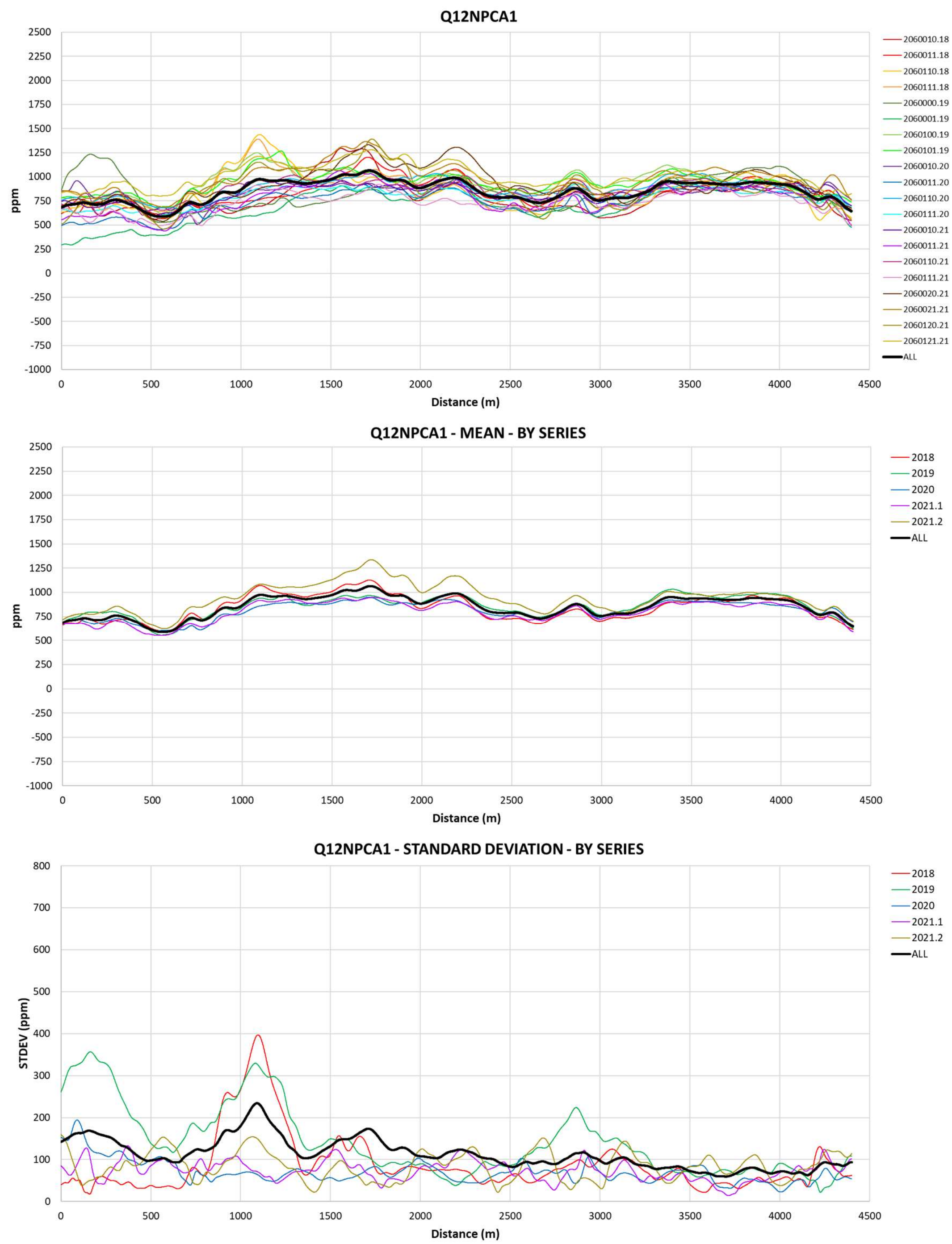

Figure 4.8: 12 kHz quadrature responses after application of Npca1 filter (Q12NPCA1 data), plotted against flight-distance, interpolated at 1 m intervals. Southern end of line (coast-line) located at 0 m distance. (Upper panel) Q12NPCA1 responses, coloured coded by flight, together with the twenty-flight mean (black line). (Middle panel) Mean Q12NPCA1 responses by series, colour-coded, and shown together with the twenty-flight mean (black line). (Lower panel) Q12NPCA1 standard deviation of the mean (STDEV) by series, colour-coded, and shown together with STDEV for all twenty lines.

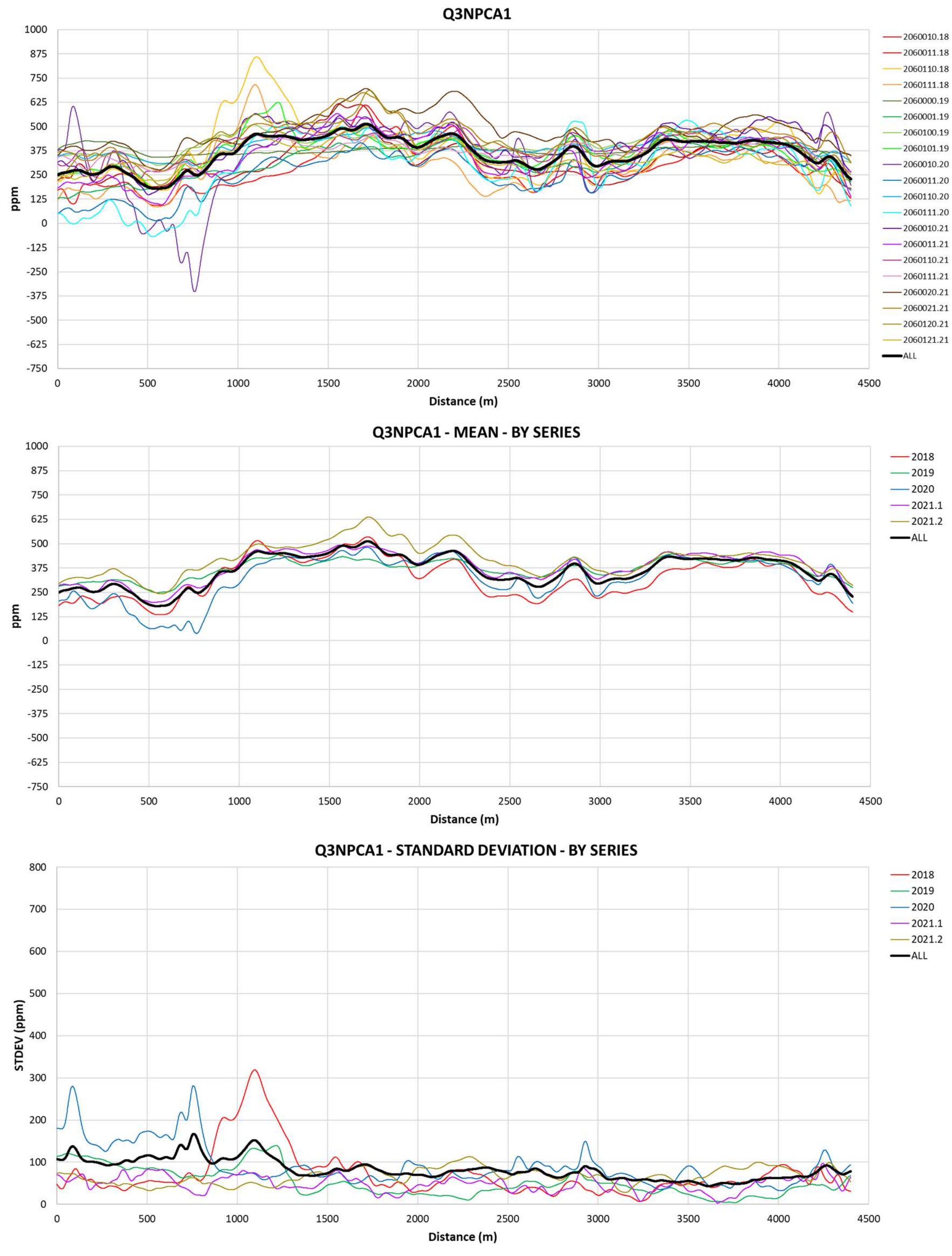

Figure 4.9: 3 kHz quadrature responses after application of Npca1 filter (Q3NPCA1 data), plotted against flight-distance, interpolated at 1 m intervals. Southern end of line (coast-line) located at 0 m distance. (Upper panel) Q3NPCA1 responses, coloured coded by flight, together with the twenty-flight mean (black line). (Middle panel) Mean Q3NPCA1 responses by series, colour-coded, and shown together with the twenty-flight mean (black line). (Lower panel) Q3NPCA1 standard deviation of the mean (STDEV) by series, colour-coded, and shown together with STDEV for all twenty lines. Note 2x increase in scale of the vertical axis for the FEM response amplitudes in the upper two panels, compared with previous 12 and 25 kHz graphs.

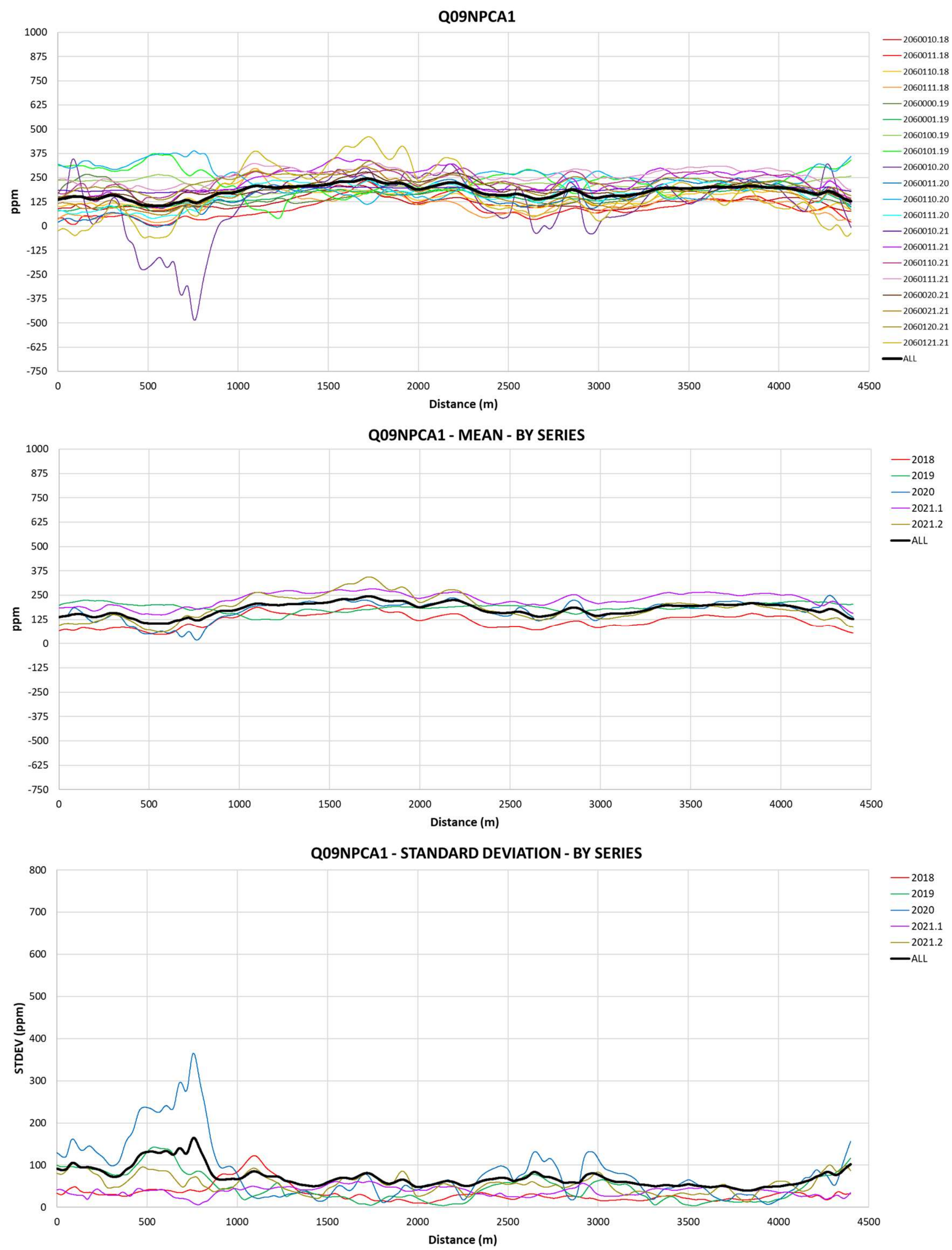

Figure 4.10: 0.9 kHz quadrature responses after application of Npca1 filter (Q09NPCA1 data), plotted against flight-distance, interpolated at 1 m intervals. Southern end of line (coast-line) located at 0 m distance. (Upper panel) Q09NPCA1 responses, coloured coded by flight, together with the twenty-flight mean (black line). (Middle panel) Mean Q09NPCA1 responses by series, colour-coded, and shown together with the twenty-flight mean (black line). (Lower panel) Q09NPCA1 standard deviation of the mean (STDEV) by series, colour-coded, and shown together with STDEV for all twenty lines. Note 2x increase in scale of the vertical axis for the FEM response amplitudes in the upper two panels, compared with previous 12 and 25 kHz graphs.

4.3 Effect of PCA Filters on FEM Data Variability

The effects of the Npca1, Npca2 and Npca3 filters on the twenty-line mean EM responses and the twenty-line standard deviations of the mean, in comparison with the original, unfiltered data, is illustrated in Figures 4.11 and 4.12 for in-phase data components and Figures 4.13 and 4.14 for quadrature components.

4.3.1 Effect of the PCA filters on the mean responses

In examining the effect of the PCA filters on the mean responses (Figures 4.11 and 4.13), it is apparent that the changes are relatively modest, particularly in the 12 and 25 kHz data. In the 0.9 and 3 kHz data, the effect of increasing PCA filter strength, from Npca3 to Npca1, is most noticeable on the southern-most 1,000 m of the line, where undulations in the mean responses in the original data (some of which are not coherent with features observed in the 12 and 25 kHz responses), are gradually subdued and then removed in the Npca1 responses. The relatively modest impact of the PCA filters on the twenty-line mean responses attests to the power of the twenty-fold 'stack' in attenuating noise in the original responses. Reviewing the original 0.9 and 3 kHz EM responses again in Figures 3.10, 3.11, 3.14 and 3.15 (upper panels) illustrates the extent of the noisy data excursions, in each of the twenty individual lines, around the mean responses.

The fact that the 'power of the stack' can attenuate the noise present in the individual lines as effectively as it has, suggests that while the noise is located at specific, discrete locations along the line, the expression of the noise is *random* from line-to-line across the twenty lines. Stacking of data (c.f. as applied in seismic-reflection data processing) is particularly effective in improving the signal-to-noise ratio of the stacked (averaged) data through the removal of random noise, with the signal-to-noise ratio being improved by a factor of $\sqrt{N}$, where N is the number of data in the stack.

The signal coherence along the test-line across all frequencies in the mean in-phase and quadrature responses in the Npca1 filtered data is notable. Lack of signal coherence in the mean responses, between the two higher frequency data components and particularly the 0.9 kHz data components, is apparent in the higher order (Npca2 and Npca3) filter results and in the original, unfiltered data.

Figure 4.11: In-phase mean responses for twenty repeat lines, plotted against distance along the test-line, interpolated at 1 m intervals, for (top panel) original data (Plev data channels), (second panel) Npca3, (third panel) Npca2 and (bottom panel) Npca1 filtered data.

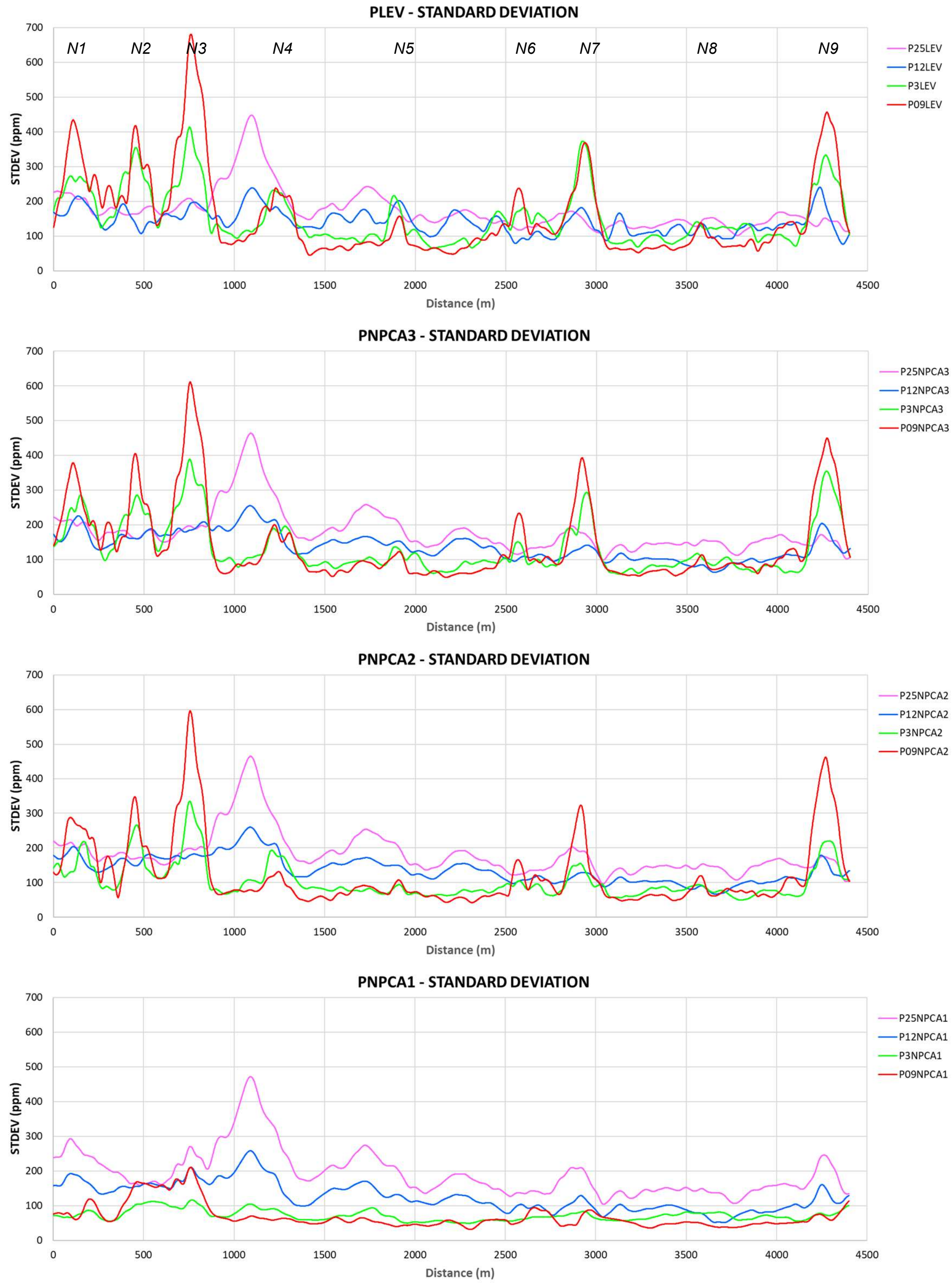

Figure 4.12: In-phase standard deviation of the mean (STDEV) for twenty repeat lines, plotted against distance along the test-line, interpolated at 1 m intervals, for (top panel) original data (Plev data channels), (second panel) Npca3, (third panel) Npca2 and (bottom panel) Npca1 filtered data. Location of standard deviation (STDEV) peaks in 3 and 0.9 kHz EM data (N1 to N9) annotated in upper panel.

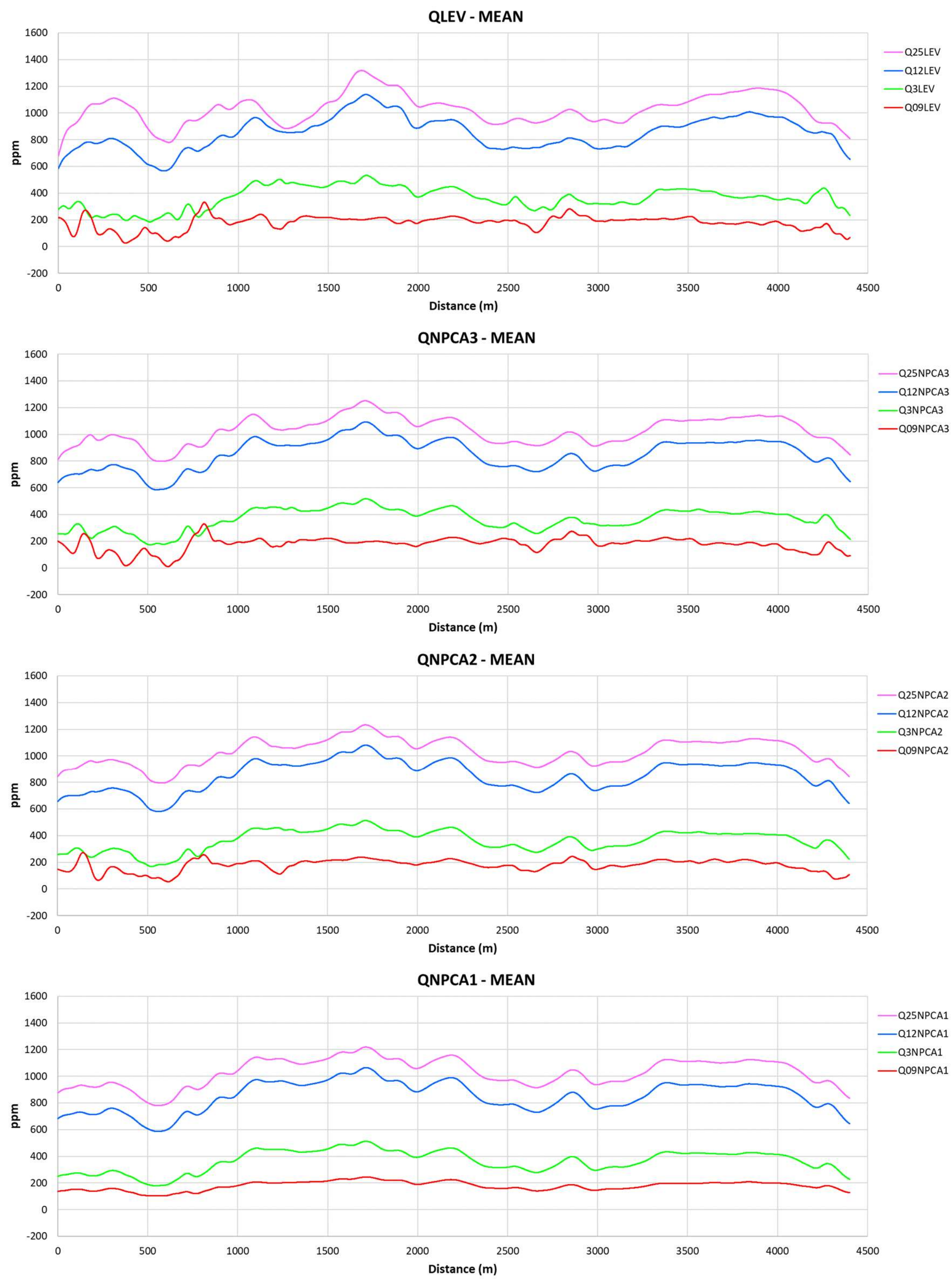

Figure 4.13: Quadrature mean responses for twenty repeat lines, plotted against distance along the test-line, interpolated at 1 m intervals, for (top panel) original data (Qlev data channels), (second panel) Npca3, (third panel) Npca2 and (bottom panel) Npca1 filtered data.

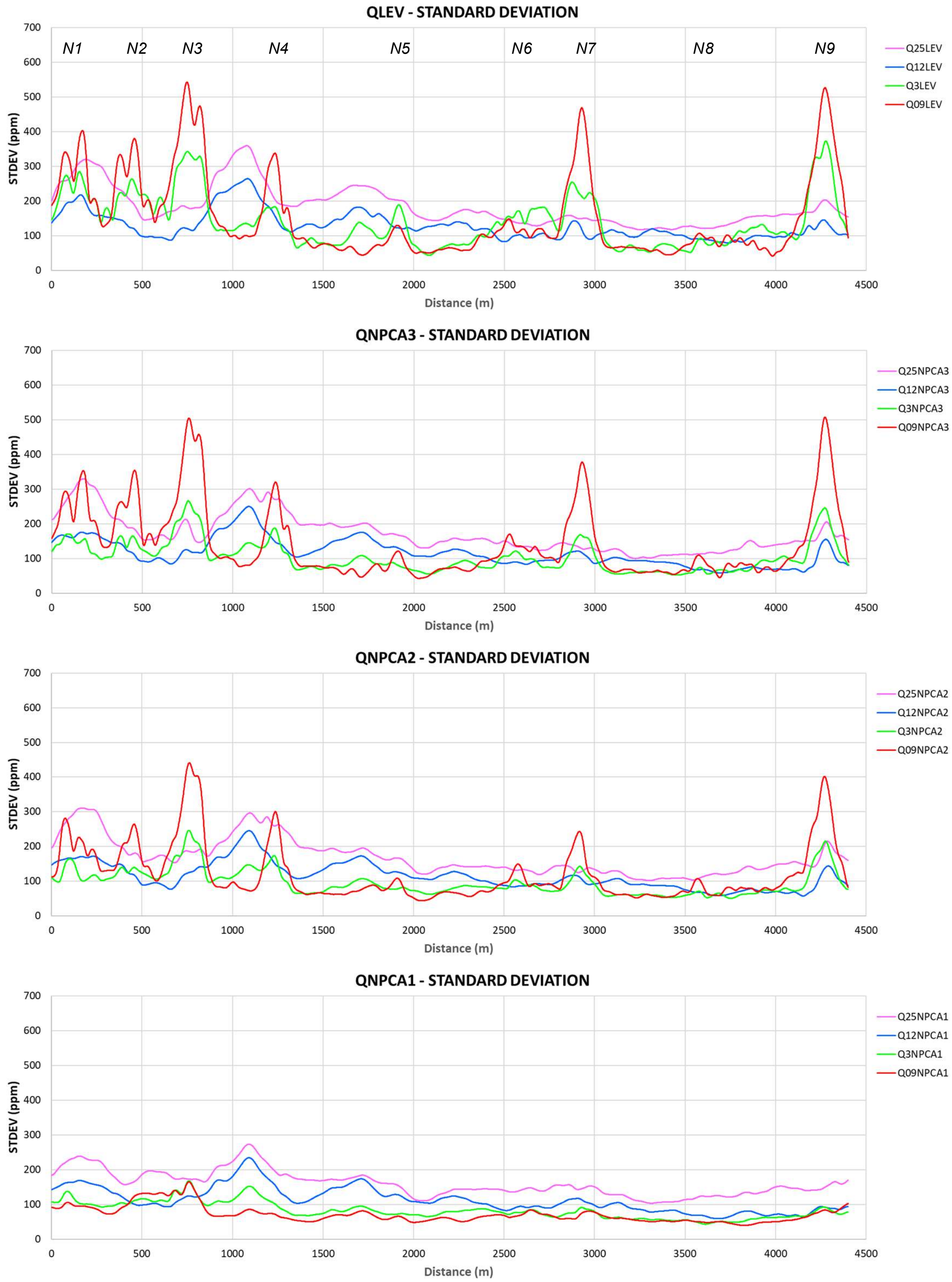

Figure 4.14: Quadrature standard deviation of the mean for twenty repeat lines, plotted against distance along the test-line, interpolated at 1 m intervals, for (top panel) original data (Qlev data channels), (second panel) Npca3, (third panel) Npca2 and (bottom panel) Npca1 filtered data. Location of standard deviation (STDEV) peaks in 3 and 0.9 kHz EM data (N1 to N9) annotated in upper panel.

4.3.2 Effect of the PCA filters on the data variability

In examining the effect of the PCA filters on the data variability (i.e., the standard deviations) (Figures 4.12 and 4.14), it is apparent that the Npca3 and Npca2 filters have relatively limited visual impact on the variability of the data at all frequencies and in both in-phase and quadrature components. While the Npca1 filter similarly has limited visual impact on the variability of the 12 and 25 kHz data, it substantially reduces the variability in the 0.9 and 3 kHz responses by removing almost entirely the nine high-standard deviation peaks from the variability profiles. The behaviour of the data variability in response to the Npca1 filter reiterates the primary conclusion in Section 4.1, which is that Principal Component 1 contains the bulk of the coherent (geological) signal in the data at all frequencies and that Principal Components 2 and 3 contain substantial signal (interpreted as noise) at 0.9 and 3 kHz that (i) is not coherent with the signal in Principal Component 1 and (ii) is highly variable from line- to-line (at specific locations along the line).

The effect of the Npca1 filter on the variability in the EM responses is further summarised in Table 4.1 and Figure 4.15, where the mean standard deviations for each four-line series and for twenty lines, before and after the filter application, are presented. Several observations may be drawn from an examination of the summary data and figures:

i. <u>Significant reduction in the data variability at 0.9 and 3 kHz</u>. The removal of the standard deviation spikes by the Npca1 filter in the 0.9 and 3 kHz in-phase and quadrature data, observed in Figures 4.12 and 4.14, has significantly reduced the mean standard deviations in all four of these EM components. Reductions in the mean standard deviations across each of the four-line series for 0.9 and 3 kHz lie in the range 35 – 95 ppm (Figure 4.15). The much-reduced mean data variability in the first principal component confirms that a significant proportion of the data variability at 0.9 and 3 kHz is found in the higher principal components (i.e., Principal Component 2 and higher), including the data variability giving rise to the standard deviation spikes.

Table 4.1: In-phase EM responses – mean variability (mean standard deviation, SD) before and after Npca1 filter, by series and for all twenty lines. Entries where mean variability increases on application of Npca1 filter annotated in red.

Series (Year)	Line Number	P25lev Mean SD All (ppm)	P25lev Mean SD Series (ppm)	P25lev After Npca1 Mean SD All (ppm)	P25lev After Npca1 Mean SD Series (ppm)	P12lev Mean SD All (ppm)	P12lev Mean SD Series (ppm)	P12lev After Npca1 Mean SD All (ppm)	P12lev After Npca1 Mean SD Series (ppm)
2018	L2060010.18	173.6	166.1	193.5	180.6	141.4	111.1	125.3	86.9
	L2060110.18								
	L2060011.18								
	L2060111.18								
2019	L2060000.19		141.2		183.2		116.3		126.7
	L2060100.19								
	L2060001.19								
	L2060101.19								
2020	L2060010.20		116.7		134.4		114.9		93.8
	L2060110.20								
	L2060011.20								
	L2060111.20								
2021.1	L2060010.21		96.7		112.0		132.3		103.8
	L2060110.21								
	L2060011.21								
	L2060111.21								
2021.2	L2060020.21		122.2		131.3		113.9		94.7
	L2060120.21								
	L2060021.21								
	L2060121.21								

Series (Year)	Line Number	P3lev Mean SD All (ppm)	P3lev Mean SD Series (ppm)	P3lev After Npca1 Mean SD All (ppm)	P3lev After Npca1 Mean SD Series (ppm)	P09lev Mean SD All (ppm)	P09lev Mean SD Series (ppm)	P09lev After Npca1 Mean SD All (ppm)	P09lev After Npca1 Mean SD Series (ppm)
2018	L2060010.18	153.9	90.8	71.8	42.1	158.8	105.6	68.3	48.1
	L2060110.18								
	L2060011.18								
	L2060111.18								
2019	L2060000.19		103.5		54.8		104.8		27.9
	L2060100.19								
	L2060001.19								
	L2060101.19								
2020	L2060010.20		170.4		77.7		172.0		88.6
	L2060110.20								
	L2060011.20								
	L2060111.20								
2021.1	L2060010.21		175.9		95.0		168.7		97.9
	L2060110.21								
	L2060011.21								
	L2060111.21								
2021.2	L2060020.21		149.5		75.8		117.4		37.8
	L2060120.21								
	L2060021.21								
	L2060121.21								

Table 4.2: Quadrature EM responses – mean variability (mean standard deviation, SD) before and after Npca1 filter, by series and for all twenty lines.

Series (Year)	Line Number	Q25lev		Q25lev After Npca1		Q12lev		Q12lev After Npca1	
		Mean SD All (ppm)	Mean SD Series (ppm)	Mean SD All (ppm)	Mean SD Series (ppm)	Mean SD All (ppm)	Mean SD Series (ppm)	Mean SD All (ppm)	Mean SD Series (ppm)
2018	L2060010.18	185.0	176.8	159.6	152.5	128.6	104.9	112.6	88.5
	L2060110.18								
	L2060011.18								
	L2060111.18								
2019	L2060000.19		183.2		143.1		145.2		140.9
	L2060100.19								
	L2060001.19								
	L2060101.19								
2020	L2060010.20		81.6		51.8		89.4		70.4
	L2060110.20								
	L2060011.20								
	L2060111.20								
2021.1	L2060010.21		75.1		44.0		104.5		74.0
	L2060110.21								
	L2060011.21								
	L2060111.21								
2021.2	L2060020.21		135.4		117.4		100.8		84.1
	L2060120.21								
	L2060021.21								
	L2060121.21								
Series (Year)	**Line Number**	**Q3lev**		**Q3lev After Npca1**		**Q09lev**		**Q09lev After Npca1**	
		Mean SD All (ppm)	**Mean SD Series (ppm)**	**Mean SD All (ppm)**	**Mean SD Series (ppm)**	**Mean SD All (ppm)**	**Mean SD Series (ppm)**	**Mean SD All (ppm)**	**Mean SD Series (ppm)**
2018	L2060010.18	142.1	105.8	82.7	71.6	154.8	91.9	71.1	32.4
	L2060110.18								
	L2060011.18								
	L2060111.18								
2019	L2060000.19		90.6		52.0		109.0		46.6
	L2060100.19								
	L2060001.19								
	L2060101.19								
2020	L2060010.20		142.7		91.6		144.6		82.8
	L2060110.20								
	L2060011.20								
	L2060111.20								
2021.1	L2060010.21		129.9		48.7		132.9		38.1
	L2060110.21								
	L2060011.21								
	L2060111.21								
2021.2	L2060020.21		147.8		67.1		140.2		55.3
	L2060120.21								
	L2060021.21								
	L2060121.21								

Figure 4.15: Change in mean variability (mean standard deviation) for eight EM data components and for each four-line series and for all twenty lines – before and after application of Npca1 filter. Top of each blue and green bar corresponds with mean variability of original EM responses, bottom of each blue bar corresponds with mean variability after applying Npca1 filter. Length of blue or green bar indicates reduction in mean variability as a result of applying the Npca1 filter. Red bars correspond with instances where application of the Npca1 filter resulted in an increase in mean variability, and where the top and bottom of the bars correspond with the mean variability after and before Npca1 filter application respectively, and the length of the bar the increase in variability.

ii. The moderate reduction in the mean data variability at 12 kHz (both in-phase and quadrature) and 25 kHz (quadrature only) confirms that much of the variability in the data at these frequencies is resident in the first principal component (i.e., rejecting Principal Components 2 and higher in the data does not significantly change the mean variability). Reductions in the mean standard deviations across each of the four-line series lie in the range 4 – 40 ppm (Figure 4.15).

iii. A moderate increase in the mean data variability in the 25 kHz in-phase component is observed, as well as in 12 kHz in-phase for the 2019 series (Figure 4.15). The reason for an increase in mean data variability in the first principal component is not immediately obvious and warrants further consideration.

4.3.3 Note on selection of appropriate order of PCA filter

The work above has illustrated that a PCA filter of order = 1 (Npca1 filter) is required to remove a signal component, characterised by strong data variability in the 0.9 and 3 kHz EM components, which is not coherent with the data signal in the 12 and 25 kHz components (and which is interpreted as a cultural noise signal). The choice of a PCA filter of order = 1 in this instance has benefited from knowledge of the data variability characteristics provided by the twenty repeat flights over the same geological terrain – and more specifically evidence of distinctly different data variability characteristics in the 0.9 and 3 kHz EM data components compared with the 12 and 25 kHz components.

Tellus production survey blocks do not benefit from the same repetition of flight lines to assist in the selection of an appropriate PCA filter order (or ‘strength’). An alternative philosophy, seeking to reconstruct the PCA filtered EM data to within the system data error, was adopted when selecting a PCA filter of order = 3 to prepare the EM data prior to GSI’s 1-D inversion modelling of the A5, A6 and Waterford blocks (e.g., GSI, 2020). Kiyan et al. (2022) have estimated (system) data errors as the standard deviation of the data acquired on four repeat flights of the Bundoran test-line in 2015 for each data component and frequency, for the highest flight altitude of 240 m (an altitude at which both EM geological signal strength and cultural noise signal strength is minimal) (Table 4.3). Average error for the in-phase data components is 55 ppm, for the quadrature components is 38 ppm and for all eight data components is 47 ppm. Table 4.3 illustrates that the intrinsic system noise or data error at 0.9 and 3 kHz is not higher than that for 12 and 25 kHz.

Table 4.3: Mean standard deviations, in ppm, of data acquired on four repeat flights of the Bundoran test-line in 2015 for each data component and frequency, for a flight altitude of 240 m. IP = in-phase and Q = quadrature. Flight lines analysed are: L2240020.15, L2240120.15, L2240030.15 and L2240130.15. Data from Kiyan et al. (2022, Table 1).

912 Hz		3005 Hz		11,962 Hz		24,510 Hz	
IP	**Q**	**IP**	**Q**	**IP**	**Q**	**IP**	**Q**
57	47	47	19	65	51	50	35

The illustrative example of Figure 4.16 (for L1379, A1 Block, from Kiyan et al., 2022) shows the difference, as a Root Mean Square Error (RMSE), between the original (input) EM data and the output data, reconstructed with an increasing number of principal components (singular values). It is apparent in Figure 4.16 that a data reconstruction using only the first, most significant, principal component (#SV = 1, or Npca1 filter of this work) results in an RMSE between the input (original) and output (reconstructed or filtered) data of over 120 ppm. It is also apparent, if an output data reconstruction to within a 50 ppm data error is required, that the first five principal components would need to be included in the reconstruction (#SV = 5, or Npca5 filter of this work).

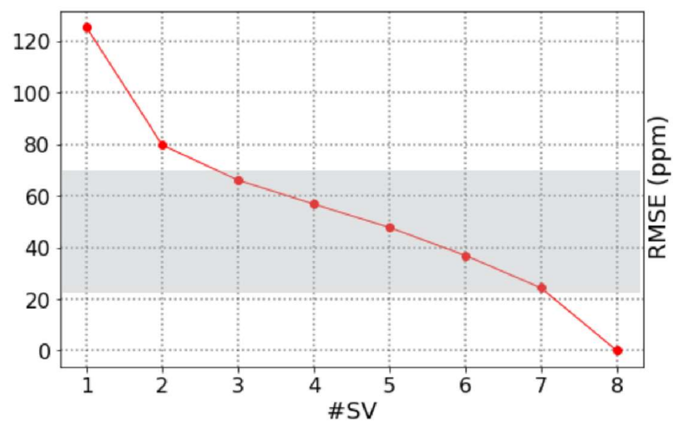

Figure 4.16: Root Mean Square Error (RMSE) for Principal Component Analysis (Singular Value Decomposition) and reconstruction of EM data from flight line L1379 from Tellus Block A1. Vertical axis: RMSE, in ppm, between original EM data and EM data reconstructed using the number of principal components (singular values) shown on the horizontal axis. Horizontal axis: number of singular values (#SV) in data reconstruction. For example, #SV = 3 indicates a reconstruction utilising the first three principal components. Illustrative error level of 50 ppm shown on graph (blue line). Figure from Kiyan et al. (2022, Figure 3).

In instances where the amplitudes of cultural noise signals greatly exceed the amplitudes of the geological signal and the system data error levels (as is the case for the 0.9 and 3 kHz data on the Waterford test-line), it is clear that the philosophy of reconstructing the data to within the system data error will lead to the inclusion (rather than exclusion) of the cultural noise signals, through incorporating a higher number of principal components, some of which contain the cultural noise signal. Such a philosophy (of reconstructing the data to within the *system* data error) may not be appropriate if the intention is to remove these high-amplitude cultural noise signals from the recorded EM response data.

5 Variability in FEM Single-Frequency Resistivity Models

5.1 Computation of Single-Frequency Resistivity Models

Half-space resistivity models, computed independently for each data frequency and at each measurement location, can be derived from the recorded FEM responses. Examining the variability of the half-space resistivity models is advantageous as the effect of variable flight clearance is accounted for, or subdued, in the resistivity models, thereby removing one of the main contributors to the variability of the FEM responses themselves. A correlation between variability in the FEM responses and variability in flight clearance, particularly for the 12 and 25 kHz responses, has been illustrated and discussed above in Section 3.

Two resistivity model datasets are available for variability analysis, derived using different approaches: (i) 'Extended Resistivity' models produced by contractor SGL and (ii) resistivity models generated by GSI using the Geosoft HEM software module. An explanation of both resistivity modelling approaches follows in Sections 5.1.1 and 5.1.2 below.

5.1.1 SGL Extended Resistivity models

SGL's 'Extended Resistivity' dataset consists of the combined results of two resistivity algorithms: a pseudo-layer resistivity derived in areas of strong EM signal (i.e., low resistivity areas) using the method of Fraser (1978), and an amplitude-altitude algorithm for areas of low EM signal (i.e., high resistivity areas) (see, e.g., SGL, 2022). The pseudo-layer resistivity algorithm uses an interpolation of an in-phase/quadrature nomogram to find an apparent resistivity and an apparent height (of the aircraft above the resistive body) at each measurement location. The apparent height parameter absorbs or subdues the effect of flight-clearance on the apparent resistivity measurement (see Fraser, 1978 for further detail). Where the in-phase signal is low over resistive ground, the pseudo-layer algorithm is substituted by an amplitude-altitude algorithm – as the total amplitude of the EM signal is still above system noise levels due to higher quadrature signal strength. A gradual transition is employed between the pseudo-layer derived resistivity values to the amplitude-altitude derived resistivity values.

As the FEM estimation of resistivity becomes unreliable over resistive terrain when the frequency/resistivity ratio is less than about 1, resistivity values in the SGL models are restricted to a maximum value equal to the transmission frequency, i.e., 912, 3005, 11962 and 24510 Ω.m (ohm.m).

5.1.2 Geosoft HEM Resistivity models

Resistivity models were derived using the Geosoft 'HEM' modelling software. In the HEM method, a single half-space resistivity value is determined through formal inversion that best matches the input in-phase, quadrature and flight clearance data at each measurement location, separately and independently for each of the four EM frequencies (Geosoft, 2005). Flight-clearance variation is explicitly accounted for in the inversions. Over resistive terrain, due to the very low EM signal strength, the HEM inversions are not always successful in converging on resistivity solutions, leading to null model solutions. A high initial (starting) resistivity value of 10,000 Ω.m was used in the inversion modelling for all frequencies, to (successfully) reduce the number of null solutions in the inversions. While the HEM models do contain resistivity solutions greater than 912 and 3005 Ω.m for the 912 and 3005 Hz frequencies respectively, the number of null solutions increases as these resistivity thresholds are reached.

5.2 Variability in SGL Extended Resistivity Models

Figures 5.1 – 5.4 that follow provide a catalogue of the variability in the SGL Extended Resistivity models along the test-line, for each of the four transmission frequencies. In each figure of the catalogue, the top panel plots individually the resistivity models for all twenty flight-lines, together with the twenty-line mean model. The middle panel plots the four-line mean resistivity model for each data series (year), together with the twenty-line mean model. The bottom panel, illustrating resistivity model variability, plots the four-line standard deviation of the mean for each data series, together with the twenty-line standard deviation. The statistics for the resistivity model data (means and standard deviations) are derived using $\log_{10}$(resistivity) values and are plotted as $\log_{10}$ values on all graphs shown in Figures 5.1 – 5.4.

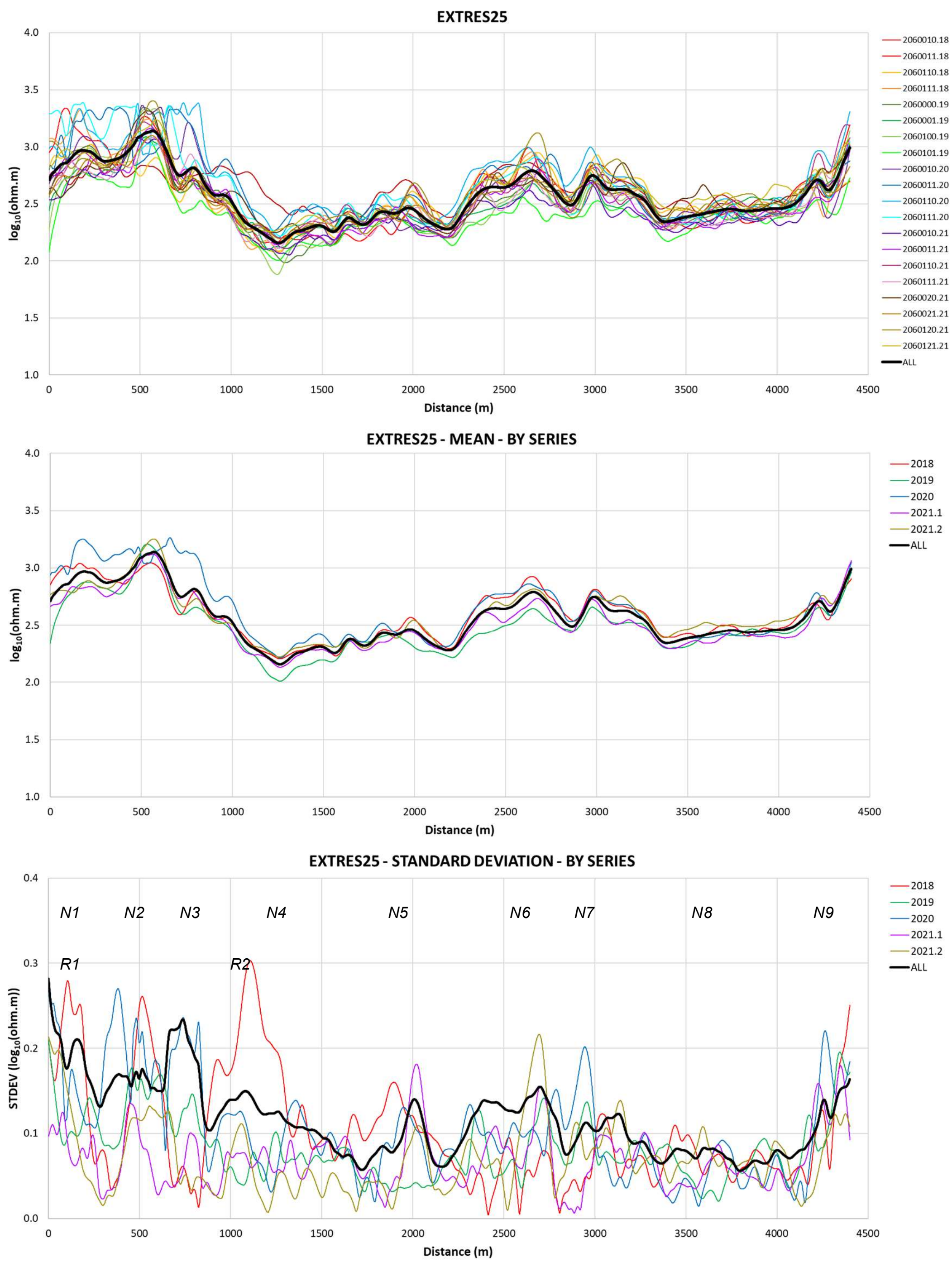

Figure 5.1: 25 kHz Extended Resistivity models (ExtendedRes25 data channel), plotted against flight-distance, interpolated at 1 m intervals. Southern end of line (coast-line) located at 0 m distance. (Upper panel) ExtendedRes25 models, coloured coded by flight, together with the twenty-flight mean (black line). (Middle panel) Mean ExtendedRes25 models by series, colour-coded, and shown together with the twenty-flight mean (black line). (Lower panel) ExtendedRes25 models standard deviation of the mean (STDEV) by series, colour-coded, and shown together with STDEV for all twenty lines. Location of STDEV peaks in 3 and 0.9 kHz EM data (N1 to N9) annotated, as well as STDEV peaks in clearance data (R1 and R2).

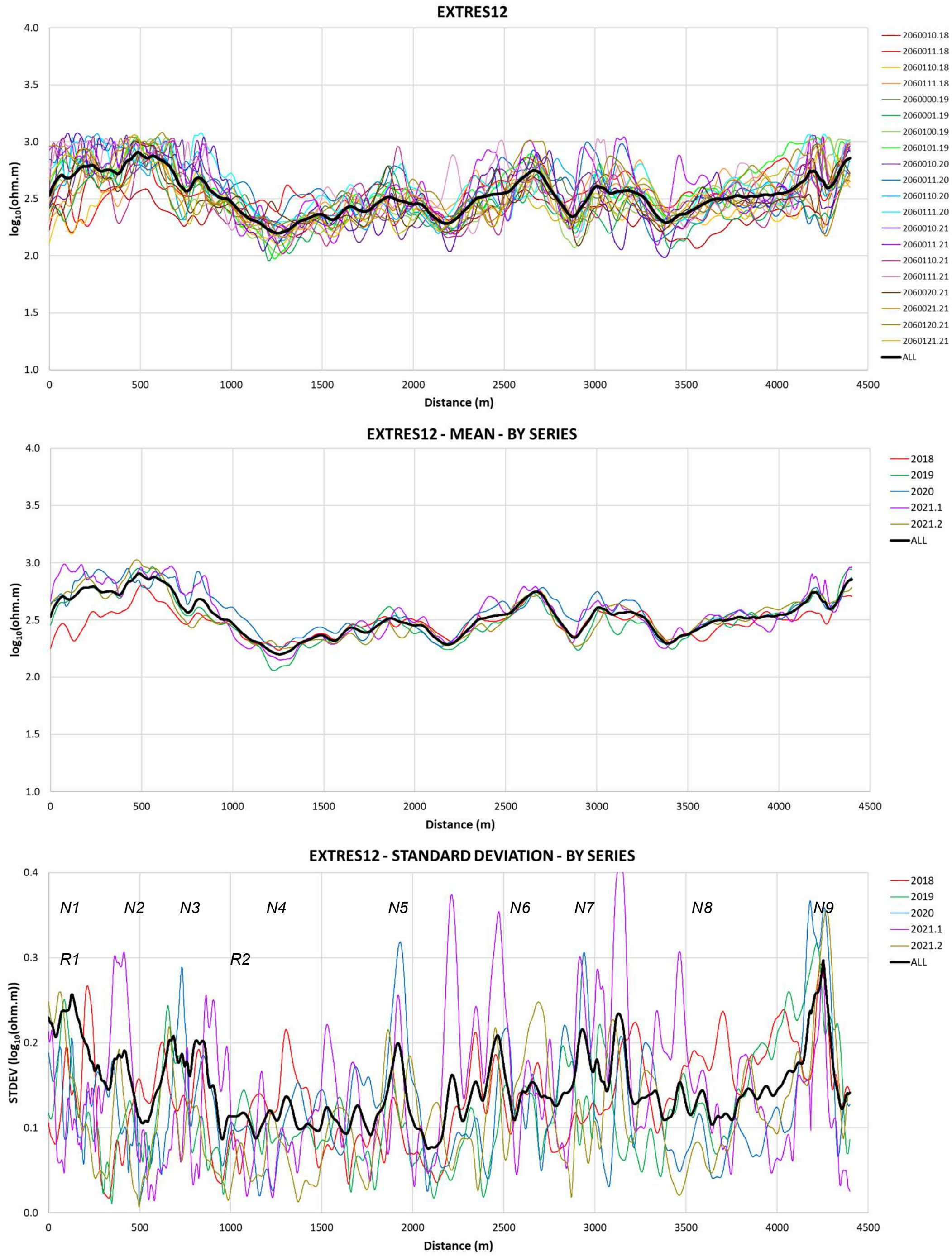

Figure 5.2: 12 kHz Extended Resistivity models (ExtendedRes12 data channel), plotted against flight-distance, interpolated at 1 m intervals. Southern end of line (coast-line) located at 0 m distance. (Upper panel) ExtendedRes12 models, coloured coded by flight, together with the twenty-flight mean (black line). (Middle panel) Mean ExtendedRes12 models by series, colour-coded, and shown together with the twenty-flight mean (black line). (Lower panel) ExtendedRes12 models standard deviation of the mean (STDEV) by series, colour-coded, and shown together with STDEV for all twenty lines. Location of STDEV peaks in 3 and 0.9 kHz EM data (N1 to N9) annotated, as well as STDEV peaks in clearance data (R1 and R2).

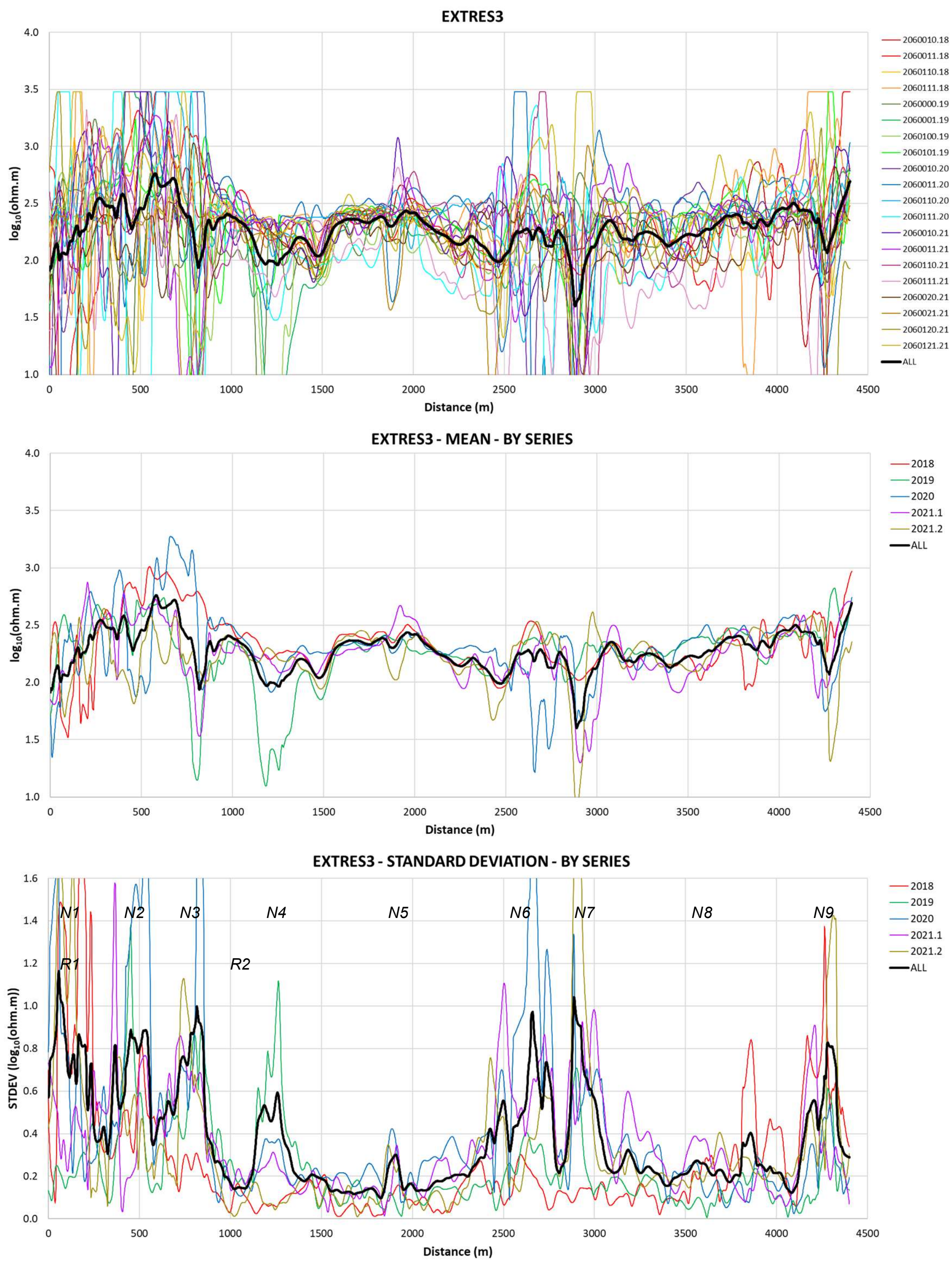

Figure 5.3: 3 kHz Extended Resistivity models (ExtendedRes3 data channel), plotted against flight-distance, interpolated at 1 m intervals. Southern end of line (coast-line) located at 0 m distance. (Upper panel) ExtendedRes3 models, coloured coded by flight, together with the twenty-flight mean (black line). (Middle panel) Mean ExtendedRes3 models by series, colour-coded, and shown together with the twenty-flight mean (black line). (Lower panel) ExtendedRes3 models standard deviation of the mean (STDEV) by series, colour-coded, and shown together with STDEV for all twenty lines. Location of STDEV peaks in 3 and 0.9 kHz EM data (N1 to N9) annotated, as well as STDEV peaks in clearance data (R1 and R2). Note 4x increase in scale of STDEV axis compared with previous 12 and 25 kHz graphs.

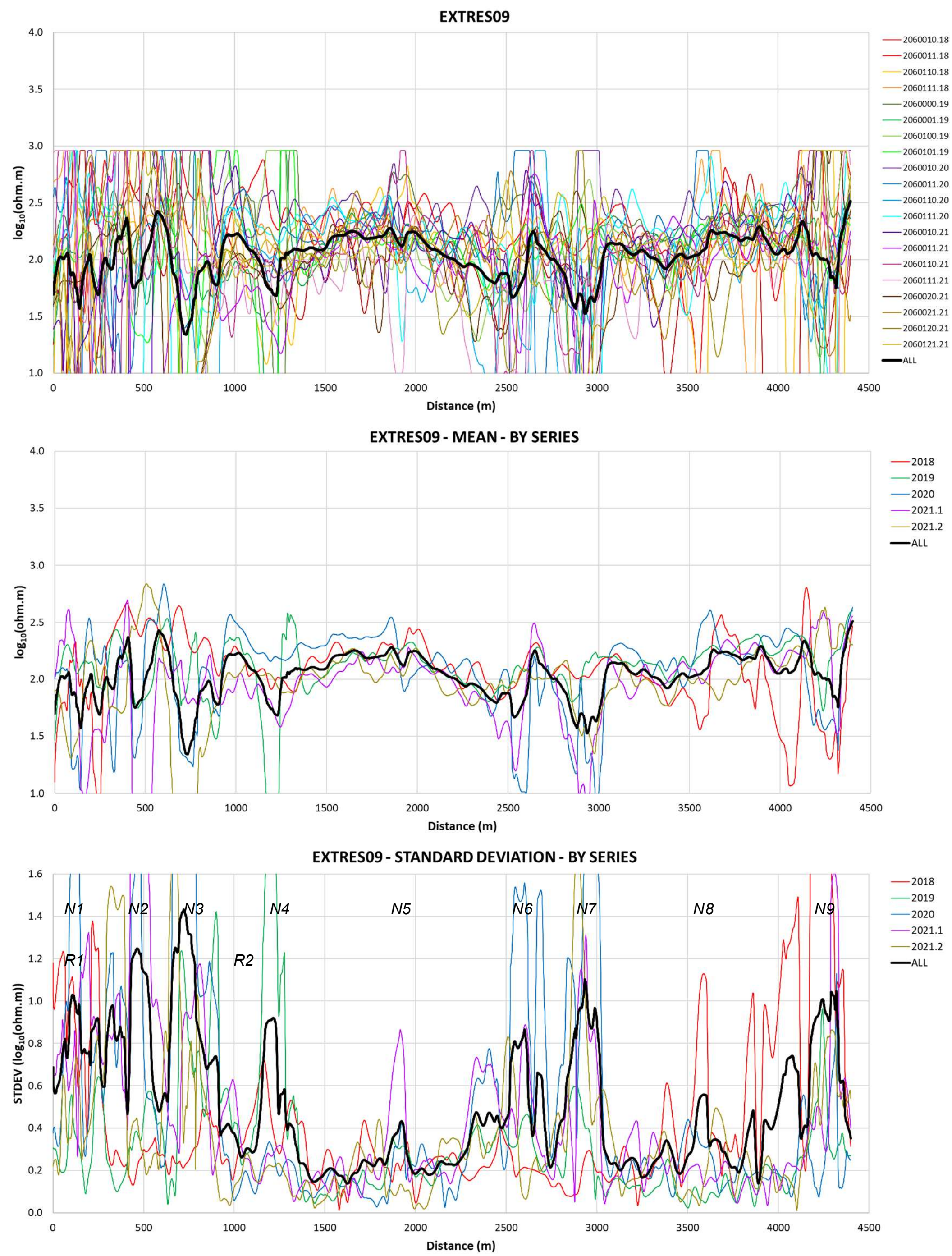

Figure 5.4: 0.9 kHz Extended Resistivity models (ExtendedRes09 data channel), plotted against flight-distance, interpolated at 1 m intervals. Southern end of line (coast-line) located at 0 m distance. (Upper panel) ExtendedRes09 models, coloured coded by flight, together with the twenty-flight mean (black line). (Middle panel) Mean ExtendedRes09 models by series, colour-coded, and shown together with the twenty-flight mean (black line). (Lower panel) ExtendedRes09 models standard deviation of the mean (STDEV) by series, colour-coded, and shown together with STDEV for all twenty lines. Location of STDEV peaks in 3 and 0.9 kHz EM data (N1 to N9) annotated, as well as STDEV peaks in clearance data (R1 and R2). Note 4x increase in scale of STDEV axis compared with previous 12 and 25 kHz graphs.

In reviewing the upper panels in each of Figures 5.1 – 5.4, the resistivity model values in the high-resistivity areas along the test-line appear to 'top-out' at maximum values that vary depending on the frequency. The 25 kHz models top-out around a maximum value of 2,522 Ω.m ($\log_{10}$ = 3.402) and the 12 kHz models at around a maximum value of 1,212 Ω.m ($\log_{10}$ = 3.083). Neither the 12 kHz nor 25 kHz models appear to have captured, in highly resistive areas, the full, upper range of resistivities present in the subsurface. The 3 kHz and 0.9 kHz models top-out (as imposed by SGL) at values equivalent to the transmission frequency, i.e., at 3,005 Ω.m ($\log_{10}$ = 3.478) and 912 Ω.m ($\log_{10}$ = 2.960), respectively.

In the 0.9 and 3 kHz models, many short-wavelength, high-resistivity spikes (truncated to the transmission frequency) and low-resistivity spikes are apparent in highly resistive areas (i.e., in high-resistivity areas indicated in the 12 and 25 kHz models) and are inferred to be noise spikes (i.e., non-geological). The mean resistivity models at 0.9 and 3 kHz, whether the twenty-line or four-line series means, appear unlikely to have recovered resistivity values close to the real subsurface resistivities in the vicinity of both the high- and low-resistivity spikes, but particularly in the vicinity of the latter.

5.3 Variability in Geosoft HEM Models

Figures 5.5 – 5.8 that follow provide a catalogue of the variability in the Geosoft HEM derived resistivity models along the test-line, for each of the four transmission frequencies. In each figure of the catalogue, the top panel plots individually the resistivity models for all twenty flight-lines, together with the twenty-line mean model. The middle panel plots the four-line mean models for each data series (year), together with the twenty-line mean model. The bottom panel, illustrating the resistivity model variability, plots the four-line standard deviation of the mean for each data series, together with the twenty-line standard deviation. As for the Extended Resistivity models, the statistics are based on $\log_{10}$(resistivity) values.

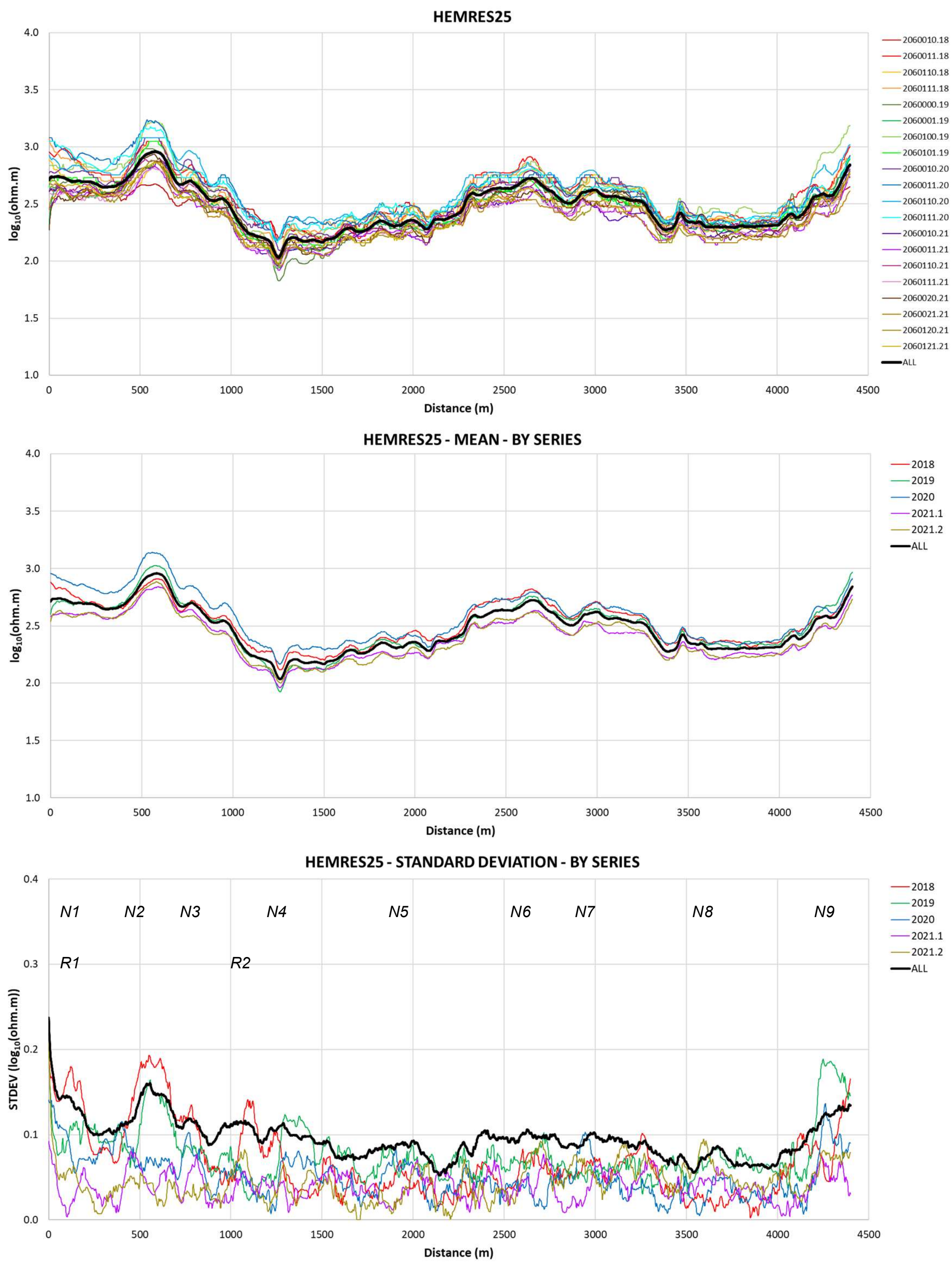

Figure 5.5: 25 kHz HEM resistivity models (HEMRes25 data), plotted against flight-distance, interpolated at 1 m intervals. Southern end of line (coast-line) located at 0 m distance. (Upper panel) HEMRes25 models, coloured coded by flight, together with the twenty-flight mean (black line). (Middle panel) Mean HEMRes25 models by series, colour-coded, and shown together with the twenty-flight mean (black line). (Lower panel) HEMRes25 models standard deviation of the mean (STDEV) by series, colour-coded, and shown together with STDEV for all twenty lines. Location of STDEV peaks in 3 and 0.9 kHz EM data (N1 to N9) annotated, as well as STDEV peaks in clearance data (R1 and R2).

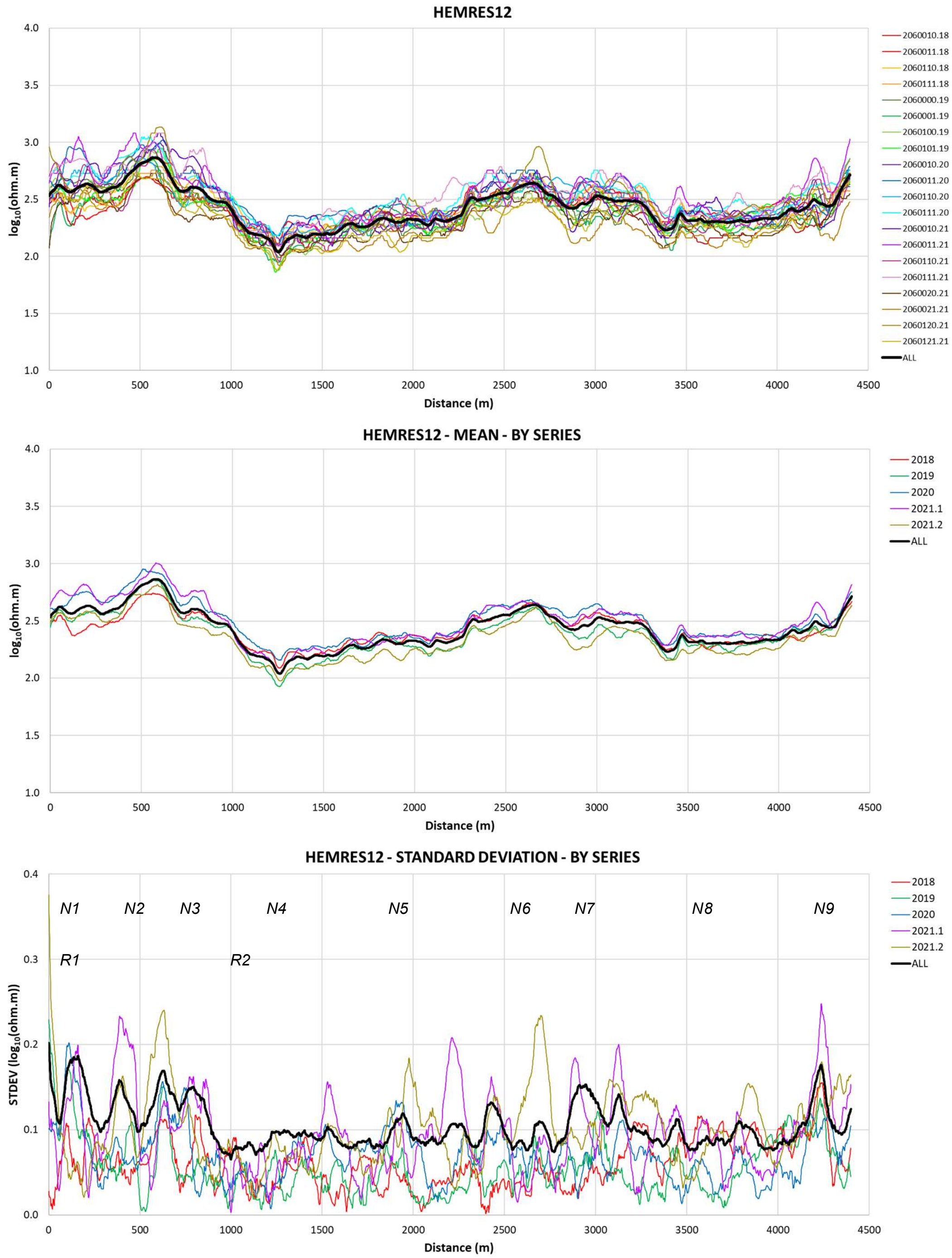

Figure 5.6: 12 kHz HEM resistivity models (HEMRes12 data), plotted against flight-distance, interpolated at 1 m intervals. Southern end of line (coast-line) located at 0 m distance. (Upper panel) HEMRes25 models, coloured coded by flight, together with the twenty-flight mean (black line). (Middle panel) Mean HEMRes12 models by series, colour-coded, and shown together with the twenty-flight mean (black line). (Lower panel) HEMRes12 models standard deviation of the mean (STDEV) by series, colour-coded, and shown together with STDEV for all twenty lines. Location of STDEV peaks in 3 and 0.9 kHz EM data (N1 to N9) annotated, as well as STDEV peaks in clearance data (R1 and R2).

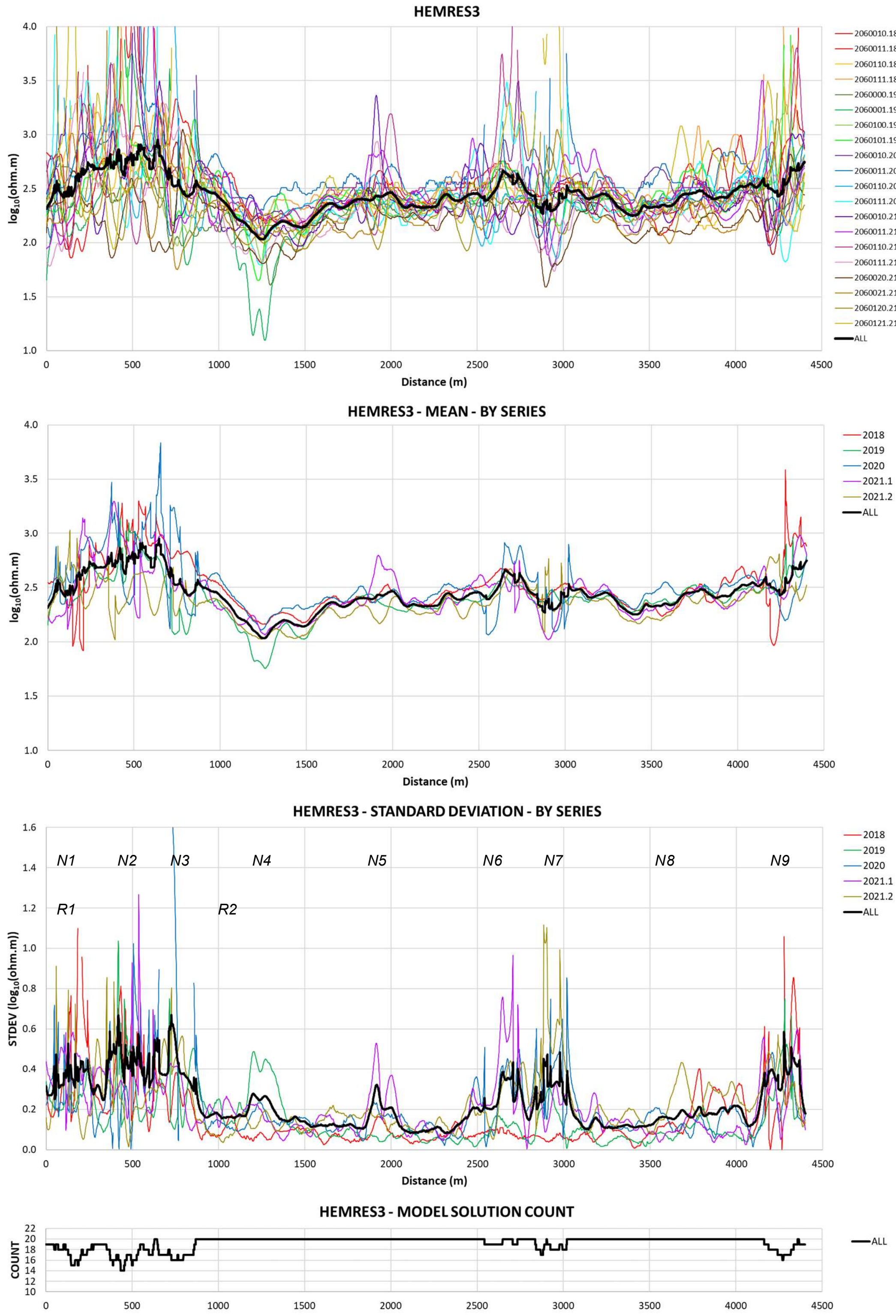

Figure 5.7: 3 kHz HEM resistivity models (HEMRes3 data), plotted against flight-distance, interpolated at 1 m intervals. Southern end of line (coast-line) located at 0 m distance. (Upper panel) HEMRes3 models, coloured coded by flight, together with the twenty-flight mean (black line). (Second panel) Mean HEMRes3 models by series, colour-coded, and shown together with the twenty-flight mean (black line). (Third panel) HEMRes3 models standard deviation of the

mean (STDEV) by series, colour-coded, and shown together with STDEV for all twenty lines. Location of STDEV peaks in 3 and 0.9 kHz EM data (N1 to N9) annotated, as well as STDEV peaks in clearance data (R1 and R2). Note 4x increase in scale of STDEV axis compared with previous 12 and 25 kHz graphs. (Lower panel) Count of model solutions contributing to the twenty-line mean and standard deviation computations. Number of solutions is less than 20 where no resistivity solution was found on one or more lines.

The HEM resistivity models at 12 and 25 kHz (upper panels Figures 5.5 and 5.6) appear to have fully recovered the upper range of subsurface resistivities in the high-resistivity sections of the test-line and are not characterised by the 'topping-out' apparent in the Extended Resistivity models at the same frequencies on some of the repeat flight-lines (Figures 5.1 and 5.2). Maximum resistivities of 1,720 Ω.m ($\log_{10}$ = 3.236) and 1,360 Ω.m ($\log_{10}$ = 3.133) are found in the 25 and 12 kHz HEM models respectively along the test-line.

While the 3 kHz and 0.9 kHz models are not explicitly limited to resistivity values equivalent to the transmission frequencies, i.e., 3,005 Ω.m and 912 Ω.m respectively, there are many null solutions in the high-resistivity sections of the test-line. The profiles illustrating the total number (count) of model solutions contributing to the twenty-line mean and standard deviation computations (the lower panels in Figures 5.7 and 5.8) indicate that up to one quarter and one half of the lines at 3 kHz and 0.9 kHz respectively lack resistivity solutions in the resistive portions of the test-line.

Similar to the Extended Resistivity models, a large number of short-wavelength, high-resistivity and low-resistivity spikes are apparent in the 0.9 and 3 kHz models, in areas of high-resistivity that are present in the 12 and 25 kHz models, which are inferred to be noise spikes (non-geological in origin). Again similarly, the mean resistivity models at 0.9 and 3 kHz, whether the twenty-line or four-line series means, appear unlikely to have recovered resistivity values close to the real subsurface resistivities in the vicinity of both the high- and low-resistivity spikes, but particularly in the vicinity of the latter.

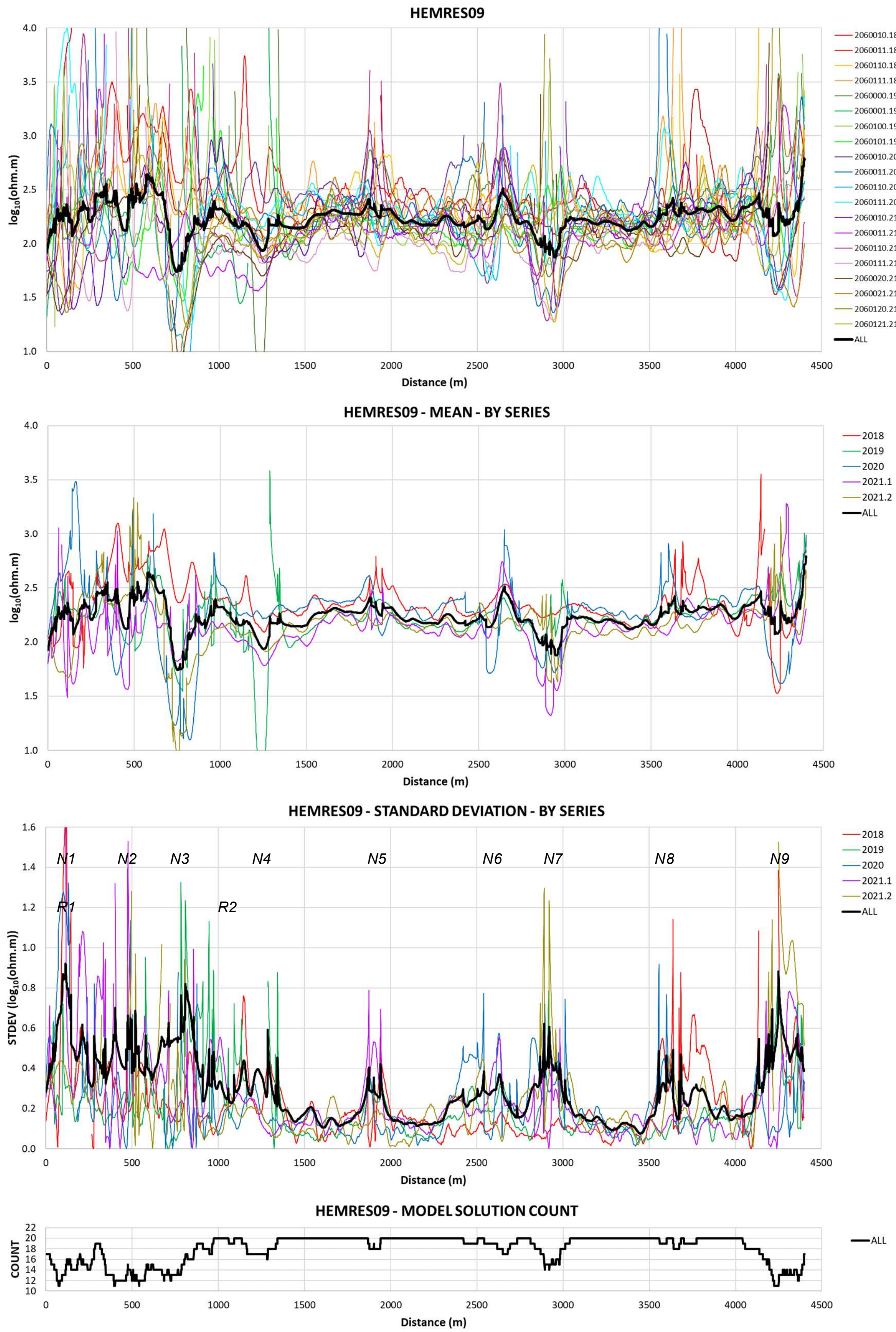

Figure 5.8: 0.9 kHz HEM resistivity models (HEMRes09 data), plotted against flight-distance, interpolated at 1 m intervals. Southern end of line (coast-line) located at 0 m distance. (Upper panel) HEMRes09 models, coloured coded by flight, together with the twenty-flight mean (black line). (Second panel) Mean HEMRes09 models by series, colour-coded, and shown together with the twenty-flight mean (black line). (Third panel) HEMRes09 models standard deviation of the

mean (STDEV) by series, colour-coded, and shown together with STDEV for all twenty lines. Location of STDEV peaks in 3 and 0.9 kHz EM data (N1 to N9) annotated, as well as STDEV peaks in clearance data (R1 and R2). Note 4x increase in scale of STDEV axis compared with previous 12 and 25 kHz graphs. (Lower panel) Count of model solutions contributing to the twenty-line mean and standard deviation computations. Number of solutions is less than 20 where no resistivity solution was found on one or more lines.

5.4 Summary of Variability in Single-Frequency Resistivity Models

The variability in the single-frequency resistivity models is assessed in two sections that follow. In the first section (Section 5.4.1), the *means* of the resistivity models on each line, at each frequency, are examined, allowing comparison with the equivalent assessment of the mean FEM response amplitudes in Section 3.1. In the second section (Section 5.4.2), changes in the resistivity model variability along the length of the test-line is examined, for all twenty lines together and for each of the four-line series, providing a comparison with the equivalent assessment of the FEM responses in Section 3.4.

5.4.1 First-order assessment

A broad, or first-order, assessment of the variability in the EM resistivity models is provided by an examination of the line averages for each of the twenty repeat flights, for each FEM frequency – as illustrated in Figures 5.9 and 5.10 for the Extended Resistivity and HEM Resistivity models respectively, and in Figure 5.11 for both sets of models and all frequencies together. For visual comparison, the average resistivity for each line at each frequency is plotted against the average for all twenty lines. The line-mean data plotted in Figures 5.9 to 5.11 are tabulated in Tables 5.1 and 5.2, together with standard deviations of the mean for each four-line series and for all twenty lines together.

While the computation of the single-frequency resistivity models is anticipated to remove or subdue the effect of flight clearance variation, differences in the mean resistivity of each repeat flight-line for each frequency may still arise through (i) differences (potentially inaccuracies) in the zero levels defined for each of the EM components for each flight-line, (ii) variable levels of cultural noise recorded on each flight line, and (iii) real differences in the subsurface resistivity structure at the time of the flights, and relevant only in considering differences between the five series of flights.

Two primary observations are apparent when examining the behaviour of the line-mean resistivity values of Figures 5.9 to 5.11:

i. The line-to-line variability of the line-mean resistivity within each group of four repeat flights and across all twenty repeat flights is significantly higher for the lower frequency 3 and 0.9 kHz data and is more marked in the Extended Resistivity models than in the HEM resistivity models. The higher variability in the lower frequency models is inferred to be the result of higher, and highly variable, cultural noise levels in these data. If variable cultural noise is the primary cause of the (mean) resistivity model variation at the 0.9 and 3 kHz frequencies, the implication is, with the exception of the Extended Resistivity 0.9 kHz models for the 2021.2 flight-series, that the cultural noise variability from flight-to-flight within each yearly series is as high as that across all twenty flights for the extended Resistivity models and almost as high for the HEM resistivity models (as illustrated by the standard deviation values recorded in Tables 5.1 and 5.2 for 0.9 and 3 kHz).

ii. The line-mean resistivity values in the Extended Resistivity models for the 12 and 25 kHz frequencies are higher than those in the HEM resistivity models (i.e., the former models are more resistive than the latter, by approximately 0.1 and 0.09 $\log_{10}(\Omega.m)$ on average for 12 and 25 kHz respectively). In contrast, line-mean resistivities in the Extended Resistivity models at 0.9 and 3 kHz frequencies are lower than those in the HEM resistivity models – on average by 0.16 and 0.2 $\log_{10}(\Omega.m)$ for 0.9 and 3 kHz respectively – and are the result of the Extended Resistivity models being restricted to maximum values of 912 and 3005 Ω.m in the high-resistivity areas of the line (see Figures 5.3 and 5.4 for the Extended Resistivity model profiles along the test-line at 3 and 0.9 kHz frequencies respectively, and Figures 5.7 and 5.8 for the HEM resistivity profiles). The HEM models have no maximum value restriction on the resistivity model solutions (although null solutions are commonly returned in the very high resistivity areas).

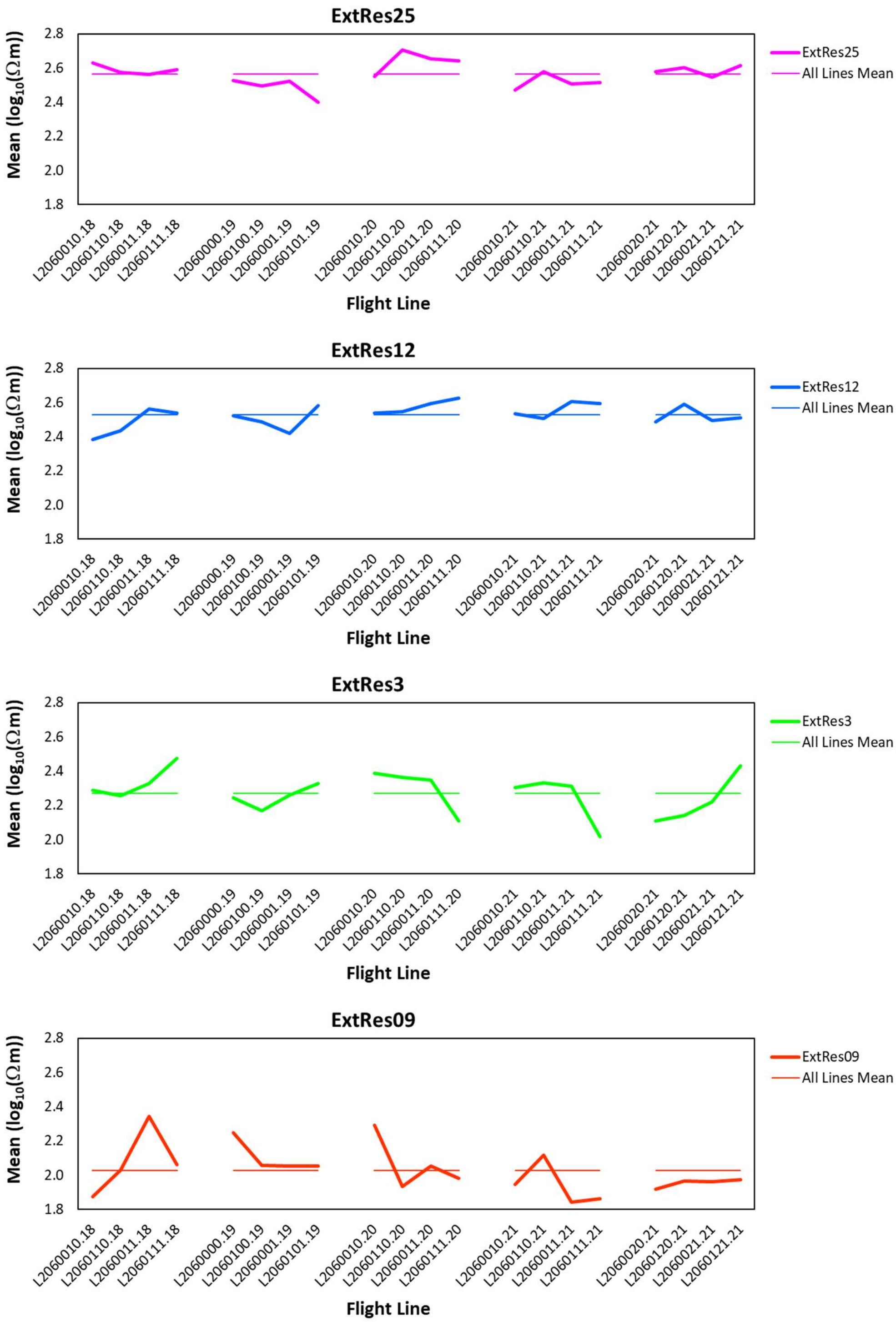

Figure 5.9: Mean log_{10} resistivity from Extended Resistivity models for each flight-line plotted against the mean for all twenty repeat flights, for (from top to bottom) 25 kHz, 12 kHz, 3 kHz and 0.9 kHz data. Data used and plotted are the 1 m resampled data. Source data given in Table 5.1.

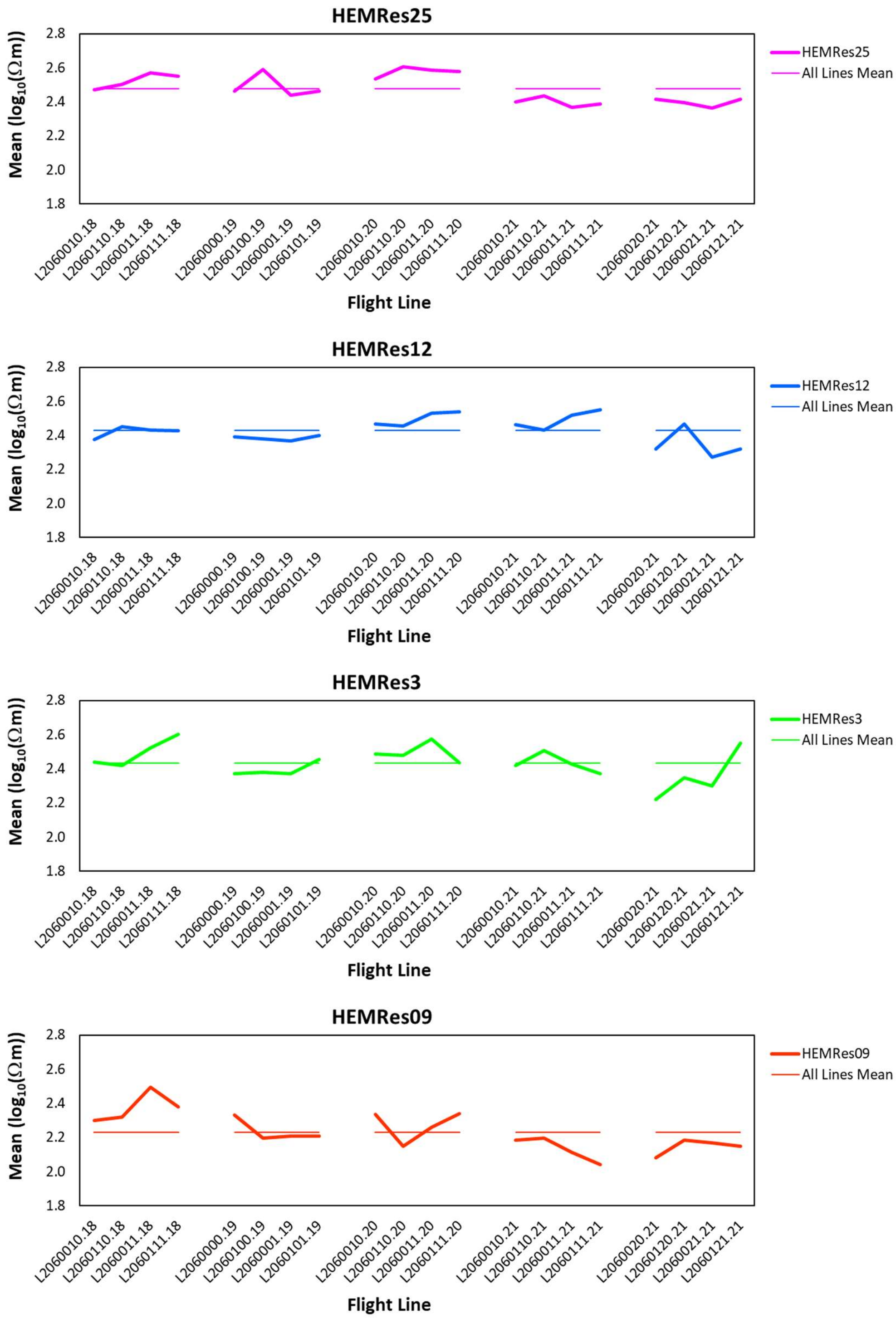

Figure 5.10: Mean log$_{10}$ resistivity from HEM Resistivity models for each flight-line plotted against the mean for all twenty repeat flights, for (from top to bottom) 25 kHz, 12 kHz, 3 kHz and 0.9 kHz data. Data used and plotted are the 1 m resampled data. Source data given in Table 5.2.

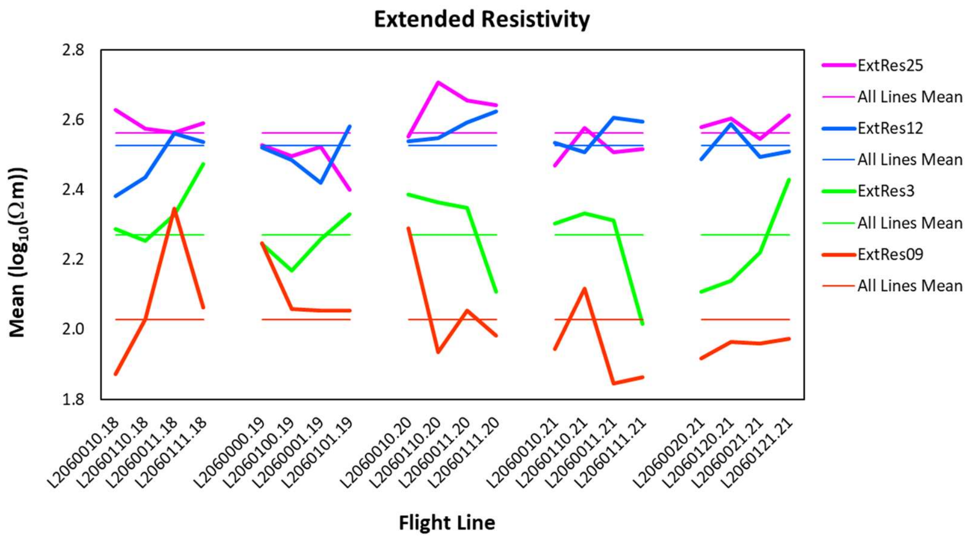

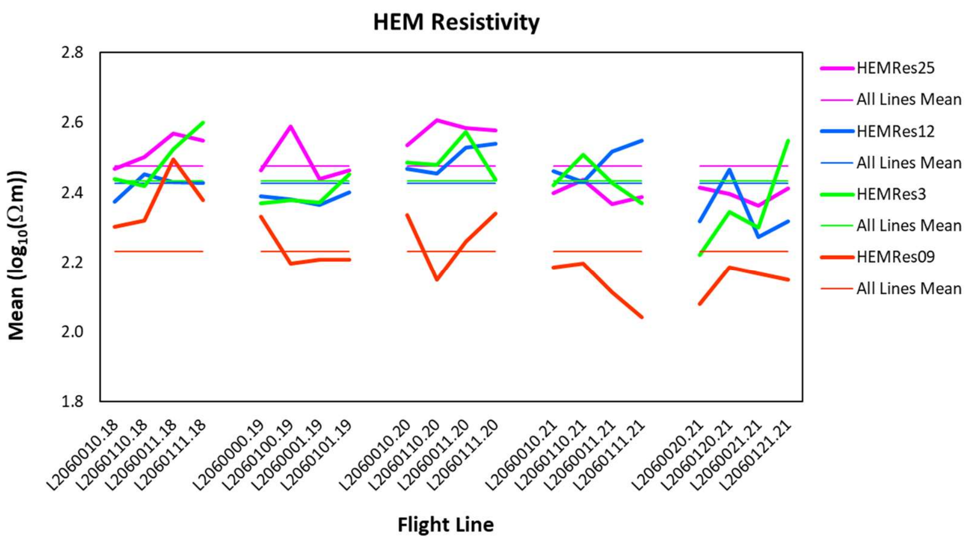

Figure 5.11: Mean log_{10} resistivity for each flight-line for Extended Resistivity models (upper figure) and HEM Resistivity models (lower figure), plotted against the average for all twenty repeat flights. Data used and plotted are the 1 m resampled data. Source data given in Tables 5.1 and 5.2.

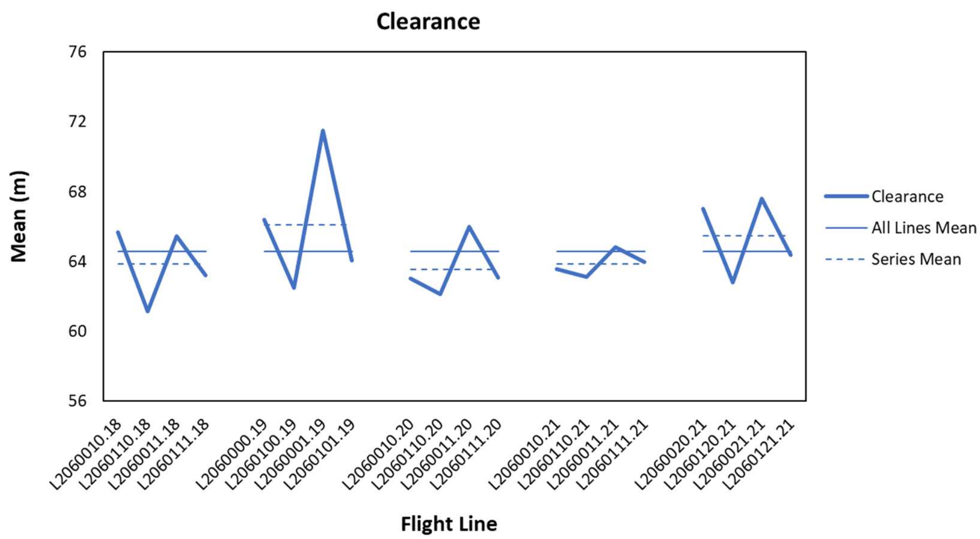

Figure 5.12: Mean flight clearance for each flight-line, plotted against the average for all twenty repeat flights (thin blue line) and the four-line average for each flight-series (thin dashed line). Data used and plotted are the original ~6 m sampled data. (Repeat of Figure 3.3).

Table 5.1. Extended Resistivity models. Summary of mean log$_{10}$ resistivity ('Line Mean') for each repeat flight for all frequencies. Also shown are mean and standard deviation (SD) of the four mean values for each series of flights and of the twenty mean values for all flights. Data used are the 1 m re-sampled data.

Series (Year)	Line Number	ExtRes25					ExtRes12				
		Line Mean (log$_{10}$ (Ωm))	Series Mean (log$_{10}$ (Ωm))	Series SD (log$_{10}$ (Ωm))	All Lines Mean (log$_{10}$ (Ωm))	All Lines SD (log$_{10}$ (Ωm))	Line Mean (log$_{10}$ (Ωm))	Series Mean (log$_{10}$ (Ωm))	Series SD (log$_{10}$ (Ωm))	All Lines Mean (log$_{10}$ (Ωm))	All Lines SD (log$_{10}$ (Ωm))
2018	L2060010.18	2.6278	2.5889	0.0282	2.5632	0.0703	2.3819	2.4788	0.0839	2.5274	0.0563
	L2060110.18	2.5748					2.4366				
	L2060011.18	2.5629					2.5602				
	L2060111.18	2.5900					2.5363				
2019	L2060000.19	2.5277	2.4863	0.0598			2.5209	2.5017	0.0678		
	L2060100.19	2.4950					2.4853				
	L2060001.19	2.5232					2.4193				
	L2060101.19	2.3992					2.5815				
2020	L2060010.20	2.5511	2.6383	0.0645			2.5387	2.5760	0.0406		
	L2060110.20	2.7062					2.5469				
	L2060011.20	2.6548					2.5936				
	L2060111.20	2.6410					2.6249				
2021.1	L2060010.21	2.4693	2.5175	0.0447			2.5350	2.5609	0.0475		
	L2060110.21	2.5773					2.5072				
	L2060011.21	2.5081					2.6060				
	L2060111.21	2.5154					2.5952				
2021.2	L2060020.21	2.5786	2.5851	0.0298			2.4866	2.5195	0.0464		
	L2060120.21	2.6027					2.5876				
	L2060021.21	2.5460					2.4946				
	L2060121.21	2.6132					2.5092				

Series (Year)	Line Number	ExtRes3					ExtRes09				
		Line Mean (log$_{10}$ (Ωm))	Series Mean (log$_{10}$ (Ωm))	Series SD (log$_{10}$ (Ωm))	All Lines Mean (log$_{10}$ (Ωm))	All Lines SD (log$_{10}$ (Ωm))	Line Mean (log$_{10}$ (Ωm))	Series Mean (log$_{10}$ (Ωm))	Series SD (log$_{10}$ (Ωm))	All Lines Mean (log$_{10}$ (Ωm))	All Lines SD (log$_{10}$ (Ωm))
2018	L2060010.18	2.2883	2.3361	0.0966	2.2708	0.1194	1.8738	2.0777	0.1963	2.0289	0.1352
	L2060110.18	2.2549					2.0290				
	L2060011.18	2.3270					2.3449				
	L2060111.18	2.4740					2.0630				
2019	L2060000.19	2.2457	2.2505	0.0659			2.2468	2.1039	0.0953		
	L2060100.19	2.1685					2.0592				
	L2060001.19	2.2586					2.0551				
	L2060101.19	2.3293					2.0543				
2020	L2060010.20	2.3865	2.3019	0.1298			2.2898	2.0656	0.1572		
	L2060110.20	2.3637					1.9361				
	L2060011.20	2.3486					2.0542				
	L2060111.20	2.1086					1.9824				
2021.1	L2060010.21	2.3022	2.2414	0.1502			1.9451	1.9428	0.1245		
	L2060110.21	2.3334					2.1177				
	L2060011.21	2.3131					1.8447				
	L2060111.21	2.0169					1.8635				
2021.2	L2060020.21	2.1081	2.2239	0.1447			1.9182	1.9546	0.0250		
	L2060120.21	2.1389					1.9656				
	L2060021.21	2.2194					1.9604				
	L2060121.21	2.4293					1.9743				

Table 5.2. HEM Resistivity models. Summary of mean $\log_{10}$ resistivity ('Line Mean') for each repeat flight for all frequencies. Also shown are mean and standard deviation (SD) of the four mean values for each series of flights and of the twenty mean values for all flights. Data used are the 1 m re-sampled data.

Series (Year)	Line Number	HEMRes25					HEMRes12				
		Line Mean ($\log_{10}$ (Ωm))	Series Mean ($\log_{10}$ (Ωm))	Series SD ($\log_{10}$ (Ωm))	All Lines Mean ($\log_{10}$ (Ωm))	All Lines SD ($\log_{10}$ (Ωm))	Line Mean ($\log_{10}$ (Ωm))	Series Mean ($\log_{10}$ (Ωm))	Series SD ($\log_{10}$ (Ωm))	All Lines Mean ($\log_{10}$ (Ωm))	All Lines SD ($\log_{10}$ (Ωm))
2018	L2060010.18	2.4691	2.5222	0.0451	2.4761	0.0837	2.3745	2.4210	0.0329	2.4271	0.0773
	L2060110.18	2.5020					2.4523				
	L2060011.18	2.5685					2.4292				
	L2060111.18	2.5493					2.4278				
2019	L2060000.19	2.4635	2.4890	0.0674			2.3897	2.3838	0.0146		
	L2060100.19	2.5886					2.3795				
	L2060001.19	2.4393					2.3658				
	L2060101.19	2.4644					2.4000				
2020	L2060010.20	2.5350	2.5759	0.0300			2.4672	2.4972	0.0427		
	L2060110.20	2.6066					2.4543				
	L2060011.20	2.5849					2.5283				
	L2060111.20	2.5771					2.5392				
2021.1	L2060010.21	2.3975	2.3970	0.0286			2.4614	2.4899	0.0535		
	L2060110.21	2.4358					2.4310				
	L2060011.21	2.3679					2.5183				
	L2060111.21	2.3869					2.5490				
2021.2	L2060020.21	2.4152	2.3964	0.0247			2.3182	2.3437	0.0846		
	L2060120.21	2.3959					2.4665				
	L2060021.21	2.3617					2.2723				
	L2060121.21	2.4128					2.3180				

Series (Year)	Line Number	HEMRes3					HEMRes09				
		Line Mean ($\log_{10}$ (Ωm))	Series Mean ($\log_{10}$ (Ωm))	Series SD ($\log_{10}$ (Ωm))	All Lines Mean ($\log_{10}$ (Ωm))	All Lines SD ($\log_{10}$ (Ωm))	Line Mean ($\log_{10}$ (Ωm))	Series Mean ($\log_{10}$ (Ωm))	Series SD ($\log_{10}$ (Ωm))	All Lines Mean ($\log_{10}$ (Ωm))	All Lines SD ($\log_{10}$ (Ωm))
2018	L2060010.18	2.4391	2.4954	0.0833	2.4335	0.0958	2.3014	2.3735	0.0870	2.2320	0.1131
	L2060110.18	2.4186					2.3207				
	L2060011.18	2.5240					2.4947				
	L2060111.18	2.5999					2.3773				
2019	L2060000.19	2.3698	2.3932	0.0401			2.3309	2.2361	0.0635		
	L2060100.19	2.3779					2.1972				
	L2060001.19	2.3720					2.2085				
	L2060101.19	2.4531					2.2077				
2020	L2060010.20	2.4857	2.4933	0.0574			2.3350	2.2711	0.0891		
	L2060110.20	2.4783					2.1493				
	L2060011.20	2.5730					2.2599				
	L2060111.20	2.4361					2.3400				
2021.1	L2060010.21	2.4203	2.4315	0.0574			2.1856	2.1339	0.0719		
	L2060110.21	2.5081					2.1957				
	L2060011.21	2.4287					2.1129				
	L2060111.21	2.3691					2.0412				
2021.2	L2060020.21	2.2211	2.3539	0.1396			2.0792	2.1454	0.0464		
	L2060120.21	2.3458					2.1849				
	L2060021.21	2.3002					2.1673				
	L2060121.21	2.5486					2.1503				

Line-mean resistivity versus line-mean clearance

As remarked in Section 3.1 in considering intra-series variation, an antithetic (inverse) relationship is often, but not always, observed between the line-mean EM response amplitudes and the line-mean flight clearances (Figures 3.1 and 3.3), with lower mean response amplitudes corresponding with higher mean clearances. If the effect of flight clearance variation on the EM response amplitudes is *not* removed in the resistivity modelling, a sympathetic relationship would be expected between the line-mean resistivities and the line-mean flight clearances, with higher mean resistivities corresponding with higher mean clearances. In comparing line-mean resistivities (Figures 5.9 to 5.11) with line-mean clearances (Figure 5.12) it is apparent, with few exceptions, that no sympathetic relationship exists between the two parameters and, therefore, that the effect of flight clearance variation on the EM responses has largely been removed in the resistivity modelling. Cross-plots of line-mean resistivity versus line-mean clearance shown in Figure 5.13 are characterised by scattered data for each series of four repeat flights and for all EM frequencies, confirming little coherence between the two parameters. Illustrative linear trendlines shown for each series have very low R^2 (coefficient of determination) values, generally << 0.2, supporting the absence of any meaningful (linear) trend between the parameters. There are two instances where a moderate sympathetic relationship is apparent between line-mean resistivity and line-mean clearance in Figures 5.9 to 5.11 and where a linear trendline in the cross-plots of Figure 5.13 is characterised by a positive slope and $R^2 > 0.5$: (i) 2021.1 series, 12 kHz, Extended Resistivity models, with $R^2 = 0.84$ and HEM resistivity models, with $R^2 = 0.55$, and (ii) 2020 series, 3 kHz, HEM resistivity model, with $R^2 = 0.72$. These trends are nevertheless weak, and no causal relationship between clearance and resistivity is necessarily implied by the data.

Line-mean resistivity versus line-mean temperature

In considering intra-series variation in line mean temperature, it was observed previously (in Section 3.1) that flight-series (of four flights) with positive gradient trendlines in cross-plots of mean EM response amplitude versus mean temperature (Figure 3.7) generally correspond with negative gradient trendlines in cross-plots of mean EM response amplitude versus mean clearance (Figure 3.4) – with the correspondence accounted for, within each flight-series, by lower mean temperatures being associated with higher mean clearances (i.e., negative gradient trendlines in the mean clearance versus mean temperature cross-plot of Figure 3.6). The difficulty in separating out the effects of temperature and clearance on the mean EM responses is ameliorated in the resistivity model data, where the effects of flight clearance variation have largely been removed, as discussed above. Cross-plots of mean resistivity versus mean temperature (Figure 5.14) are characterised by tight data clusters within each flight-series at 12 and 25 kHz, with no consistent or discernible trends apparent. While the data clusters are more dispersed in the cases of the 0.9 and 3 kHz resistivity models, inferred to be due to the impact of cultural noise of the line-mean resistivities, there are similarly no consistent trends apparent in the relationship between resistivity and temperature within each flight-series.

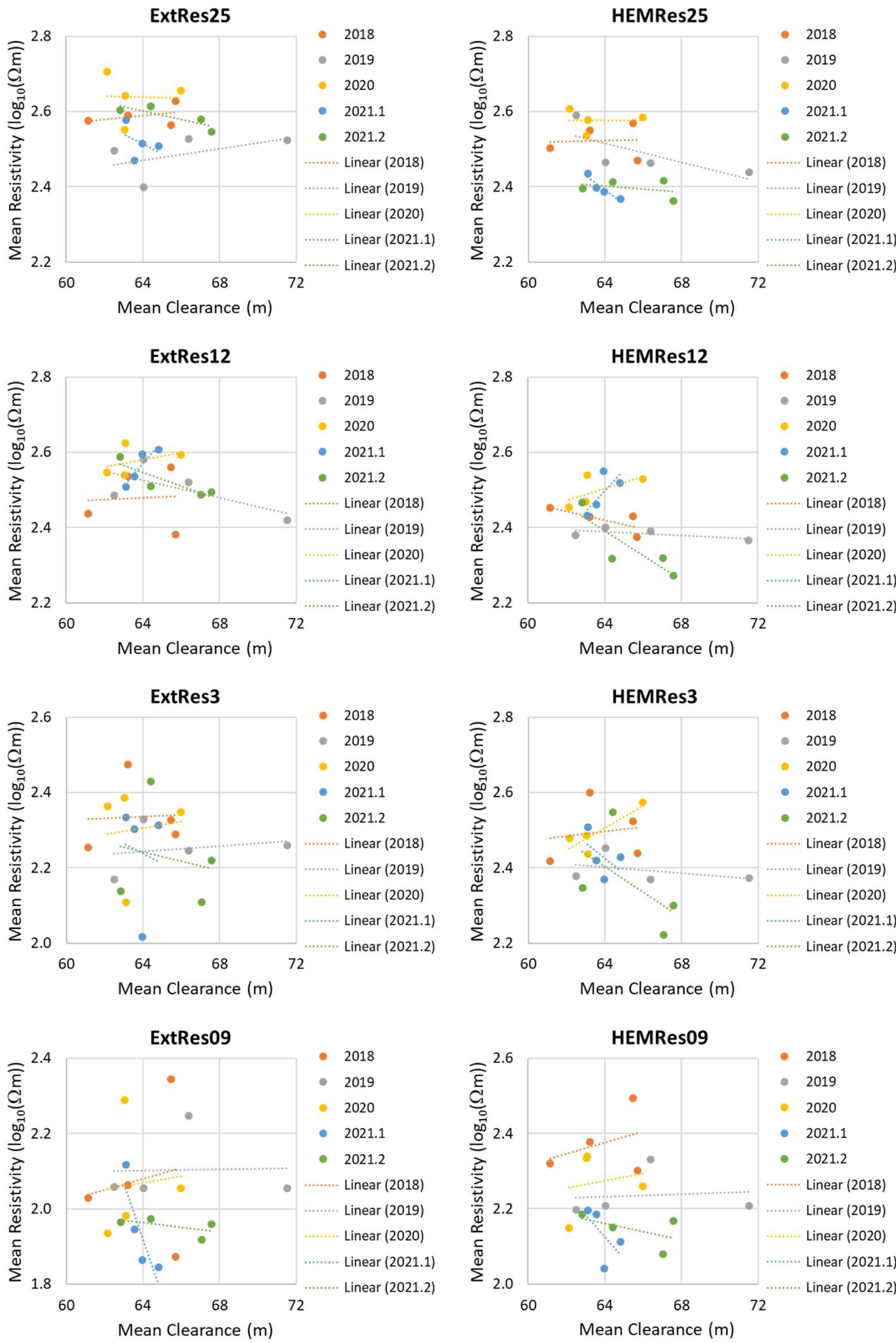

Figure 5.13: Cross-plots of mean resistivity (log_{10}) versus mean flight clearance for each repeat flight-line, colour coded by flight-series (year). Four panels to left show Extended Resistivity models at each frequency, four panels to right show HEM Resistivity models. Note change in minimum and maximum values on vertical axes from plot to plot, with constant dynamic range of 0.6 $log_{10}(\Omega.m)$ for all plots. A linear trendline is shown for illustrative purposes in the cross-plots for each flight-series (consisting of four repeat flight-lines).

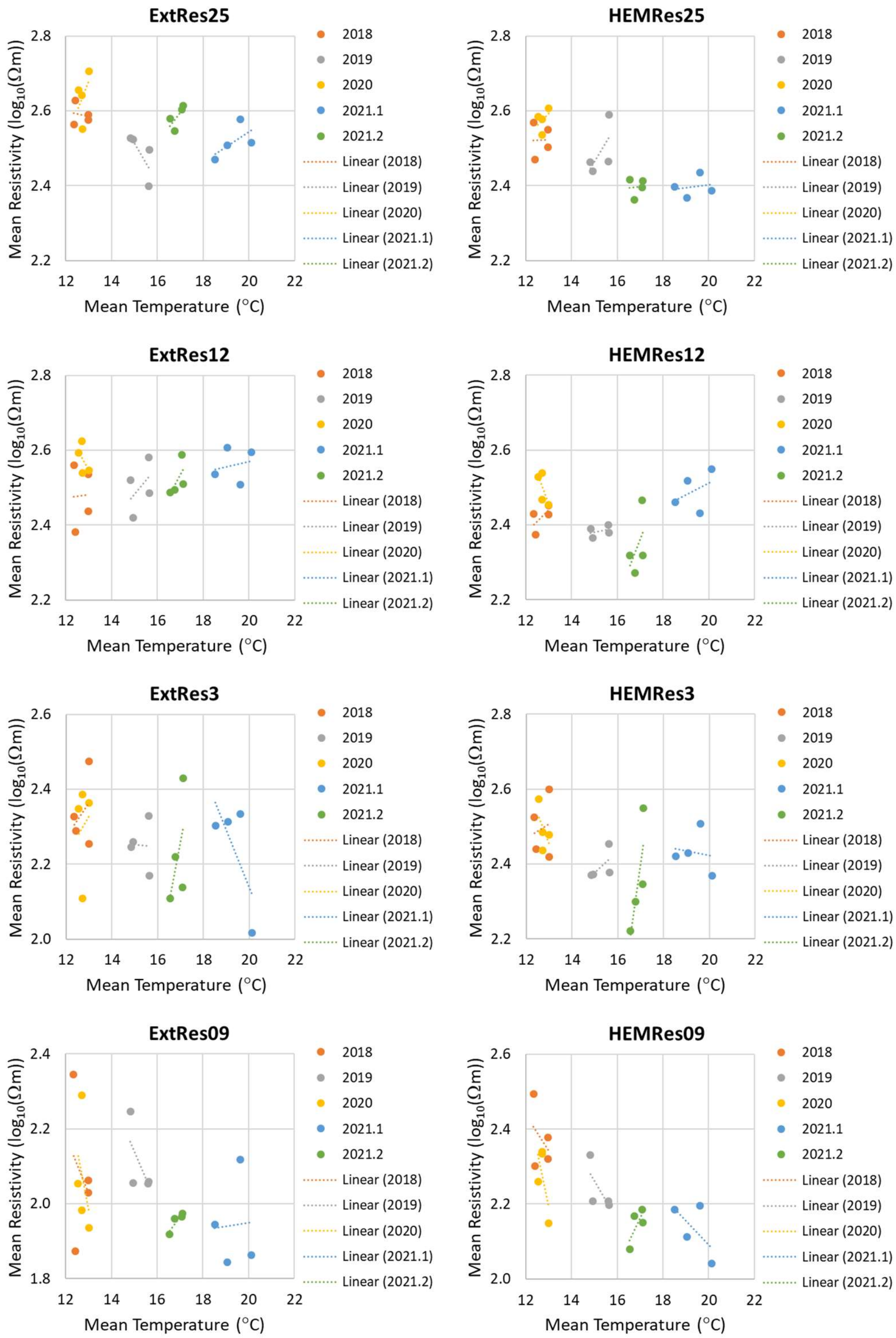

Figure 5.14: Cross-plots of mean resistivity (log$_{10}$) versus mean temperature for each repeat flight-line, colour coded by flight-series (year). Four panels to left show Extended Resistivity models at each frequency, four panels to right show HEM Resistivity models. Note change in minimum and maximum values on vertical axes from plot to plot, with constant dynamic range of 0.6 log$_{10}$(Ω.m) for all plots. A linear trendline is shown for illustrative purposes in the cross-plots for each flight-series (consisting of four repeat flight-lines).

The inter-series variation apparent in the mean EM response amplitude versus mean temperature cross-plots examined previously (in Figure 3.7) generally does not define any systematic relationship between the two parameters from series-to-series. The one exception observed is in the 25 kHz in-phase (P25lev) data, where a trend of increasing EM response amplitudes with increasing temperature from series-to-series is apparent. Similar to the EM response amplitudes, the line-mean resistivity versus line-mean temperature cross-plots of Figure 5.14 show no consistent and systematic relationship between the two parameters from series-to-series, with the exception, again, of the 25 kHz resistivity model data, where series with higher mean resistivities appear to be associated with lower mean temperatures. The 25 kHz cross-plots (for both the Extended Resistivity and HEM resistivity model data) may reflect real shallow subsurface resistivity and hydrogeological variation from series-to-series, with series-to-series temperature variation being a proxy for time-of-year, seasonal and/or rainfall variation.

Line-mean resistivities are plotted against the month-of-year for each series of data acquisition in Figure 5.15. The two lower-temperature series of 2018 and 2020, corresponding with higher mean resistivities at 25 kHz (Figure 5.14), were acquired during April and October respectively. MET Éireann monthly rainfall data for the years 2019 – 2021, available online for two rainfall stations closest to the test-line, are plotted in Figure 5.16. The total monthly rainfall for each flight-series is annotated in Figure 5.16 (note that the '2018' flight-series was flown in 2019 on 22nd April). The higher total rainfall recorded in April 2019 (2018 flight-series) and in October 2020 (2020 series) would appear, superficially at least, to be inconsistent with the higher 25 kHz resistivities of the 2018 and 2020 flight-series – as higher water-saturation levels in the shallow subsurface or a shallower water table, during higher rainfall periods, might be expected to lead to lower resistivities. Similarly, the lower 25 kHz line-mean resistivities of the 2019, 2021.1 and 2021.2 flight-series appear inconsistent with the generally lower monthly rainfall recorded during the months of July (particularly) and September.

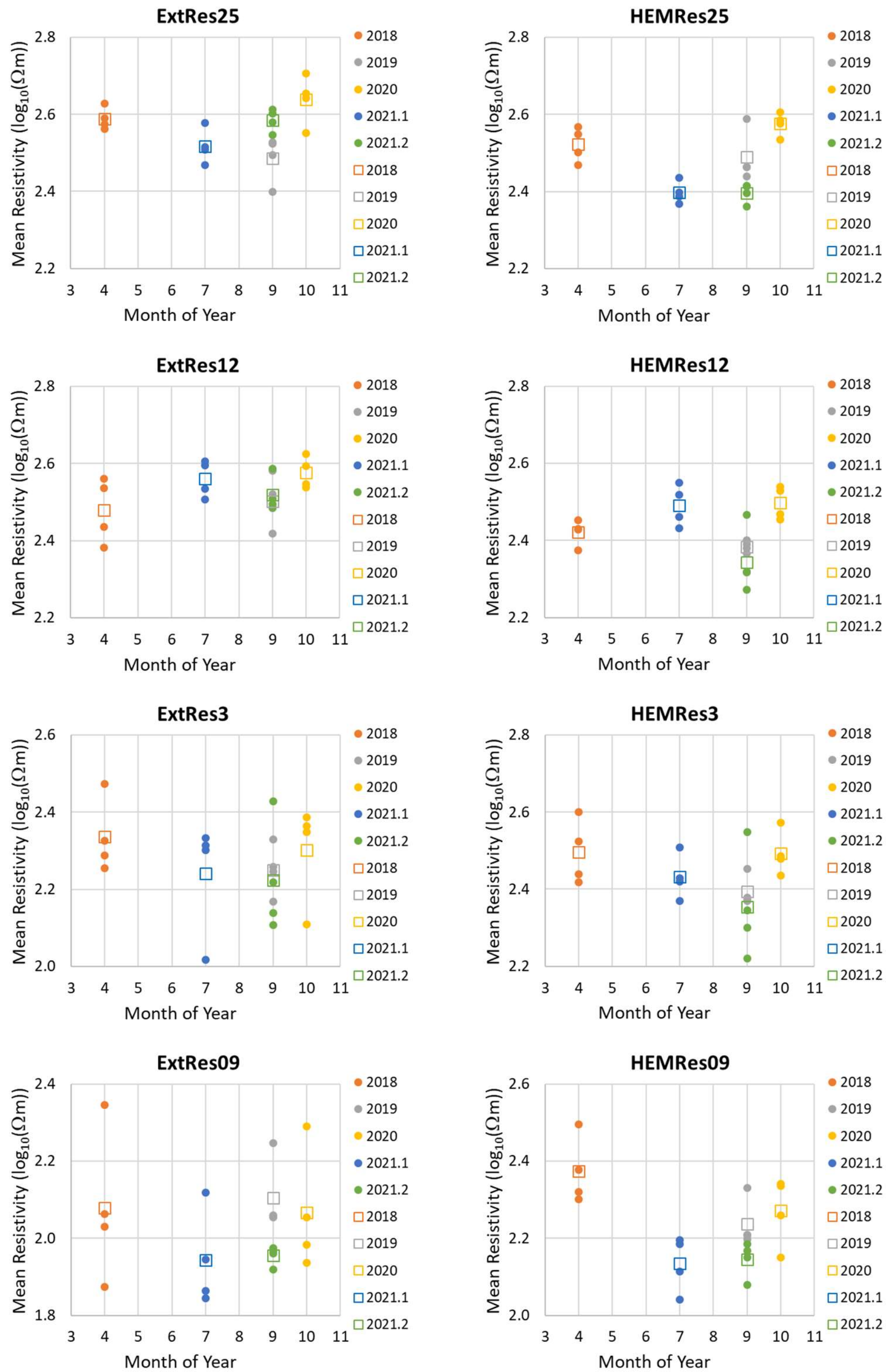

Figure 5.15: Cross-plots of mean resistivity ($\log_{10}$) versus month of year for each repeat flight-line, colour coded by flight-series (year). Square symbols for each series indicate the mean resistivity for all four repeat flights. Four panels to left show Extended Resistivity models at each frequency, four panels to right show HEM Resistivity models. Note changes in minimum and maximum values on vertical axes from plot to plot, with constant dynamic range of 0.6 $\log_{10}(\Omega.m)$ for all plots.

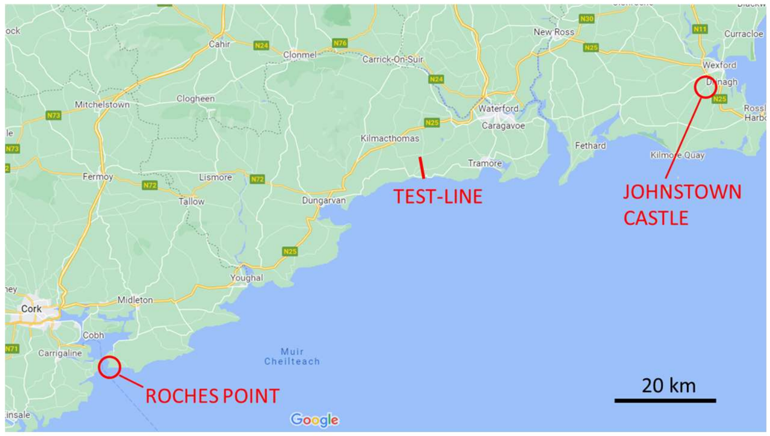

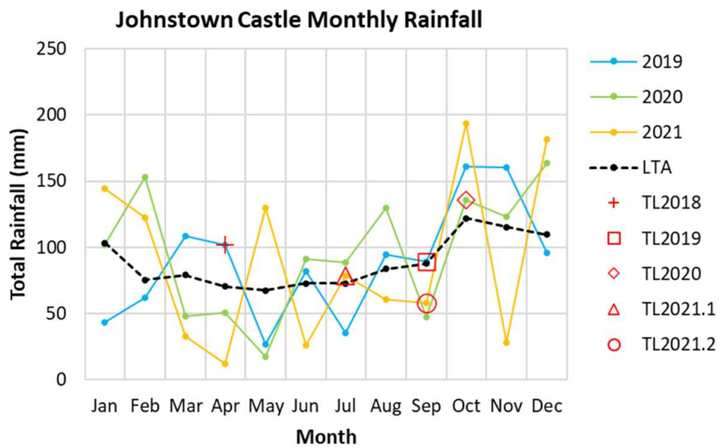

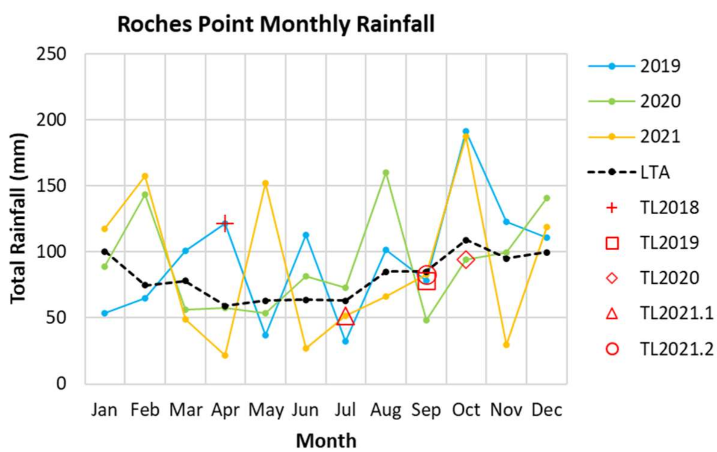

Figure 5.16: Monthly rainfall records for 2019 – 2021 from Johnstown Castle and Roche Point stations (from MET Éireann available monthly data, https://www.met.ie/climate/available-data/monthly-data). (Top) Rainfall station locations. (Middle) Johnstown Castle station, total monthly rainfall by month. (Bottom) Roches Point station, total monthly rainfall by month. Open red symbols indicate rainfall for the year and month of each of the test-line series flown (prefix 'TL' in legend). LTA is the long-term rainfall average, 1981 – 2010, at each rainfall station. Note that the '2018' series was flown in 2019 on 22nd April.

Higher temporal resolution (e.g., daily) rainfall data, if available on request from MET Éireann, might be used more fruitfully to examine the rainfall in the days or weeks immediately prior the acquisition of each test-line flight-series. However, whether the differences observed between the resistivity means of the five flight-series are statistically significant, and potentially indicative of seasonal variation, will require the application of appropriate statistical tests (for example, a t-test). Such tests are, however, beyond the scope of the current analysis. It is unlikely that variation in the mean resistivities of the 0.9 and 3 kHz data will provide any insights into potential deeper-subsurface, seasonal hydrogeological variation given the significant impact of variable cultural noise levels on the mean resistivities at these frequencies.

5.4.2 Along-line variability in resistivity models

Figures 5.17 – 5.22 provide a catalogue of summary plots of the variability in the Extended Resistivity and HEM resistivity models along the test-line, for all twenty lines together and for each series of four lines separately. All four EM frequencies are shown together in the figures. For comparison, plots of the variability in the recorded EM in-phase and quadrature responses are also shown in the figures.

The behaviour of the variability observed in the resistivity models in the 12 and 25 kHz data is distinctly different from that of the 0.9 and 3 kHz data. In the case of the 12 and 25 kHz data, the variability in the original EM responses, ascribed primarily to flight clearance variation, is significantly reduced in the resistivity models. In the case of the 0.9 and 3 kHz data, the high-amplitude variability peaks present in the EM responses (labelled N1 to N9 in the figures), ascribed to cultural noise variation, are carried through into the resistivity models. Peaks in variability in the 0.9 and 3 kHz resistivity models are located primarily over resistive terrain found at the northern and southern ends of the test line, as well as towards the middle of the test-line. The high variability peaks visible in the 0.9 and 3 kHz resistivity models are generally not apparent in the 12 and 25 kHz models, except for a few moderate increases in variability in the 12 kHz models at coincident locations (e.g., location N9, particularly in the Extended Resistivity models).

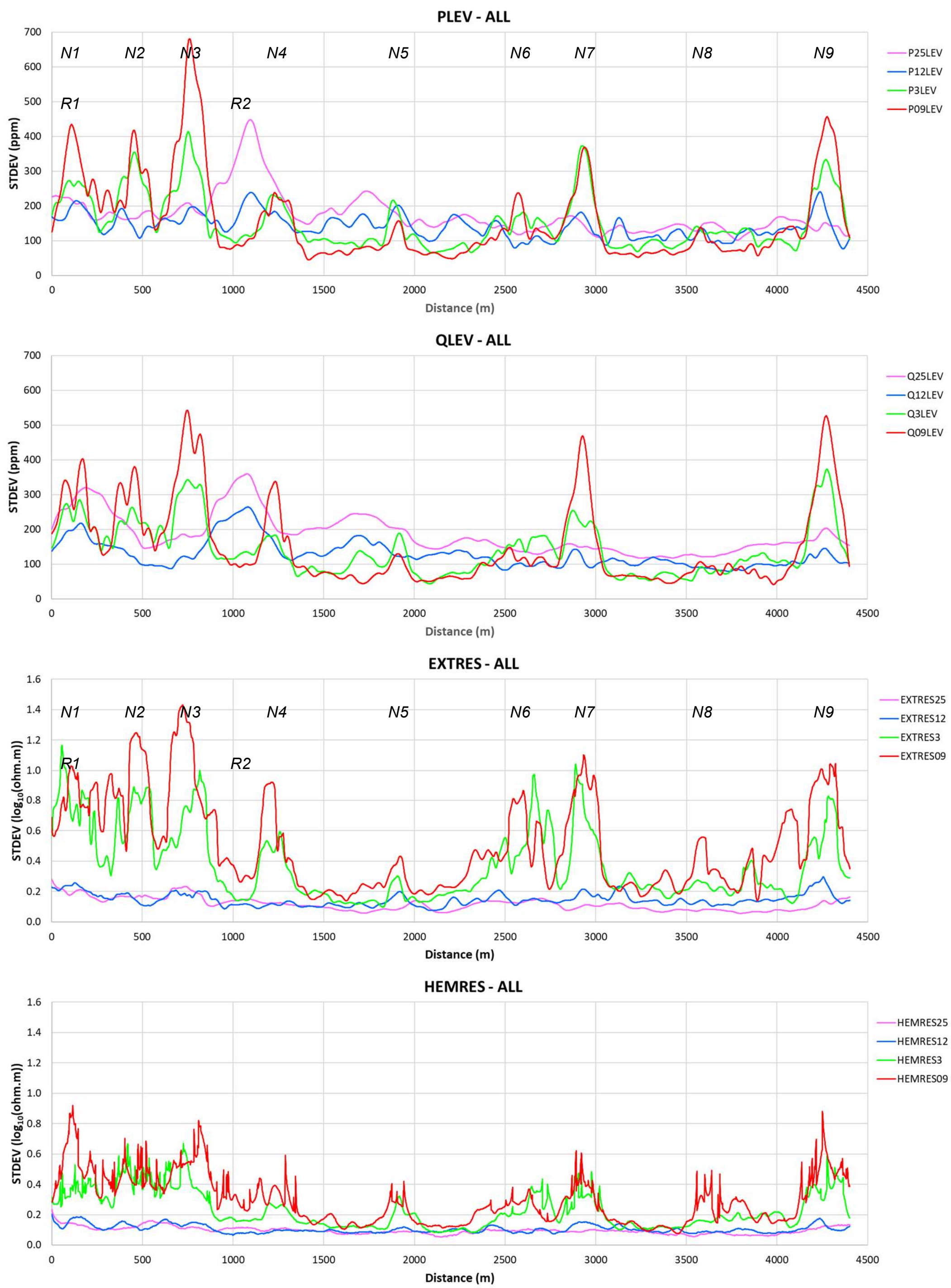

Figure 5.17: Summary of single-frequency resistivity model variability <u>for all twenty lines</u>. Standard deviation of the mean for twenty repeat lines, plotted against distance along the test-line, for (top panel) in-phase data (Plev data channels), (second panel) quadrature data (Qlev data channels), (third panel) Extended Resistivity models and (bottom panel) HEM Resistivity models. Location of standard deviation (STDEV) peaks in 3 and 0.9 kHz EM data (N1 to N9) and in clearance data (R1 and R2) annotated in top and third panels.

Figure 5.18: Summary of single-frequency resistivity model variability for <u>2018 series of lines</u>. Standard deviation of the mean for four repeat lines, plotted against distance along the test-line, for (top panel) in-phase data (Plev data channels), (second panel) quadrature data (Qlev data channels), (third panel) Extended Resistivity models and (bottom panel) HEM Resistivity models. Location of standard deviation (STDEV) peaks in 3 and 0.9 kHz EM data (N1 to N9) and in clearance data (R1 and R2) annotated in top and third panels.

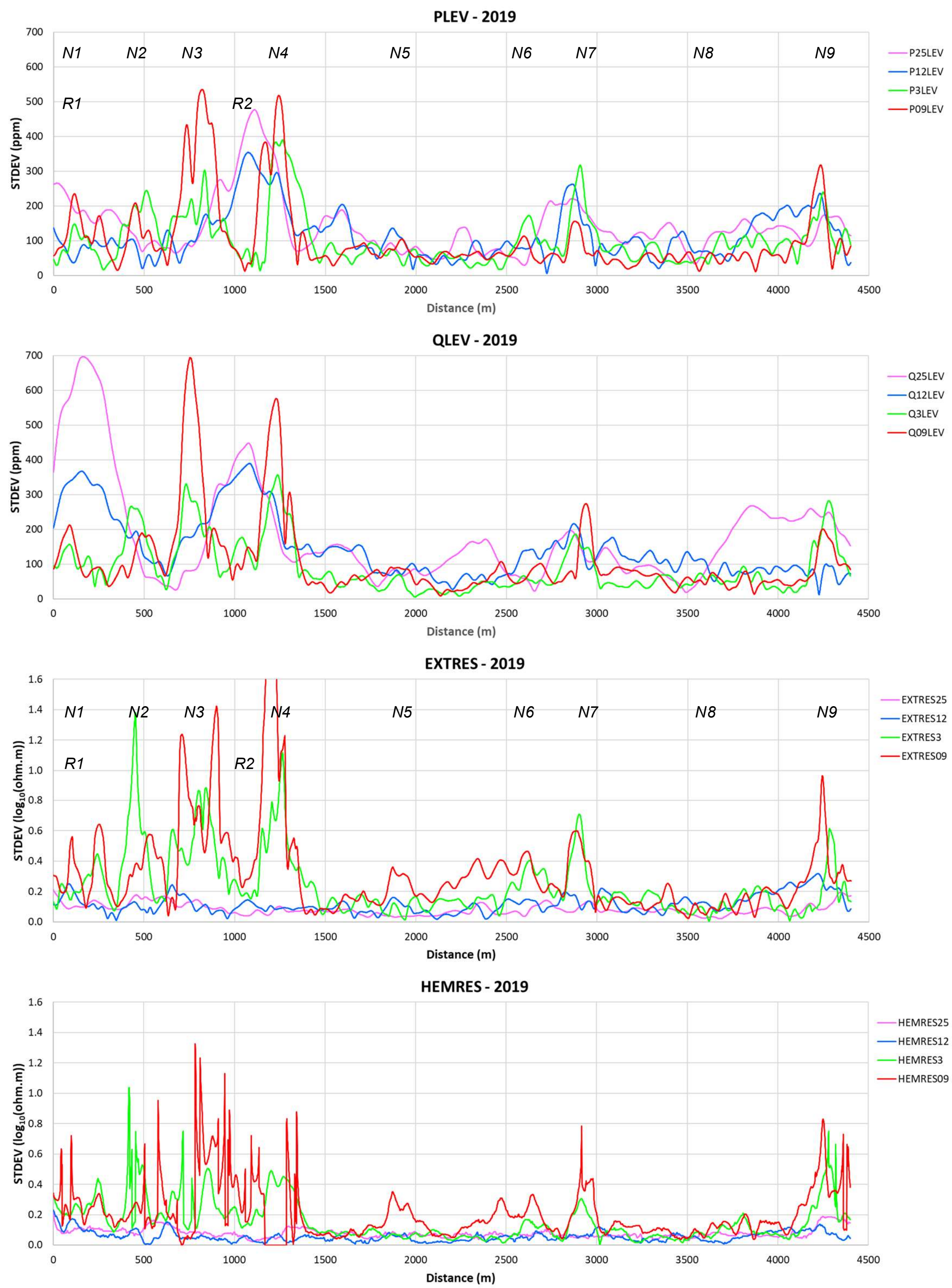

Figure 5.19: Summary of single-frequency resistivity model variability for <u>2019 series of lines</u>. Standard deviation of the mean for four repeat lines, plotted against distance along the test-line, for (top panel) in-phase data (Plev data channels), (second panel) quadrature data (Qlev data channels), (third panel) Extended Resistivity models and (bottom panel) HEM Resistivity models. Location of standard deviation (STDEV) peaks in 3 and 0.9 kHz EM data (N1 to N9) and in clearance data (R1 and R2) annotated in top and third panels.

Figure 5.20: Summary of single-frequency resistivity model variability for <u>2020 series of lines</u>. Standard deviation of the mean for four repeat lines, plotted against distance along the test-line, for (top panel) in-phase data (Plev data channels), (second panel) quadrature data (Qlev data channels), (third panel) Extended Resistivity models and (bottom panel) HEM Resistivity models. Location of standard deviation (STDEV) peaks in 3 and 0.9 kHz EM data (N1 to N9) and in clearance data (R1 and R2) annotated in top and third panels.

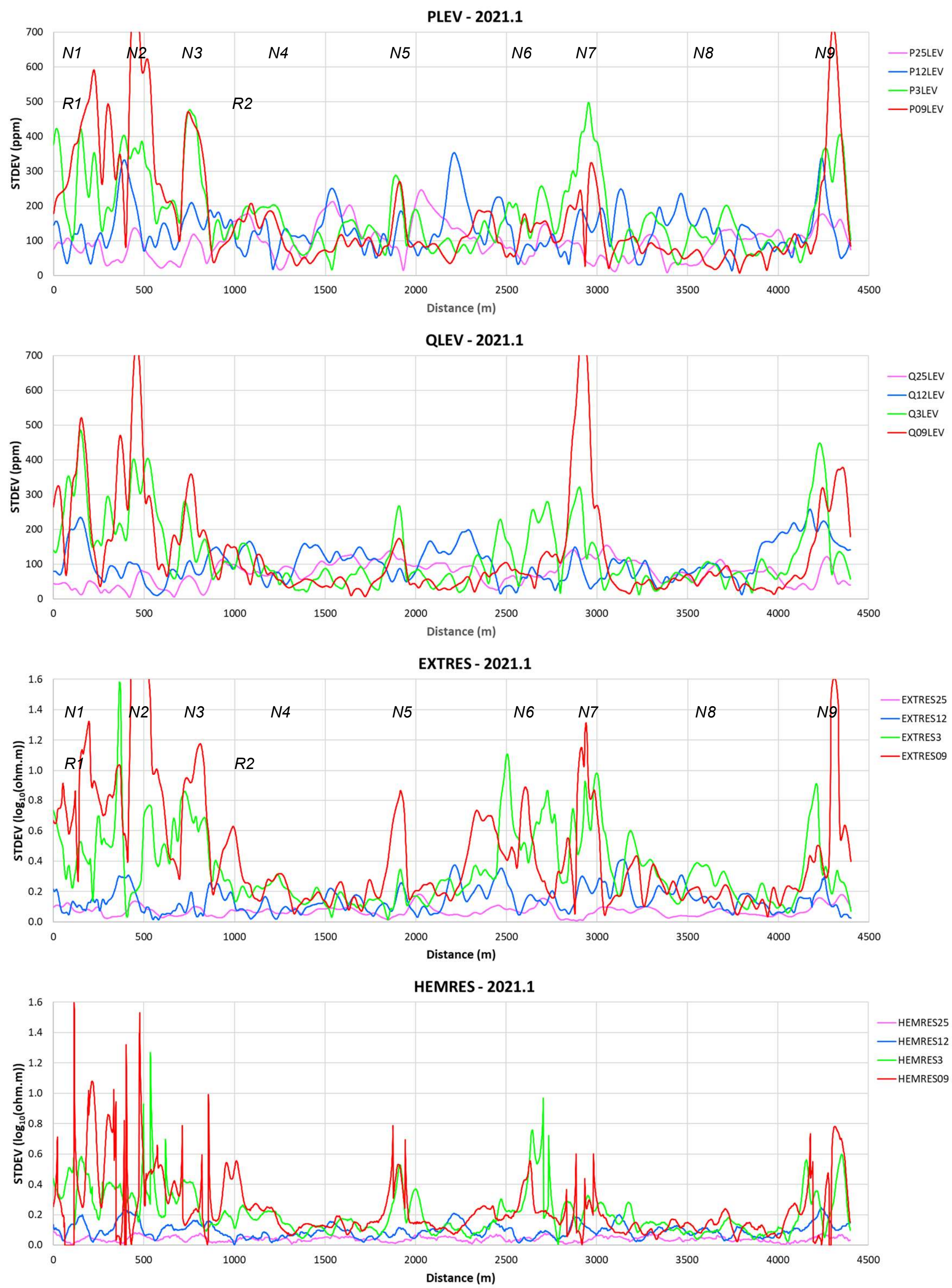

Figure 5.21: Summary of single-frequency resistivity model variability for <u>2021.1 series of lines</u>. Standard deviation of the mean for four repeat lines, plotted against distance along the test-line, for (top panel) in-phase data (Plev data channels), (second panel) quadrature data (Qlev data channels), (third panel) Extended Resistivity models and (bottom panel) HEM Resistivity models. Location of standard deviation (STDEV) peaks in 3 and 0.9 kHz EM data (N1 to N9) and in clearance data (R1 and R2) annotated in top and third panels.

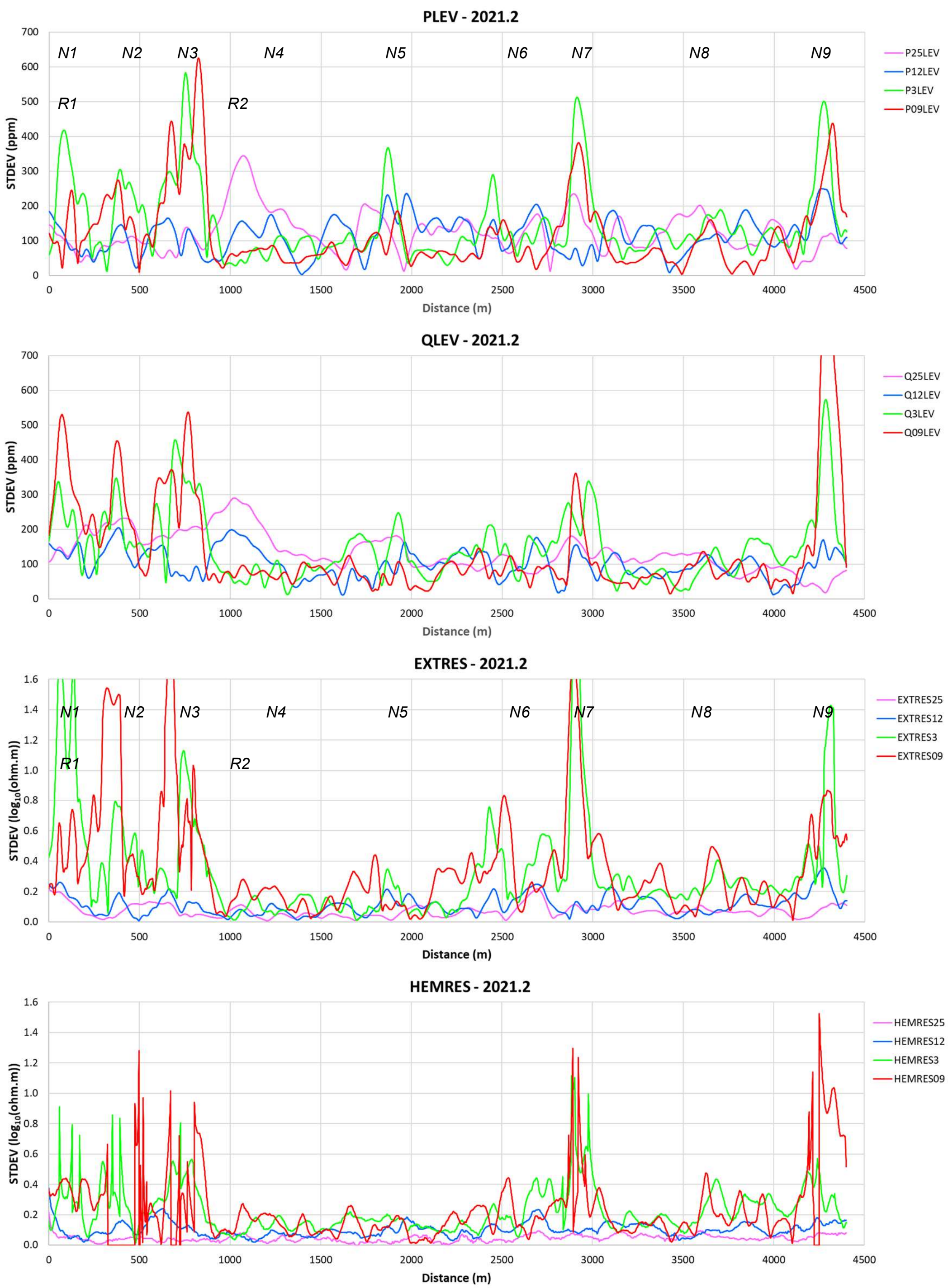

Figure 5.22: Summary of single-frequency resistivity model variability for <u>2021.2 series of lines</u>. Standard deviation of the mean for four repeat lines, plotted against distance along the test-line, for (top panel) in-phase data (Plev data channels), (second panel) quadrature data (Qlev data channels), (third panel) Extended Resistivity models and (bottom panel) HEM Resistivity models. Location of standard deviation (STDEV) peaks in 3 and 0.9 kHz EM data (N1 to N9) and in clearance data (R1 and R2) annotated in top and third panels.

As the variability in the 12 and 25 kHz resistivity models appears relatively weakly affected by cultural noise, in comparison with the lower frequencies, it may provide a reasonable basis for estimating the uncertainties present in the resistivity models, i.e., the uncertainty in measuring the resistivity of the subsurface (at 12 and 25 kHz). As the swath widths of the four repeat flights flown during each of the five series are small, in both inline and transverse directions, compared with the EM footprint (as discussed in Section 2.4), each repeat flight should be sensitive to the 'same' geological structure, with the mean of the four flights providing the best estimate of the 'real' resistivity structure at each location.

At 25 kHz, the mean standard deviations (Tables 5.3 and 5.4) for the five four-flight series lie in the range 0.07 – 0.11 $\log_{10}(\Omega.m)$ for the Extended Resistivity Models and 0.04 – 0.08 $\log_{10}(\Omega.m)$ for the HEM resistivity models. At 12 kHz, the mean standard deviations for the five four-flight series lie in the range 0.11 – 0.15 $\log_{10}(\Omega.m)$ for the Extended Resistivity Models and 0.06 – 0.10 $\log_{10}(\Omega.m)$ for the HEM resistivity models.

While the standard deviations (*SD*) reflect the size of the dispersion of the resistivity dataset around the mean value, a better estimate of the uncertainties in the measurement of resistivity may be provided by the standard error of the mean ($SEM = SD/\sqrt{N}$, where N is the sample size), which measures how far the mean of the recorded data is likely to be from the true population mean (or real ground resistivity). As $\sqrt{N} = 2$ for each of the four-flight series, the **standard errors of the mean** for the flight-series are as follows:

- For 25 kHz, the mean standard errors for the four-flight series lie in the range 0.04 – 0.06 $\log_{10}(\Omega.m)$ for the Extended Resistivity Models and 0.02 – 0.04 $\log_{10}(\Omega.m)$ for the HEM resistivity models.

- For 12 kHz, the mean standard errors for the four-flight series lie in the range 0.06 – 0.08 $\log_{10}(\Omega.m)$ for the Extended Resistivity Models and 0.03 – 0.05 $\log_{10}(\Omega.m)$ for the HEM resistivity models.

The lowest standard error of the mean of 0.02 $\log_{10}(\Omega.m)$ corresponds with an error of 4.7 Ω.m at 100 Ω.m and 47 Ω.m at 1000 Ω.m, or approximately 5%. The highest standard error of the mean of 0.08 $\log_{10}(\Omega.m)$ corresponds with an error of 20 Ω.m at 100 Ω.m and 202 Ω.m at 1000 Ω.m, or approximately 20%. A similar error analysis would not be (geologically) meaningful for the 0.9 and 3 kHz resistivity model solutions. As many of the resistivity solutions in the 0.9 and 3 kHz EM data reflect the amplitude of the cultural EM noise signal, rather than the amplitude of the geological EM response, particularly in high-resistivity areas, the calculated mean resistivity values do not closely approximate the 'real' subsurface resistivity structure. The standard deviations and standard errors of the mean, therefore, do not reflect an uncertainty in estimating the geological resistivity structure, but rather reflect the variability in the cultural noise signal.

Table 5.3: Mean Extended Resistivity model variability (standard deviation), by series and for all twenty lines.

<table>
<tr><th rowspan="2">Series (Year)</th><th rowspan="2">Line Number</th><th colspan="2">ExtRes25</th><th colspan="2">ExtRes12</th><th colspan="2">ExtRes3</th><th colspan="2">ExtRes09</th></tr>
<tr><th>Mean SD All (log10 (Ωm))</th><th>Mean SD Series (log10 (Ωm))</th><th>Mean SD All (log10 (Ωm))</th><th>Mean SD Series (log10 (Ωm))</th><th>Mean SD All (log10 (Ωm))</th><th>Mean SD Series (log10 (Ωm))</th><th>Mean SD All (log10 (Ωm))</th><th>Mean SD Series (log10 (Ωm))</th></tr>
<tr><td rowspan="4">2018δ8</td><td>L2060010.18</td><td rowspan="20">0.1160</td><td rowspan="4">0.1025</td><td rowspan="20">0.1467</td><td rowspan="4">0.1337</td><td rowspan="20">0.3783</td><td rowspan="4">0.2618</td><td rowspan="20">0.5082</td><td rowspan="4">0.4285</td></tr>
<tr><td>L2060110.18</td></tr>
<tr><td>L2060011.18</td></tr>
<tr><td>L2060111.18</td></tr>
<tr><td rowspan="4">2019</td><td>L2060000.19</td><td rowspan="4">0.0820</td><td rowspan="4">0.1178</td><td rowspan="4">0.2423</td><td rowspan="4">0.3209</td></tr>
<tr><td>L2060100.19</td></tr>
<tr><td>L2060001.19</td></tr>
<tr><td>L2060101.19</td></tr>
<tr><td rowspan="4">2020</td><td>L2060010.20</td><td rowspan="4">0.1046</td><td rowspan="4">0.1268</td><td rowspan="4">0.4150</td><td rowspan="4">0.4955</td></tr>
<tr><td>L2060110.20</td></tr>
<tr><td>L2060011.20</td></tr>
<tr><td>L2060111.20</td></tr>
<tr><td rowspan="4">2021.1</td><td>L2060010.21</td><td rowspan="4">0.0704</td><td rowspan="4">0.1451</td><td rowspan="4">0.3531</td><td rowspan="4">0.4511</td></tr>
<tr><td>L2060110.21</td></tr>
<tr><td>L2060011.21</td></tr>
<tr><td>L2060111.21</td></tr>
<tr><td rowspan="4">2021.2</td><td>L2060020.21</td><td rowspan="4">0.0711</td><td rowspan="4">0.1124</td><td rowspan="4">0.3353</td><td rowspan="4">0.3671</td></tr>
<tr><td>L2060120.21</td></tr>
<tr><td>L2060021.21</td></tr>
<tr><td>L2060121.21</td></tr>
</table>

Figures 5.23 and 5.24 plot the mean resistivity model variability (standard deviation) for the test-line for each series of flights and, in the case of Figure 5.23, also for all twenty repeat flights. Results for both the Extended Resistivity and HEM resistivity models are shown. A few observations may be made:

i. Model variability increases with decreasing frequency – except for the HEM resistivity models for the 2018 and 2019 series, where the 12 kHz models are characterised by the lowest variability.

ii. The variability in the two lower frequency models (0.9 and 3 kHz) is significantly higher than in the two higher frequency models (12 and 25 kHz). There is some suggestion, particularly in the Extended Resistivity models, that the variability characteristics of the two frequency pairs are different and independent of each other and are the result of different factors or causes. For example, the sympathetic increase or decrease in the variability of the 0.9-3 kHz pair from series-to-series is mostly not shared with the 12-25 kHz pair.

It has already been observed in sections above that high and variable cultural EM noise levels appear to be the main control on the 0.9 and 3 kHz resistivity model variability. With the effect of EM noise being much lower in the 12 and 25 kHz frequencies, it may be the case that the variability in the resistivity models at these frequencies reflects the 'whole-system' measurement accuracy, which incorporates, for example, the system electronic noise, the accuracy of the zero level calibrations and drift corrections, the accuracy of the resistivity modelling methods and the extent to which flight clearance variation is accounted for in the modelling.

Table 5.4: Mean HEM resistivity model variability (standard deviation), by series and for all twenty lines.

Series (Year)	Line Number	HEMRes25		HEMRes12		HEMRes3		HEMRes09	
		Mean SD All ($\log_{10}$ (Ωm))	Mean SD Series ($\log_{10}$ (Ωm))	Mean SD All ($\log_{10}$ (Ωm))	Mean SD Series ($\log_{10}$ (Ωm))	Mean SD All ($\log_{10}$ (Ωm))	Mean SD Series ($\log_{10}$ (Ωm))	Mean SD All ($\log_{10}$ (Ωm))	Mean SD Series ($\log_{10}$ (Ωm))
2018	L2060010.18	0.0956	0.0684	0.1049	0.0600	0.2282	0.1567	0.2925	0.2201
	L2060110.18								
	L2060011.18								
	L2060111.18								
2019	L2060000.19		0.0776		0.0556		0.1559		0.2075
	L2060100.19								
	L2060001.19								
	L2060101.19								
2020	L2060010.20		0.0514		0.0704		0.2129		0.2178
	L2060110.20								
	L2060011.20								
	L2060111.20								
2021.1	L2060010.21		0.0395		0.0959		0.2135		0.2380
	L2060110.21								
	L2060011.21								
	L2060111.21								
2021.2	L2060020.21		0.0441		0.1013		0.2287		0.2384
	L2060120.21								
	L2060021.21								
	L2060121.21								

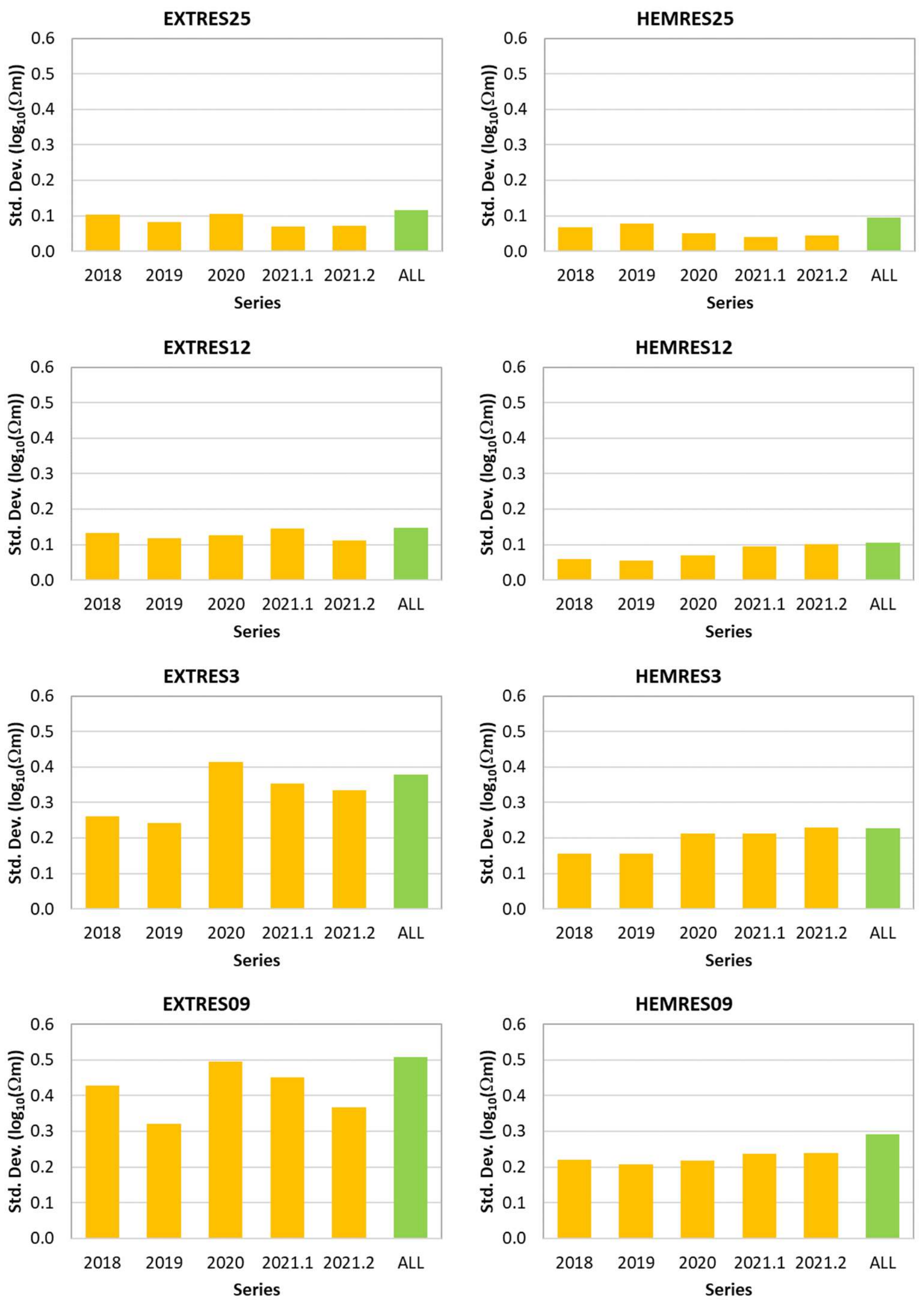

Figure 5.23: Four panels to left: Bar plots of mean data variability (standard deviation) for Extended Resistivity models, by series and for all twenty lines. Four panels to right: Bar plots of mean data variability (standard deviation) for HEM resistivity models, by series and for all twenty lines. Data plotted taken from Tables 5.3 and 5.4.

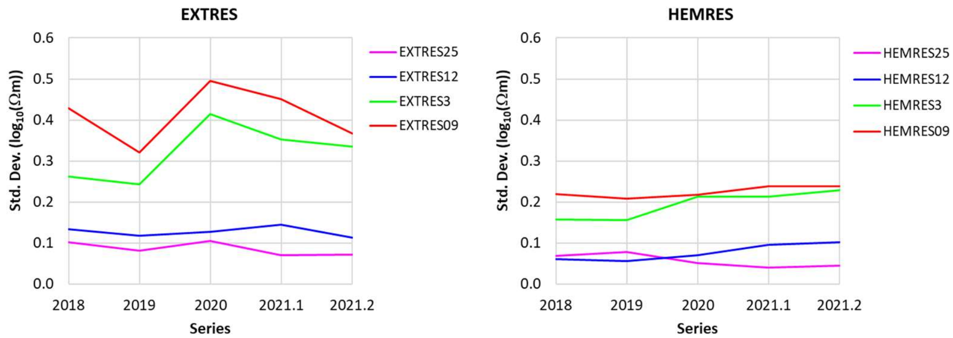

Figure 5.24: Plots of mean data variability (standard deviation) by series for (left) Extended Resistivity models and (right) for HEM resistivity models. Data plotted taken from Tables 5.3 and 5.4.

6 Variability in FEM 1-D Inversion Resistivity Models

As a further means of assessing the variability in the test-line FEM data, 1-D smooth, layered resistivity models have been computed by inversion using *aempy* software (Kiyan et al., 2022). Computed 1-D resistivity inversion models at each measurement location are gridded and plotted as 2-D resistivity cross-sections along the repeat flight-lines. Resistivity inversion cross-sections are presented here for all twenty repeat flights, using resistivity models derived from both the original FEM responses (the 'lev' data channels) (Figures 6.7 to 6.11) and the Npca1 filtered FEM responses (as described in Section 4) (Figures 6.12 to 6.16).

The inversion strategy and inversion parameters applied to the test-line data have followed those applied in the production inversion of the Tellus Waterford Block (GSI, 2020). Using the Waterford Block inversion parameters allows advantage to be taken of the pre-inversion parameter testing carried out prior to the Waterford Block inversions and also to allow direct comparison between the test-line inversions and the production inversions on adjacent flight lines (although this comparison is outside the scope of work reported on in this report).

2-D resistivity cross-sections are presented here with the purpose of facilitating a visual and qualitative assessment of the variability in the models. A quantitative assessment of the inversion models is beyond the current scope of work. Future quantitative assessment, of both the 'lev' and 'Npca1' resistivity models, might follow an analysis approach analogous to that applied to EM response data and the single frequency resistivity model data and might include:

i. <u>Assessment of variability in the model RMS errors</u>. Such analysis would help understand how the quality of the fit of the models to the observed data varies along the test-line.

ii. <u>Assessment of variability in the misfit between the observed data and the model predictions</u> (misfit = predicted response minus observed response), for all eight EM data components. Such analysis would help understand which data components are best and worst fit by the inversion modelling and how the size of the misfit and the variability in the misfit, for each data component, varies along the test-line.

iii. Assessment of the variability in the resistivity models themselves by examining the resistivity variability of, perhaps, the shallowest twenty-six depth layers (all < 100 m depth), or a smaller subset of these layers at selected depths (see Table 6.2 for a description of the layer-depth scheme). Such analysis would help understand which depth ranges in the models are subject to the least or most variability and how that variability varies along the test-line.

The *aempy* Toolbox was developed by Duygu Kiyan and Volker Rath at Dublin Institute for Advanced Studies during a GSI 'Short Call' funded research project (Kiyan and Rath, 2017; Kiyan et al., 2022). The Toolbox is a flexible, open-source package of software providing capacity for the 1-D inversion of frequency- and time-domain airborne EM data. The software is written in the *Python* language and calls on several numerical packages in *Python*, namely *numpy*, *scipy* and *matplotlib*. Capacities of the toolbox are implemented in a number of high-level scripts that cover a full EM inversion work-flow from (i) loading and reformatting of raw EM data, (ii) pre-processing of EM responses, (iii) inversion modelling and (iv) visualisation of outputs. *aempy* scripts were further modified by GSI to facilitate (i) automation of the process of running inversions on multiple flight lines, (ii) implementation of GSI's preferred production inversion strategy and (iii) output of the resistivity inversion models in a file format compatible with *Geosoft* software. *Geosoft* software has been used by GSI to 'clean' the inversion models by rejecting poor model solutions based on a number of QC criteria (although no model cleaning has been applied to the model results presented here) and to plot 2-D resistivity sections.

6.1 *aempy* 1-D Inversion Modelling Method

6.1.1 Tikhonov-type regularised 1-D layered inversion

The computational core of the Tikhonov-type 1-D layered inversion in *aempy* is based on an adapted forward modeller taken from the well-tested *AirBeo* open-source (*Fortran 90*) code. This code was originally developed by Australia's CSIRO and the AMIRA consortium (the latest version of which is available from https://sourceforge.net/projects/p223suite). The inversion code in *aempy* is customised for the physical configuration of the current

Tellus airborne FEM system: the AEM-05 system, which operates at four frequencies (912 Hz, 3005 Hz, 11962 Hz, and 24510 Hz), with vertical, co-planar transmitter and receiver coils (VCP or CpX configuration) mounted at the tips of the aircraft wings with fixed coil separations of 21.35 m for 912 and 3005 Hz and 21.38 m for 11962 and 24510 Hz.

Up to seven geophysical parameters can be included in the 1-D models for inversion: layer thickness, electrical resistivity, relative dielectric constant (although negligible for Tellus EM frequencies), relative magnetic permeability and three Cole-Cole induced polarisation (IP) parameters (chargeability, time constant and frequency constant). The Waterford test-line data presented here were inverted for a single parameter only, resistivity, using a fixed layer thicknesses and depth scheme for all sites (as defined in Table 6.2). The single-parameter, fixed-layer inversions should, in principle, provide the best possible resolution in estimating resistivity values. In only inverting for resistivity, there is, however, potential for distortion of the resistivity estimates when modelling the EM responses over highly magnetic or highly polarisable lithologies (e.g., clays and disseminated sulphides).

For data input, any of the individual eight EM data components can be flagged as active or inactive for the inversion – all eight components were flagged as active for the test-line inversions. Data errors for the eight components can be individually specified – all data components were assigned an error of 60 ppm for the test-line inversions. EM measurement sites can also be excluded from the inversion using flight clearance and power-line monitor thresholds – neither threshold was applied to exclude data for the test-line inversions.

The theoretical and numerical basis for the Tikhonov-type inversion scheme implemented in *aempy* is outlined in detail Kiyan and Rath (2017) and Kiyan et al. (2022). From a practical user's perspective, there are three parameters requiring definition that control the inversion and the characteristics of the output models: the data errors, and the two regularisation parameters, $\tau 0$ and $\tau 1$. The parameter $\tau 0$ controls the freedom of the inversion model to diverge from the defined starting (*a priori*) model, with larger $\tau 0$ values providing less freedom. The parameter $\tau 1$ controls the smoothness of the model (in a 1-D, vertical sense), with larger $\tau 1$ values producing smoother models. Assignment of a data error to each of the EM data components controls the 'weighting' placed on those components in the inversion. Lower errors provide a stronger weighting. Data errors therefore have the practical effect of focussing the inversion on different regions of the subsurface: for example, lower errors assigned to higher frequency data will tend to weight the inversion towards resolving shallower resistivity structure, and vice versa for lower errors assigned to lower frequency data and deeper structure. Given the importance of these three parameters in controlling the inversion outputs, it is beneficial to carry out tests on the inversion dataset, to identify appropriate values for them and to understand how their variation affects the shape and quality of fit of the output resistivity models. These tests were carried out for the Waterford Block data prior to the production inversion of these data (and are reported on in GSI, 2020), and the same parameters have been used for the Waterford test-line data.

6.1.2 Inversion modelling strategy

<u>Non-independent Inversion</u>

The *aempy* Tikhonov-type inversion code provides two options for the *a priori* (starting) model used at each EM measurement site (keeping in mind that the 1-D inversions are run on a line-by-line basis):

i. A half-space with a user defined resistivity value, referred to as **'independent' inversion**.

ii. The previous site's resistivity model (with the starting model for the first site on the line being a half-space with a user defined resistivity value), referred to as **'non-independent' inversion**.

Like other geophysical methods, EM modelling is subject to equivalence – in which different possible model solutions can satisfy equally well the observed EM response data, to within data error. The EM method is particularly sensitive to conductive subsurface bodies, specifically to their conductance (the conductivity-thickness product) and is particularly subject to equivalence in the modelling of conductors (i.e., a thinner, more conductive body producing an equivalent EM response to a thicker, less conductive body).

In running independent inversions at each site, there is no restriction placed on the possibility of adjacent sites converging on different, but equivalent, model solutions, potentially leading to discontinuous or blocky resistivity model sections along flight lines. The use of the previous site's model as the starting model, as done in non-independent inversions, attempts to direct the inversion towards convergence on a model that does not deviate dramatically from the previous site's model, unless required to do so by the

EM data. Choice of the inversion regularisation parameter $\tau 0$, which controls the freedom of divergence from the starting model, provides a means of controlling how rapidly site-to-site inversions can respond to lateral changes in geology when using non-independent modelling.

While independent and non-independent inversions produce models with similar RMS errors, and which are therefore quantitatively equally valid model solutions, greater lateral continuity of features is generally observed in non-independent inversion models and is preferred as being more geologically realistic and more interpretable. The trade-off required between lateral model continuity and vertical resolution when employing independent inversions also makes an independent inversion strategy less favourable (i.e., vertically smoother models are required to ensure smoother lateral continuity along the flight-line).

Non-independent modelling was adopted for the Waterford test-line inversions.

Forward-Reverse Averaging of Non-independent Inversion Models (FRA Strategy)

Running non-independent inversions (i.e., using the previous site's model as the starting model) raises the possibility that resulting model sections may be somewhat different depending on the line direction in which the inversions are run. It also presents the possibility of running inversions in both line directions, assessing the differences between the two models and deriving an average model from two equally valid model solutions – a strategy referred to as the 'forward-reverse-average' (FRA) strategy. The FRA strategy has been tested and used in the production inversion of the Waterford Block data (GSI, 2020) as well in the production inversions of the A5 and A6 Blocks.

Non-independent inversion, coupled with the 'forward-reverse-average' strategy, was used in the inversion of the Waterford test-line data.

Model sensitivities

A useful, post-inversion output provided by the *aempy* code is the model **sensitivity matrix** (essentially the inversion Jacobian matrix). It describes the sensitivity of the EM responses to changes in the model resistivity, separately for each layer at depth in the model. Numerically, sensitivity, S, is defined as the derivative of the EM response, $g(m)$, with respect to the model parameter, m (resistivity):

$$S = \delta g(m) / \delta m \quad (3)$$

where the net sensitivity is provided by the sum of the sensitivities of all eight data responses (components). Where a large change in model resistivity (for a particular depth layer) produces a small change in the predicted EM response, that part of the model might be regarded as poorly constrained, as the EM data are insensitive to it. As the Jacobian matrix in the inversion is weighted by the data errors, higher data errors lead to lower model sensitivities. Sensitivities are intimately connected to the specifics of the EM data acquisition system and the inversion parameterisation: e.g., the frequencies used and the coil geometry, the flight clearance, the data errors assigned, and the thickness of the model layers (thinner layers correspond with lower sensitivities). It is therefore very difficult to assign a universal sensitivity threshold above which a model solution might be regarded as reliable.

While sensitivity can be used as a practical means of identifying and rejecting poorly constrained parts of the inversion models and has been utilised in the rejection of poor model solutions in production datasets released by GSI (e.g., Waterford Block, GSI, 2020), it has not been used to reject model solutions in the Waterford test-line cross-sections presented here.

6.1.3 Inversion parameters and workflow

Tikhonov-type 1-D inversions were run on all twenty repeat flights on the Waterford test-line, on a line-by-line basis, using non-independent inversions coupled with the forward-reverse-average (FRA) strategy. The inversion parameters and workflow are summarised in Table 6.1. The 1-D layered-model scheme consists of 35 subsurface layers, with layer thickness increasing logarithmically from 2 m at surface to 9.6 m at 170 m depth. Depths to the mid-point of each layer are specified in Table 6.2. Inversion parameters used are the same as used for the inversion Waterford Block 1-D production inversions.

Table 6.1: Inversion parameters and workflow.

PROCESSING STEP	SOFTWARE	PARAMETERS AND COMMENTS
Pre-processing		
Data import	*Geosoft*	Import into *Geosoft*. SGL delivery DLV2402. Input data file: [GSI_TESTLINE_FEM.xyz].
Smoothing of radar altimeter data	*Geosoft*	Low-pass filter, 5-fiducial.
Data export	Geosoft	Export data channels required by *aempy*: line name, ITM_X, ITM_Y, MSLHGT, RADAR_LP5, In-phase 0.9 kHz to 25 kHz, Quadrature 0.9 kHz to 25 kHz, PLM_nT.
Data import	*aempy*	Import into *aempy* software.
De-noising of EM data	*aempy*	Principal Component Analysis filter (when used): Npca1 filter, retaining singular value 1 only.
Tikhonov-type 1-D regularised inversion		
Data inversion on a line-by-line, site-by-site basis	*aempy*	Number of layers (excluding final half-space): 35.
		Layer thickness: increasing logarithmically, 2.0 m at surface to 9.6 m at 170 m depth.
		Starting model for first site on line: 100 ∧.m half-space.
		Starting model for all other sites on line: previous site's 1-D model.
		Inversion direction on line: forward and reverse directions (i.e., two inversions per site).
		τ0 regularisation parameter (closeness to starting model): 0.05.
		τ1 regularisation parameter (model smoothness): 6.0.
		Data errors: 60.0 ppm for all 8 EM data components.
Model averaging	*aempy*	Compute average of forward and reverse direction inversion runs: resistivity model (and percentage difference between two resistivity models with respect to average model), model sensitivity, RMS errors and predicted EM responses.
Data output	*aempy*	Output in *Geosoft* .XYZ format: model resistivity, model percentage difference, model sensitivity (all three parameters sorted into depth channels), RMS error, predicted and observed EM responses for 8 components.

Table 6.2: Model layer depths used in inversion of the EM data (depths recorded correspond with depth at the mid-point of the layer).

Depth Layer	D1	D2	D3	D4	D5	D6	D7	D8	D9
Depth (to mid-layer) (m)	1.0	3.0	5.2	7.4	9.8	12.3	14.9	17.6	20.5

Depth Layer	D10	D11	D12	D13	D14	D15	D16	D17	D18
Depth (to mid-layer) (m)	23.4	26.6	29.9	33.3	36.9	40.7	44.7	48.9	53.2

Depth Layer	D19	D20	D21	D22	D23	D24	D25	D26	D27
Depth (to mid-layer) (m)	57.8	62.6	67.7	72.9	78.5	84.3	90.4	96.7	103.4

Depth Layer	D28	D29	D30	D31	D32	D33	D34	D35	
Depth (to mid-layer) (m)	110.4	117.8	125.5	133.6	142.1	150.9	160.3	169.8	

6.1.4 Example *aempy* inversion model results

1-D inversions, using the same inversion parameters, were run on both the original FEM response data and the FEM responses after application of a Principal Component Analysis 'Npca1' filter. As discussed above (in Sections 4.2 and 4.3), application of the Npca1 filter, which retains only the first (strongest) Principal Component in the data reconstruction, was observed to retain most of the data and data variability in the four higher-frequency EM data components (in-phase and quadrature at 12 and 25 kHz) while removing a large proportion of the data and data variability in the four lower-frequency EM components (in-phase and quadrature at 0.9 and 3 kHz). The data variability removed in the 0.9 and 3 kHz data has been argued above (Section 4.3) as consisting of cultural noise signal that is not correlated with the (geological) signal of the 12 and 25 kHz data components.

Example 1-D resistivity inversion models for lines L2060100.19 and L2060011.21, plotted along the line as a 2-D resistivity section, are illustrated in Figures 6.1 to 6.4, showing models derived from both the original and Npca1 filtered FEM data. The resistivity sections shown are the 'average models', being the average of the forward and reverse direction inversions. Averages are computed based on $\log_{10}$ resistivity (Ω.m) values. Note the very high vertical exaggeration (VE) in the cross-sections, where VE = 7.

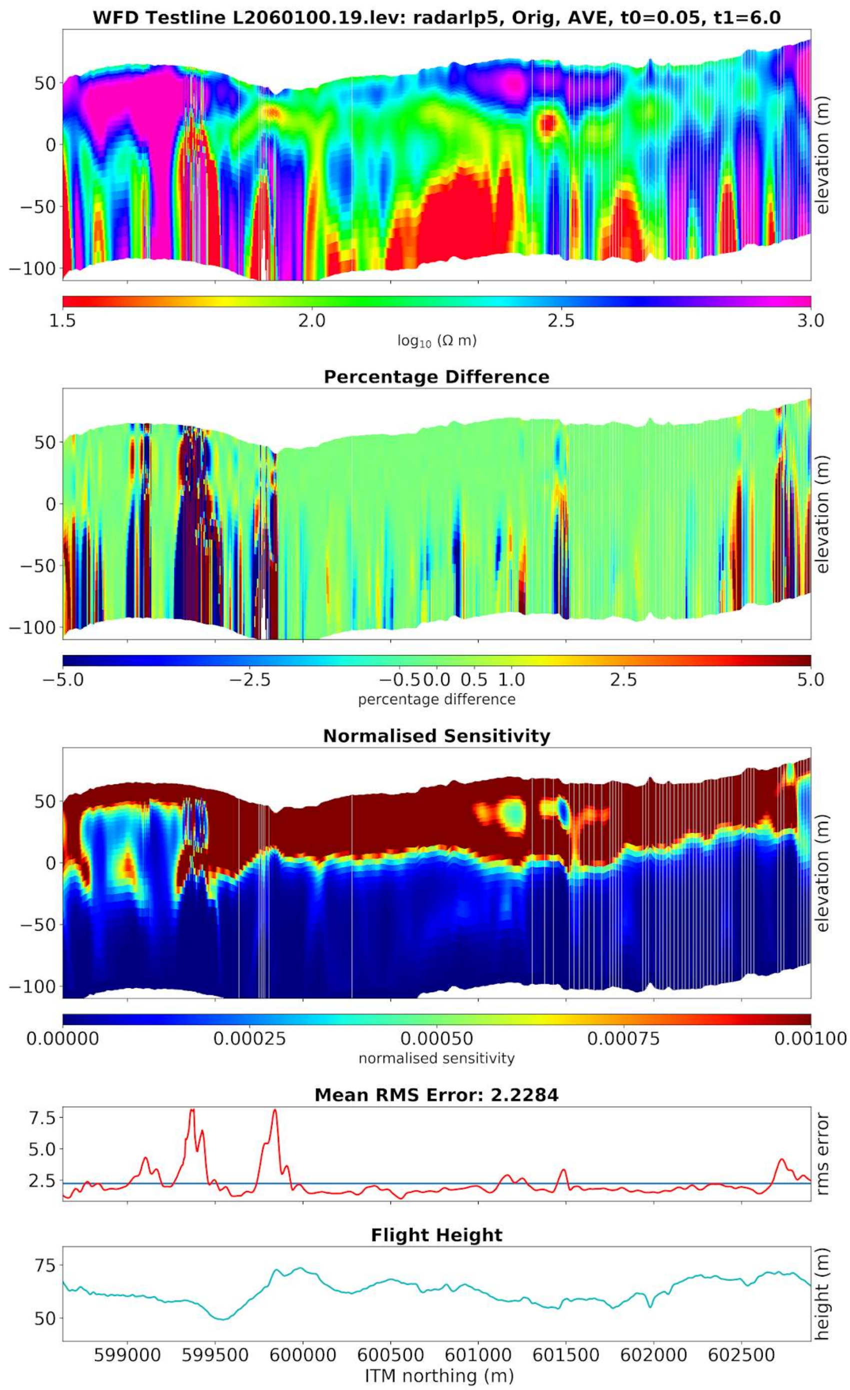

Figure 6.1: L2060100.19: Inversion of original FEM response data ('lev' data). (Top) Resistivity model – average of forward and reverse direction resistivity models. (Second) Percentage difference – difference between forward and reverse direction resistivity models with respect to average model. (Third) Normalised sensitivity – average of forward and reverse direction model sensitivities, normalised (divided) by maximum sensitivity for the line. (Fourth) RMS error – average of forward and reverse direction model RMS errors. Mean RMS error for line shown (horizontal blue line). (Bottom) Flight clearance. Coastline to left of section. VE = 7.

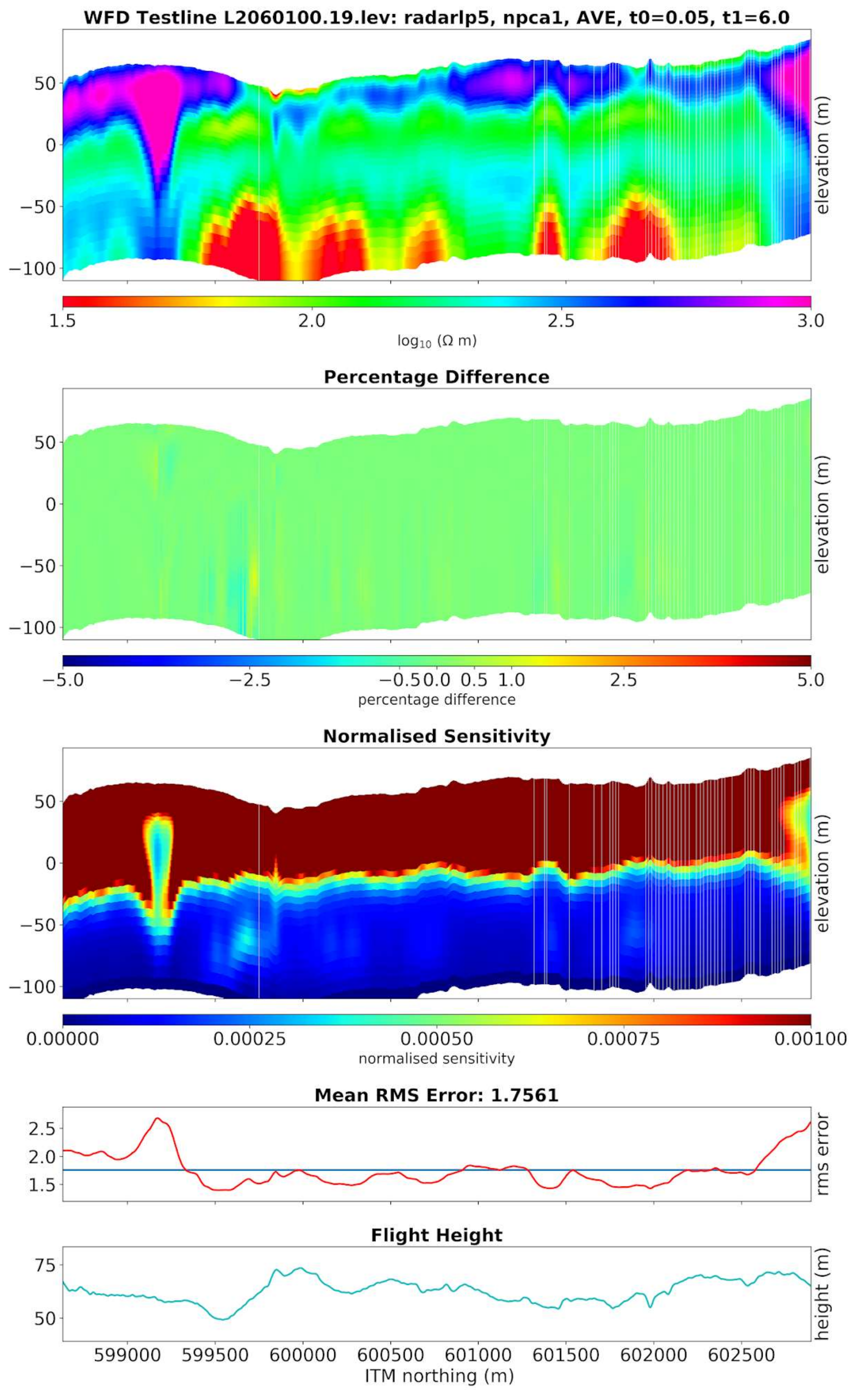

Figure 6.2: <u>L2060100.19: Inversion of Npca1 filtered FEM response data</u>. (Top) Resistivity model – average of forward and reverse direction resistivity models. (Second) Percentage difference – difference between forward and reverse direction resistivity models with respect to average model. (Third) Normalised sensitivity – average of forward and reverse direction model sensitivities, normalised (divided) by maximum sensitivity for the line. (Fourth) RMS error – average of forward and reverse direction model RMS errors. Mean RMS error for line shown (horizontal blue line). (Bottom) Flight clearance. Coastline to left of section. VE = 7.

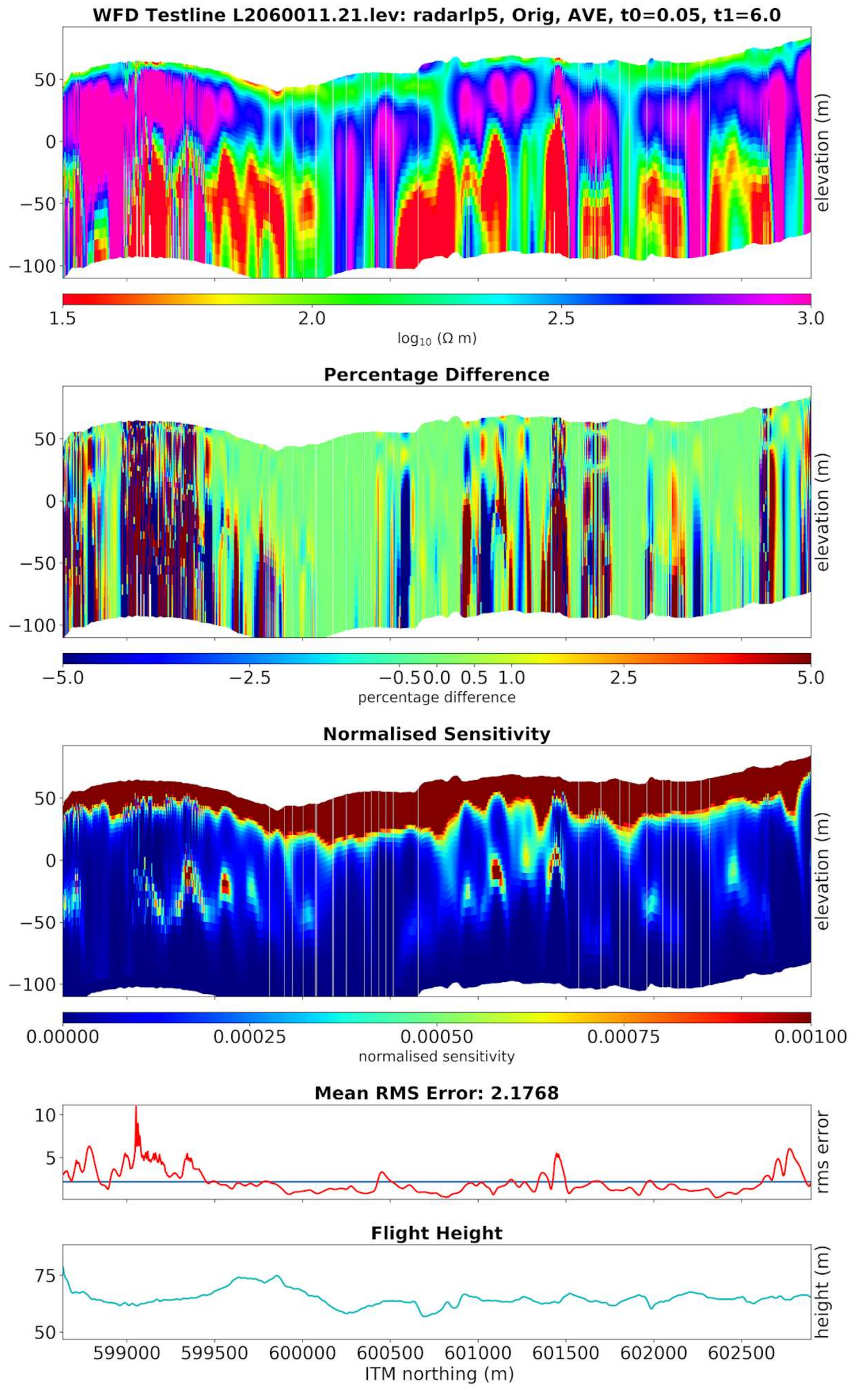

Figure 6.3: <u>L2060011.21: Inversion of original FEM response data</u> ('lev' data). (Top) Resistivity model – average of forward and reverse direction resistivity models. (Second) Percentage difference – difference between forward and reverse direction resistivity models with respect to average model. (Third) Normalised sensitivity – average of forward and reverse direction model sensitivities, normalised (divided) by maximum sensitivity for the line. (Fourth) RMS error – average of forward and reverse direction model RMS errors. Mean RMS error for line shown (horizontal blue line). (Bottom) Flight clearance. Coastline to left of section. VE = 7.

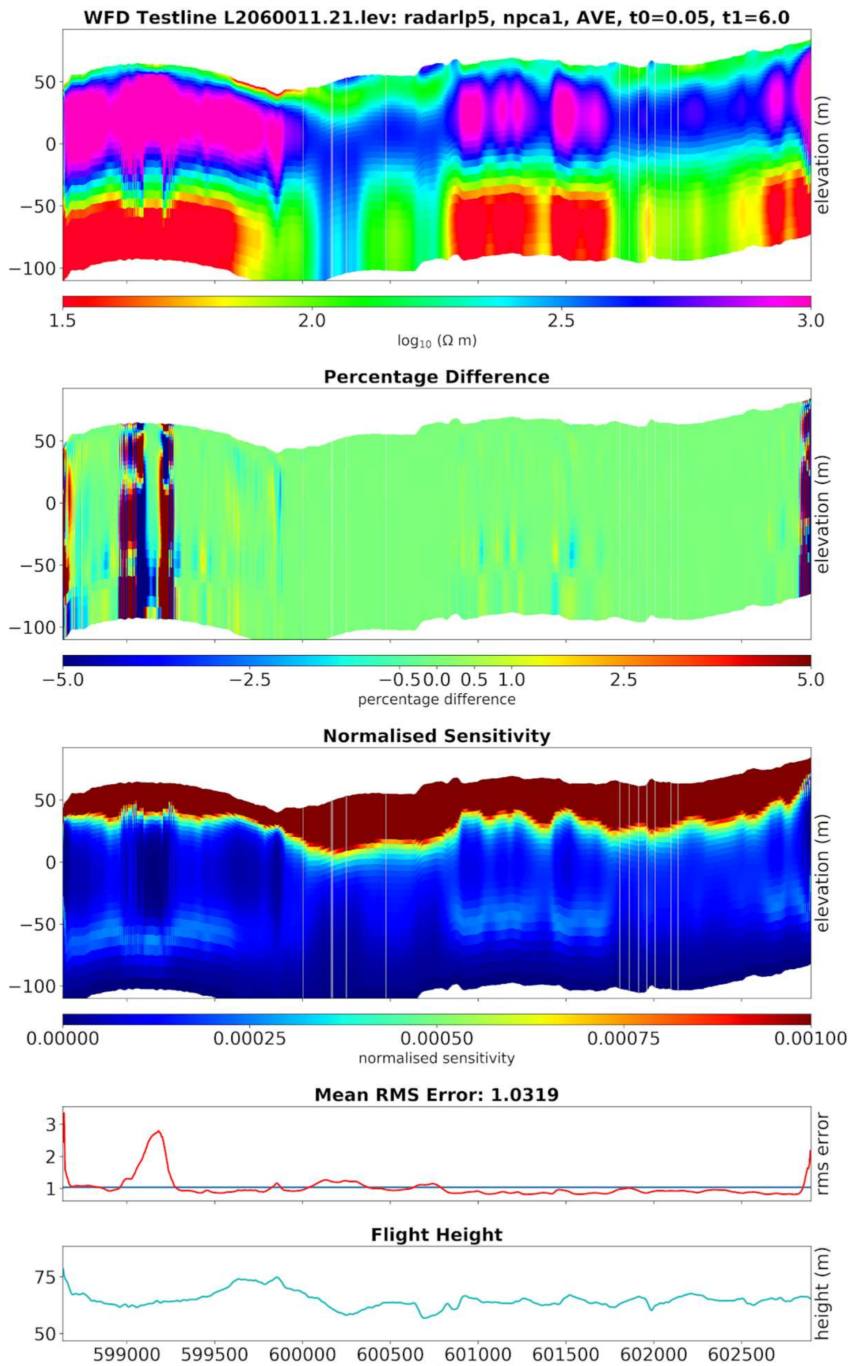

Figure 6.4: <u>L2060011.21: Inversion of Npca1 filtered FEM response data</u>. (Top) Resistivity model – average of forward and reverse direction resistivity models. (Second) Percentage difference – difference between forward and reverse direction resistivity models with respect to average model. (Third) Normalised sensitivity – average of forward and reverse direction model sensitivities, normalised (divided) by maximum sensitivity for the line. (Fourth) RMS error – average of forward and reverse direction model RMS errors. Mean RMS error for line shown (horizontal blue line). (Bottom) Flight clearance. Coastline to left of section. VE = 7.

Several 'QC parameters' are also displayed in Figures 6.1 to 6.4: (i) The percentage difference section, being the difference between the forward and reverse direction resistivity models relative to the average model. The average model and the differences are computed based on $\log_{10}$ resistivity (Ω.m) values. (ii) The model sensitivity section, with sensitivity normalised (by division) by the maximum sensitivity on the line. (iii) The site RMS error profile along the line.

It is clear in comparing the resistivity models and QC sections derived from the original data (Figures 6.1 and 6.3) with those derived from the Npca1 filtered data (Figures 6.2 and 6.4), that the Npca1 models are characterised by significantly greater lateral continuity and stability. Lack of inversion stability in the original data models is particularly reflected in the percentage difference sections, where large positive and negative percentage-difference anomalies are apparent at many locations along the line, in some cases limited to the deeper parts of the model (where model sensitivity is lower) and, in other cases, throughout the depth column. Large percentage differences, whether positive or negative, indicate that the inversions, and the final models that the inversions converge on, are very sensitive to the starting model (being the previous site's model). Sensitivity to the starting model suggests less certainty in the final model. Very sharp lateral transitions in resistivity are found in the original data resistivity models at locations of high percentage difference – introducing both very high and very low resistivity anomalies into the models, particularly at depth, and which are absent in the Npca1 data models. It is probable (in the absence of an examination of the misfits between the observed and predicted data for each of the eight data components) that the high and low resistivity anomalies introduced into the original data models result from the inversions attempting to model the high amplitude cultural noise signals in the EM response data at 0.9 and 3 kHz frequencies and are not geological in origin.

Model sensitivity is dependent on resistivity and the model depth, and is low in the most resistive parts of the models and at depths below 50 – 80 m. The low resistivity units present below ~100 m depth in the models, most readily apparent in the Npca1 models, are characterised by very low sensitivities and are therefore poorly constrained and should not be interpreted with any certainty.

Table 6.1. Model RMS errors for 1-D inversions run on original EM responses ('lev' data) and on EM responses filtered with Principal Component Analysis filter retaining first principal component only (Npca1 filter). Mean RMS error ('Line Mean') shown for each repeat flight-line. Also shown is the mean for each series of four flights and for all twenty repeat flights together.

Series (Year)	Line Number	Original LEV Data			NPCA1 Filtered Data		
		Line Mean	Series Mean	All Lines Mean	Line Mean	Series Mean	All Lines Mean
2018	L2060010.18	1.5479	1.5973	1.9445	0.9884	1.0642	1.1618
	L2060110.18	1.3408			0.7287		
	L2060011.18	1.8093			1.3046		
	L2060111.18	1.6910			1.2350		
2019	L2060000.19	1.5315	1.7379		1.0219	1.1822	
	L2060100.19	2.2284			1.7561		
	L2060001.19	1.3027			0.6244		
	L2060101.19	1.8889			1.3265		
2020	L2060010.20	2.1326	2.2389		1.3725	1.2867	
	L2060110.20	2.5834			1.6627		
	L2060011.20	1.9733			0.9741		
	L2060111.20	2.2663			1.1375		
2021.1	L2060010.21	1.9627	2.0409		0.8608	0.9539	
	L2060110.21	1.9198			0.8576		
	L2060011.21	2.1768			1.0319		
	L2060111.21	2.1043			1.0654		
2021.2	L2060020.21	2.1383	2.1074		1.6312	1.3218	
	L2060120.21	1.7538			0.7325		
	L2060021.21	2.2410			1.4584		
	L2060121.21	2.2965			1.4650		

First-order assessment of model RMS errors

RMS errors are substantially reduced in the Npca1 data models compared with the original data models (Table 6.1 and Figure 6.5). The line-mean RMS errors for each repeat flight line (Figure 6.5) indicate that the errors are consistently higher in the original data models, for all flight-series and particularly for the 2020, 2021.1 and 2021.2 series of flights. Variation in the line-mean RMS errors of the Npca1 data models is more consistent from series-to-series, and generally oscillate around the twenty-line mean (with the exception of the 2021.1 series, where mean RMS errors are consistently low). The high RMS error series of 2020, 2021.1 and 2021.2, in the original data models, correspond with series characterised by higher mean variability in the in-phase and quadrature responses at 0.9 and 3 kHz (Figure 3.31). It appears likely, therefore (again, in the absence of an examination of the misfits between the observed and predicted data separately for each of the eight data components) that the higher mean RMS errors of the 2020, 2021.1 and 2021.2 data series (for the original data models) are due to higher misfits of the more variable (and, therefore, noisier) 0.9 and 3 kHz EM responses. Furthermore, the lower RMS errors of the Npca1 data models compared with the original data models are likely due to better fits to the 0.9 and 3 kHz EM responses, which in the Npca1 data are characterised by significantly reduced data variability and cultural noise levels.

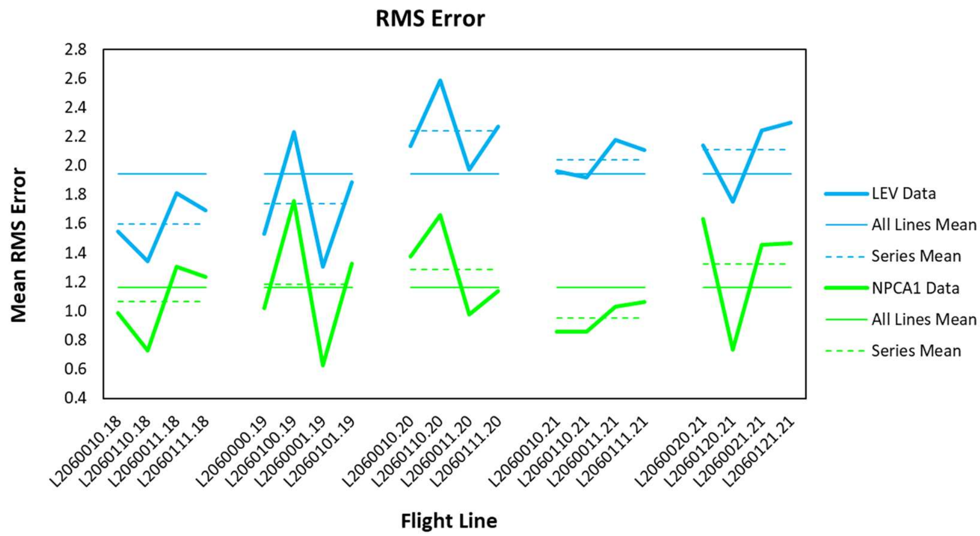

Figure 6.5: Mean RMS error for 1-D inversion models for each flight-line for (in blue) original ('lev') EM response data and (in green) Npca1 filtered EM responses. RMS errors shown against the mean for all twenty flight lines (thin solid lines) and the mean for each four-line flight-series (thin dashed lines). Source data given in Table 6.1.

The pattern of changes observed in line-mean RMS error within each series of repeat flights (often a 'saw-tooth' pattern) (Figure 6.5) is sympathetic with the pattern of changes in line-mean flight clearance (Figure 3.3 and repeated in Figure 5.12) in the case of three series (2018, 2021.1 and 2021.2), where higher line-mean RMS errors broadly correspond with higher line-mean clearances. Line-mean RMS errors and line-mean clearances appear antithetic (inverse) in the case of two series (2019 and 2020). The sympathetic and antithetic association between line-mean RMS error and line-mean flight clearance is illustrated in the cross-plots of Figure 6.6, where a positive slope is evident in the illustrative linear trendlines shown for the 2018, 2021.1 and 2021.2 series, and a negative slope for the 2019 and 2020 series. To a first order, there is no definitive and consistent association between higher flight clearances and higher RMS errors in the 1-D inversion models.

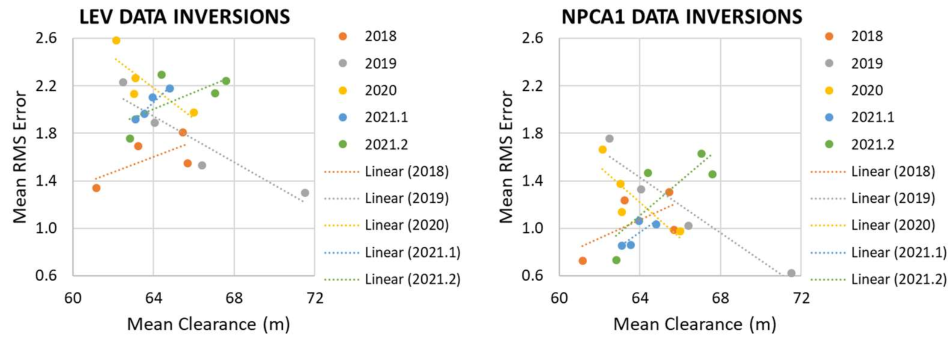

Figure 6.6: Cross-plots of mean model RMS error versus mean flight clearance for each repeat flight-line, colour coded by flight-series (year). (Left panel) RMS errors for 1-D inversions of original EM responses ('lev' data). (Right) RMS errors for 1-D inversions of Npca1 filtered EM responses. A linear trendline is shown for illustrative purposes in the cross-plots for each flight-series (consisting of four repeat flight-lines).

6.2 *aempy* 1-D Inversion Model Sections

2-D resistivity cross-sections for each set of four repeat flights, for each annual series, are presented below for 1-D inversions run on the original ('lev') EM responses (Figures 6.7 to 6.11) and on the Npca1 filtered EM responses (6.12 to 6.16). The same colour scale (linear, 1.5 – 3.0 $\log_{10}(\Omega.\mathrm{m})$) is used for all resistivity sections so that direct comparisons may be made between the different sections. The overall RMS error for each line is annotated on the right-hand side of each cross-section.

The degree of variability (or similarity) between the cross-sections presented in Figures 6.7 to 6.16 is largely left to the visual assessment of the reader. A number of broad observations are, however, made here.

i. As previously illustrated for the two examples of lines L2060100.19 and L2060011.21 (Figures 6.1 to Figure 6.4), all the Npca1 models are characterised by significantly greater lateral continuity and stability. The original-data models are broadly comprised of the same, or very similar, underlying resistivity structure present in the Npca1 models, onto which short-wavelength, very-high and very-low resistivity structures are superimposed, most visibly in the depth range below about 50 m, but extending upwards to shallower depths in places. The sharp transitions from conductive to resistive features observed in the original-data model sections are unlikely to be of geological origin, as explained below.

Any sharp lateral resistivity transitions that are present in the subsurface geology along the flight-line will express themselves as smooth transitions in the EM responses, due to the relatively large size of the EM footprint (Section 4). While 'sharp-boundary' 2-D EM inversions may have some success in recovering sharp geological boundaries in the resulting subsurface resistivity models, the 1-D inversions of this study will carry the smoothed geological transitions (in the EM responses) forward into the subsurface resistivity models. Very sharp lateral resistivity (geological) transitions should therefore not be expected in the 2-D resistivity cross-sections (derived from 1-D inversion models).

ii. An initial appraisal of the twenty repeat flights for each dataset, i.e., examining the original dataset and the Npca1 dataset separately, suggests quite high variability between the resistivity sections, and certainly in detail. To a first order, however, all sections capture similar broad variation in resistivity along the line, consisting of resistive terrain on the southern and northern ends of the profile and near the centre of profile, with more conductive terrain between the resistive areas. These broad zones or areas are labelled, from the south to north, 'Resistive 1' to 'Resistive 3' and 'Conductive 1' and 'Conductive 2' in Figures 6.7 to 6.16. The lateral extent, maximum resistivity and depth extent of each resistive area is variable from line-to-line. The 'conductive' areas are moderately conductive, with resistivities ranging from around 100 Ω.m ($\log_{10}$ = 2, in green colours) to around 400 Ω.m ($\log_{10}$ = 2.6, in oranges), and their expression is more variable in the sections, with a 100 Ω.m, ~30 m thick layer, being present at surface or near-surface in some cases, and in other cases a similar 100 Ω.m layer is found beneath a 400 Ω.m, ~30 m thick layer at surface. The expression of areas 'Resistive 2' and 'Conductive 2' is variable across the sections, and in many cases a clear distinction between these two areas is not apparent in the sections.

It is not immediately apparent from a visual inspection of the sections, particularly the clearer/cleaner Npca1 sections, whether the variability in the resistivity model sections is greater between series (indicating potential seasonal variation in the shallow resistivity structure) or whether the variability is equally as significant between the four repeat flights within each series. A more detailed assessment than is possible within the scope of this work will be required to understand which aspects of the EM response variability account for the variability, in detail, of the resistivity inversion models. A more detailed assessment might follow the lines of investigation suggested at the start of this section (Section 6), examining the variability and changes in variability along the length of the test-line: (i) Assessment of variability in the model RMS errors, (ii) assessment of variability in the misfits between the observed data and the model predictions, for all eight EM response components, and (iii) assessment of variability in the resistivity models themselves, by examining the resistivity variability of, for example, the shallowest twenty-six depth layers (< 100 m depth), or a selected subset of depth layers at different depths.

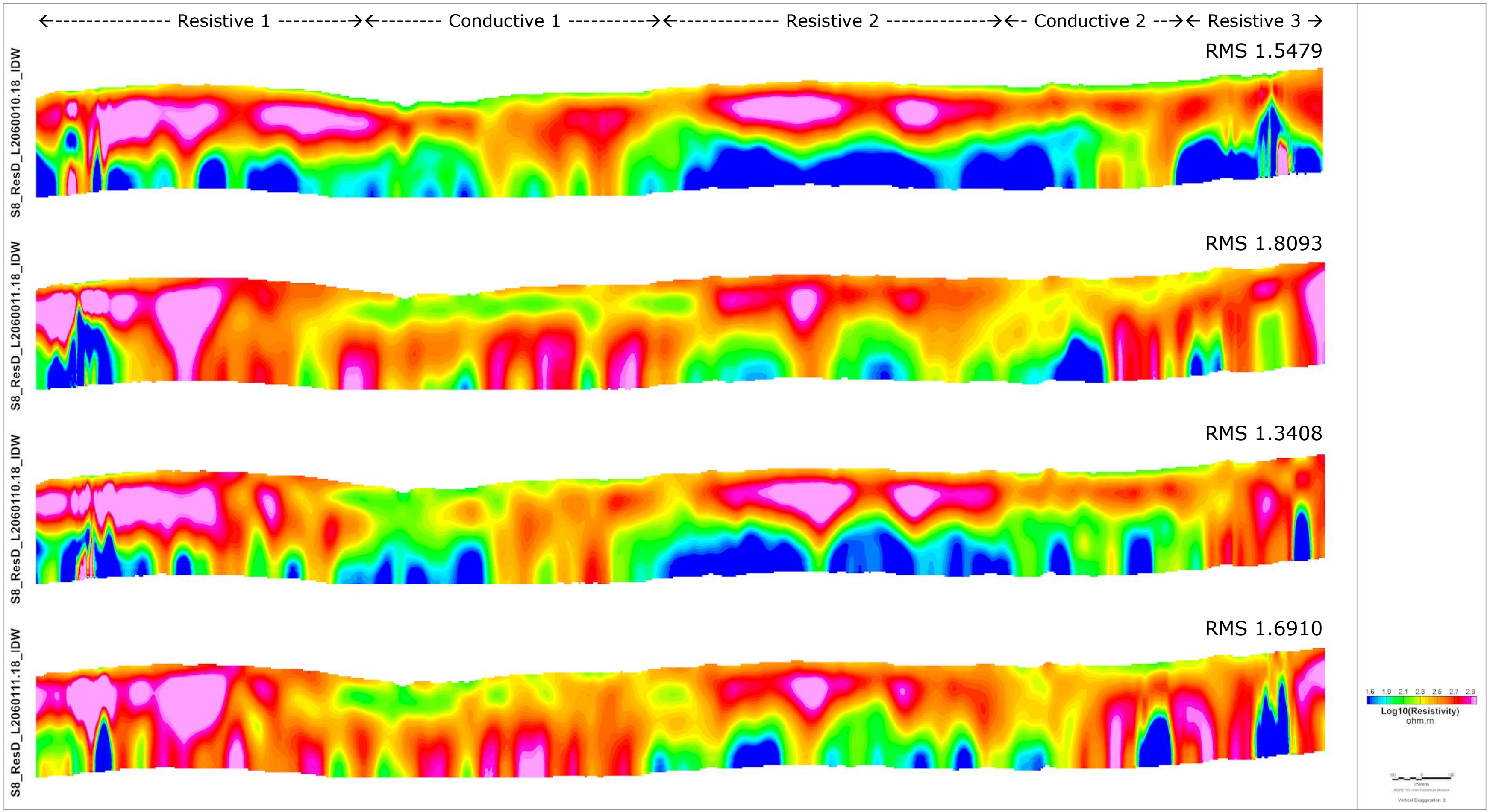

Figure 6.7: Original FEM response data: 2018 series. 1-D inversion model resistivity sections. Line length 4.4 km, model depth extent below surface 104 m. Vertical exaggeration 3:1. SSE end of line (coastline) to left of section. Grid cell dimensions 7.2 x 2 m (horizontal x vertical), Inverse Distance Weighted, log_{10} resistivity values.

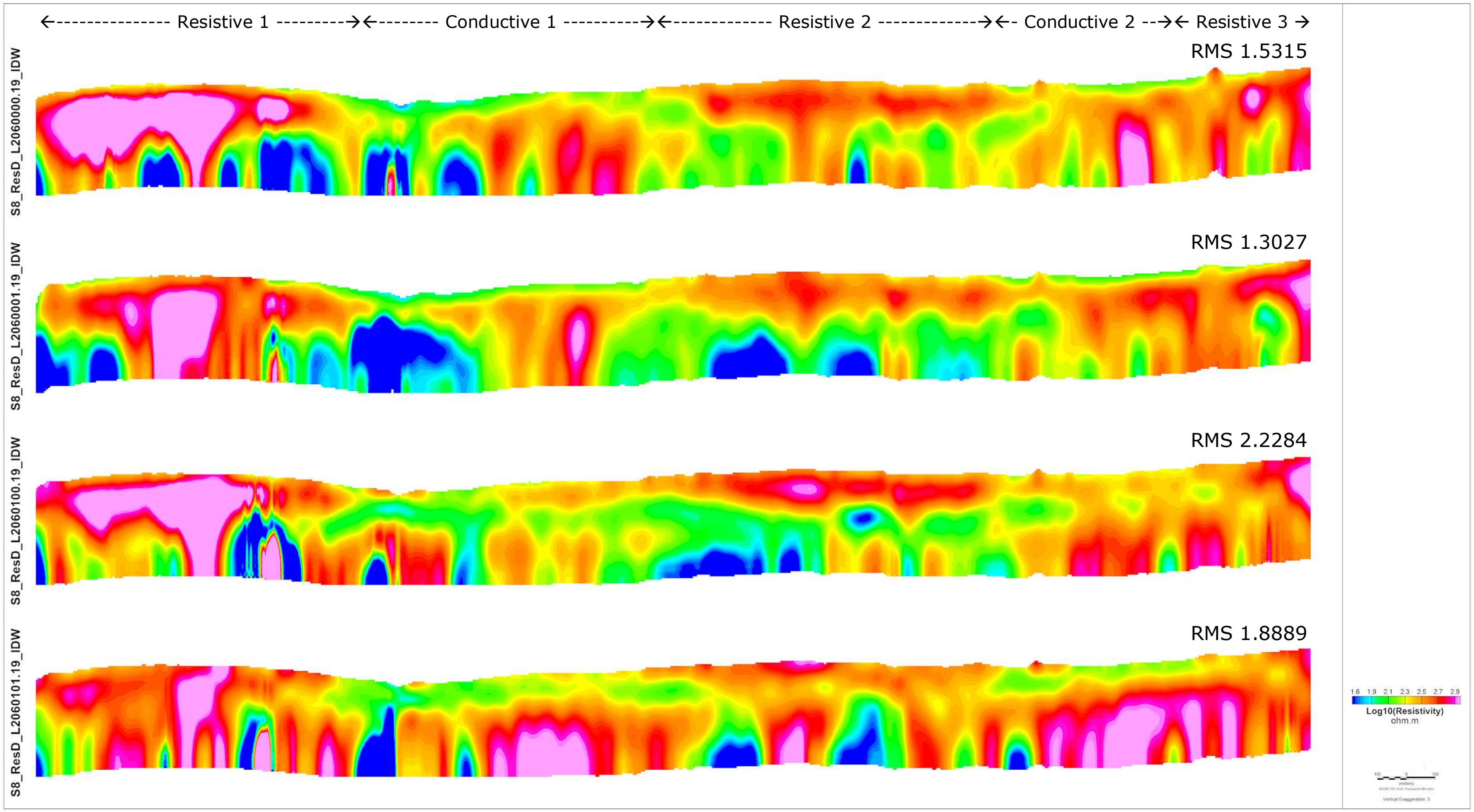

Figure 6.8: <u>Original FEM response data: 2019 series</u>. 1-D inversion model resistivity sections. Line length 4.4 km, model depth extent below surface 104 m. Vertical exaggeration 3:1. SSE end of line (coastline) to left of section. Grid cell dimensions 7.2 x 2 m (horizontal x vertical), Inverse Distance Weighted, log_{10} resistivity values.

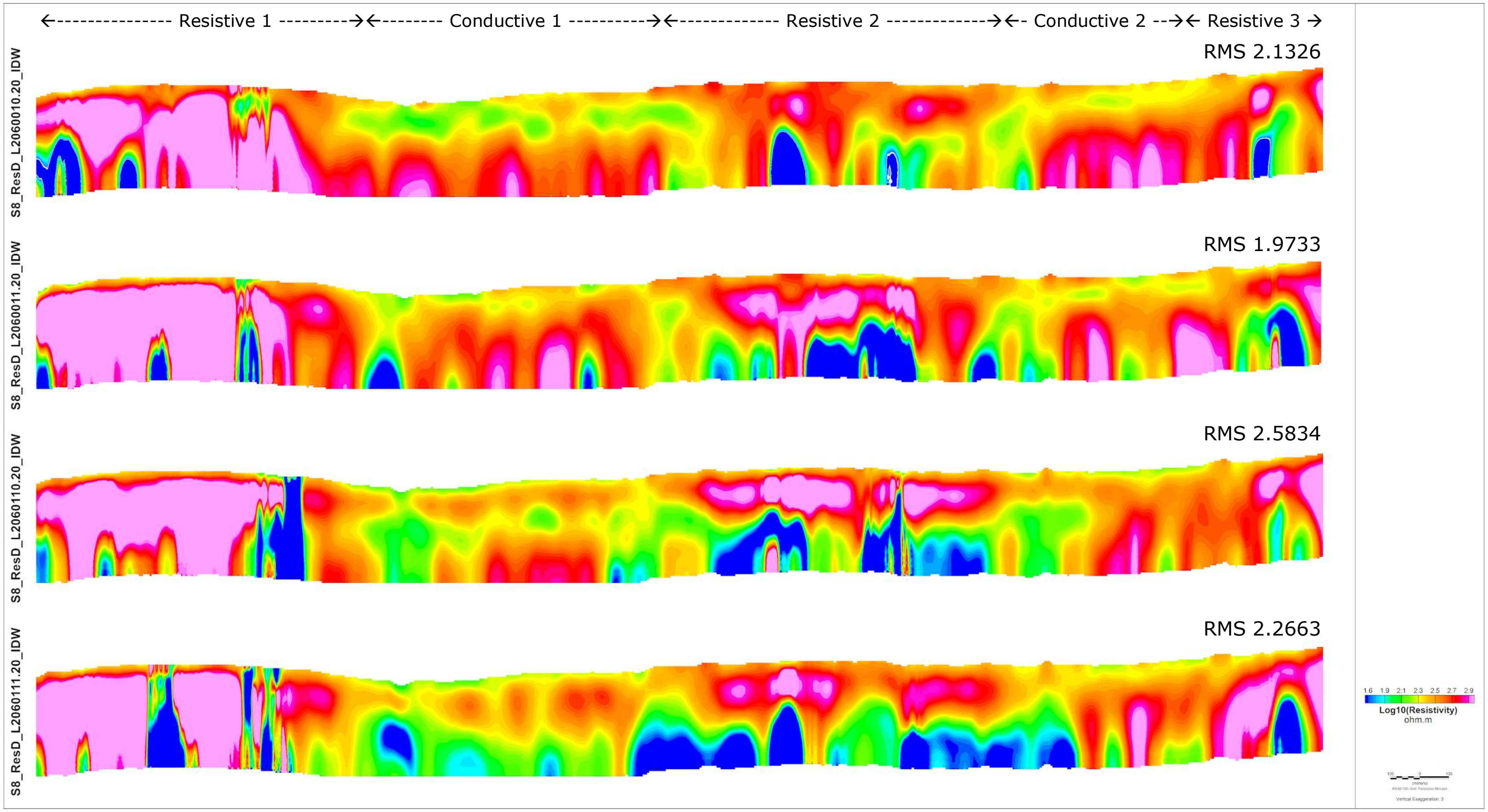

Figure 6.9: <u>Original FEM response data: 2020 series</u>. 1-D inversion model resistivity sections. Line length 4.4 km, model depth extent below surface 104 m. Vertical exaggeration 3:1. SSE end of line (coastline) to left of section. Grid cell dimensions 7.2 x 2 m (horizontal x vertical), Inverse Distance Weighted, log_{10} resistivity values.

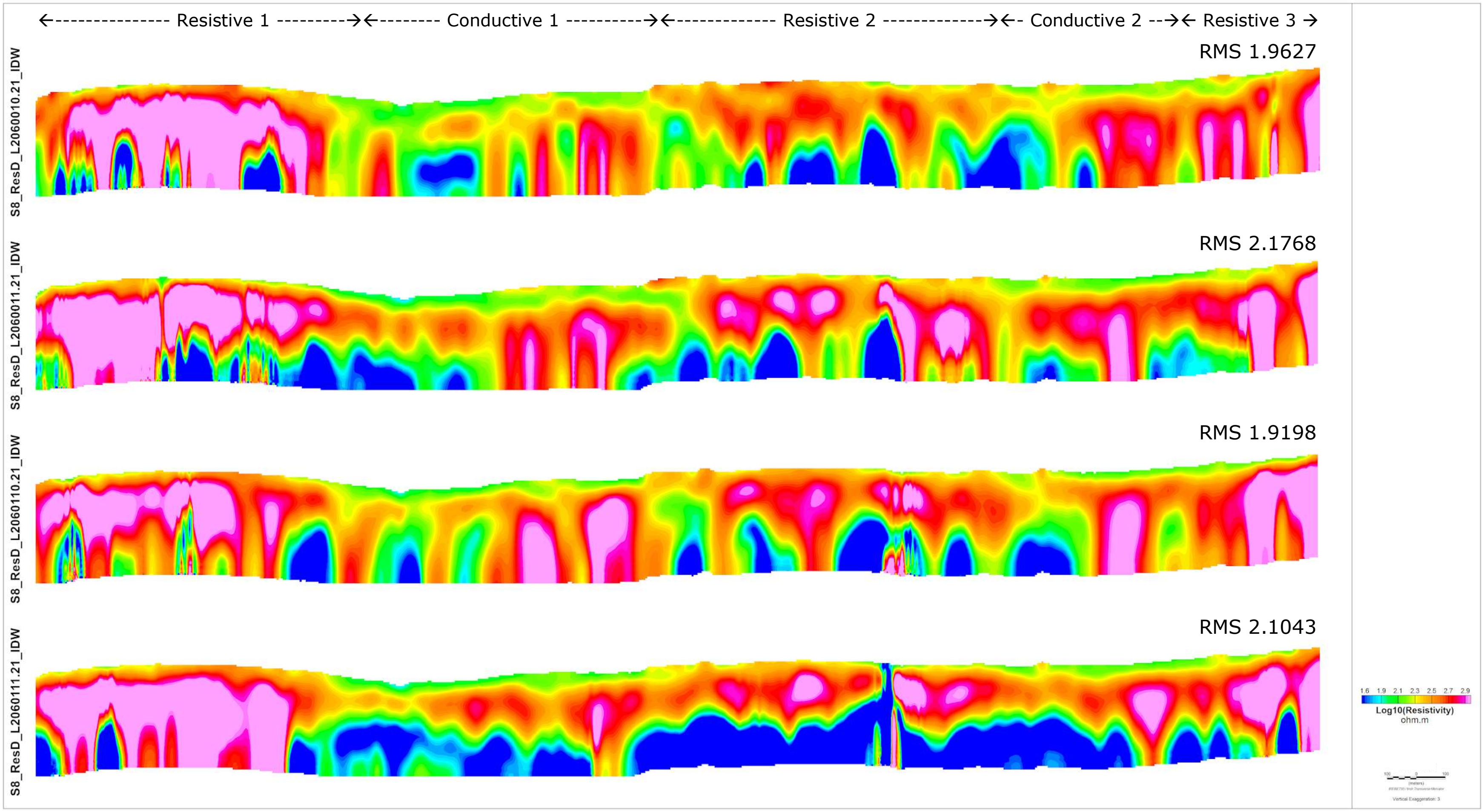

Figure 6.10: <u>Original FEM response data: 2021.1 series</u>. 1-D inversion model resistivity sections. Line length 4.4 km, model depth extent below surface 104 m. Vertical exaggeration 3:1. SSE end of line (coastline) to left of section. Grid cell dimensions 7.2 x 2 m (horizontal x vertical), Inverse Distance Weighted, log$_{10}$ resistivity values.

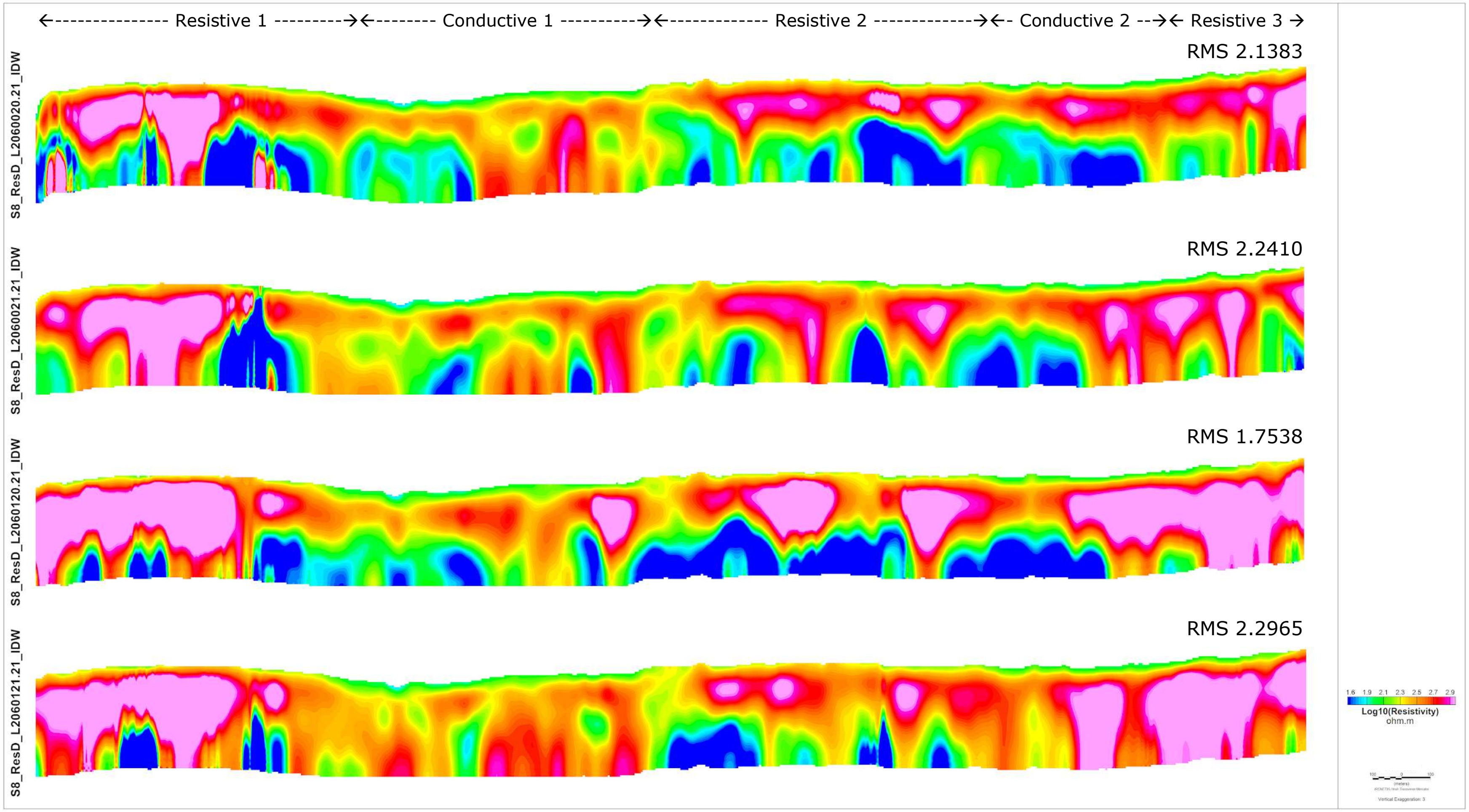

Figure 6.11: <u>Original FEM response data: 2021.2 series</u>. 1-D inversion model resistivity sections. Line length 4.4 km, model depth extent below surface 104 m. Vertical exaggeration 3:1. SSE end of line (coastline) to left of section. Grid cell dimensions 7.2 x 2 m (horizontal x vertical), Inverse Distance Weighted, log$_{10}$ resistivity values.

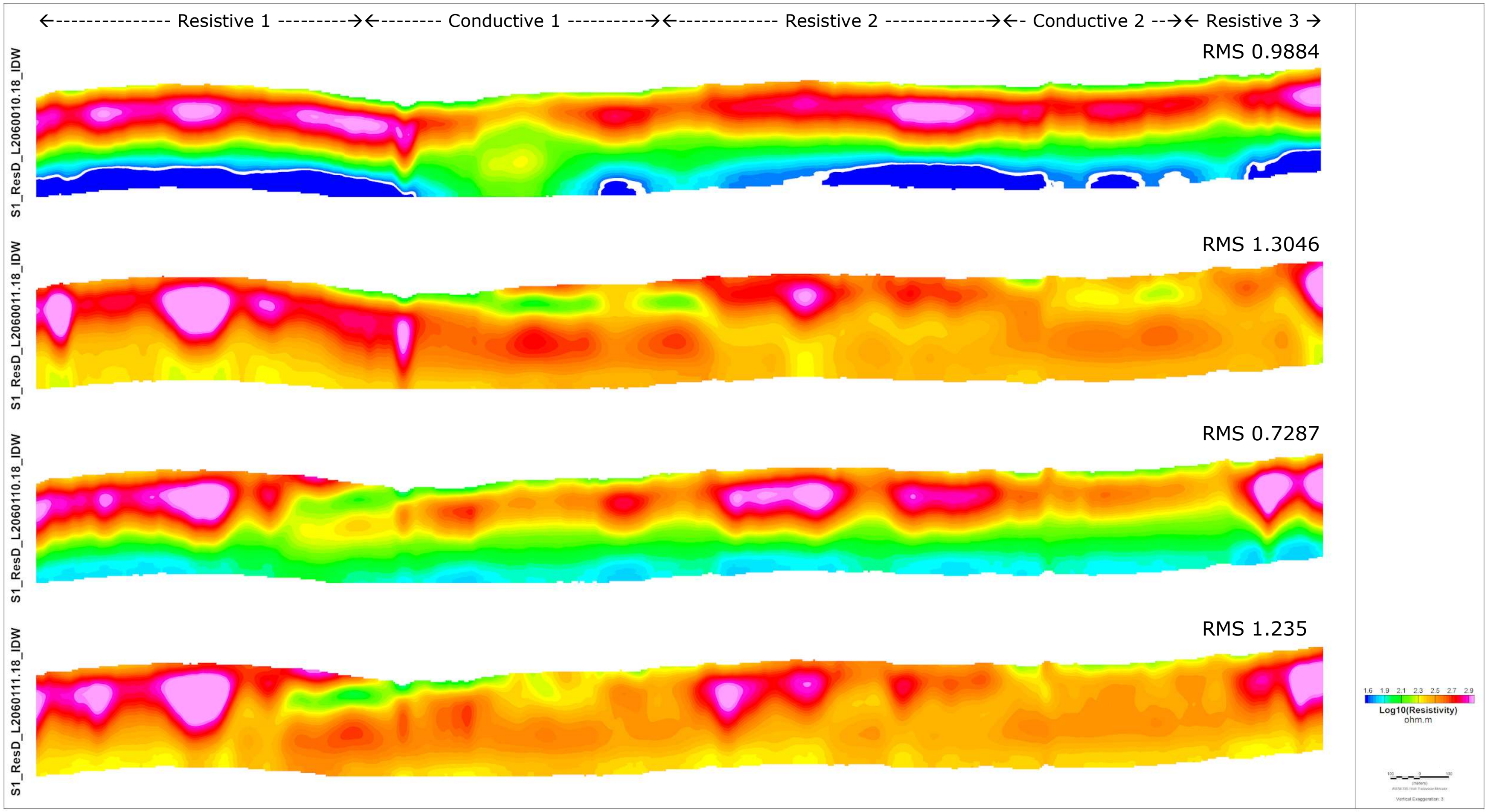

Figure 6.12: <u>Npca1 FEM response data: 2018 series</u>. 1-D inversion model resistivity sections. Line length 4.4 km, model depth extent below surface 104 m. Vertical exaggeration 3:1. SSE end of line (coastline) to left of section. Grid cell dimensions 7.2 x 2 m (horizontal x vertical), Inverse Distance Weighted, log_{10} resistivity values.

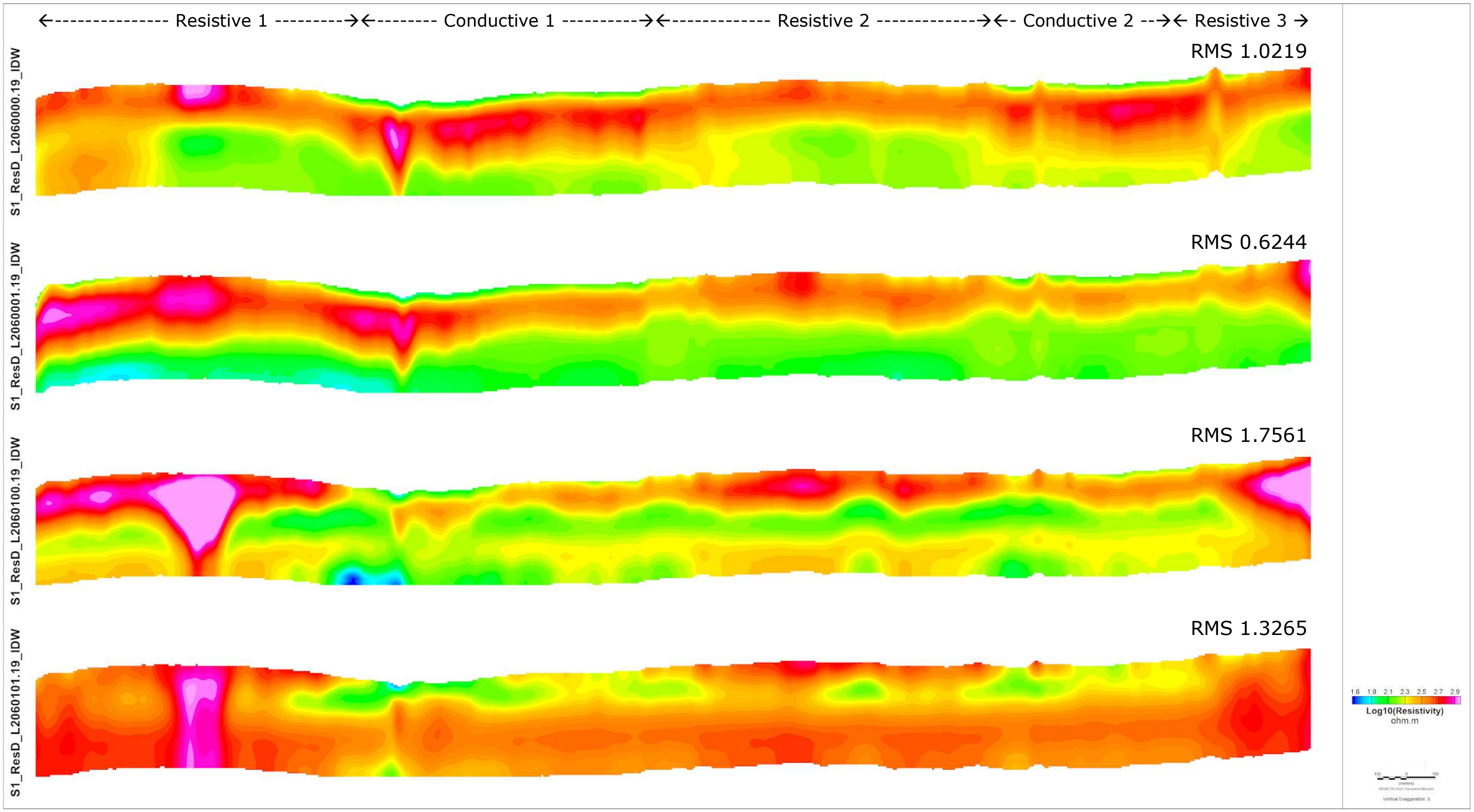

Figure 6.13: <u>Npca1 FEM response data: 2019 series</u>. 1-D inversion model resistivity sections. Line length 4.4 km, model depth extent below surface 104 m. Vertical exaggeration 3:1. SSE end of line (coastline) to left of section. Grid cell dimensions 7.2 x 2 m (horizontal x vertical), Inverse Distance Weighted, log_{10} resistivity values.

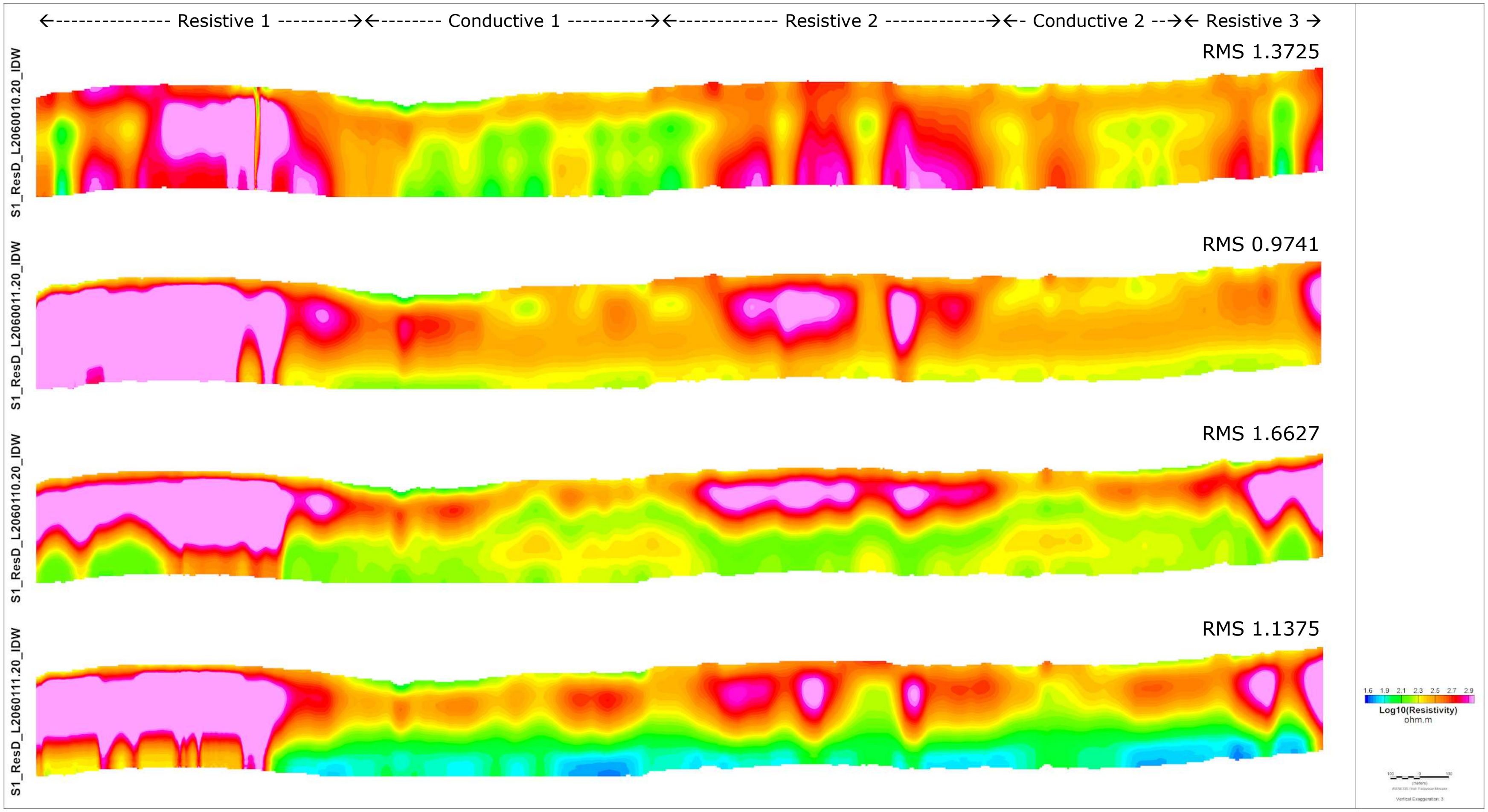

Figure 6.14: <u>Npca1 FEM response data: 2020 series</u>. 1-D inversion model resistivity sections. Line length 4.4 km, model depth extent below surface 104 m. Vertical exaggeration 3:1. SSE end of line (coastline) to left of section. Grid cell dimensions 7.2 x 2 m (horizontal x vertical), Inverse Distance Weighted, log_{10} resistivity values.

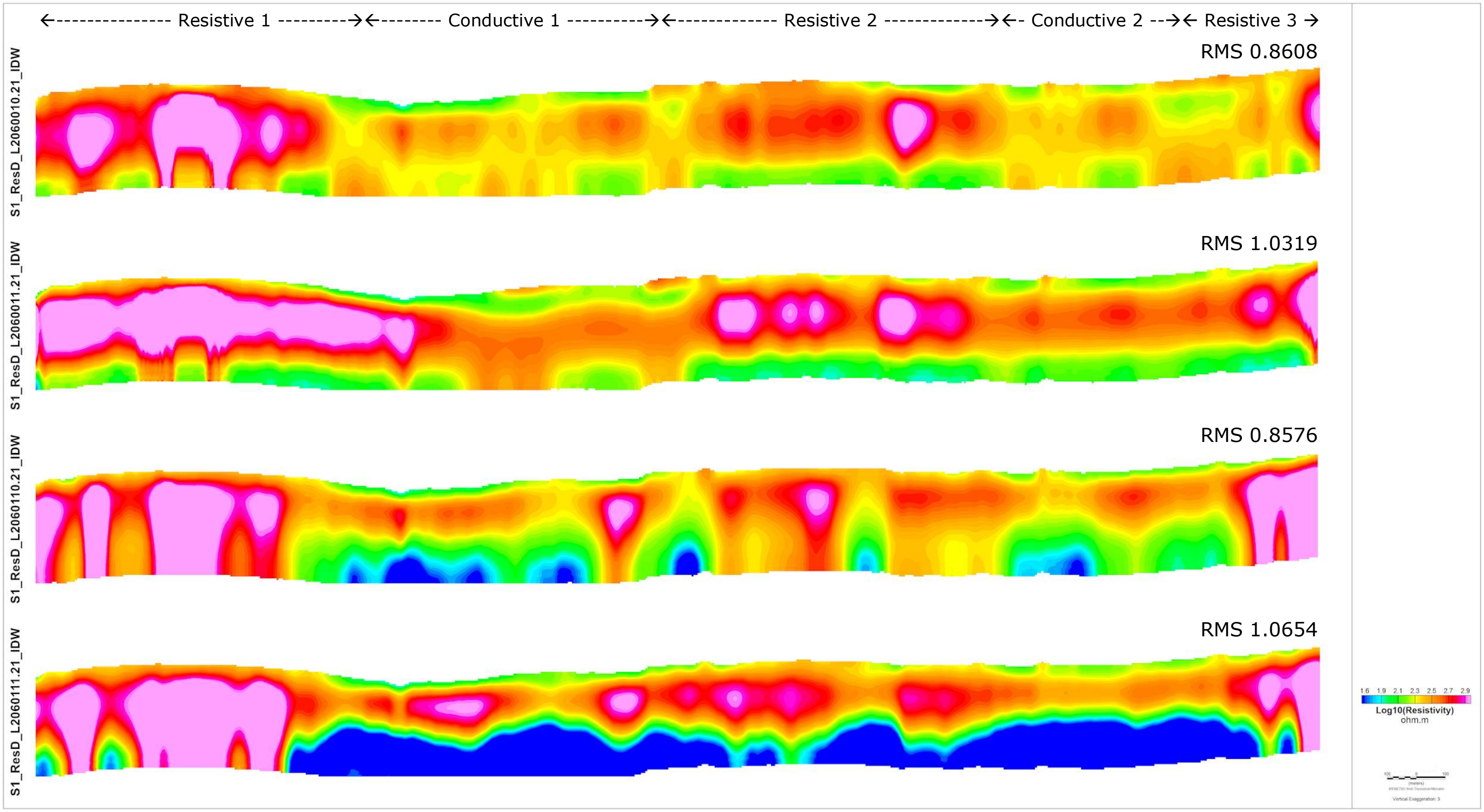

Figure 6.15: <u>Npca1 FEM response data: 2021.1 series</u>. 1-D inversion model resistivity sections. Line length 4.4 km, model depth extent below surface 104 m. Vertical exaggeration 3:1. SSE end of line (coastline) to left of section. Grid cell dimensions 7.2 x 2 m (horizontal x vertical), Inverse Distance Weighted, log_{10} resistivity values.

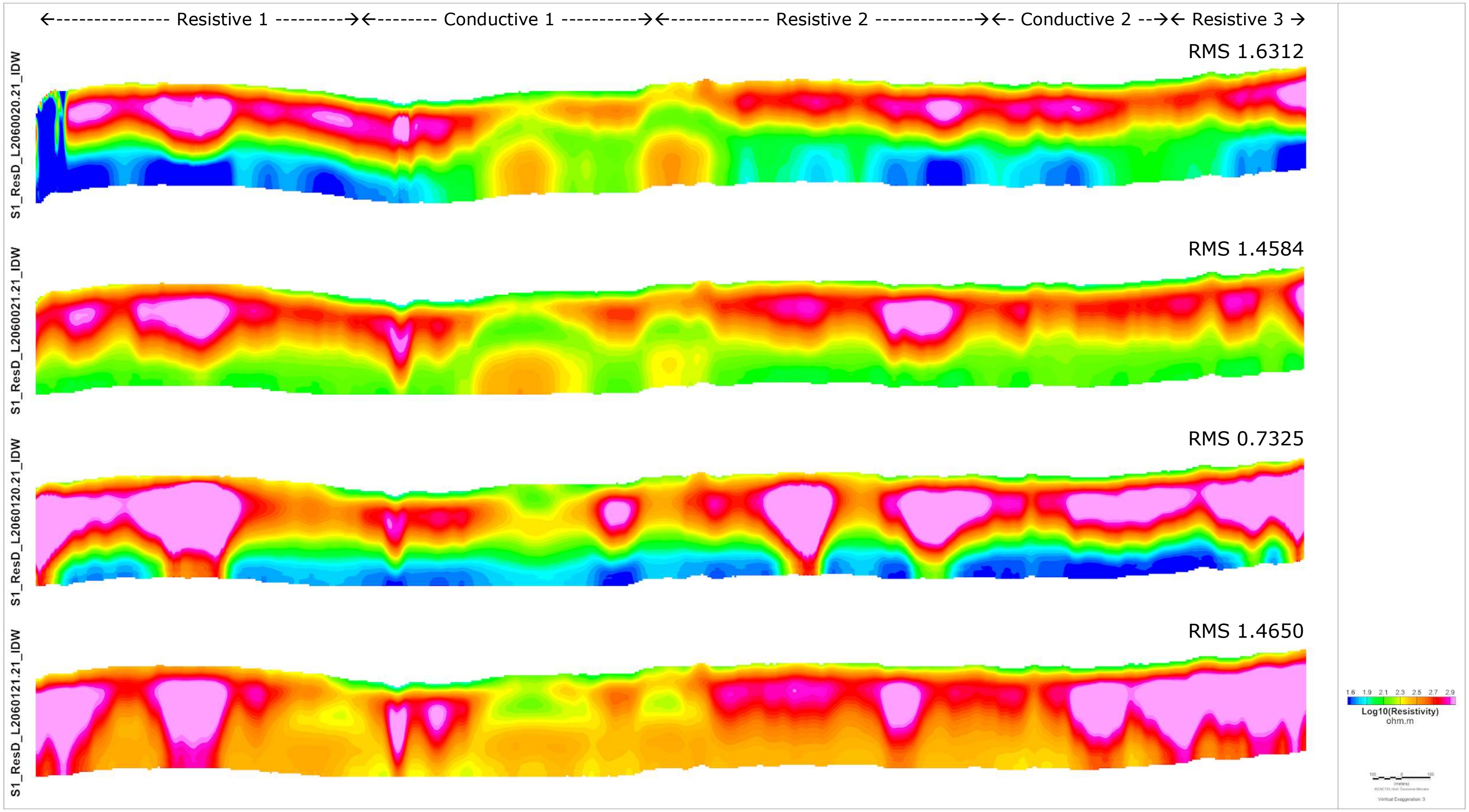

Figure 6.16: <u>Npca1 FEM response data: 2021.2 series</u>. 1-D inversion model resistivity sections. Line length 4.4 km, model depth extent below surface 104 m. Vertical exaggeration 3:1. SSE end of line (coastline) to left of section. Grid cell dimensions 7.2 x 2 m (horizontal x vertical), Inverse Distance Weighted, log_{10} resistivity values.

7 Conclusions and Recommendations

Variability in Tellus FEM data acquired during twenty repeat flights along the onshore portion of the Waterford test-line has been assessed. Five sorties (series), of four repeat flights each, were flown between 2019 and 2021. Data variability was assessed statistically by computing data means and standard deviations of the mean, across all twenty flights and across the four flights of each series. To facilitate the computation of the statistics, FEM (and other complimentary) data were interpolated and sampled at a constant 1 m distance interval along the flight lines, starting from a zero-distance reference-line, oriented perpendicular to the flight-line direction, located at the southern end of the onshore part of the test-line. A tightly constrained 'one-way' cubic spline was used for the interpolation, to avoid overshoot and undershoot of peaks and troughs in the original data. Computing averages (and standard deviations) at each distance interval along the line effectively amounts to an averaging of the data in a direction perpendicular to the flight-line direction.

Variability of the eight recorded EM responses (P09lev, P3lev, P12lev, P25lev, Q09lev, Q3lev, Q12lev and Q25lev data channels) along the test-line was assessed. Variability in flight clearance, flight speed, flight heading, power-line monitor, temperature, topography, perpendicular distance from the 'average' line and swath-width was also assessed to identify parameters that might correlate with and account for any variability observed in the FEM responses.

Variability in resistivity models derived independently for each FEM frequency was also assessed. Two resistivity datasets were evaluated: SGL's 'Extended Resistivity' models and Geosoft HEM resistivity models. The advantage in assessing the resistivity models is that the effect of flight-clearance variability on the FEM responses is, in principle, subdued or removed.

Principal Component Analysis filters were applied to the FEM response data (implemented using *aempy* software) to assess whether the filter application results in a reduction in the variability of the EM responses and to gain insights into the nature of the EM data signals – both geological and cultural noise signals – that might account for the observed FEM response variability.

1-D EM resistivity inversion models were computed for all twenty repeat flights, using the *aempy* code, to assess the extent to which variability in the FEM responses results in variability in the output resistivity models. Potential variability in the FEM responses due to variability in flight-clearance is effectively removed through the inversion process as clearance is an input parameter accounted for in the inversion models. 1-D models (in the form of gridded 2-D resistivity cross-sections), derived from both the original FEM response data and 'Npca1' filtered FEM responses, are presented for visual assessment in the report. The 'Npca1' filter is a Principal Component Analysis filter that retains only the most significant Principal Component of the data in the reconstructed (filtered) FEM responses and therefore provides opportunity to model the EM signal that is coherent across all eight FEM data components.

7.1 Conclusions

i. The wavelength content of the FEM data was examined using 1-D FFT (Fast Fourier Transform) spectral analysis of the in-phase and quadrature data profiles, for each of the four frequencies, along the repeat flight-lines. The analysis indicated no data signal present above background noise levels for wavelengths less than 30 m, and negligible signal content along the profiles at wavelengths less than about 100 m. In the absence of significant signal wavelengths (λ) less than 100 m, a λ/16 criterion (defining the maximum allowable in-line shift of anomalies) suggests that reliable averaging of the data (and computation of standard deviation statistics) across the ~15 m swath-width of the repeat test flights will be maintained for all geological strike-angles up to around 22° (where strike-angle is defined with respect to the perpendicular to the flight-line direction). Allowing for a minimal contribution of wavelengths less than 150 m to the recorded data, reliable data averages and standard deviations might be maintained up to geological strike-angles of around 32°.

ii. The lateral size of the 'at surface' EM induction footprint was examined by referring to the previous work of Liu and Becker (1990), Kovacs et al. (1995), Beamish (2003) and Yin et al. (2014). With the exception of Beamish (2003), the studies define the footprint size based on the sub-surface volume (and corresponding surface area) contributing 90% of the secondary magnetic signal at the EM receiver. Beamish (2003) defines a smaller footprint, based on a subsurface volume (and surface area) accounting for ~63% of the electric-field induced by the EM transmitter. The at-surface EM footprint for the horizontal magnetic dipole (HMD), vertical co-planar (VCP) loop configuration of the Tellus system is oval in shape, with its long axis oriented perpendicular to the flight-line direction. The primary control on the size of the footprint is the flight-height, and secondary controls are the transmitter frequency and the ground resistivity – the footprint is larger for greater flight-heights, lower frequencies and higher resistivities. The absolute minimum size of the footprint for a 60 m flight-height is ~80 m, for all frequencies, defined for an infinitely conductive subsurface (Liu and Becker, 1990 and Kovacs et al., 1995, using a 90% of magnetic signal criterion). For a 10 kHz transmitter frequency, 60 m flight-height and ground resistivities of 10 Ω.m and 1000 Ω.m, the long-axis footprint dimensions (perpendicular to the flight-line direction) are 159 m and 337 m respectively (Yin et al., 2014, using a 90% of magnetic signal criterion) and 134 m and 181 m respectively (Beamish, 2003, using a ~63% of electric-field criterion).

The primary conclusion is that, for a 60 m flight-height, for all four Tellus frequencies and for all ground resistivities encountered, the size of the EM footprint perpendicular to the flight-line direction is large with respect to the ~17 m maximum swath-width of the twenty repeat flights. Very similar EM responses (of geological origin) should, therefore, be expected on each of the four repeat flights flown within each flight-series. Real subsurface hydrogeological (and hence resistivity) variation may, however, be expected between each of the five separate flight-series.

iii. Variability in the 12 and 25 kHz FEM responses. The primary control observed on the variability of the 12 and 25 kHz FEM responses is variability in flight clearance. Within each series of four repeat flights (intra-series variation) an inverse correlation is observed between line-mean EM response amplitude and line-mean flight clearance, with higher clearances corresponding with lower EM response amplitudes, for both the in-phase and quadrature components. Locations of high EM response (intra-series) variability along the test-line correspond with locations of high flight-clearance variability. Inter-series variation (i.e., across all twenty repeat flights acquired during the five series flown) in line-mean EM response amplitudes is markedly higher for the 25 kHz and 12 kHz EM responses, for both in-phase and quadrature components, than for the 0.9 and 3 kHz responses. Inter-series variation in mean flight-clearance appears unlikely to account for the inter-series variation in mean EM response amplitudes at 25 and 12 kHz, which may be better accounted for by (i) real seasonal variation in the shallow subsurface resistivity structure, (ii) differences (potential inaccuracies) in the zero levels defined for each of the EM components for each flight-line and flight-series (dependent on calibration and drift corrections applied) and/or (iii) variable levels of cultural noise recorded during each flight-series. The impact of cultural noise on the 12 and 25 kHz EM responses appears, however, to be relatively insignificant when compared to its impact on the 0.9 and 3 kHz responses.

iv. Variability in the 0.9 and 3 kHz FEM responses. Variability in the 0.9 and 3 kHz EM responses is characterised by lower sensitivity to flight-clearance variability than for the 12 and 25 kHz data: while some sensitivity to flight clearance is apparent in the quadrature components at both frequencies, little sensitivity is apparent in the in-phase components. The dominant cause of variability in the 0.9 and 3 kHz EM responses is interpreted to be variability in the cultural noise signal recorded on each of the twenty repeat flights (a signal variability that is not in evidence in the data of the two higher frequencies – see discussion below on the Principal Component Analysis results). Peaks in EM response variability (i.e., standard deviation) are observed at nine distinct locations along the test-line (referred to as locations N1 to N9 in the report and figures). While all nine data variability peaks are apparent in the twenty-line standard deviation profiles, various subsets of the nine appear in the five different series (of four lines each), indicating that the noise sources at each location along the line were not all 'active' during all of the five flight-series. The distinct variability peaks observed in the 0.9 and 3 kHz EM responses for each of the four-line series, inferred to be the result of cultural noise, suggests that either (i) the noise signal is temporally variable over the time period between each of the four flights, or (ii) the noise signal recorded depends strongly on the distance between the aircraft and the noise source, which is different on each of the four repeat flights of each series (by up to a maximum distance of 14 m).

v. Correlation between EM response variability and variability in other measured parameters. Along-line profiles of variability in flight clearance, flight speed, flight heading, powerline monitor, temperature, topography, perpendicular distance from the ‘average’ line and flight swath-width have been visually compared with variability in the data of the eight EM responses. Two spatial correlations were identified: (i) between flight-clearance variability and EM response variability at 12 and 25 kHz, and (ii) between powerline monitor variability and EM response variability at 0.9 and 3 kHz, at the location of the single high-voltage powerline crossing the test-line (at noise location N4). It has proven difficult to track visually any further obvious correlations between the EM response variability and the variability in the measured/calculated parameters. The possibility of applying multivariate statistical approaches to draw out correlations between the standard deviation (variability) profiles of all the measured parameters and the EM responses is worth considering.

vi. Effect of Principal Component Analysis (PCA) filters on FEM data variability. The effects of Npca1, Npca2 and Npca3 Principal Component Analysis filters, applied to the EM response data, have been examined in comparison with the original, unfiltered data. The Npca1 filter retains only the first, most significant, principal component in the output (filtered) FEM data, the Npca2 filter retains the first two most significant principal components, and the Npca3 filter retains the first three. Considering the 12 and 25 kHz FEM data and examining the PCA filter impact on the twenty-line variability (standard deviation) along the test-line, it is apparent that there is only a moderate change in the data variability as the PCA filter strength is increased from Npca3 to Npca1, and compared with the original data. The implication is that the bulk of the data variability at 12 and 25 kHz is resident in the first principal component, and that the second and third principal components add little to the data variability. Considering the 0.9 and 3 kHz FEM data, the profiles of (twenty-line) variability along the test-line are little changed in the original, Npca3 and Npca2 datasets, with all these datasets retaining the nine high data-variability peaks along the line (these peaks inferred, as discussed above, to be the result of variability in the cultural noise signal). In contrast, the data variability is substantially reduced in the 0.9 and 3 kHz Npca1 datasets, with the nine high data-variability peaks being largely subdued or absent. The behaviour of the data variability across all four data frequencies in response to the Npca1 filter is interpreted as indicating that Principal Component 1 contains the bulk of the coherent (geological) signal in the data at all frequencies and that

Principal Components 2 and 3 contain substantial signal (interpreted as noise) at 0.9 and 3 kHz that (i) is not coherent with the signal in Principal Component 1 and (ii) is highly variable from line-to-line (at specific locations along the line).

vii. Variability in single-frequency resistivity models at 0.9, 3, 12 and 25 kHz. Two sets of single-frequency resistivity models were examined: contractor SGL's 'Extended Resistivity' models and GSI's HEM resistivity models (derived by half-space inversion using Geosoft's HEM software module). The former models are restricted to an upper resistivity limit equal to the transmission frequency. Although the HEM models have no explicit upper resistivity limit applied to the models, it is the case that many null model solutions are returned for the 0.9 and 3 kHz EM data over highly resistive portions of the test-line. In contrast with the EM response data (and particularly the 12 and 25 kHz data components), it is apparent, with few exceptions, that no sympathetic relationship exists between line-mean resistivities and line-mean clearances and that the effect of flight clearance variation on the EM responses has largely been removed in the resistivity modelling. In the case of the 12 and 25 kHz data, the along-line variability observed in the original EM responses, ascribed primarily to flight clearance variation, is significantly reduced in the resistivity models. In the case of the 0.9 and 3 kHz data, the high-amplitude variability peaks present in the EM responses (i.e., the variability peaks present at locations N1 to N9), ascribed to cultural noise variation, are carried through into the resistivity models. Both sets of resistivity models are characterised by poor recovery of subsurface resistivity in resistive areas in the 0.9 and 3 kHz data, largely due to cultural noise. Cultural noise in the EM responses gives rise to very high and very low resistivity spikes on the test-line, often in close proximity to each other, and in such instances, neither the twenty-line nor the four-line series resistivity-means are likely to have recovered resistivity values close to the real subsurface resistivity.

Standard errors of the mean (derived from the data standard deviations) for the resistivity models for each series of four flights at 12 and 25 kHz lie in the range 0.02 – 0.08 $\log_{10}(\Omega.m)$ (or 5 – 20% error). A similar error assessment is not meaningful for the 0.9 and 3 kHz resistivity models as they are dominated by the effects of cultural noise – the measured variability does not reflect an uncertainty in estimating the geological resistivity structure, but rather reflects the variability in the cultural noise signal. With the effects of EM cultural noise being much lower in the 12 and 25 kHz frequencies, it may be the case that the variability in the resistivity models at these frequencies reflects the 'whole-system' measurement accuracy, which incorporates, for example, the system electronic noise, the accuracy of the zero level calibrations and drift corrections, the accuracy of the resistivity modelling methods and the extent to which flight clearance variation is accounted for in the modelling.

viii. Appraisal of 1-D inversion resistivity models, derived for all twenty repeat flights using both the original ('lev') EM response data and the Npca1 filtered EM responses. Layered, 1-D resistivity models at each measurement location were derived using *aempy* software and subsequently gridded to produce 2-D resistivity cross-sections for each repeat line for visual appraisal. Comparing the original-data models and the Npca1 models for each repeat flight, the latter are characterised by significantly greater lateral continuity and stability. The original-data models are broadly comprised of the same, or very similar, underlying resistivity structure present in the Npca1 models, onto which short-wavelength, very-high and very-low resistivity structures are superimposed, most visibly in the depth range below about 50 m but extending upwards to shallower depths in places. The sharp lateral transitions from conductive to resistive features observed in the original-data model sections are interpreted to be artefacts arising from the modelling of cultural noise signals in, primarily, the 0.9 and 3 kHz EM data and are unlikely to be of geological origin. It is not immediately apparent from a visual inspection of the sections, particularly the clearer/cleaner Npca1 sections, whether the variability apparent in the resistivity model sections is greater between series (potentially indicating seasonal variation in the shallow resistivity structure) or whether the variability is equally as significant between the four repeat flights within each series. A more detailed quantitative assessment than has been possible within the scope of this work (and suggested in the recommendations below) will be required to understand which aspects of the EM response data variability account for the variability, in detail, of the resistivity inversion models.

7.2 Recommendations for Future Work

Several recommendations are made for work that aims to provide further understanding of the variability observed in the FEM responses and in the derived resistivity models.

i. Investigate, on the ground, the nine test-line locations corresponding with data variability peaks in the 0.9 and 3 kHz EM data: locations N1 to N9, as shown in Figure 3.30, with ITM X and Y coordinates provided in Table 3.4. It would be useful to examine circumstances on the ground at each of the nine locations, to see if a potential source of noise can be identified, possibly in discussion with local farmers.

ii. Investigate, potentially in collaboration with GSI's Groundwater and Quaternary Geology sections, the characteristics of the Quaternary overburden and shallow hydrogeology around the test-line. Consider, as well, high-temporal resolution (daily) rainfall records from the nearest measurement stations to the test-line, particularly for the weeks or the month immediately preceding each of the test flight-series. It would be useful to assess whether the variations observed from series-to-series in line-mean resistivities at 25 kHz, and the differences apparent between the 2-D resistivity model cross-sections from series-to-series, might be correlated with seasonal variations in rainfall and in the characteristics and behaviour of the shallow hydrogeological environment (and therefore in the shallow resistivity structure).

iii. Prior to committing to the work of (ii) above, however, it would be sensible to first assess whether the differences observed between the line-mean resistivities at 25 kHz (and possibly 12 kHz) from series-to-series are statistically significant, using appropriate statistical tests (for example, a t-test).

iv. It was found difficult to identify visually all possible correlations between the EM response data variability and the variability in the measured/calculated parameters (i.e., flight clearance, flight speed, flight heading, powerline monitor, temperature, topography, perpendicular distance from the 'average' line and flight swath-width). It would be worthwhile considering the possibility of applying multivariate statistical approaches to draw out correlations, if present, between the standard deviation (variability) profiles of the eight EM data components (or the resistivity models at each frequency) and the standard deviation profiles of all the measured/calculated parameters. The analysis might examine correlations in the variability across all twenty lines and across each of the four lines of each flight-series independently.

v. The 1-D resistivity inversion models that were computed in the course of this work have been presented, for visual and qualitative assessment, as 2-D resistivity cross-sections. Further insights into the variability of the EM data and the inversion models would be provided by additional *quantitative* assessment of the variability in the misfits of the models to the observed data and in the resistivity models themselves. Both the original-data ('lev') and 'Npca1' 1-D resistivity inversion models might be subjected to an analysis approach analogous to that applied to EM response data – i.e., computation of standard deviations across all twenty lines and across the four lines of each flight-series. The analysis might include assessment of: (i) variability in the model RMS errors, (ii) variability in the misfit between the observed data and the model predictions for each of the eight EM data components, and (iii) variability in the resistivity models themselves by examining the resistivity variability of, for example, the shallowest twenty-six depth layers (< 100 m depth), or of a selected subset of depth layers at different depths. The analysis would help understand which of the eight EM data components are characterised by the greatest variability in their modelling misfit and which model depths correspond with the greatest variability in their resistivity solutions.

vi. The effectiveness of the Principal Component Analysis (PCA) 'Npca1' filter in substantially removing cultural noise signals from the 0.9 and 3 kHz EM responses has been illustrated in the work of this report. While a 'weaker' Npca3 filter has been applied previously to Tellus EM data by GSI, in the 1-D inversion modelling of the A5, A6 and Waterford Blocks (the Npca3 filter being chosen for reasons described in the report above), the results presented here provide good motivation for further testing the broader application of the 'stronger' Npca1 filter to Tellus data. Further test work could consist of applying the Npca1 filter to the data of one full Tellus survey block and computing HEM single-frequency resistivity models for the block. The Npca1 EM responses and HEM resistivity models could then be compared with the original EM responses and HEM resistivity models derived from the original data – comparing both data profiles along individual lines and gridded maps of the datasets, and assessing whether geological mapping potential and lateral continuity is enhanced in the lower 0.9 and 3 kHz frequencies (through the removal of EM cultural noise), and whether the 12 and 25 kHz frequencies have suffered any loss of geological resolution through application of the filter.

While it is the case that EM cultural noise is resident in principal components 2 and higher in the Waterford test-line data, it may not be the case everywhere in Ireland. The repeat data acquired on GSI's Bundoran test-line in Co. Donegal could be similarly analysed, providing opportunity to assess the EM cultural noise characteristics in a different part of Ireland, and to assess the appropriate 'strength' of PCA filter best suited to attenuating it.

8 References

Beamish, D., 2003. Airborne EM footprints. *Geophysical Prospecting*, 51(1), 49–60, doi:10.1046/j.1365-2478.2003.00353.x.

Fraser, D.C., 1978. Resistivity mapping with an airborne multicoil electromagnetic system. *Geophysics*, 43, 144–172, doi.org/10.1190/1.1440817.

Geosoft, 2005. *HEM System – Helicopter Electromagnetic Data Processing, Analysis and Presentation System for Oasis montaj v6.2*. Tutorial and User Guide, Geosoft Incorporated, Toronto, Canada, February 2005, pp. 71.

Golub, G. and van Loan, C.F., 1996. *Matrix Computations*. The Johns Hopkins University Press, Baltimore, Maryland, 3rd Edition, pp. 694.

GSI, 2020. *Tellus Waterford (WFD) Block: aempy Electromagnetic Inversion Report*. Technical Report, Geological Survey Ireland, July 2020, pp. 77, https://gsi.geodata.gov.ie/downloads/Geophysics/Reports/Waterford_2016_AEMPY_EM_Inversion_Report.pdf

Kiyan, D. and Rath, V., 2017. *Inverse Methods for Airborne Electromagnetic Data from the Tellus Surveys: The aempy Toolbox*. Unpublished Report and User Manual, Dublin Institute for Advanced Studies, Ireland, March 21, 2017, pp. 34.

Kiyan, D., Rath, V., Muller, M.R., Ture, M.D. and Hodgson, J., 2022. 1-D Inversion of Frequency-Domain Airborne Electromagnetic Data using the Open-Source aempy Toolbox. *Journal of Applied Geophysics*, 198, doi:10.1016/j.jappgeo.2022.104562.

Kovacs, A., Holladay, J.S. and Bergeron, C.J., 1995. The footprint/altitude ratio for helicopter electromagnetic sounding of sea-ice thickness: Comparison of theoretical and field estimates. *Geophysics*, 60, 374–380, doi:10.1190/1.1443773.

Lanczos, C., 1961. *Linear Differential Operators*. D. Van Nostrand Co. Ltd, London, pp. 576.

Liu, G. and Becker, A., 1990. Two-dimensional mapping of sea ice keels with airborne electromagnetics. *Geophysics*, 55, 239–248, doi: 10.1190/1.1442832.

Minsley, B.J., Smith, B.D., Hammack, R., Sams, J.I. and G. Veloski, G., 2012. Calibration and filtering strategies for frequency domain electromagnetic data. *Journal of Applied Geophysics*, 80, 56–66.

Reninger, P.-A., Martelet, G., Deparis, J., Perrin, J. and Y. Chen, Y., 2011. Singular value decomposition as a denoising tool for airborne time domain electromagnetic data. *Journal of Applied Geophysics*, 75(2), 264–276.

SGL, 2022. *Fixed-Wing High-Resolution Aeromagnetic, Gamma ray Spectrometric and Frequency-Domain Electromagnetic Survey Tellus A9 Block, Republic of Ireland 2021 for The Geological Survey, Ireland*. Technical Report, Sander Geophysics Limited, Ottawa, Canada, March 2022, pp. 197, https://gsi.geodata.gov.ie/downloads/Geophysics/Reports/GSI_Tellus_TR_904_000.pdf

SRS1 Software, 2015. SRS1 Cubic Spline for Excel. Freeware available online at www.srs1software.com/SRS1CubicSplineForExcel.aspx.

Yin, C., Huang, X., Liu, Y. and Cai, J., 2014. Footprint for frequency-domain airborne electromagnetic systems. *Geophysics*, 79(6), E243–E245, doi:10.1190/GEO2014-0007.1.